Wegener Center for Climate and Global Change
University of Graz

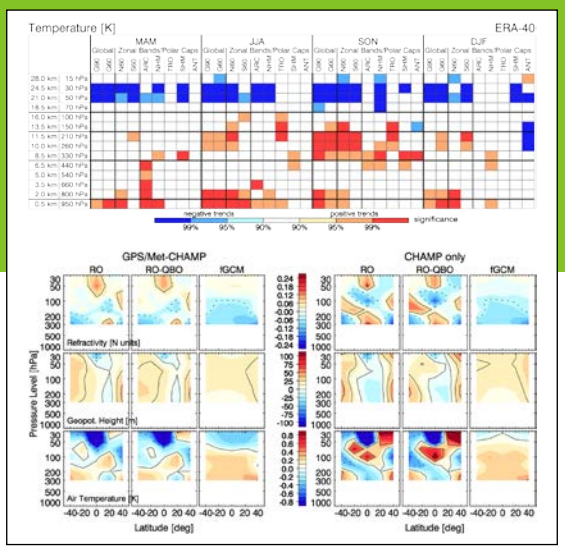

Scientific Report No. 38-2010

Exploring Trend Indicators of Climate Change From Radio Occultation and Optimal Trend Detection

Bettina C. Lackner

July 2010

Financially supported by

FWF
Der Wissenschaftsfonds.

Wegener Center
www.wegcenter.at

UNI GRAZ

The **Wegener Center for Climate and Global Change** combines as an interdisciplinary, internationally oriented research center the competences of the University of Graz in the research area „Climate, Environmental and Global Change“. It brings together, in a dedicated building close to the University central campus, research teams and scientists from fields such as geo- and climate physics, meteorology, economics, geography, and regional sciences. At the same time close links exist and are further developed with many cooperation partners, both nationally and internationally. The research interests extend from monitoring, analysis, modeling and prediction of climate and environmental change via climate impact research to the analysis of the human dimensions of these changes, i.e., the role of humans in causing and being effected by climate and environmental change as well as in adaptation and mitigation. (more information at www.wegcenter.at)

The present report is the result of a PhD thesis work completed in May 2010. The work was funded by the Austrian Science Fund (FWF) under research grants P18733-N10 (INDICATE), P21642-N21 (TRENDEVAL), and by the NSF grant ATM-0296007.

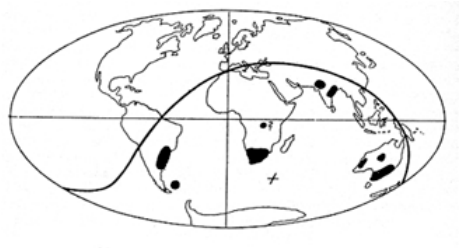

Alfred Wegener (1880-1930), after whom the Wegener Center is named, was founding holder of the University of Graz Geophysics Chair (1924-1930) and was in his work in the fields of geophysics, meteorology, and climatology a brilliant, interdisciplinary thinking and acting scientist and scholar, far ahead of his time with this style. The way of his ground-breaking research on continental drift is a shining role model — his sketch on the relationship of the continents based on traces of an ice age about 300 million years ago (left) as basis for the Wegener Center Logo is thus a continuous encouragement to explore equally innovative scientific ways: *paths emerge in that we walk them* (Motto of the Wegener Center).

Wegener Center Verlag • Graz, Austria

ISBN 978-3-9502940-5-7

July 2010

Contact: Dr. Bettina C. Lackner
bettina.lackner @uni-graz.at

Wegener Center for Climate and Global Change
University of Graz
Leechgasse 25
A-8010 Graz, Austria
www.wegcenter.at

DI Mag[a]. Bettina C. Lackner

Exploring Trend Indicators of Climate Change From Radio Occultation and Optimal Trend Detection

Dissertation

zur Erlangung des akademischen Grades einer
Doktorin der Naturwissenschaften
an der naturwissenschaftlichen Fakultät der
Karl-Franzens-Universität Graz

Betreuer:

Univ.-Prof. Mag. Dr. Gottfried Kirchengast

Dr. Andrea K. Steiner

Graz, Mai 2010 — editiert Jänner 2011

Wegener Zentrum für Klima und Globalen Wandel,
Institutsbereich Geophysik, Astrophysik und
Meteorologie des Institutes für Physik
Karl-Franzens-Universität Graz

Abstract

The upper troposphere-lower stratosphere (UTLS) region is reacting particularly sensitive to climate change and variations of its key parameters are promising candidates for the monitoring and diagnosis of climate change. The satellite-based radio occultation (RO) method provides high quality measurements of atmospheric parameters in the UTLS featuring characteristics such as long-term stability, self-calibration, and very good height resolution. This thesis assesses the potential of RO parameters as climate change indicators and the climate change detection capability of the RO record.

For the trend indicator study, 2 re-analyses and 3 representative global climate models (GCM) were used as proxy data for the still short RO record. Seasonal means were systematically explored to find the most robust and sensitive trend indicators based on agreement amongst single model simulations, statistical trend significance, and goodness-of-fit. Different investigated spatial domains allowed a mapping of regions particularly suitable as trend indicators. Refractivity, pressure and respective layer gradients alone turned out as adequate trend indicators. In addition, temperature is a sensitive indicator directly showing UT warming and LS cooling.

For climate signal detection an optimal fingerprinting method was applied to the monthly mean RO record. UTLS trends of RO refractivity, geopotential height, and temperature were investigated for two periods. Characteristics of the data and atmospheric variability patterns were discussed. Results showed that a climate change signal consistent with the projections of the GCMs can be detected for temperature with 90 % confidence. Lower confidence levels are achieved for the refractivity record. For geopotential height the results are uncertain as the variances between models and observations were found to be only marginally consistent.

Overall the results underline the benefit of RO data for climate science.

Zusammenfassung

Die Region der oberen Troposphäre und unteren Stratosphäre (UTLS) reagiert besonders empfindlich auf den Klimawandel. Veränderungen von Schlüsselparametern in dieser Region sind vielversprechende Kandidaten zur Beobachtung des Klimawandels. Die satellitenbasierte Radiookkultationsmethode (RO) stellt hochqualitative Messungen atmosphärischer UTLS Parameter zur Verfügung, die Charakteristika wie Langzeitstabilität, Selbstkalibrierung und sehr gute Höhenauflösung aufweisen. Diese Dissertation beinhaltet eine Potenzialanalyse verschiedener Radiookkultationsparameter als Klimawandelindikatoren und eine Klimawandeldetektionstudie basierend auf RO Daten.

In der Trendindikatorenstudie wurden Proxydaten von 2 Reanalysen und 3 globalen Klimamodellen für den noch kurzen RO Datensatz verwendet. Saisonale Mittelwerte wurden systematisch analysiert, um die robustesten und sensitivsten Trendindikatoren zu finden, welche auf der Übereinstimmung von Trends verschiedener Simulationen, statistischer Trendsignifikanz, und Anpassungsgüte basieren. Die Untersuchung mehrerer Regionen erlaubte eine Identifikation von Gebieten, welche gut als Trendindikatoren geeignet sind. Refraktivität, Druck und die entsprechenden Schicht-Gradienten erwiesen sich als adäquate Trendindikatoren der UTLS.

Die Detektion eines anthropogen bedingten Klimasignals in monatlichen RO Daten wurde mit einer Fingerprinting Methode untersucht. UTLS Trends in Refraktivität, geopotentieller Höhe und Temperatur wurden für 2 Perioden analysiert. Datencharakteristika und Muster atmosphärischer Variabilität wurden diskutiert. Die Resultate zeigen für Temperatur ein Klimaänderungssignal konsistent zu den Modellprojektionen auf einem 90 % Signifikanzniveau. Geringere Signifikanzniveaus werden für Refraktivität erzielt, während für geopotentielle Höhe noch Unsicherheiten bezüglich der Varianzen zwischen Modellen und Beobachtungen bestehen.

Die Ergebnisse unterstreichen den Nutzen der RO Daten für die Klimaforschung.

Hinter meiner, vorder meiner, links, rechts güts nix
Ober meiner, unter meiner siach i nix.
Spür nix, hear nix und i riach nix.
Denk i nix und red i nix und tu i nix.
Waun da Wind wahd in de Gossn
waun da Wind wahd am Land
waun da Wind wahd, do steckt da
sein Köpferl in Sand.

aus Arik Brauer's beinhartem Protestlied "Sein Köpferl im Sand", 1971
... ein sehr menschliches aber, auch aus klimawissenschaftlicher Sicht,
nicht sinnvolles Verhalten.

Acknowledgments

Writing a thesis is a lonesome work. But until I could start to put my results down on paper, many people have given me their support to come this far.

I am very thankful to *Prof. Gottfried Kirchengast*, head of the Wegener Center, for advising me as PhD student, for his experienced guidance, for teaching me to scrutinize my work, for opening doors to other institutions, and for exemplifying to take pleasure in doing research through his own life. His proposals were always a valuable enrichment of my work.

Many thanks to *Dr. Andrea Steiner*, project leader of the Austrian Science Fund projects INDICATE and TRENDEVAL, for giving me the opportunity to participate in the projects and thereby to accomplish this thesis. I am very grateful for her scientific input and feedback in numerous discussions, for encouraging and financing me to present my research at various conferences, for facilitating my research stay in Edinburgh, and for the chocolate bars in lean times.

I feel very fortunate to have had the chance to be familiarized with the optimal fingerprinting technique by *Prof. Gabi Hegerl* at the School of GeoSciences, University of Edinburgh. I want to thank her very much for her scientific support and guidance, for the time she dedicated to answer my endless questions, and for the warm welcome and financial support she gave me in Edinburgh. Thanks also for being available as second assessor of the thesis, I hope that at least some sections will give her new insights in our data and therefore compensate for the time she had to spend for the assessment.

I thankfully acknowledge the discussions with and the support from my colleagues at the Wegener Center. The ARSCliSys research group is thanked for the provision of RO data. I especially thank *Florian Ladstädter*, my colleague in the INDICATE project team, for various discussions and great support in all computer and programming issues, and *Barbara Pirscher* for the provision of RO data.

Furthermore, I most sincerely thank my husband *Rudi*, who, like a breakwater wall, tried hard to keep away from me, or to calm at least, the rough seas live offered during the last years.

Building my work on several data sets, I acknowledge the following institutions for providing their data sets. UCAR/CDAAC (Boulder, CO, USA) is acknowledged for the provision of GPS/MET and CHAMP RO phase delay and orbit data. ECMWF (Reading, UK) is acknowledged for access to their global operational analysis, re-analysis and forecast data, Hadley Centre/MetOffice (Exeter, UK) for the provision

of HadAT2 radiosonde data; NOAA/OAR/ESRL PSD, Boulder, Colorado, USA, for making available NCEP Re-analysis derived data; I acknowledge the modeling groups, the Program for Climate Model Diagnosis and Intercomparison (PCMDI) and the WRCP's Working Group on Coupled Modelling (WGCM) for their roles in making available the WRCP CMIP3 multi-model dataset. Support of this dataset is provided by the Office of Science, US Department of Energy. The Climate Prediction Center (US) is acknowledged for making ENSO and QBO indices available.

This work was funded by the Austrian Science Fund (FWF) under research grants P18733-N10 (INDICATE), P21642-N21 (TRENDEVAL), and by the NSF grant ATM-0296007.

Contents

List of Acronyms

Symbols

N refractivity. 8, 22, 50, 53, 61, 62, 71, 92, 93, 155, 157

T temperature. 9, 22, 46, 50, 53, 61, 71, 92, 93, 157

W mass of condensed water in the atmosphere. 10

Z geopotential height. 22, 40, 43, 44, 49, 50, 61, 62, 64, 66, 71, 72, 83, 85, 89, 90, 92, 93, 136, 155, 157

α bending angles. 8, 22, 50

f frequency. 9

n_e electron density. 9

p pressure. 9, 22, 40, 43, 46, 49, 50, 53, 61, 62, 64, 66, 71–73, 85, 89, 90, 92, 98, 125, 136, 155, 157

p_w partial water vapor pressure. 9

q specific humidity. 13, 46, 50

20C3M climate of the 20th century experiment. 32–34, 40, 64, 94

A

AIRS Atmospheric Infrared Sounder. 16

AMSU Advanced Microwave Sounding Unit. 16

ANN annual mean. 44, 68, 75, 78, 80, 85, 86, 88–90, 136

AR4 Fourth Assessment Report. 2, 30–35, 37, 38, 49, 50, 66, 89, 91, 92, 104, 129, 135, 154

C

CCM Community Climate Model. 31

CCSM3 Community Climate System Model 3. 2, 31, 33, 35, 37, 40, 48, 64, 69, 70, 76, 78, 83, 89, 94, 120, 121, 130–132, 135, 155

CDAAC COSMIC Data Analysis and Archive Center. 21

CH_4 methane. 33

CHAMP Challenging Mini-Satellite Payload. vii, 2, 15–18, 21–24, 38, 40, 64, 93–96, 115–120, 122, 124–133, 137

CLIPS Climatology Processing System. 15, 22

CMIP3 phase 3 of the Coupled Model Intercomparison Project. 30

CO_2 carbon dioxide. 3, 4, 6, 27, 33, 34, 38

CONTROL second statistically independent sample of PICTRL data. 97, 98, 100–102, 122, 127, 128, 132, 133, 137

CPC Climate Prediction Center. 104

CSM Climate System Model. 31

D

D&A detection and attribution. 91

DJF December–January–February. 44, 64, 68–72, 75, 76, 78–80, 85, 86, 88

DOF degrees of freedom. 57–59

E

ECHAM5 ECMWF Hamburg Model. 2, 13, 14, 31, 33, 35, 37, 38, 40, 48, 63, 64, 66, 67, 69, 70, 78, 83, 89, 92, 94, 120, 121, 135, 136, 155, 158

ECHAM ECMWF–MPI-M Hamburg [general circulation model]. 31

ECMWF European Centre for Medium-Range Weather Forecasts. vii, 8, 11, 12, 15–18, 27, 31, 166

ECV Essential Climate Variables. 6

EGM96 Earth Gravity Model 1996. 12

EGOPS End-to-End Generic Occultation Performance Simulation and Processing System. 41–43, 46, 151

ENSO El Niño-Southern Oscillation. viii, 26, 31, 53, 60, 92, 96, 103–108, 110–114, 126, 129, 133, 137

Envisat Environmental Satellite. 17

EOF Empirical Orthogonal Function. 97–103, 106, 122–133

ERA-40 ECMWF Re-Analysis. 2, 11, 12, 15, 26–28, 40, 43, 48, 52, 53, 60, 61, 64–66, 68–71, 73–75, 78–82, 86–90, 92, 96, 105, 106, 108, 110–114, 120, 122, 135, 136, 155–157

ESG Earth System Grid. 31

F

F11 trichlorofluoromethane. 33

F12 dichlorodifluoromethane. 33

fGCM average of the 20 SRES A2 and B1 GCM simulations. 94–98, 100, 101, 104, 111, 115, 117, 119–125, 129–132

FORMOSAT-3/COSMIC Formosa Satellite Mission #3/Constellation Observing System for Meteorology, Ionosphere, and Climate. 15, 17, 38, 83

G

GCM General Circulation Model. 1, 2, 30–33, 35, 36, 38–41, 43, 44, 46, 48–50, 60, 61, 64–73, 75–80, 83, 84, 86, 88–97, 100, 103, 104, 106, 111, 112, 117, 119–121, 123, 129, 130, 133, 135–138, 156–158

GCOS Global Climate Observing System. 5, 6

GDP gross domestic product. 34

GHG Green House Gas(es). 4, 7, 17, 27, 28, 32, 34, 37, 102, 115, 125, 127

GNSS Global Navigation Satellite System. 1, 7, 16, 18, 135, 138

GOF goodness of fit. 58, 60, 61, 75–81, 83, 85, 86, 89, 136, 155–158

GOMOS Global Ozone Monitoring for Occultation of Stars. 17

GPS Global Positioning System. 6–8, 10, 17, 21

GPS/MET Global Positioning System/Meteorology. vii, 2, 11, 12, 15–18, 21–23, 38, 40, 90, 93–96, 107, 115–119, 122, 124–133, 137, 138

GRACE Gravity Recovery and Climate Experiment. 15, 17

H

HadAT2 Hadley Centre gridded free-atmosphere temperatures from radiosondes. viii, 2, 24, 26, 92, 96, 117–119, 133, 137

HadC Hadley Centre for Climate Prediction and Research. 31, 32

HadCM3 Hadley Centre Coupled Model, version 3. 2, 31–33, 35, 38, 48, 64, 69, 78, 83, 89, 94, 120, 121, 135, 155

I

IASI Infrared Atmospheric Sounding Interferometer. 16

IDL Interactive Data Language. 44, 106

INDICATE Indicators of Atmospheric Climate Change from Radio Occultation. 40

IPCC Intergovernmental Panel on Climate Change. 2, 4, 27, 30–35, 37, 38, 49, 50, 66, 76, 89, 91, 92, 104, 129, 135, 154

IPCC$^+$ IPCC (2007) regions and large-scale zonal mean bands. 50, 51, 75, 81, 154

IR Infrared. 7

J

JJA June–July–August. 44, 68, 75, 78, 80–82, 86, 88–90, 136

L

LEO Low Earth Orbit. 7, 8, 10

LS lower stratosphere. 6, 10, 17, 27, 37, 38, 44, 47, 50, 64–66, 68–70, 72, 75–78, 80, 82, 83, 85, 86, 88–90, 92, 95, 113, 117, 119, 120, 122, 129, 136

M

MAECHAM5 Middle Atmosphere Mode of ECMWF Hamburg Model, version 5. 37, 48, 49, 66–68, 89, 136, 156–158

MAM March–April–May. 44, 64, 66–68, 75, 80, 86, 88

MetOp Meteorological Operational satellite. 16

MIPAS Michelson Interferometer for Passive Atmospheric Sounding. 17

MLR multiple linear regression. 103–105, 108, 112–116

MPI Max Planck Institute. 169

MPI-M Max Planck Institute for Meteorology. 31, 37, 166

MSISE-90 Extended Mass Spectrometer–Incoherent Scatter Model of the Upper Atmosphere. 11, 12

MSL mean sea level. 12, 22, 39, 40, 43, 44, 136

MSU/AMSU (Advanced) Microwave Sounding Unit. 7, 17, 18, 91, 92

MW Microwave. 7, 46

N

N_2O nitrous oxide. 33

NCAR National Center for Atmospheric Research. 26, 28, 31

NCEP National Centers for Environmental Prediction. 26, 28, 31

netCDF Network Common Data Format. 29, 38

NH Northern Hemisphere. 116, 117

NOAA National Oceanic and Atmospheric Administration. 104

NRA NCEP/NCAR Re-Analysis. 2, 26–29, 43, 48, 61, 64, 65, 68–70, 135, 155–157

O

O_3 ozone. 27, 33, 35, 37

OLS ordinary least-squares. 97, 98, 101, 104

OPSv54 Occultation Processing System Version 5.4. 9–12, 22

P

PCMDI Program for Climate Model Diagnosis and Intercomparison. 30, 35, 40

PDF Portable Document Format. 155

PICTRL pre-industrial control experiment. 32–34, 40, 96–103, 106, 111, 120–122, 125, 133

ppmv parts per million by volume. 3, 38

Q

QBO Quasi-Biennial Oscillation. viii, 31, 53, 64, 92, 95, 96, 103–109, 111–114, 117, 119, 120, 122, 123, 129, 133, 137

R

R^2 coefficient of determination. 58

RMS root mean square. 6

RO Radio Occultation. vii, 1, 2, 6–10, 12, 14–19, 21–25, 30, 38–40, 44, 47–50, 61, 63–65, 73, 81, 83, 85, 86, 89–102, 104–125, 127, 129–133, 135–138, 155

S

SAC-C Satélite de Aplicaciones Científicas-C. 15, 17

sfu solar flux unit. 115

SI Système International d'Unités/International System of Units. 10

SNR signal-to-noise ratio. 47, 49, 58, 70, 83, 89, 90, 97, 102, 136

SO_4 sulfate. 33

SON September–October–November. 44, 68, 69, 78, 80, 86, 88–90, 136

SRES Special Report on Emission Scenarios. 32–35, 37, 40, 49, 61, 63, 70, 75, 130, 131

SS sum of squares. 56

SSE sum of squares of errors. 55, 58, 59, 104

SSR regression sum of squares. 57, 58

SST total sum of squares. 57, 58

T

TP tropopause. 47, 50, 53, 77, 78, 80, 88

U

UCAR University Corporation for Atmospheric Research. 21

UG University of Graz. 171

UK United Kingdom. 24, 31, 32

UKMO UK Met Office. 31

UNEP United Nations Environment Programme. 4

USA United States of America. 26–28, 31

UT upper troposphere. 6, 10, 17, 33, 44, 50, 53, 64, 71, 72, 75, 77, 78, 80, 82, 85, 86, 88, 89, 110, 113, 116, 119, 120, 122

UTC Universal Time Coordinated. 28, 40

UTLS upper troposphere-lower stratosphere. 1, 6, 7, 10, 12, 14, 16–18, 38, 44, 47–49, 61, 66, 72, 73, 76, 77, 80, 85, 86, 89–93, 95, 103–105, 107, 108, 110, 112, 113, 125, 129, 130, 133, 135–138

UV Ultraviolet. 6

W

WCRP World Climate Research Programme. 30

WEGC Wegener Center for Climate and Global Change [University of Graz]. 7, 9, 11, 12, 14–16, 22, 37, 40

WGS 84 World Geodetic System 1984. 12

WMO World Meteorological Organization. 4

1 Introduction

In the context of atmospheric sciences, the last century can be deemed to be a *century of data*. New technologies and measuring systems, such as radiosondes and later satellites with various instrumentation, led to an even increasing amount of in-situ and remote sensing data. For the first time it was possible to monitor the Earth's atmosphere continuously from surface to high altitudes on a global scale. Additionally, increasing computing power enabled the operation of complex global climate models, adding oodles of model data to the observations. The quantity of new data, above all in former inaccessible regions, certainly led to a better physical understanding of atmospheric processes and thus to improvements of climate models. But for climate science, data quality is equally essential as data quantity. To monitor climate and to detect changes in atmospheric parameters, not only global coverage, but also well-resolved, accurate, and long-term stable measurements are required. Data gained from the Global Navigation Satellite System (**GNSS**) Radio Occultation (**RO**) method, an active remote sensing technique, offer these quality characteristics and therefore are predisposed to serve as climate benchmark record.

This thesis was incorporated in the project INDICATE—Indicators of Atmospheric Climate Change from Radio Occultation. The central aim of the project was the systematic exploration and provision of benchmark indicators of atmospheric climate change for the upper troposphere-lower stratosphere (**UTLS**) with regard to parameters made available by the RO method, i.e. refractivity, pressure, geopotential height, and temperature. On the one hand, the most robust and sensitive RO climate change indicators should be determined by means of classical trend testing, on the other hand, a new inter-active visualization tool was employed for the analysis. The latter was part of a second PhD work within the project. INDICATE also intended to analyze the detection capability of RO data by an optimal detection method and in doing so to validate the skill of General Circulation Models (GCM) with RO data. The thesis is structured in the following way:

- Chapter 2 introduces principles of climate monitoring and respective data requirements. An executive summary on the RO method, including the retrieval scheme and provided parameters, is given. The derivation of RO based climatologies is addressed as well as RO missions and climate monitoring studies based on RO data.
- In chapter 3 all data sets are introduced. For RO data, the emphasis is on

the characteristics of the Global Positioning System/Meteorology (**GPS/MET**) and Challenging Mini-Satellite Payload (**CHAMP**) records, which were used in this thesis. As additional observational data record, the Hadley Centre gridded free-atmosphere temperatures from radiosondes (**HadAT2**) are presented. Furthermore, the characteristics of two re-analyses (ECMWF Re-Analysis (**ERA-40**) and NCEP/NCAR Re-Analysis (**NRA**)) and three General Circulation Model (**GCM**)s (Community Climate System Model 3 (**CCSM3**), ECMWF Hamburg Model (**ECHAM5**), and Hadley Centre Coupled Model, version 3 (**HadCM3**)) are discussed. The employed Intergovernmental Panel on Climate Change (**IPCC**) Fourth Assessment Report (**AR4**) experiments and their characteristics are detailed and the pre-treatment of all data sets to obtain data with a common resolution in space and time is described.

- Chapter 4 contains the study of the RO-accessible climate change indicators. It details the spatio-temporal study setup, the investigated parameters, and the chosen method to gain the indicators. The results include an assessment of climate trends in all parameters, given on constant pressure levels and on constant geopotential height levels, and an analysis of the data variability and trends as produced by the different data sets. Autocorrelation considerations, the temporal representation of trends, trend significances and goodness-of-fit results are discussed in detail as these quantities were used to determine the RO indicator regions.
- In chapter 5, the climate change detection study based on the combined GPS/MET–CHAMP record is presented. This chapter comprises a detailed and step-by-step description of the optimal fingerprinting technique used and a summary on multiple linear regression, which was employed to assess the influence of atmospheric patterns on the trends. These patterns are discussed in detail as well as the trend patterns of the RO and the GCM records. The discussion includes the RO fingerprint patterns, the consistency of observed and model variance, and a detection stability test based on GCM data only.
- A summary and conclusions, given in chapter 6 with focus on the climate change indicator study and the detection study, conclude this thesis.
- Three appendices are attached. The first one, appendix A, gives a general description of polynomial and spline interpolation and a detailed one of the adapted interpolation method used to gain data sets with a common resolution. The second, appendix B, tabulates the region definitions used within the climate change indicator study. The third, appendix C, specifies the content of the enclosed DVD.

2 Radio Occultation and Climate Monitoring

2.1 Climate Monitoring

Weather and climate conditions have always been influencing human life, nevertheless globally distributed continuous records of atmospheric parameters, such as surface temperature or pressure are only available after around 1850. Many of the first empirical climate change studies are based on these long-term surface temperature observations, which often were combined to calculate global means. Certainly, longer records exist for single spots, as for example from the Austrian monastery *Stift Kremsmünster*, which provides the longest continuous Austrian temperature record dating back to 1767. These single records are very precious for regional studies but of limited value for global climate change research.

First theoretical calculations of human induced climate change were accomplished by the Swedish scientist Svante Arrhenius during the last years of the 19th century. Motivated to solve the then much discussed riddle of the cause of prehistoric Ice Ages, he calculated that doubling atmospheric carbon dioxide ($\mathbf{CO_2}$) would rise Earth's temperature by some 5°C to 6°C (Weart 2003). Nevertheless, it was doubted for a long time that human activities could influence the composition of the atmosphere or that possibly emerging atmospheric changes could not be overcome by human technology. In the second half of the 20th century, human's influence on the Earth's climate system gained slowly broader interest, and—even though still vividly debated—it also became more and more *visible* in various atmospheric data, as e.g., in Keeling's CO_2 curve. Figure 2.1 shows the annual mean atmospheric CO_2 concentration for 1744 to 2009. Before 1958, the data are based on an ice core of the Siple Station[1] in West Antarctica (Neftel et al. 1985). The actual *Keeling curve* starts in 1958, the plotted data are based on monthly in situ air measurements at the Mauna Loa Observatory in Hawaii[2] (Keeling et al. 2005). At the end of 2009, the atmospheric CO_2 concentration was close to 388 parts per million by volume (**ppmv**), which means an increase of nearly 40 % of the preindustrial value of 280 ppmv from about 1850. With the establishment of upper air observations, such as radiosondes in the 1960s and the implementation of space-borne measurement systems in the late 1970s (Karl et al. 2006), research could be

[1] available from `http://cdiac.ornl.gov/trends/co2/siple.html`, Feb 2010
[2] available from `http://scrippsco2.ucsd.edu`, Feb 2010

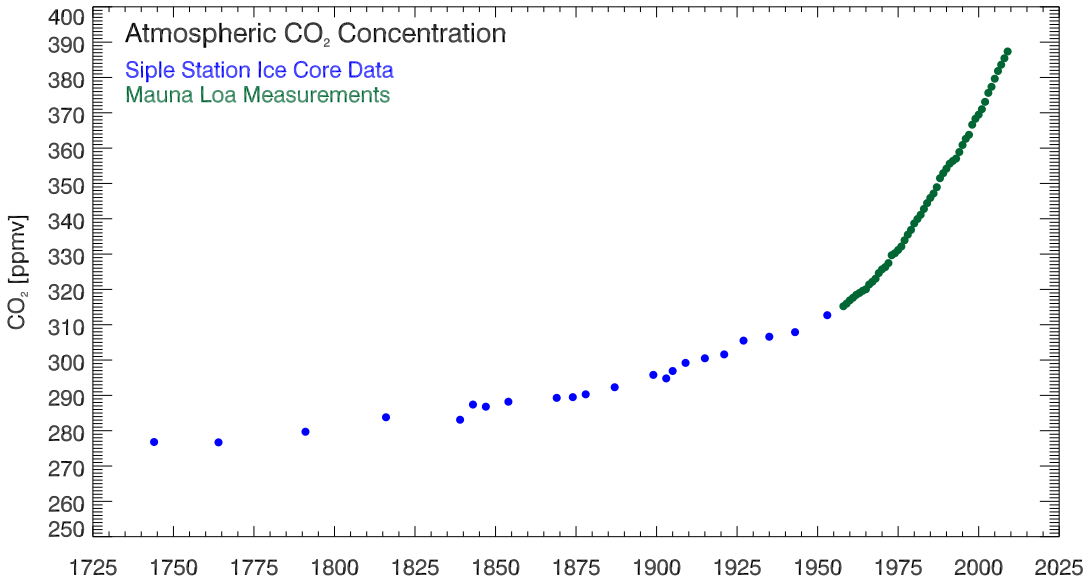

Figure 2.1: Annual mean atmospheric CO_2 concentration from 1744 to 2009 based on Siple ice core (West Antarctica) data and Mauna Loa (Hawaii) measurements.

extended into higher levels of the atmosphere and into remote areas. Satellites allowed for the formation of a global picture by ensuring global coverage of measurements.

In the beginning of the 1980s, scientific consensus about the role of anthropogenic Green House Gas(es) (**GHG**) emissions on climate change started to form. In 1989, the Intergovernmental Panel on Climate Change (**IPCC**) was established by the World Meteorological Organization (**WMO**) and the United Nations Environment Programme (**UNEP**)" to provide the governments of the world with a clear scientific view of what is happening to the world's climate"[3]. In its first assessment report in 1990 (Houghton et al. 1990), the importance of climate change as a topic being provoked by and affecting all countries was stressed. The second assessment report (Houghton et al. 1995) stated that "the balance of evidence suggests a discernible human influence on global climate" and that "climate is expected to continue to change in the future". The third report (Houghton et al. 2001) also addressed the human impact on climate change, declaring that "there is new and stronger evidence that most of the warming observed over the past 50 years is attributable to human activities". Besides, it was noted that "further action is required to address remaining gaps in information and understanding" and named in this regard among other things the need for "systematic observations and reconstructions" as high priority areas. Thus, the call for long-term climate data, being free from artifacts of changes in observing system technology or

[3] `www.ipcc.ch`

1	The impact of new systems or changes to existing systems should be assessed prior to implementation.
2	A suitable period of overlap for new and old observing systems is required.
3	The details and history of local conditions, instruments, operating procedures, data processing algorithms and other factors pertinent to interpreting data (i.e., metadata) should be documented and treated with the same care as the data themselves.
4	The quality and homogeneity of data should be regularly assessed as a part of routine operations.
5	Consideration of the needs for environmental and climate-monitoring products and assessments, such as IPCC assessments, should be integrated into national, regional and global observing priorities.
6	Operation of historically-uninterrupted stations and observing systems should be maintained.
7	High priority for additional observations should be focused on data-poor regions, poorly observed parameters, regions sensitive to change, and key measurements with inadequate temporal resolution.
8	Long-term requirements, including appropriate sampling frequencies, should be specified to network designers, operators and instrument engineers at the outset of system design and implementation.
9	The conversion of research observing systems to long-term operations in a carefully-planned manner should be promoted.
10	Data management systems that facilitate access, use and interpretation of data and products should be included as essential elements of climate monitoring systems.

Table 2.1: The 10 GCOS basic climate monitoring principles (from `http://www.wmo.int/pages/prog/gcos/documents/GCOS_Climate_Monitoring_Principles.pdf`, Feb 2010).

analysis methods, went hand in hand with the recognition of climate change and was also due to the need of data for evaluating climate simulations of improved models (e.g., Goody et al. 2002; Karl and Trenberth 2003).

Based on perceived shortcomings of existing observation methods, requirements for a climate observing system, including not only climate observations but also processing and support systems, were discussed (e.g., Trenberth et al. 2002). In 1992, the Global Climate Observing System (**GCOS**), which was established to provide information on and to ensure the monitoring of our climate system. A revised set of 10 basic climate monitoring principles (see Table 2.1) was released, addressing the need for

long-term quality and stability, pre-conditions to obtain consistent continuous data for long periods. There is a consensus that satellite data are needed to obtain a global perspective and guarantee observations in the long run (Trenberth et al. 2002). Many of the current upper air observing systems were designed to improve weather forecasts, where stability of the measurements over longer periods is not the primary goal and thus these systems do not fulfill requirements for climate monitoring. Accuracy is another crucial issue for climate monitoring, since parameter changes over a decade or century are of interest and even small changes in the observing system matter.

Beside the monitoring principles, GCOS defined a set of so called Essential Climate Variables (**ECV**), which comprise for the free atmosphere, the focus region of this work, among others temperature and water vapor. As observation requirements for temperature, GCOS notes e.g., a minimum resolution of 500 km horizontally, 0.5 km vertically for temperature in the upper troposphere (**UT**) and 3 km vertically in the lower stratosphere (**LS**), and a root mean square (**RMS**) accuracy of < 0.5 K. The ECV should support the work of climate scientist and "are technically and economically feasible for systematic observation"[4]. One main use of these observations is to be compared with climate model predictions for model evaluation and improvements. Moreover, any quantity that can be derived from ECV and can also be measured, may serve as climate variable. Beside Keeling's CO_2 measurements, Goody et al. (2002) note molecular refractivity derived from Global Positioning System (**GPS**) Radio Occultation (**RO**) measurements as another promising climate variable of high absolute accuracy and reproducibility.

This work focuses on the use of RO data for upper troposphere-lower stratosphere (**UTLS**) climate monitoring. This atmospheric region, which is here defined as between around 5 km and 35 km height, is governed by a complex interaction between dynamics, transport, radiation, chemistry, and microphysics (Mohanakumar 2008) and thus reacts particularly sensitive to climate change. While all processes are more or less equally important in the troposphere, the thermal state of the stratosphere is mainly governed by radiative processes, driven by ozone, carbon dioxide, and water vapor concentrations (Andrews et al. 1987; Holton 2004). Until around the year 2000, stratospheric ozone depletion, which is now stabilizing due to the Montreal Protocol[5], led to an intensified stratospheric temperature decrease, as less stratospheric ozone converts less solar Ultraviolet (**UV**) radiation into heat radiation. As a parallel effect, an increase in atmospheric CO_2 (see Figure 2.1) leads as well to a stratospheric temperature decrease (Laštovička et al. 2006), as more CO_2 increases the thermal emissivity of

[4] `http://www.wmo.int/pages/prog/gcos/index.php?name=EssentialClimateVariables`, Feb 2010

[5] The *Montreal Protocol on Substances that Deplete the Ozone Layer*, which came into force in 1989 and has been ratified by 196 states, is a successful international treaty to protect the ozone layer by phasing out the production and consumption of ozone-depleting chemicals, as e.g., chlorofluorocarbons or halons. Until 2009, almost 95 % of all ozone-depleting substances have been phased out (United Nations Environment Programme, Ozone Secretariat 2009).

the stratosphere. Furthermore, as long as no new global thermo-dynamical equilibrium is achieved, less Infrared (**IR**) radiation from the troposphere reaches the stratosphere, both leading to a net energy loss in the stratosphere. As to water vapor, tropospheric warming leads to an increase in the troposphere, but relative humidity remains rather constant (Soden and Held 2006). The development of stratospheric water vapor is still under discussion (Solomon et al. 2010). Stratospheric water vapor arises on the one hand from oxidation of methane (mainly at higher levels) and on the other hand from uplift of tropospheric water vapor in the tropics. Acting as GHG, stratospheric water vapor also cools the stratosphere and warms the troposphere.

Linear global surface temperature trends are determined as 0.75 K±0.18 K for the 100 year period 1906 to 2005 (IPCC 2007), the linear surface trend over the last 50 years is nearly twice as large. For the period 1979 to 2007, trends of 0.13 K±0.03 K per decade are observed (Allison et al. 2009). The stratosphere featured a much stronger cooling signal of around 0.5 K per decade for the 1997 to 2007 period, based on (Advanced) Microwave Sounding Unit (**MSU/AMSU**) and different radiosonde data sets (Randel et al. 2009).

2.2 The Radio Occultation Method

A record suitable for climate monitoring should supply above all vertically well-resolved, accurate, long-term stable, and consistent data, which capture the mean state and the variability of the atmosphere with an accuracy better than the expected changes. For the UTLS, these data qualities can be provided by RO measurements based on Global Navigation Satellite System (**GNSS**) signals (e.g., Leroy et al. 2006*a;* Steiner et al. 2007; Foelsche et al. 2008*a*).

The RO method is a remote sensing technique, which delivers information about the thermodynamic state of the Earth's atmosphere. As an active limb sounding technique, it makes use of electromagnetic signals from artificial sources, such as satellite signals. Usually, GPS signals are used to scan the atmosphere near-vertically due to the relative motion between the GNSS (GPS) transmitter satellite and the receiver instrument onboard a Low Earth Orbit (**LEO**) satellite, resulting in vertical profiles of atmospheric parameters. The GPS radio signal passes across the atmosphere while being refracted until—from the viewpoint of the LEO—the GNSS satellite sets or rises from behind the Earth (see Figure 2.2). Detailed descriptions of the RO method are given by Kursinski et al. (1997) in general or by Pirscher (2010). The latter provides a comprehensive delineation of the Wegener Center for Climate and Global Change (**WEGC**) retrieval scheme, which was employed for all RO data used in this work. A flow chart of this retrieval process is given in Figure 2.3, a tabulated description on the processing steps in the retrieval is provided in Table 2.2 (Steiner et al. 2009*a*).

The measured RO quantity are phase changes of the two GPS Microwave (**MW**)

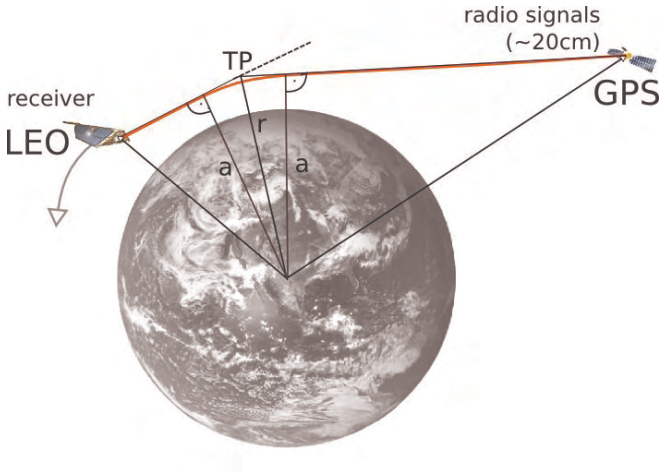

Figure 2.2: RO geometry: The radio signal (red) is transmitted from a GPS satellite, refracted by the Earth's refractivity field and received from a LEO satellite. TP is named tangent point, a impact parameter, and r tangent point radius.

frequencies, $f_1 = 1575.42\,\text{MHz} \equiv \lambda_1 \approx 19.0\,\text{cm}$ and $f_2 = 1227.60\,\text{MHz} \equiv \lambda_2 \approx 24.4\,\text{cm}$, as a function of time. Together with precise orbit information, bending angles (α) as a function of the impact parameter a (Figure 2.2), which is the perpendicular distance between the asymptotes of the signal rays and the center of refraction (center of the Earth), can be calculated. On its way through the atmosphere, the GPS radio signal is influenced by the ionosphere and the neutral atmosphere. Since the goal of the method is the retrieval of information of the neutral atmosphere, ionospheric influences are to be removed. The ionospheric correction can be coped with a linear combination of the bending angles of the two GPS frequencies (Vorob'ev and Krasil'nikova 1994). External a priori information is only used for bending angle initialization at high altitudes via statistical optimization (Gobiet and Kirchengast 2004; Gobiet et al. 2007), which stabilizes the retrieval in respect to residual ionospheric errors, which depend on solar variability. Therefore, European Centre for Medium-Range Weather Forecasts (**ECMWF**) forecast profiles are employed. Application of an Abel transformation leads to refractivity (N) profiles as a function of height, which is given by the tangent point radius (Figure 2.2). Refractivity is linked to the refractive index n, being close to unity in the free atmosphere, via the relation

$$N(h) = [n(h) - 1]\ \ 10^6, \tag{2.1}$$

where h is the height above the Earth's ellipsoid. Microwave refractivity is usually

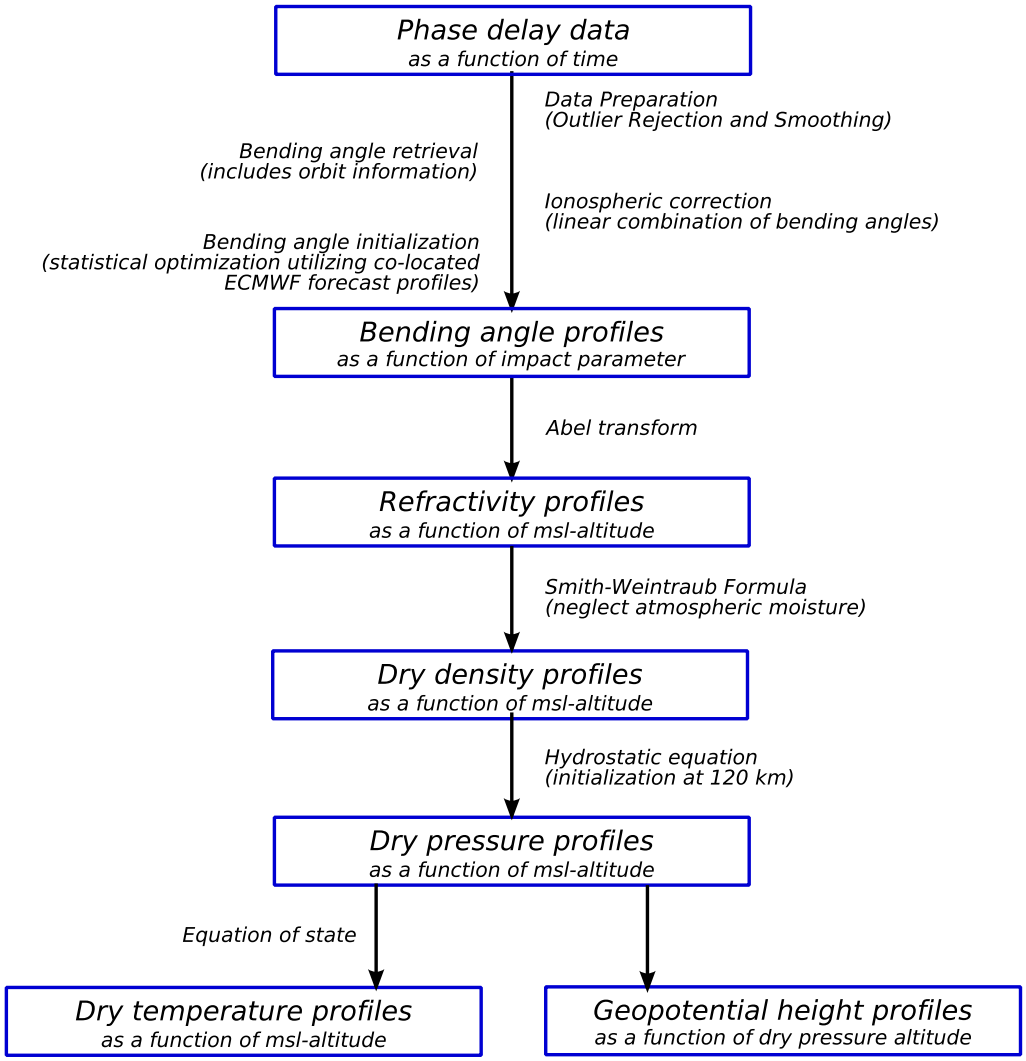

Figure 2.3: The RO retrieval as implemented in WEGC OPSv54, provided by B. Pirscher (Pirscher 2010).

defined as (e.g., Kursinski et al. 1997)

$$N = 77.6\ \frac{p}{T} + 3.73 \times 10^5\ \frac{p_\mathrm{w}}{T^2} - 4.03 \times 10^7\ \frac{n_\mathrm{e}}{f^2} + 1.4W, \tag{2.2}$$

with the quantities pressure (p) in hPa, temperature (T) in K, partial water vapor pressure ($p_\mathbf{w}$) in hPa, electron density ($n_\mathbf{e}$) in electrons/m^3, transmitter frequency (f)

in Hz, and the mass of condensed water in the atmosphere (W) in g/m^3. The four terms reflect the influence of the dry atmosphere (first term), the moist atmosphere (second term), the ionosphere (third term), and the influence from scattering through liquid water and ice contents (fourth term). The (first order) ionospheric influence can be removed either through a combination of phases at two frequencies or through a combination of bending angles. The last term of equation (2.2) can be neglected, for the contribution to refractivity is very small as RO is almost insensitive to clouds. In the OPSv54 retrieval, the second term is also ignored, as it is implemented as a so-called *dry air retrieval*. This is justified as long as atmospheric moisture is small, being the case in the UTLS (further considerations are discussed in section 2.3). Thus, the first term of equation (2.2) can be used to calculate density profiles, which lead via the hydrostatic equation to dry pressure. The latter leads to geopotential height and via the equation of state to dry temperature, completing the set of dry parameters that can be obtained without additional atmospheric information from the RO technique.

The measurement principle and the orbits of the satellites involved, determine the characteristics of the RO method. The RO data's ability for climate monitoring is guaranteed by long-term stability, which is based on the use of relative (phase delays) instead of absolute measurements. Therefore, measurements of different satellites or sensors can be combined without the need of temporal overlapping, as long as the same processing scheme is employed (Hajj et al. 2004; Foelsche et al. 2009*a*). As the measurands (time delays of phases) are based on precise atomic clocks, they are also traceable to a Système International d'Unités/International System of Units (**SI**) base unit (Leroy et al. 2006*a*). Essentially all weather capability is granted since the GPS radio signals are virtually insensitive to clouds and in addition, the signals are not influenced by or depending on sunlight, so that measurements can be performed during day and night. Near polar orbits ensure global coverage of measurements with already a single LEO satellite. A receiver, which is only able to track setting occultations, can provide around 250 profiles per day. Twice as much profiles can be obtained by receivers, which can additionally track rising occultations. As limb sounding technique, RO measurements feature a high vertical resolution (around 0.5 km to 1.5 km in the UT to LS) and a low horizontal resolution (around 200 km to 300 km), which is no disadvantages for meso- to large-scale climate applications since RO profiles are averaged anyway.

WEGC OPSv54 Processing Steps & Description
Early outlier rejection 3σ-outlier rejection on 50 Hz sampling rate L1 and L2 phase delay data, based on a one-second moving average window over the profile.
Phase delay smoothing Smoothing of 50 Hz phase delay profiles using regularization filtering (third order norm, regularization parameter = 10^5, Syndergaard (1999)).
Bending angle retrieval Geometric optics retrieval (Kursinski et al. 1997) at both L1 and L2 frequencies.
Ionospheric correction Linear combination of L1 and L2 bending angles (Vorob'ev and Krasil'nikova 1994). Correction is applied to low-pass filtered bending angles (1 km moving average), L1 high-pass contribution is added after correction (Hocke et al. 2003). L2 bending angles < 15 km derived via L1-extrapolation.
Statistical optimization of bending angles Statistical optimization of bending angles between 30 km and 120 km with inverse covariance weighting (Healy 2001; Rieder and Kirchengast 2001; Gobiet and Kirchengast 2004). Vertically correlated background (corr. length 10 km) and observation (corr. length 2 km) errors. Observation error estimated from variance of observed profile between 65 km and 80 km. Background error: 15 %. Background information: collocated profiles derived from ECMWF 24h/30h forecast files (T42L60; resp. T42L91 as of 01/02/2006), ECMWF Re-Analysis (**ERA-40**) for Global Positioning System/Meteorology (**GPS/MET**) data. Above $\approx$ 60/80 km: Extended Mass Spectrometer–Incoherent Scatter Model of the Upper Atmosphere (**MSISE-90**) (Hedin 1991).
Abel transform to refractivity Numerical integration over bending angle (Simpson's trapezoidal rule) from each height (impact parameter) to 120 km. Impact parameter to height conversion with radius of curvature at mean tangent point location (Syndergaard 1998).

continued on next page

WEGC OPSv54 Processing Step & Description
Refractivity smoothing (resolution-conserving) Blackman-windowed-Sinc filter (<1 km moving average) for resolution-conserving filtering of residual numerical processing noise.
Dry air retrieval pressure initialization Hydrostatic integral initialization at 120 km: pressure = pressure(MSISE-90); no initialization below 120 km (downward integration). Dry geopotential height relative to Earth Gravity Model 1996 (**EGM96**); Smith-Weintraub equation and equation of state (ideal gas) to obtain dry temperature;
Temperature smoothing (resolution-conserving) Same filtering as for refractivity smoothing.
Lower cut-off altitude The lower-most altitude, where retrieved data is kept, is set to the altitude, where significant impact parameter ambiguities occur (impact parameter increase > 0.2 km from one data point to the next downwards).
External quality control (for outlier profiles) Refractivity and temperature: rejection if $\Delta N > 10\,\%$ in 5 km–35 km and/or $\Delta T > 20$ K in 8 km–25 km. Reference: collocated ECMWF analysis profiles (T42L60 resp. T42L91 as of 01/02/2006), ERA-40 re-analysis for GPS/MET data.
Reference frame, vertical coordinate Earth figure: World Geodetic System 1984 (**WGS 84**) ellipsoid; Vertical coordinate: mean sea level (**MSL**) altitude; conversion of (ellipsoidal) height to MSL altitude (at mean tangent point location) via EGM96 geoid smoothed to $2^\circ \times 2^\circ$ resolution.

Table 2.2: Overview on WEGC OPSv54 retrieval chain Steiner et al. (2009*a*).

2.3 Radio Occultation Data

2.3.1 *Dry* Parameters—the RO Specialty

The RO method provides vertically good resolved profiles of bending angles, refractivity, density, dry pressure, dry temperature, and geopotential height for the UTLS. The *dry* add-on for parameters is typical for RO data, which are gained in a dry air retrieval (see section 2.2), as it is the case for the WEGC OPSv54 retrieval. *Dry* means that only the first right-hand side term is considered for refractivity in equation (2.2),

which yields for dry temperature the following relation:

$$N = k_1 \frac{p}{T} \tag{2.3}$$

$$T_{\mathrm{dry}} = k_1 \frac{p_{\mathrm{dry}}}{N}. \tag{2.4}$$

The connection between *dry* and *physical* temperature can be derived by expressing N in equation (2.4) by using the first (dry) and second (wet) term of equation (2.2) and ignoring for clarity the small difference of p and p_{dry}:

$$\begin{aligned} T_{\mathrm{dry}} &= k_1 \frac{p}{N} \\ &= k_1 p \left(\frac{1}{\frac{k_1 p}{T} + \frac{k_2 p_{\mathrm{w}}}{T^2}} \right) \\ &= \frac{k_1 p}{\frac{1}{T}\left(\frac{k_1 pT + k_2 p_{\mathrm{w}}}{T}\right)} \\ &= T \frac{k_1 p}{k_1 p \left(1 + \frac{k_2}{k_1}\frac{p_{\mathrm{w}}}{pT}\right)} \\ &= T \frac{1}{1 + \frac{k_2}{k_1}\frac{p_{\mathrm{w}}}{pT}} \end{aligned} \tag{2.5}$$

Above ≈5 km, assuming typical temperatures of 240 K, the term $\frac{k_2}{k_1}\frac{p_{\mathrm{w}}}{pT} \ll 1$ and equation (2.5) can be approximated by

$$\begin{aligned} T_{\mathrm{dry}} &\approxeq T \left(1 - 20\frac{p_{\mathrm{w}}}{p}\right) \\ &\approxeq T\left(1 - 12.4q\right), \end{aligned} \tag{2.6}$$

where the specific humidity (q) is given in kg/kg (Foelsche et al. 2008*b*). The equation shows that, if water vapor is available, dry temperature is always lower than physical temperature. Thus, as long as water vapor does not decrease as the climate warms (it is in fact increasing, e.g., Held and Soden 2006), dry trends can never exceed physical trends. Figure 2.4 depicts the mean difference between physical and dry temperature for March, June, September, and December zonal means between 1000 hPa and 30 hPa height. Preindustrial control model data (ECMWF Hamburg Model (**ECHAM5**)/run1, see section 3.3 for a detailed description of the data) were used and dry temperature was determined by means of equation (2.6).

While large deviations of several tens of Kelvin may occur in the troposphere, above 300 hPa, the differences between dry and physical temperature are mostly below 1 K. Largest dry-physical differences occur in the tropics, where most of the atmospheric water vapor is present. Pole-wards of 40°N and 40°S, the deviations are always < 0.5 K.

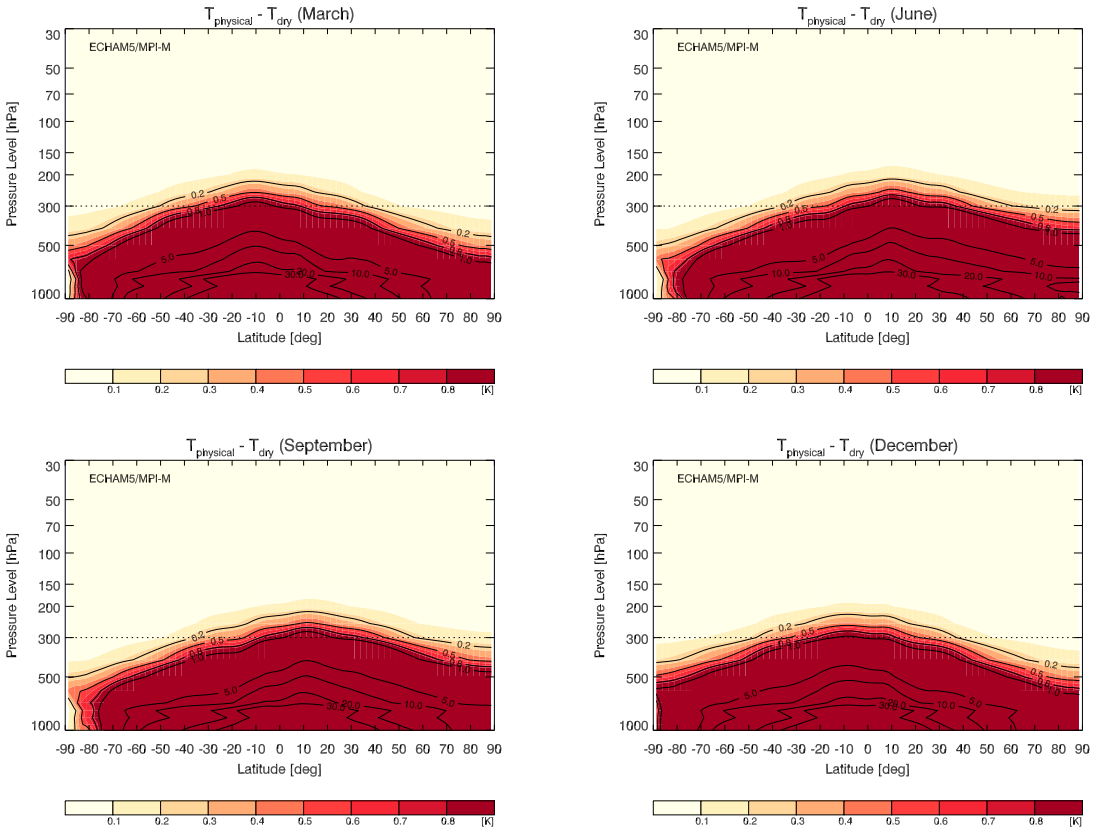

Figure 2.4: Differences between physical and dry temperatures based on ECHAM5 pre-industrial control simulations for March (top left), June (top right), September (bottom left), and December (bottom right). The 300 hPa level is marked as it is the lowest UTLS level used within this work.

Above 200 hPa, differences are < 0.1 K everywhere. In the mid- to lower troposphere the moist-dry ambiguity inherent in refractivity can only be resolved by means of background information, such as temperature and surface pressure for the retrieval of humidity (Kursinski and Hajj 2001) or humidity and surface pressure for the retrieval of temperature. An optimal estimation retrieval (e.g., Healy and Eyre 2000) can be employed alternatively, which is planned to be implemented in the next WEGC processing version.

2.3.2 RO Climatologies

The RO method provides profiles of atmospheric parameters, which are distributed more or less uniformly across the globe. These single profiles, each one given for a

latitude and longitude defined by the tangent point, can be combined into global climatologies. As long as the same processing scheme is employed, single profiles from different satellite missions can be combined without the need of inter-satellite calibration (Foelsche et al. 2009*b*). The WEGC Climatology Processing System (**CLIPS**), described in detail by Pirscher (2010), provides a suitable tool to derive climatologies and their characteristics. To optimally average the single profiles to global monthly climatologies, all profiles of one month are first aggregated into so-called *fundamental* bins, which are non-overlapping areas with a horizontal resolution of 5° in latitude and 60° in longitude. In the vertical, the profiles are interpolated to an equidistant grid with a grid-point distance of 200 m. The mean bin profile is determined by averaging all profiles after weighting every single one with the cosine of its geographical latitude. As single satellite missions do not always provide an adequate number of profiles for each fundamental bin, a basic climatology of zonal means of 10° bands in latitude is built. Therefore, each zonal mean profile is weighted with the number of profiles available in its bin. By averaging over latitudes, the data are weighted with the cosine of the mean latitude (see Pirscher 2010). The so gained monthly mean climatologies are the basic RO data used within this work.

Beside the calculation of climatologies, the CLIPS also provides error estimates for the very same. Systematic differences between ECMWF analyses and RO climatologies are determined as co-located ECMWF profiles (co-located in time and space) minus mean RO profiles in each bin. For the GPS/MET satellite mission (see section 2.3.3), ERA-40 data are used to calculate systematic differences for the data used in this work, as ERA-40 features for the relevant period a better vertical resolution (60 levels up to 0.1 hPa, see Uppala et al. 2005) than the then used ECMWF analysis (31 levels up to 10 hPa, see Untch and Simmons 1999). The sampling error gives an estimate for deviations in the RO climatologies due to uneven sampling in space. The error is assessed as the difference between the mean of the co-located profiles and the mean of all reference profiles within a bin (Pirscher 2010).

2.3.3 RO Missions

The GPS/MET experiment aboard MicroLab 1 was the proof of concept mission for the RO technique (Ware et al. 1996). First RO measurements were available in spring 1995 and the satellite delivered data for several periods until 1997. Continuous RO measurements are available from mid 2001 until 4 October 2008 from the Challenging Mini-Satellite Payload (**CHAMP**) satellite (Wickert et al. 2001; Wickert et al. 2004).

Ongoing satellite missions are the Argentine Satélite de Aplicaciones Científicas-C (**SAC-C**) (e.g., Hajj et al. 2004), the Gravity Recovery and Climate Experiment (**GRACE**) (e.g., Beyerle et al. 2005; Wickert et al. 2005), and the Formosa Satellite Mission #3/Constellation Observing System for Meteorology, Ionosphere, and Climate (**FORMOSAT-3/COSMIC**), a six satellites constellation which provides about 2500

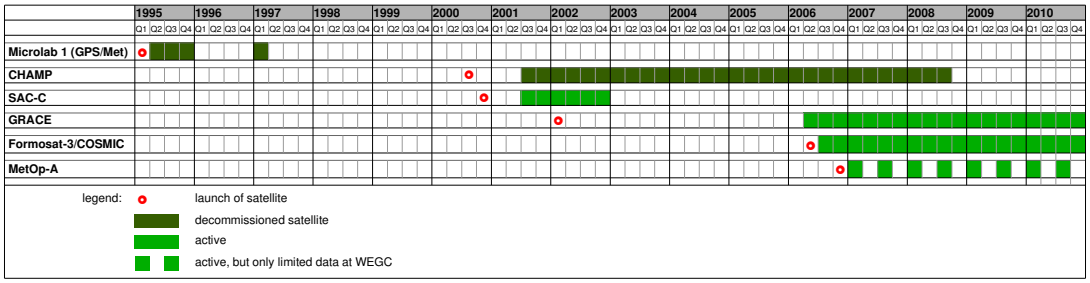

Figure 2.5: Periods of RO measurements from different satellite missions available at WEGC (March 2010). Monthly data are assigned to the respective quarter.

observations per day for finer-resolved climatologies (e.g., Anthes et al. 2008). The Meteorological Operational satellite (**MetOp**) is a series of three satellites launched in sequence to operate 14 years from 2006 (e.g., Loiselet et al. 2000; Luntama et al. 2008). RO measurements will be provide at least until 2020. Additional missions are projected and will ensure the establishment of a multi-decadal RO data record for climate monitoring.

With GPS/MET, CHAMP, and the ongoing missions, a total period of more than 14 years of RO measurements is currently available for climate change studies.

2.4 Climate Monitoring Studies Based on RO Data

The use of RO data for numerical weather prediction has already been analyzed in several studies. The ECMWF assimilates RO measurements since September 2006 in its systems. Healy and Thépaut (2006) or Buontempo et al. (2008), e.g., showed that despite the rather small number of occultations entering the assimilation, significant positive impacts in UTLS temperature and geopotential height fields are achieved. Cardinali (2009) showed in forecast sensitivity calculations that RO measurements considerably decrease ECMWF forecast errors (RO shows after the Advanced Microwave Sounding Unit (**AMSU**), the infrared measurement systems IASI and AIRS, and aircraft measurements the largest contribution to forecast error reduction). The utility of RO data for climate monitoring has not yet been definitely proven, but many studies have addressed this question. In this section, selected studies being of importance for this work or addressing RO data retrieved at the WEGC and their characteristics, are presented.

First RO studies were based on simulated RO or proxy data. Steiner et al. (2001) investigated the change detection capability of GNSS occultation sensors by means of an end-to-end occultation observing system simulation experiment over a 25-year period. Foelsche et al. 2008*a* tested the climate trends detection ability of a GNSS RO

observing system based on the a middle atmosphere model. Inspecting 25-year trends of refractivity, pressure, geopotential height, and temperature, they found that for optimized UTLS monitoring the combined information of the key RO parameters can be used. Ringer and Healy (2008) used RO bending angle profiles, simulated with a state-of-the-art global coupled climate model, to examine the effect of increasing GHG in the UTLS. They also estimated climate change detection times in UTLS bending angle trends with 10 to 16 years, a period which is already covered by real RO measurements.

Beside simulated or proxy data, also real RO data were used to assess the climate monitoring utility of the RO method. Many of these studies were based on measurements of the CHAMP satellite, which provides the first long-term RO record. Schmidt et al. (2004), e.g., demonstrated the potential use of GPS RO for climate monitoring of UTLS by analyzing tropical CHAMP temperatures. The launch of further RO missions allowed also to estimate consistency between climatologies derived from measurements of different satellites. Hajj et al. (2004) showed, e.g., a remarkable consistency between data from the German satellite CHAMP and the Argentine satellite SAC-C. Similar excellent consistency results were gained more recently by Foelsche et al. (2009*a*) for different FORMOSAT-3/COSMIC and CHAMP satellite RO products. They found that seasonal temperature climatologies of the different satellites were, after removing the climatologies' sampling error, in agreement to within $< 0.1\,\mathrm{K}$ in the UTLS. Monthly mean tropical tropopause temperatures and altitudes were within 0.2 K to 0.5 K and 50 m to 100 m, respectively. These results support the use of RO data for climate monitoring, as data from different missions can be combined without the need for inter-calibration, as long as the same processing scheme is employed. Schmidt et al. (2010) analyzed trends in tropopause heights based on CHAMP, GRACE, and FORMOSAT-3/COSMIC data, which show an global increase of 5 m to 9 m per year. A first climate change detection study was performed by Steiner et al. (2009*a*), analyzing climate trends of the combined GPS/MET/CHAMP data record within 1995 to 2008. A significant cooling trend signal was found in the LS for February, while the UT warming signal is still obscured by El Niño variability.

RO data also have been compared to other global data sets, such as satellite products, re-analyses or data from numerical weather prediction. Gobiet et al. (2007) evaluated RO profiles with regard to their bias-free asserted characteristics. They focused on the impact of a priori information for high-altitude initialization of bending angles, affecting the usable altitude range of the gained profiles. CHAMP data were validated against data from the Environmental Satellite (**Envisat**) instruments Michelson Interferometer for Passive Atmospheric Sounding (**MIPAS**) and Global Ozone Monitoring for Occultation of Stars (**GOMOS**) and atmospheric analyses. A RO temperature bias of $< 0.2\,\mathrm{K}$ was determined for the 10 km to 30 km height range. Steiner et al. (2007) compared RO data to temperature data provided by different institutions gained from the lower stratospheric channel of MSU/AMSU, to radiosonde data and to ECMWF analyses.

Therefore, they calculated synthetic RO, radiosonde, and analyses temperatures

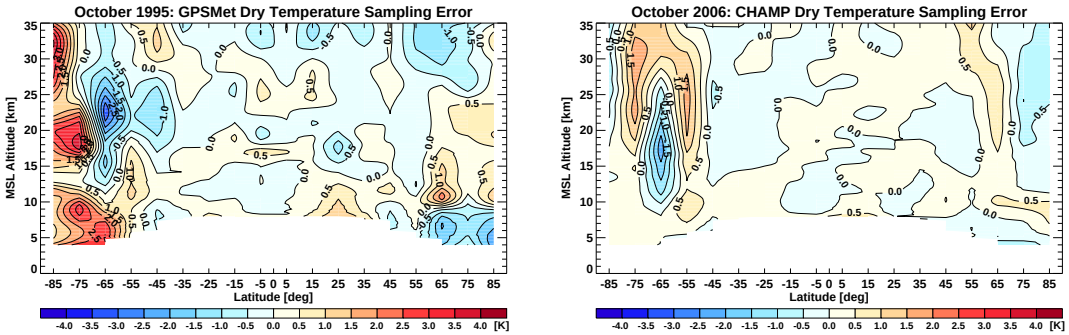

(a) GPS/MET sampling error

(b) CHAMP sampling error

Figure 2.6: *(a)* GPS/MET temperature sampling error climatology for October 1995. *(b)* CHAMP temperature sampling error climatology for October 2006. *Source:* `www.globclim.org`.

comparable to MSU/AMSU. For temperature anomalies very good agreement between the data sets was found, except the radiosondes show large variability. Statistically significant trend differences were determined primarily in the tropics between RO and MSU/AMSU, which allows the assumption of either so far unknown sources of error in the RO record or unresolved biases in the MSU/AMSU data (Steiner et al. 2009*b*). Validation of RO temperature climatologies against ECMWF analyses, carried out by Borsche et al. (2007), showed the importance of vertical resolution in atmospheric analyses. Systematic differences between RO and ECMWF climatologies of 1 K to 2 K in the tropical tropopause decreased significantly after doubling the amount of UTLS levels in the ECMWF analyses in 2006.

To make optimal use of RO data in climate monitoring, complete error characteristics of the data as well as estimates of structural uncertainty are important. A study by Steiner and Kirchengast (2005) provides empirical RO error characteristics based on quasi-realistically simulated GNSS RO data in reference to ECMWF analysis fields. For refractivity profiles, a relative standard deviation of 0.10 % to 0.75 % and a relative systematic deviation to the ECMWF analysis of < 0.1 % was identified between 5 km and 40 km height. For temperature, a standard deviation of 0.2 K to 1 K between 3 km and 31 km height and a systematic deviation to ECMWF of < 0.1 K to 0.5 K below 33 km and of < 0.1 K below 20 km was found. The UTLS sampling error, which is due to uneven and sparse sampling in space and time, is shown in Figure 2.6 for one month of GPS/MET and one month of CHAMP measurements. Between 50°N and 50°S, the error is < 0.3 K (Steiner et al. 2009*a*).

The total climatological error, which is dominated by the sampling error, was estimated to be < 0.5 K by Foelsche et al. (2008*b*). Structural uncertainty, defined as

unintentional bias arising from the chosen methodological approaches (Thorne et al. 2005*b*), was recently analyzed for RO refractivity climatologies from four different processing centers by Ho et al. (2009). They showed that the absolute values of fractional refractivity anomalies are $\leq 0.2\,\%$ between 8 km and 25 km height and constant in time. Thus, the uncertainty in trends was estimated with $\pm 0.04\,\%$ per 5 years and between $0.01\,\%$ and $0.03\,\%$ per 5 years after removing the sampling errors, which are different for the processing centers due to different quality control methods. Both, error analyses as well as structural uncertainty estimates underline the value of RO data for climate applications and as benchmark data set.

3 Datasets and Data Preparation

To determine trend indicators for Radio Occultation (**RO**) parameters and for the climate change detection study, further data sets were employed besides the RO data. These data were used for three purposes:

1. as proxies, since the RO record only covers a limited period so far,
2. for comparisons with RO results, and
3. because of requirements of the implemented methods.

In this chapter, all data sets and their characteristics are presented and the data pretreatment is described in detail. An overall picture of all data used within this study is given in Table 3.3 at the end of section 3.3.

3.1 Observational Data

Two kinds of observational data sets were used: the RO record, the main focus of attention in this study, which is introduced in section 3.1.1 and a radiosonde record for comparison reasons, presented in section 3.1.2.

3.1.1 RO Data from GPS/Met and CHAMP

The RO method, data, and missions are described in general in section 2.2 and section 2.3. The data themselves are primarily used in the detection study, which is presented in chapter 5. For the trend indicator study, presented in chapter 4, proxy data, which are available for longer time periods, are employed.

As RO measurements from different satellites can be combined without need for inter-calibration (see section 2.4), data from two satellite missions, namely Global Positioning System/Meteorology (**GPS/MET**) and Challenging Mini-Satellite Payload (**CHAMP**) (see section 2.3.3) were used. The setup of the detection study is thus closely tied to the availability of GPS/MET and CHAMP measurements. GPS/MET measurements are provided by University Corporation for Atmospheric Research (**UCAR**)/ COSMIC Data Analysis and Archive Center (**CDAAC**) for four prime times, periods within 1995 to 1997, when anti-spoofing[1] was turned off (Schreiner et al. 1998). Here,

[1] Anti-spoofing, short A-S, means that the P-code, which is modulated on both Global Positioning System (**GPS**) frequencies, is encrypted to guard against fake transmissions of satellite data (`http://tycho.usno.navy.mil/gpsinfo.html`, April 2010).

two out of the four periods are used, which supply sufficient measurements to calculate monthly climatologies. The GPS/MET measurements are complemented with data from CHAMP, which offers the first long-term record of RO measurements. CHAMP data are used for the period September 2001 to February 2008, without July and August 2006, when only sparse measurements were available. In total, 78 months spanning intermittently a more than 12 year period, were used.

The Wegener Center for Climate and Global Change (**WEGC**) Occultation Processing System Version 5.4 (**OPSv54**) retrieval and Climatology Processing System (**CLIPS**) provide monthly mean zonal climatologies with a horizontal resolution of 10° in latitude and a vertical resolution of 200 m in altitude (from 200 m to 35000 m). The following parameters are supplied: bending angles (α) as function of impact altitude, refractivity (N), dry pressure (p), dry temperature (T) as function of mean sea level (**MSL**) altitude, and dry geopotential height (Z) as a function of pressure altitude.

The detection study is based on refractivity, geopotential height, and temperature trends on constant pressure levels. As the climatologies of these parameters are originally given as function of MSL altitude, they were transformed to pressure level data as described in section 3.4. The RO data were used between 50°S and 50°N and between 300 hPa ($\approx$ 8500 m) and 30 hPa ($\approx$ 24 500 m) height. The spatial limitations in latitude and height were chosen in order to guarantee smallest RO errors (see section 2.4 and Figure 2.6).

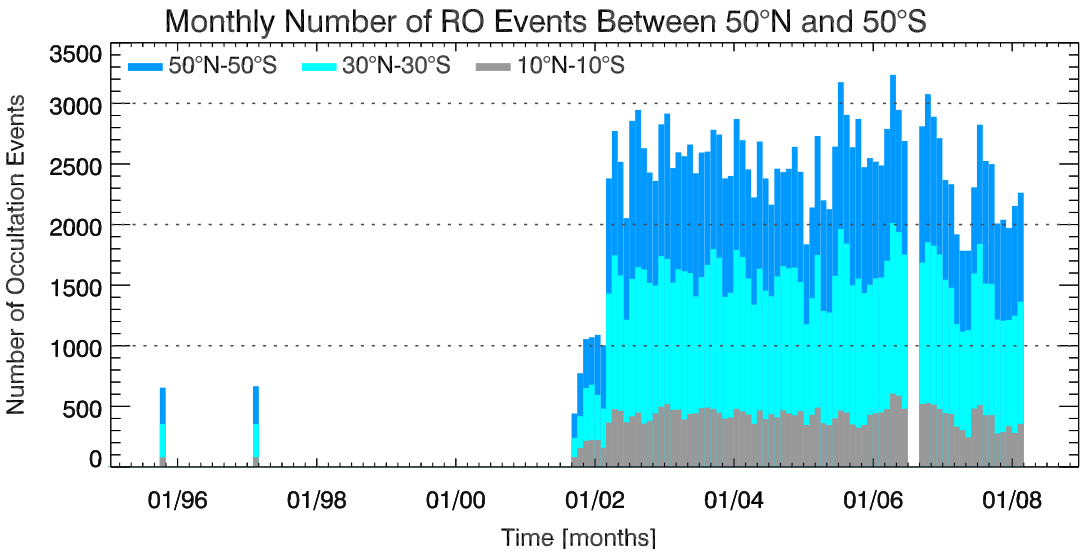

Figure 3.1: Temporal evolution of number of RO measurements at three latitudinal bands of the GPS/MET and CHAMP data used within this study.

Figure 3.1 depicts the number of RO events provided by the two satellites for the period covered in this study. The different colors mark the number of events in three latitudinal bands, as used in the detection study. Between 50°S and 50°N, CHAMP provides on average 2500 profiles (around 1000 profiles during its first 6 months of measurement) per month, GPS/MET around 650 profiles. The spatial distribution as well as a histogram for the occultation events allocated to 20° latitudinal bands is depicted for the two GPS/MET months in Figure 3.2 and for one representative CHAMP month, January 2006, in Figure 3.3. Even though GPS/MET provided less occultation events per month, the available profiles are quite uniformly distributed across the latitudes with around 120 occultation events in each 20° latitudinal band. The tropical band shows slightly less events, which is due to orbit characteristics and geometrical issues (surface area of a sphere depending on latitude).

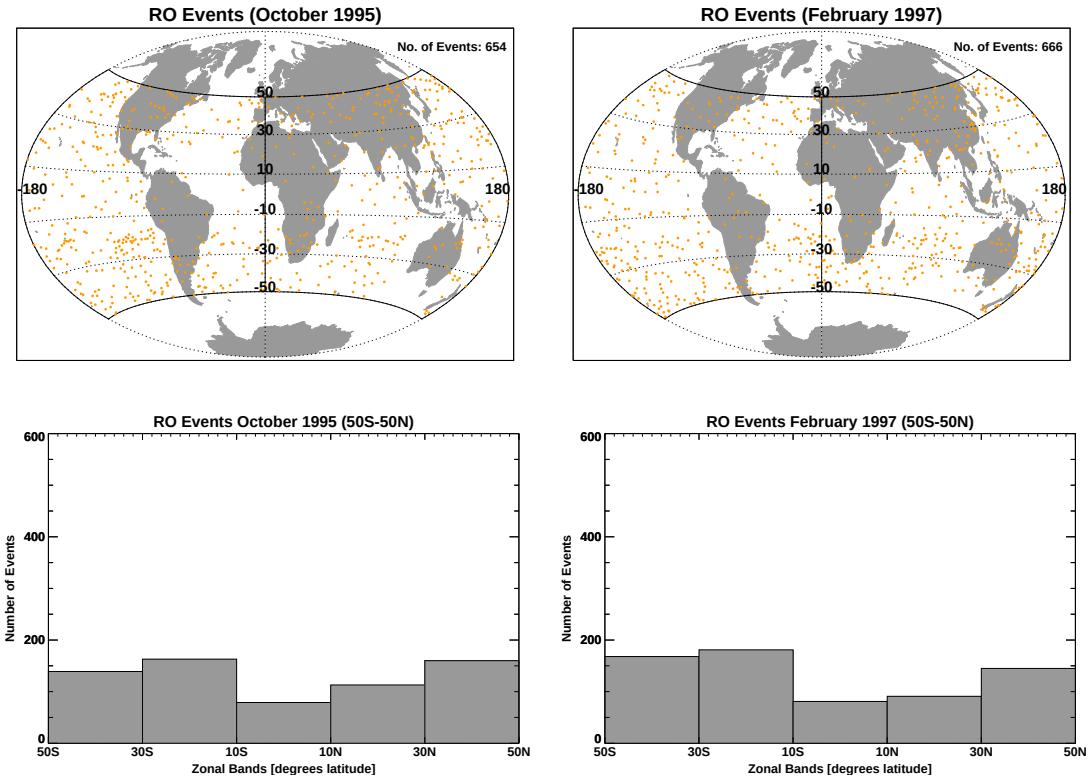

Figure 3.2: *upper panels* Spatial distribution of RO events from GPS/MET in October 1995 (left) and February 1997 (right). *lower panels* Number of RO events per latitudinal bin of 20°. The y-axis is scaled to allow for direct comparison with CHAMP results, depicted in Figure 3.3.

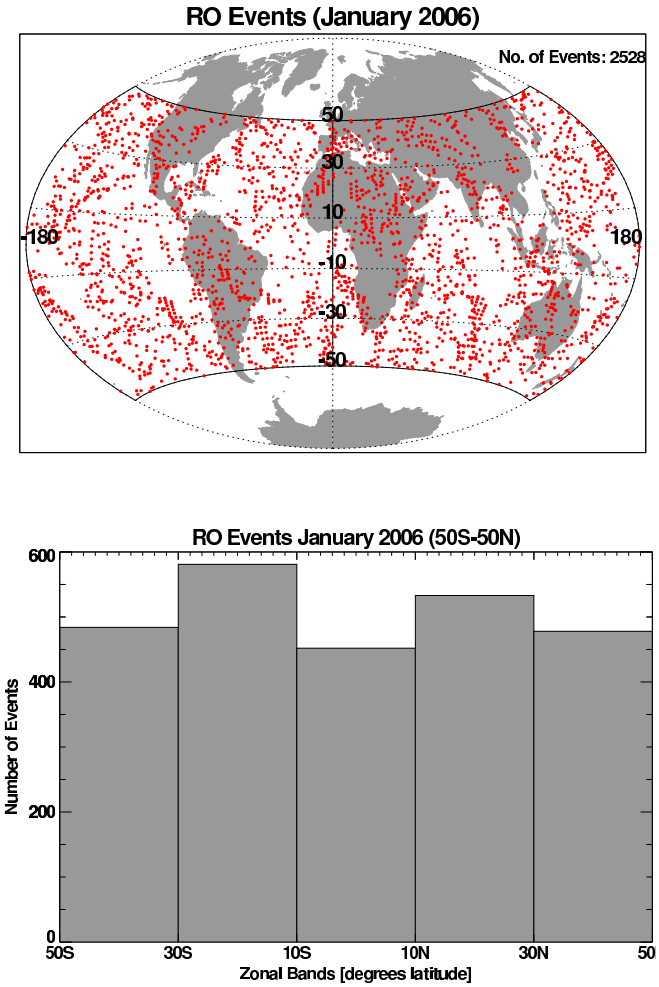

Figure 3.3: *above* Usual spatial distribution of RO events from CHAMP for January 2006 (as an example for month). *below* Number of RO events per latitudinal bin of 20°.

For the trend indicator study, the RO data were *only* used to compare with reanalyses and model variability. Therefore, a zonal mean resolution of several degrees in latitude was employed.

3.1.2 Radiosonde Data

Due to lacking months of RO measurements within 1995 and 2001, a second observational data record was employed in the detection study, namely the Hadley Centre gridded free-atmosphere temperatures from radiosondes (**HadAT2**) record[2] from the United Kingdom (**UK**) Met Office Hadley Centre (Thorne et al. 2005*a*). The monthly data set is available in a horizontal resolution of 10° in latitude and with a vertical

[2]available from `http://hadobs.metoffice.com/hadat/hadat2.html`, Feb 2010

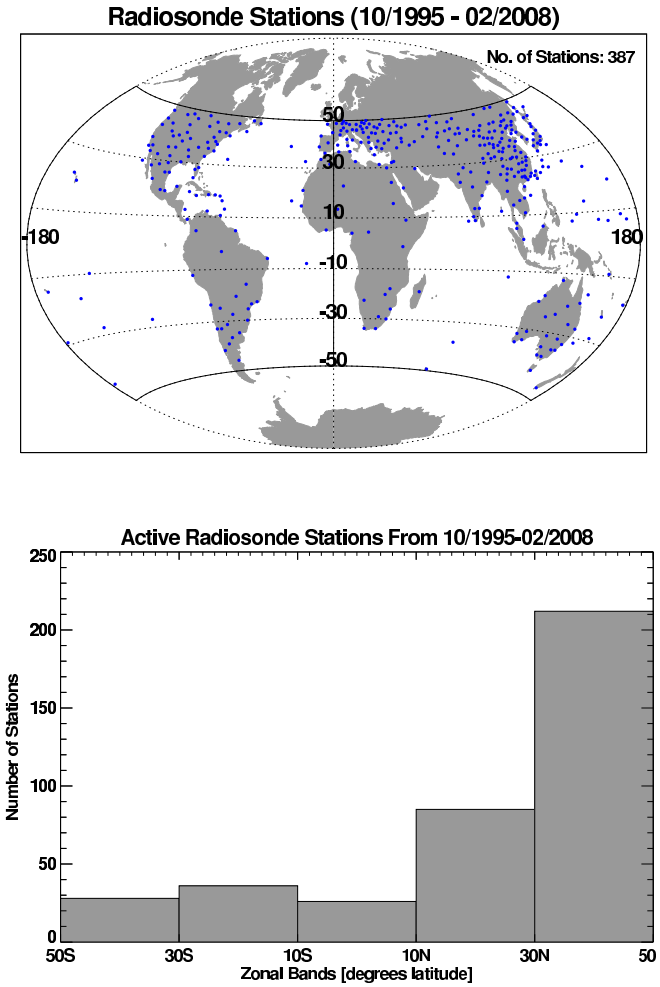

Figure 3.4: *above* Stations with radiosondes measurements between 50°N/S in at least one month within October 1995 to February 2008. *below* Number of radiosondes stations per latitudinal bin of 20°.

resolution of 9 pressure levels (850 hPa, 700 hPa, 500 hPa, 300 hPa, 200 hPa, 150 hPa, 100 hPa, 50 hPa, and 30h Pa). Only temperature anomalies are available, which are based on the monthly 1966 to 1995 mean. The provided zonal mean values are gained by simply averaging over all available station data in the respective latitudinal band.

Figure 3.4 shows all stations that delivered measurements for the used radiosonde data for at least one month within October 1995 to February 2008 and a histogram of station numbers for 20° latitudinal bands between 50°S and 50°N. The station data used for the figure are based on monthly station time series, which are also available on the Hadley Centre radiosonde web-page. The number of monthly measurements is of course higher than the number of stations, as generally one or two radiosondes are launched each day, but the spatial distribution is nevertheless poor compared to RO data (compare Figure 3.4 to Figure 3.2 or Figure 3.3). Figure 3.5, taken from

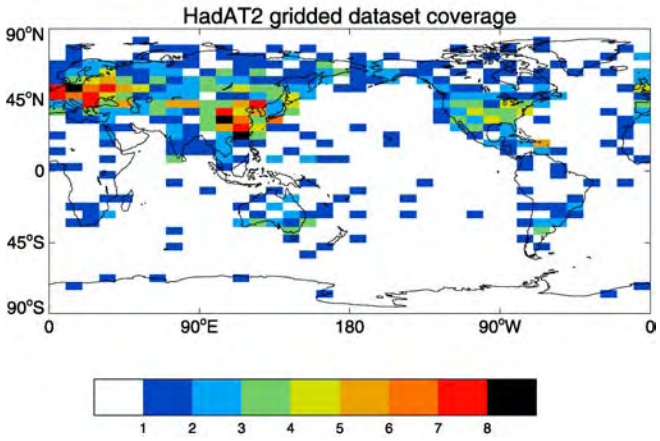

Figure 3.5: Grid box station coverage for HadAT2 products with the maximum number of stations used (actual data coverage varies over time and with height). *Source:* Thorne et al. (2005*a*), Figure 7.

Thorne et al. (2005*a*), depicts for comparison only the grid box station coverage for all latitudes. Both figures show that the stations are not well distributed. Most are positioned at the northern mid-latitudes, while the tropics and southern latitudes are insufficiently covered. No station exists in the Niño regions, which are often used to define El Niño-Southern Oscillation (**ENSO**) events based on changes in sea surface temperatures of the equatorial Pacific between ±5°N/S and between 160°E and 90°W. Thus the poor spatial sampling will influence zonal mean radiosonde climatologies at low and southern latitudes.

Radiosondes also feature daytime biases arising from solar heating of the temperature sensors, which are most pronounced in the stratosphere, where they can amount to several degrees (Sherwood et al. 2005). Radiosondes data discontinuities are also influenced by time-varying biases, different data adjustments and processing methods, and changes in stations and instrumentation types (Karl et al. 2006). Nevertheless, radiosondes are valuable for climate monitoring, as they offer the longest record of hight-resolved measurements extending into the stratosphere.

3.2 Re-analyses

The 45-year ECMWF Re-Analysis (**ERA-40**) was used as proxy data record in the trend indicator study and to analyze large-scale atmospheric patterns in the detection study. In the trend study, the NCEP/NCAR Re-Analysis (**NRA**) from the National Centers for Environmental Prediction (**NCEP**) and the National Center for Atmospheric Research (**NCAR**), United States of America (**USA**), was also included.

Uppala et al. (2005) define a re-analysis as an analysis of past observational data using a fixed, tried, and tested data assimilation system. Thus re-analyses avoid data inhomogeneities due to changes in the assimilation system and provide records with continuous spatial and temporal coverage, which is not always made available by single

observational data. Nevertheless, re-analyses have known shortcomings, e.g., due to changes in the assimilation of different data types, such as the inclusion of satellite data in the late 1970s. Satellite data led to better results and strongly influenced stratospheric data, so that trends, which span the period before and after the satellite era, are not robust but mirror the different amount and quality of information entering the assimilation system.

3.2.1 ERA-40 Re-Analysis

The ERA-40 record (for detailed information see Simmons and Gibson 2000; Uppala et al. 2005), completed in 2003, provides global atmosphere and surface conditions for the period 1957 to 2002. As a follow-up project of the earlier ERA-15 re-analysis, it is regarded as a second generation re-analysis, which benefits from the experiences made with ERA-15 and developments in the European Centre for Medium-Range Weather Forecasts (**ECMWF**) forecasting system.

ERA-40 makes use of the ECMWF Integrated Forecasting System, which was applied operationally from mid-2001 to beginning of 2002. Some modifications were implemented, such as three-dimensional variational (instead of four-dimensional variational) data assimilation and a coarser horizontal resolution.

The re-analysis includes ozone distribution (from observations or parameterized, when no observations were available), radiation budget, hydrological cycle, soil temperature and moisture, and ocean waves. Temporally fixed but spatially varying aerosol concentrations were prescribed. For carbon dioxide ($\mathbf{CO_2}$) and other Green House Gas(es) (**GHG**) Intergovernmental Panel on Climate Change (**IPCC**) specified trends were employed.

ERA-40 assimilated conventional data, such as measurements from various national meteorological centers from Europe, America, Australia, or Japan. For the upper stratosphere (above 10 hPa), remote areas, and for some atmospheric parameters such as ozone ($\mathbf{O_3}$), satellite data were the only source of information. They were assimilated first in 1973 but enhanced since 1979 (see Figure 3.6 for a schematic illustration of data involved in the assimilation).

Even though ERA-40 shows certain shortcomings, it is said to reproduce global-mean temperature trends and low-frequency variability over much of the troposphere and the lower stratosphere (**LS**) sufficiently well, especially after the late 1970s, when satellite data are included. Reichler and Kim (2008) found ERA-40 to match best the observations when the climate mean state was considered. Compared to the first generation re-analyses, such as ERA-15 or the USA NRA, ERA-40 certainly constitutes advances due to taking into account newer methods and data sources.

ERA-40 features a vertical resolution of 60 levels with a top level at 0.1 hPa and a horizontal resolution of T159, which corresponds to ≈125 km. For this study, monthly mean temperature, geopotential, and specific humidity fields for the surface and the

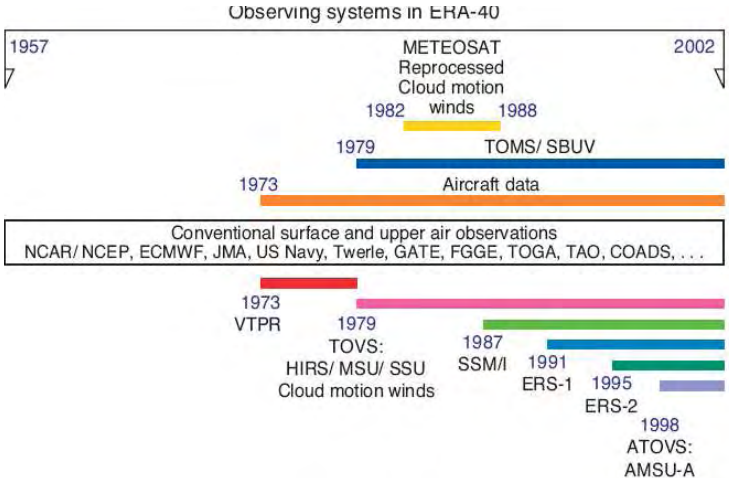

VTPR	Vertical Temperature Profile Radiometer
TOVS	TIROS (Television InfraRed Observational Satellite) Operational Vertical Sounder
HIRS	High-resolution InfraRed Sounder
SSU	Stratospheric Sounding Unit
AMV	Atmospheric Motion Vectors
SSM/I	Special Sensor Microwave/Imager
ERS	ESA Remote-sensing Satellite
ATOVS	Advanced TOVS
AMSU	Advanced Microwave Sounding Unit

[2] Satellite instrument acronyms

Figure 3.6: Schematic illustration of the use of observing systems in ERA-40 (*Source:* Uppala et al. 2005, p. 4).

free atmosphere (23 pressure levels from surface to 1 hPa height) were used. The data is provided for every six hours (00 Universal Time Coordinated (**UTC**), 06 UTC, 12 UTC, and 18 UTC) from 1957 to 2002 and is made available via `http://data.ecmwf.int/data/`. In this study only data from 1980 onwards were used.

3.2.2 NRA Re-Analysis

Beside the European re-analysis ERA-40, the USA NCEP/NCAR re-analysis, NRA (for details see Kalnay et al. 1996; Kistler et al. 2001), was employed in the trend study. The NRA belongs to the first generation of re-analyses and is based on a data assimilation and operational forecast model version of January 1995. NRA provides atmospheric and surface fields from 1948 to nearly present.

The model includes parameterizations of all major physical processes. According to Trenberth et al. (2007), the re-analysis includes errors in radiative forcings as it did not allow for changes in GHG increases over the record. The parameter fields are assigned into four classes (A to D), depending on the influence of observational and model data on the variable. All parameters used in this study, except specific humidity, belong to the most reliable A class, which indicates that the variable is strongly influenced by observed data. Specific humidity is part of the B class, which contains variables that are not only determined by observations but also influenced by the model.

As for ERA-40, NRA data are strongly influenced by the comprehension of satellite data in 1979, and Kistler et al. (2001) claim the reanalysis after 1979 as most reliable. Concerning trend estimates based on NRA, they propose to compare the agreement of

trends of the southern and northern hemisphere (agreement could increase confidence in trends) or to compare the trends from NRA to those from other re-analyses. Trend agreement between different reanalyses may again increase their reliability, although they note that this fact is not sufficient to ensure it.

NRA has a vertical resolution of 28 levels, with 7 levels above 100 hPa and a top level of 3 hPa, so that the stratosphere at 10 hPa is not strongly affected by the top boundary conditions. Specific humidity is only provided for the troposphere/ tropopause region from 1000 hPa to 300 hPa. The horizontal resolution is T62, which corresponds to ≈ 209 km. Monthly mean atmospheric pressure level fields for temperature, geopotential height, and specific humidity are provided as Network Common Data Format (**netCDF**) files from `http://www.esrl.noaa.gov/psd/data/gridded/reanalysis/reanalysis.html`.

3.3 Model Data

Climate models are mathematical descriptions of the Earth's atmosphere, including different climate components and feedbacks depending on the model's complexity. They comprise known physics of the atmosphere, often complemented by the physics of the ocean, ice-sheets, and land surface. Thus, models are simplifications of the reality. McGuffie and Henderson-Sellers (2005) note two kind of simplifications that have to be implemented: (1) simplification of processes, which are caused by a lack of information, of understanding, or caused by insufficient computer resources, and (2) simplifications in the spatio-temporal resolution due to data availability and computational constraints.

Concerning the spatial modelling, two approaches are established: finite and spectral fields. *Finite grids*, also addressed as latitude-longitude grids, arrange the atmosphere in a series of boxes, which are usually spaced in latitude and longitude. Each box is characterized by a vector of data values used to solve the atmospheric equations. Atmospheric phenomenons within a grid box cannot be resolved correctly. The size of the box is connected with the temporal resolution. The time steps must be shorter than the time needed for information to propagate through a grid box.

Spectral models (for details see, e.g., McGuffie and Henderson-Sellers 2005) make use of the spherical coordinate system of the Earth and represent the climatological variables in the horizontal as finite series of waves with different wavelengths. The vertical representation still follows a grid point space. The horizontal waves are Fourier transforms of the original data and are periodic for one latitudinal band. The resolution of spectral models is given by the wavenumber of the truncation, i.e. the number of waves that are used to represent a variable in a latitudinal band. As the grid point model cannot resolve phenomenons within a grid box, the spectral model is limited by the truncation number (M). There are three main types of truncation: triangular,

rhomboidal, and trapezoidal truncation. They are based on the number of the largest Fourier wavenumber, the highest degree of associated Legendre polynomial, and the highest degree of the Legendre polynomial of order zero used to define the spherical harmonics. The most commonly used triangular truncation, abbreviated with a capital "T" followed by the truncation number, e.g., T42, shows roughly the same resolution in latitude and longitude. The coefficients of the spherical harmonics can be used to represent the variable values again in a latitude-longitude grid, which is then called a *gaussian grid* and abbreviated by a capital "N" followed by a number indicating the number of latitudes between equator and pole. It shows an irregular spacing of the latitudes, but is symmetrical about the equator and linked to the spectral truncation type. Triangular truncation, e.g., leads to (3M+1) grid points for the longitudes and to $\frac{1}{2}$(3M+1) grid points for the latitudes when converted into a gaussian grid.

The model's abilities are not only influenced by horizontal but also by the vertical resolution and by boundary conditions at the top level. The vertical resolution of models is generally based on discrete levels. Fields are commonly given either as function of *height* or as function of *pressure level*. If height is used as reference coordinate, two different reference surfaces can be used:

- the Earth's ellipsoid, with the vertical resolution denoted as *height* and
- the Earth's geoid, with the vertical resolution denoted as *altitude*.

For pressure-based vertical resolutions, the fields are given at certain constant pressure levels, which is the simplest basis for the equation of motions in the atmosphere. Height and pressure surfaces can intersect mountains and thus "disappear" over parts of the model domain (Cianflone and Weingroff 1997). Thus, other vertical formulations, such as σ-levels of η-levels, which follow a (smoothed) surface, are used as well.

All model data (including the re-analyses) used in this study are provided on pressure levels, while the RO data are given on altitude levels. The conversion from altitude to pressure levels and vice versa is detailed in section 3.4.

3.3.1 IPCC AR4 Models

For the trend indicator and the detection study three selected General Circulation Model (**GCM**) are used, which were collected by the Program for Climate Model Diagnosis and Intercomparison (**PCMDI**) to contribute to the phase 3 of the Coupled Model Intercomparison Project (**CMIP3**) and to the Fourth Assessment Report (**AR4**) of the IPCC. The whole data set is also addressed as World Climate Research Programme (**WCRP**) CMIP3 multi-model data set.

According to Randall et al. (2007), there is considerable confidence that the AR4 models provide credible quantitative estimates of future climate change, particularly at continental and larger scales, even though the confidence in the estimates is higher for some variables, such as temperature, than for others. Most of the models need no

flux adjustments, which were previously needed to guarantee a stable climate. This is as well the case for the three selected GCMs in this study. Furthermore, progress had been made compared to former models in regard to the representation of large-scale climate processes, such as the ENSO. Nevertheless, other atmospheric patterns such as the Quasi-Biennial Oscillation (**QBO**) still could not be resolved by the models.

The three selected GCMs are the

- Community Climate System Model 3 (**CCSM3**), from NCEP/NCAR, USA;
- ECMWF Hamburg Model (**ECHAM5**), from Max Planck Institute for Meteorology (**MPI-M**), Hamburg, Germany; and the
- Hadley Centre Coupled Model, version 3 (**HadCM3**), from Hadley Centre for Climate Prediction and Research (**HadC**) of UK Met Office (**UKMO**), UK.

All model output data are made available via the Earth System Grid (**ESG**), `www.earthsystemgrid.org` (March 2010).

CCSM3

In 1983, the Community Climate Model (**CCM**) was created by NCAR as a freely available global atmosphere only model[3]. Around 10 years later, the model was extended to a Climate System Model (**CSM**), which included beside the atmospheric model, an ocean, sea ice, and land surface model. The third model version, CCSM3 (for details see Collins et al. 2006), whose data are used in this study, was released in June 2004. It is a coupled climate model composed of four separate models for the Earth's atmosphere, the ocean, land surface, and sea-ice. For the IPCC AR4, CCSM3 was run in a T85 resolution (160 latitude and 256 longitude grid points) with 26 levels in the vertical (top level at 2.2 hPa, see Randall et al. 2007).

ECHAM5

ECHAM5 (Roeckner et al. 2003*a*) is the 5th generation of the ECMWF–MPI-M Hamburg (**ECHAM**) general circulation model. The first two letters in the model acronym, "EC" stand for ECMWF, as the model has been developed from the ECMWF operational forecast model (version 1989), the remaining "HAM" refers to Hamburg, Germany, where a comprehensive parameterization package was developed. As a coupled model, it combines models for the atmosphere, ocean, sea-ice, and land, the latter including the ice sheets. Originally, ECHAM5 can be applied in various horizontal resolutions (T21, T31, T42, T63, T85, T106, and T159), for the AR4 output, a T85 resolution was employed. In the vertical, there are two standard configurations, one with 19 and one with 31 vertical levels, out of which the latter was used. Both feature a top level at

[3] `http://www.ccsm.ucar.edu`, March 2010

10 hPa. The higher vertical resolution shows a better zonal mean climate state with increasing higher horizontal resolutions (Roeckner et al. 2003*b*).

HadCM3

Developed in 1998, the HadCM3 (Gordon et al. 2000; Pope et al. 2000; Johns et al. 2003) is a coupled GCM developed by the HadC, UK. As the other two models described, the model needs no flux adjustment. This is one major difference to its precursor model and it was due to improvements of the atmosphere and ocean model, including higher ocean resolution. The HadCM3 has two components, an atmospheric model and an ocean model, which also includes a sea ice model. Compared to the other models, the AR4 output data show a coarser resolution with 73 latitude and 96 longitude grid points (comparable to a T42 spectral resolution) and 19 levels in the vertical. The top level is specified with 39.2 km (Randall et al. 2007).

Different GCM Experiments and Forcings Used for the GCMs

In this section, different experiments, such as those based on emission scenarios of the AR4 and the forcings used in the GCMs are presented. For the IPCC AR4, various experiments were implemented, from which data of four experiments were used in this study:

1. pre-industrial control experiment (**PICTRL**), the
2. climate of the 20th century experiment (**20C3M**), and the
3. Special Report on Emission Scenarios (**SRES**) A2 experiment, and the
4. SRES B1 experiment.

As mentioned above, the used GCMs can be run for many years without showing a shift in the mean climate. Such long-term GCM simulations can be used to estimate the natural climate variability. Therefore, the IPCC AR4 models provide a so-called PICTRL. For this experiment, the models are run with no anthropogenic[4] or natural[5] forcings for at least 100 years, so that any residual, unforced drift can be removed from those experiment results, which are run with perturbations. Forcings in GCMs are generally defined as changes in the background conditions that are external to the model calculations (e.g., Schmidt et al. 2004). Figure 3.7 shows exemplarily the variability (standard deviation) of temperature fields for the three used models. The

[4]Generally, human-induced changes in well-mixed GHG associated with fossil fuel burning, in (sulphate) aerosols, in ozone, or in land surface properties are among other things considered as anthropogenic forcings.

[5]Natural forcings are commonly defined as changes in the climate system due to orbital or solar irradiance changes or as impacts due to volcanic events.

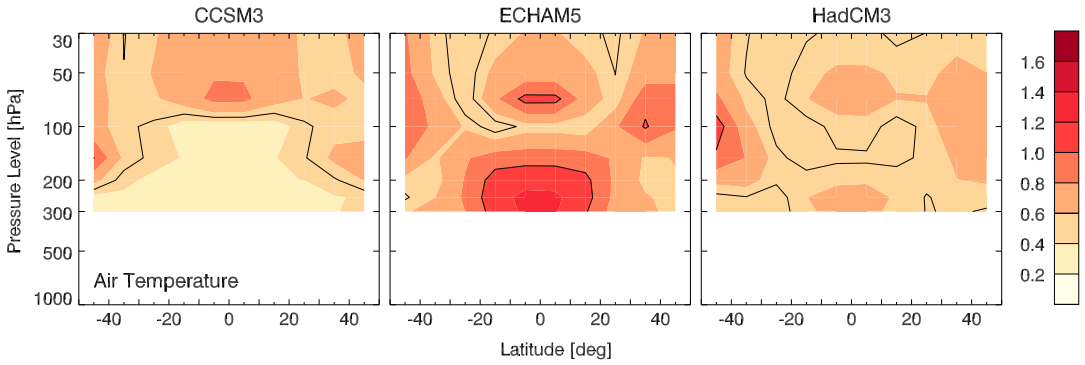

Figure 3.7: Standard deviation of monthly mean time series of PICTRL temperature fields between 50°N and 50°S and 300 hPa to 30 hPa for the three GCMs employed in this study: CCSM3 (left), ECHAM5 (middle), and HadCM3 (right).

calculations are based on all available PICTRL data. The figure illustrates well the differences between the models: While HadCM3 features a more a less uniform spatial variability in temperature, ECHAM5 shows highest variability values in the tropical upper troposphere (**UT**) and CCSM3 in the tropical stratosphere, but the amplitude being less than in ECHAM5. Regarding the three models, ECHAM5 generally exhibits largest internal variability and CCSM3 the lowest one, while HadCM3 is somewhere in between. Overall they cover a representative range of variability as stated by Hegerl et al. (2007, p. 686) in the IPCC AR4 "There is no evidence that the variability in paleoclimatic reconstructions that is not explained by forcings is stronger than that in models and simulations of the last 1 kyr".

The 20C3M runs are initialized from a point in a PICTRL run and should cover the period of ≈1850 to 2000. The different modelling groups used various combinations of forcings and different forcing datasets for the 20th century. For ECHAM5, e.g., only anthropogenic forcings, such as CO_2, methane (**CH_4**), nitrous oxide (**N_2O**), trichlorofluoromethane (**F11**), dichlorodifluoromethane (**F12**), O_3, and sulfate (**SO_4**) were employed.

Besides past (PICTRL) and present (20C3M) climate simulations, future climate projections are available. In 1992, first emission scenarios to drive GCMs were published from the IPCC. Based on model developments and increased understanding of the climate system, a new set of scenarios was considered as necessary in 1996.

In the SRES, Nakićenović et al. (2000) describe scenarios as images of the future, or alternative futures. The images should assist the understanding of possible future developments including climate modeling, the assessment of impacts, adaption, and mitigation, as many physical and social systems are not entirely understood. Each of the images is equally likely to become true or not as the future of our climate

system will be strongly influenced by future GHG emissions, which are in turn results of demographic and socio-economic developments and technological changes. Based on possible developments and changes, four different SRES storylines were developed. Each of the storylines embraces a set of scenarios, called families, namely A1, A2, B1, and B2. The following list summarizes the main points of the storylines as defined by Nakićenović et al. (2000):

- **A1 storyline** a future world of very rapid economic growth, global population that peaks in mid-century and declines thereafter, and the rapid introduction of new and more efficient technologies; convergence among regions, increased cultural and social interactions, with a substantial reduction in regional differences in per capita income; splits in three groups that describe alternative directions of technological change in the energy system with different emphasis:
  - A1FI: fossil intensive,
  - A1T: non-fossil energy sources,
  - A1B: balance across all sources.
- **A2 storyline** a very heterogeneous world; self-reliance and preservation of local identities; continuously increasing global population, economic development is primarily regionally oriented and per capita economic growth and technological change are slower than in other storylines.
- **B1 storyline** convergent world with the same global population as in the A1, but rapid changes in economic structures toward a service and information economy, with reductions in material intensity, and the introduction of clean and resource-efficient technologies; emphasis on global solutions to economic, social, and environmental sustainability, including improved equity, but without additional climate initiatives.
- **B2 storyline** a world with emphasis on local solutions to economic, social, and environmental sustainability; continuously increasing global population at a rate lower than A2, intermediate levels of economic development, and less rapid and more diverse technological change than in the B1 and A1; focus on local and regional levels.

Within this study, in addition to the PICTRL and 20C3M, SRES A2 and SRES B1 simulations of the selected models were employed. In Table 3.1, selected driving forcings, such as population or gross domestic product (**GDP**), as well as different GHG emissions for the past (1990) and projected future in 2020, 2050, and 2100 are presented (for the overall specifications see Nakićenović et al. 2000). The CO_2 concentrations are assessed by means of Figure 10.26 in the IPCC AR4 (Meehl et al. 2007).

The CO_2 concentration in 2100 relative to the 1980 to 2000 mean can be related to mean surface temperature changes. For the B1 scenario, the ensemble mean of

		SRES A2			SRES B1		
	1990	2020	2050	2100	2020	2050	2100
population (billion)	5.3	8.2	11.3	15.1	7.6	8.7	7.0
world GDP (10^{12}US$/yr)	21.0	41.0	82.0	243.0	53.0	136.0	328.0
CO_2, fossil fuel [Gt/yr]	6.0	11.0	16.5	28.9	10.0	11.7	5.2
CO_2, land use [Gt/yr]	1.1	1.2	0.9	0.2	0.6	-0.4	-1.0
SO_2 [Mt/yr]	70.9	100.0	105.0	60.0	75.0	69.0	25.0
CH_4 [Mt/yr]	310.0	424.0	598.0	889.0	377.0	359.0	236.0
CO_2 concentration [ppm][a]	360[b]		520	850		480	600

[a] approximate values, based on Figure 10.26 in Meehl et al. (2007, p. 803)
[b] approximate value for 2000

Table 3.1: Overview on SRES A2 and B1 driving forcings and emissions for 2020, 2050, and 2100, compared to 1990 values (Nakićenović et al. 2000).

all IPCC AR4 models yields then an increase in surface temperature of $\approx 2°$ in 2100 with respect to the 1980 to 2000 mean, the A2 scenario an $\approx 3.9°$ surface temperature increase.

Even though all AR4 models were based on the SRES, differences remain, e.g., in the forcings used or the model resolution. The three GCMs of this study perform without flux-corrections and include stratospheric O_3 depletion and recovery forcings (Roeckner et al. 2005, J. Meehl, NCAR/USA, T. Johns, Met Office/UK, J. Gregory, Met Office/UK, personal communication, 12/2007), which is particularly important for an adequate simulation of stratospheric temperatures (Forster et al. 2007). According to an analysis of Reichler and Kim (2008), the models belong to the five best performing models without flux-correction, meaning that they show good agreement with observations in their time-mean state of the climate. Table 3.2 gives an overview on the forcings used in the perturbed experiments of the used models, the vertical characteristics of the models, and the number of simulations that were used per scenario. The information in the table is based on the "Model Information of Potential Use to the IPCC Lead Authors and the AR4" for CCSM3, ECHAM5, and HadCM3, which is made available on the PCMDI web-page at `http://www-pcmdi.llnl.gov/ipcc/model_documentation/ipcc_model_documentation.php` and on two publications (Johns et al. 2003; Cordero and de Forster 2006).

Figure 3.8 shows annual mean "global" mean (60°N to 60°S) temperature data for all GCM simulations and the two re-analyses for the whole period considered in the trend indicator study at two selected pressure levels. The volcanic forcing, which is only present in CCSM3, is clearly visible at the 30 hPa level (less pronounced also at the

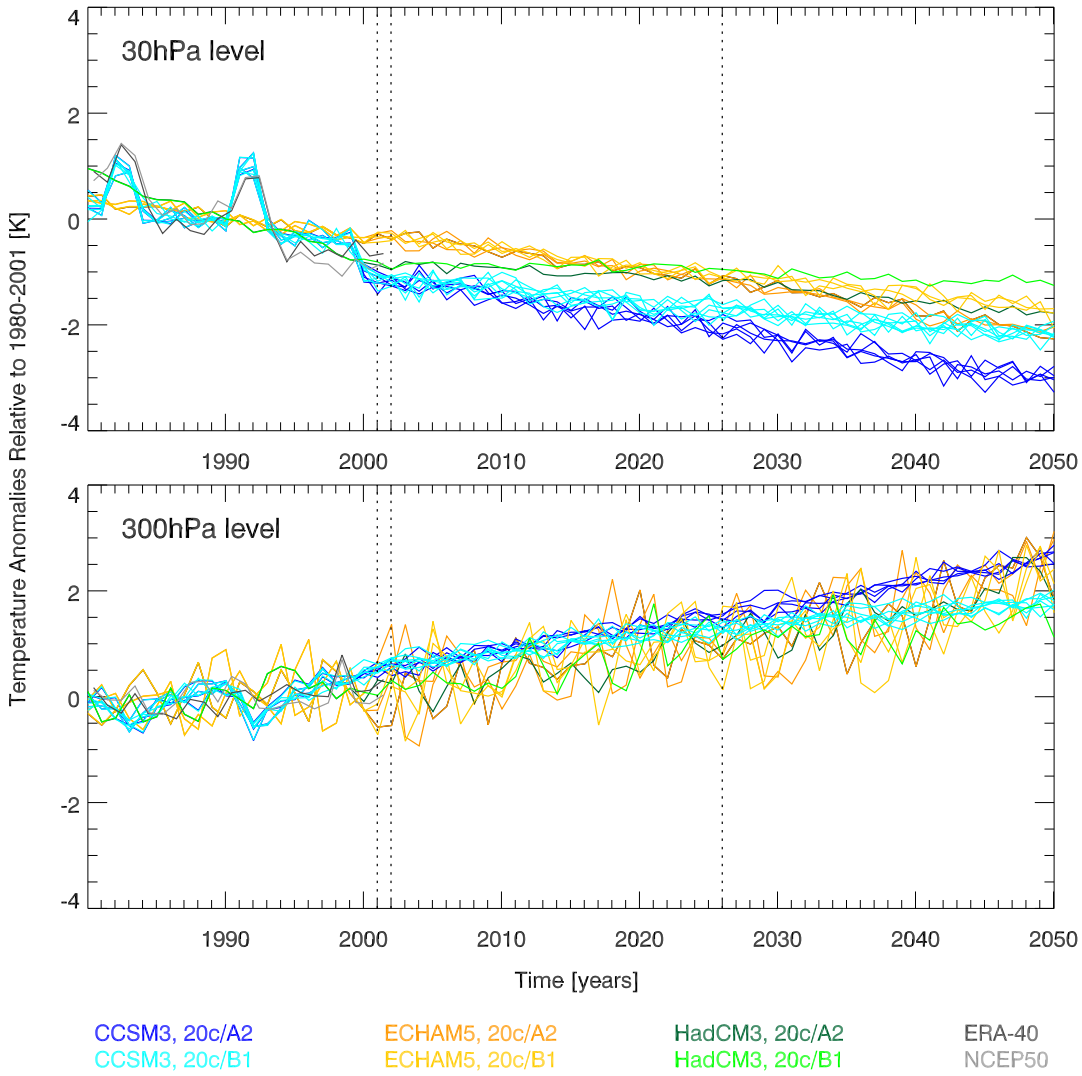

Figure 3.8: Annual mean temperature data of global mean data between 60°N and 60°S for the period 1980 to 2050 for all 20 used GCM simulations and the two re-analyses at 30 hPa (top) and 300 hPa (bottom). The vertical dotted lines mark the start and end points of the different periods analyzed.

	CCSM3	**ECHAM5**	**HadCM3**
GHG, strat. O3, aerosols	Y	Y	Y
volcanos (aerosols)	Y	N	N
number of levels	26	31	19
strat. levels ($> 200\,\text{hPa}$)[a]	13	9	NA
top level	2.2 hPa	10 hPa	39.2 km ($\approx$3 hPa)
number of experiments			
20C3M	7	3	2
A2	5	3	1
B1	7	3	1
PICTRL	2	1	1
PICTRL years in total	730	506	341

[a]Number of stratospheric levels ($> 200\,\text{hPa}$) as used in the experiment runs of the models. The number of provided levels is given in Table 3.3.

Table 3.2: Overview on forcings used in perturbed experiments, vertical model resolution (vertical levels, top level, stratospheric levels), and number of simulations per experiment used in this study. "Y" stands for a used forcing, "N" for a missing forcing, and "NA" for a value not available.

300 hPa level) at the beginning of the time period. It mirrors two volcanic eruptions, one from El Chichón, Mexico, 3 April 1982, and one from Pinatubo, Philippines, 15 June 1991. The influence of the different forcings in SRES A2 and SRES B1 becomes obvious around 2020. From then on, the simulations of the two scenarios start to spread and differ by around 1 K in 2050. The plot also visualizes well the stronger tropospheric variability of ECHAM5 compared to CCSM3 data.

3.3.2 Middle-Atmosphere Model

IPCC AR4 models feature low top levels and thus are said to simulate the LS not correctly. Therefore, data from the Middle Atmosphere Mode of ECMWF Hamburg Model, version 5 (**MAECHAM5**) (Manzini et al. 1997; Manzini and McFarlane 1998; Manzini et al. 2006*b*), using 39 model levels up to 0.01 hPa ($\approx$ 80 km), were applied to compare with the AR4 models with lower top levels. The data were processed at MPI-M by Luis Kornblüh using a T42L39 resolution, the respective volume files were calculated at WEGC by Ulrich Foelsche. The model was run with GHG, aerosols, and O_3 forcings based on the IS92a emission scenario (e.g., Houghton et al. 2001), which

features a projected atmospheric CO_2 concentration of 700 parts per million by volume (**ppmv**) in 2100 (Foelsche et al. 2008*a*). The data are employed in the trend indicator study for the period 2001 to 2025.

3.4 Data Preparations

As all data sets, provided as netCDF files, come in with different resolutions and as function of different parameters (most are given as function of pressure), the re-analyses and GCMs were brought to a *study resolution* in a first step. It is given as follows:

- **horizontal resolution**: 72 latitudinal ($-88.75°$ to $88.75°$, negative values indicate southern latitudes) and 144 longitudinal ($-178.75°$ to $178.75°$, negative values indicate western longitudes) grid points, which corresponds to a $2.5° \times 2.5°$ grid or a T42 resolution;
- **vertical resolution**: 18 pressure levels from surface to the LS, including the 1000 hPa, 925 hPa, 850 hPa, 775 hPa, 700 hPa, 600 hPa, 500 hPa, 400 hPa, 300 hPa, 250 hPa, 200 hPa, 150 hPa, 100 hPa, 70 hPa, 50 hPa, 30 hPa, 20 hPa, and 10 hPa level;
- **temporal resolution**: monthly mean data.

The basic horizontal resolution is based on the horizontal elongation of RO profiles, which is ≈ 300 km, corresponding to a $2.5° \times 2.5°$ grid in latitude and longitude or a spectral T42 resolution. The two observational data sets, RO and radiosondes, feature zonal means with a 10° resolution in latitude. This is due to the limited number of RO events and radiosonde stations, which does not permit the basic $2.5° \times 2.5°$ grid for monthly mean data. The resolution of smaller scales is possible for RO data, when occultation events from more satellites are used as, e.g., provided from Formosa Satellite Mission #3/Constellation Observing System for Meteorology, Ionosphere, and Climate (**FORMOSAT-3/COSMIC**). Nevertheless, the focus in this study is on single satellite climatologies based on GPS/MET and CHAMP.

A benefit of RO climatologies is their good vertical resolution. To be able to compare RO and model data, it was necessary to surrender this data advantage. The basic vertical resolution was geared towards the available pressure levels in the IPCC AR4 models, as defined above, with focus on the upper troposphere-lower stratosphere (**UTLS**) between 300 hPa and 30 hPa, where a dry atmosphere can be assumed. Single missing levels, such as the 70 hPa level in HadCM3 or the 20 hPa level in HadCM3 and ECHAM5, were gained by interpolation of the respective fields.

In the following, the different steps to harmonize the data are described in general, data set specific treatments are mentioned as appropriate.

	observations		**re-analyses**		**global climate models**			
	RO	**HadAT2**	**ERA**	**NRA**	**CCSM3**	**ECHAM5**	**HadCM3**	**MA-ECHAM5**
data center	WEGC	HadC/ Met Office	ECMWF	NCEP/ NCAR	NCEP/ NCAR	MPI-M	HadC/ Met Office	MPI-M
reference	Gobiet and Kirchengast (2004); Pirscher (2010)	Thorne et al. (2005*b*)	Simmons and Gibson (2000); Uppala et al. (2005)	Kistler et al. (2001)	Collins et al. (2006)	Roeckner et al. 2003*a*; Roeckner et al. 2003*b*	Gordon et al. 2000; Pope et al. 2000	Manzini et al. 2006*b*; Manzini et al. 2006*a*
provided resolution	10°×zonal 175 levels	10°×zonal 9 levels	2.5°×2.5°, 23 levels	2.5°×2.5°, 17 levels	T85L17 1.4°×1.4°	T63L16 ≈ 1.9°×1.9°	2.5°×3.75°, 15 levels	T42L39 ≈ 2.5°×2.5°
min, max level	200 m, 35000 m	850 hPa, 30 hPa	surface, 1 hPa	surface, 10 hPa	surface, 10 hPa	surface, 10 hPa	surface, 10 hPa	surface, 0.01 hPa
period used	1995,1997, 2001–2008	1995–2008	1980–2001	1980–2001	1980–2001 2001–2025 2001–2050	1980–2001 2001–2025 2001–2050	1980–2001 2001–2025 2001–2050	2001–2025
parameter	$N(h)$, $Z(p), p(h)$, $T(h)$	$T(p)$	$Z(p), T(p)$, $q(p)$	$Z(p), T(p)$, $q(p)$	$Z(p), T(p)$, $q(p)$	$Z(p), T(p)$, $q(p)$	$Z(p), T(p)$, $q(p)$	$Z(p), T(p)$, $q(p)$
trend study			Y	Y	Y	Y	Y	Y
detection study	Y	Y	Y		Y	Y	Y	

Table 3.3: Summary of data set characteristics for observations, re-analyses and GCMs as provided by the different data centers. Indicated are references to the data, their resolutions, the periods and parameters analyzed, and the data utilization in trend indicator or detection study (marked with "Y"). RO parameters are given as functions of MSL-altitude (h), all other parameters are given as function of pressure (p).

3.4.1 Combination of Files

As the original files provided by the different data centers comprised in most cases longer time ranges than needed for the study, the required period was cut out or occasionally various files were combined. The goal for the forced GCMs was to provide monthly time series spanning from December 1960 to December 2064. For the re-analyses the target period was December 1960 to August 2002, the last month of available data from ERA-40. As the data were also used in other studies of the project Indicators of Atmospheric Climate Change from Radio Occultation (**INDICATE**), discrepancies to the above noted periods (see, e.g., Table 3.3) are due to the use of shorter records for this thesis. Concerning the forced GCMs, it was thus necessary to combine the respective 20C3M simulations with the SRES A2 and the SRES B1 simulation. The information about which 20C3M simulation has to be combined with which forced simulation is available from the PCMDI web page at `http://www-pcmdi.llnl.gov/ipcc/time_correspondence_summary.pdf`.

PICTRL data of one simulation, which were split into several files, were combined into a single file to facilitate further calculations. This applied to the first CCSM3 PICTRL simulation, which is a combination of 3 files (covering the time periods 280 to 359, 360 to 439, and 440 to 509). The second CCSM3 PICTRL simulation is a combination of 7 files spanning the time range 300 to 799. The ECHAM5 PICTRL simulation is made up of 5 individual files comprising the period 2150 to 2655.

ERA-40 monthly means were provided for 4 time slices, namely at 00 UTC, 06 UTC, 12 UTC, and 18 UTC. To obtain one single monthly mean data file, the values of the 4 time slices were averaged (using a simple arithmetic average).

The WEGC ROclimatologies are provided as one file per month containing the monthly means of all parameters from one satellite (GPS/MET or CHAMP). The files were combined to have a single file at hand comprising all parameters for the whole period analyzed. Furthermore, as RO data are provided as a function of MSL-altitude, they were also transformed into data as a function of p and as a function of z.

3.4.2 Data Interpolation

The data sets are made available with different horizontal and vertical resolution (see Table 3.3). To facilitate further calculations and make model and re-analyses output comparable to RO data, GCMs and re-analyses where interpolated to a common grid, as defined at the beginning of section 3.4. The spatial interpolation method applied is presented in the following.

In general, interpolation is the technique of estimating *new* values from known ones. In this context, *new* does not mean that more information will be available after the interpolation. The change from one resolution to another is named *regridding*. For a given grid point field, only a certain amount of points is known, but not the

appropriate analytical function. Based on the set of tabulated data it is possible to calculate intermediate values. The determination of these values is based upon an interpolating function that establishes a relationship between the discrete data points. Unlike curve-fitting algorithms, interpolation requires the interpolating function to be an exact fit at each of the tabulated data points.

The goal of interpolation is to find a function g, diverging as little as possible from a function f. Furthermore, the approximation error at a finite number (n) of so called nodes $\mathrm{x}_k,\ k = 1, \ldots, n$, has to be zero. The given pairs $(\mathrm{x}_k, f(\mathrm{x}_k)) \in \mathbb{R}^2$ are called interpolation points or nodes, the $f(\mathrm{x}_k) = \mathrm{y}_k$ are the interpolation values.

There are many different interpolation methods, such as polynomial or spline interpolation. Depending on the given discrete data points, the methods generally differ, among other things, in accuracy, smoothness of the interpolant, or number of data points needed. A summary of the basic interpolation theory for spline and polynomial interpolation, including linear and 4-point polynomial interpolation (cubic interpolation) as special polynomial interpolation cases, is given in appendix A.

Horizontal Interpolation

The horizontal interpolation method used for this study is based on cubic interpolation (cf.appendix A.1). An End-to-End Generic Occultation Performance Simulation and Processing System (**EGOPS**) Fortran 90 subroutine[6] for adapted polynomial interpolation of atmospheric fields was used to regrid the GCMs and re-analyses. The method is described by the authors as "cubic interpolation between 2nd and 3rd point using two derivatives from finite differences and two values". It generally makes use of four points (i.e. the neighboring points and their next neighbors), except at the field boundaries. Three different cases may occur, depending on the position of the required point according to the four used points:

1. **default**: the required value is situated between the 2nd and 3rd given point (Figure 3.9, middle);
2. **left-side margin**: the required value is situated between the 1st and 2nd point of the given array. In this case, only three points are used for interpolation (Figure 3.9, left);
3. **right-side margin**: the required value is situated between the last two values of the array. In this case, the three last values of the array are used for interpolation (Figure 3.9, right).

The Gorbunov–Steiner formulation for this problem is to use two combined polynomials, resulting in P_{weights}, which pass through two middle points. One polynomial, the cubic P_{f_i}, is fitted to the function values f_2 and f_3 of x_2 and x_3, the other, the

[6] "Weight4" written by M. E. Gorbunov and A. K. Steiner, 1999.

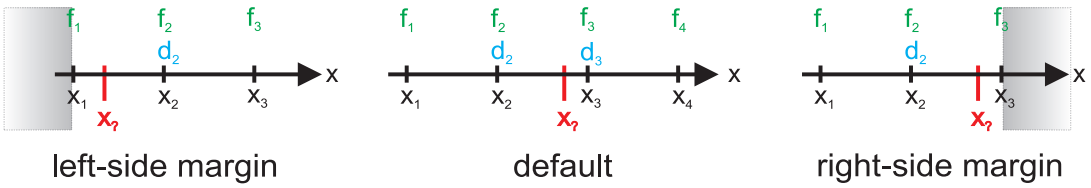

Figure 3.9: EGOPS subroutine "Weight4" cases for cubic interpolation method. The x_i stand for the abscissa values, the f_i for the ordinate values, the d_i for the mean slope between the two adjacent (d_{i-1}, d_{i+1}) values, see equation (3.3) and equation (3.4).

quadratic P'_{d_i}, to the mean slope between three points. For example, the mean slope of the function between x_1, x_2, and x_3, is denoted as d_2, the mean slope between x_2, x_3, and x_4, is denoted as d_3.

For the four given points $(x_1, f_1), (x_2, f_2), (x_3, f_3), (x_4, f_4)$, the interpolation polynomial is chosen in a way that between x_2 and x_3 the following four boundary conditions, defining the four coefficients of the cubic polynomial, are fulfilled:

$$f(x_2) = f_2 \tag{3.1}$$

$$f(x_3) = f_3 \tag{3.2}$$

$$\frac{\mathrm{d}f}{\mathrm{d}x}\,|_{x=x_2} = \frac{1}{2}\left(\frac{f_3 - f_2}{x_3 - x_2} + \frac{f_2 - f_1}{x_2 - x_1}\right) = d_2 \tag{3.3}$$

$$\frac{\mathrm{d}f}{\mathrm{d}x}\,|_{x=x_3} = \frac{1}{2}\left(\frac{f_4 - f_3}{x_4 - x_3} + \frac{f_3 - f_2}{x_3 - x_2}\right) = d_3 \tag{3.4}$$

AAs $f(x)$ is a linear function of f_1, f_2, f_3, f_4, it can be written as

$$f(x) = P_1 f_1 + P_2 f_2 + P_3 f_3 + P_4 f_4, \tag{3.5}$$

where P_1, P_2, P_3, P_4 are universal polynomials. The weights (w_i) for the f_i are the coefficients of the combined cubic and quadratic polynomials:

$$P_{\text{weights}} = w_1 f_1 + w_2 f_2 + w_3 f_3 + w_4 f_4. \tag{3.6}$$

The derivation of the weighting factors for the three different cases (default, left and right side margin) is presented in the appendix, section A.3.

The new interpolated horizontal field yields from multiplying the longitudinal vector of weights $(\mathbf{w}_{\text{longitude}})$ with the matrix multiplied horizontal partial atmospheric field $(\mathbf{x})$ and latitudinal vector of weights $(\mathbf{w}_{\text{latitude}})$:

$$\mathbf{x}_{\text{interpolated}} = \mathbf{w}_{\text{longitude}} \cdot (\mathbf{x}\ \mathbf{w}_{\text{latitude}}). \tag{3.7}$$

According to Gorbunov and Steiner (1999), the advantage of this formulation compared to standard spline interpolation is that the adapted polynomial interpolation

only needs four points (three points at the borders) to define the interpolating function, while a spline needs all points. Furthermore, the adapted polynomial interpolation leads to fields being continuous, even in their first derivative.

Vertical Interpolation

Vertical interpolation of GCM and re-analysis fields was only necessary for single missing levels, as most required levels were already given in the original fields. Spline interpolation (see appendix, section A.2) was used for missing temperature and geopotential height levels. Linear interpolation (see appendix, section A.1) was applied for specific humidity. Spline interpolation was not possible for the latter, as some models lacked lower troposphere values and spline interpolation requires complete vertical profiles without missing values to determine the coefficients properly.

Further Adjustments During the Interpolation Calculations

While the GCMs and the NRA provide geopotential height (Z) fields as function of pressure, ERA-40 makes the geopotential, $\phi(p)$ [m^2/s^2], available. The geopotential is the sum of the gravitational potential and the centripetal potential (e.g., Peixoto 2007). It is defined as the work done to lift a mass of 1 kg from MSL to a certain point in the atmosphere with an elevation z, and can be written as:

$$\Phi(\varphi, z) = \int_0^{z'} g(\varphi, z')\, dz. \tag{3.8}$$

In equation (3.8), g is the gravitational acceleration [m/s^2], φ the (geodetic) latitude, and z the geometric elevation, which is defined as elevation above the Earth's geoid (which corresponds to the MSL). The geopotential height is then the vertical coordinate relating to the Earth's MSL. It is given as

$$Z(\Phi), = \frac{\Phi(z)}{g_{\mathrm{MSL}}(\varphi)}, \tag{3.9}$$

and can be considered as a gravity adjusted height. In the regridding routine for ERA-40 geopotential fields, the surface gravity acceleration for each latitude, $g_{\mathrm{MSL}}(\varphi)$, was determined by means of the EGOPS function "Gravity", in order to facilitate the calculation of geopotential height fields.

3.4.3 Conversion from Pressure Level Data to Geopotential Height Data and Vice-Versa

For the trend indicator study, trends were analyzed for fields as function of pressure and as function of geopotential height. Therefore, GCM and re-analysis fields had

to be converted from pressure dependency to geopotential height dependency. The geopotential heights were chosen to feature a more or less even spacing in the UTLS (smaller height steps in the UT, larger in the LS) and to be close to the given pressure levels, using U.S. Standard Atmosphere 1976 (National Oceanic and Atmospheric Administration et al. 1976) properties. The U.S. Standard Atmosphere 1976 provides atmospheric density, temperature, and pressure from surface to 1000 km height for annual mean, global mean conditions at 45°N, assuming dry and homogeneously mixed air below 86 km. Figure 3.10 shows the relation between geometric altitude (which differs from Z by less than 100 m below 25 km altitude) and pressure. In the plot, the used geopotential height and pressure levels are marked with green and blue bars, respectively. The conversion was implemented with Interactive Data Language (**IDL**), using linear interpolation routines for single vertical profiles. As GCMs and re-analyses data for temperature, geopotential height, specific humidity, and refractivity were derived as a function of pressure, they could be easily converted into geopotential height dependent fields. The geopotential height fields themselves were converted to pressure fields as a function of geopotential height. For the latter,the natural logarithm of the given pressure levels was used for the interpolation.

RO data were converted into pressure dependent data for the use in the trend detection study. RO refractivity, geopotential height, dry temperature, and pressure fields are provided at MSL-altitudes with a vertical resolution of 200 m. The data were linearly interpolated to geopotential height dependent data, making use of the provided pressure and geopotential height fields. Similar to the GCMs and the re-analyses, the interpolation was based on the natural logarithm of the given pressure profiles to gain pressure as a function of geopotential height.

3.4.4 Temporal Resolutions and Temporal and Spatial Averaging

Temporal Averaging

All data were provided in a monthly mean resolution. Seasonal and annual means for the trend indicator study, were gained by averaging the respective months arithmetically. The winter season is based on the December–January–February (DJF) average, the spring season on the March–April–May (**MAM**) average, summer season on the June–July–August (**JJA**) average, and fall season on the September–October–November (**SON**) average. For annual mean (**ANN**) data, arithmetic means of all months within one calendar year were calculated.

Spatial Averaging

Besides temporal averaging, spatial averaging was employed for both, the trend indicator and the trend detection study (for details of the resolutions see chapter 4 and chapter 5). While averages over longitudes, including zonal means, are commonly

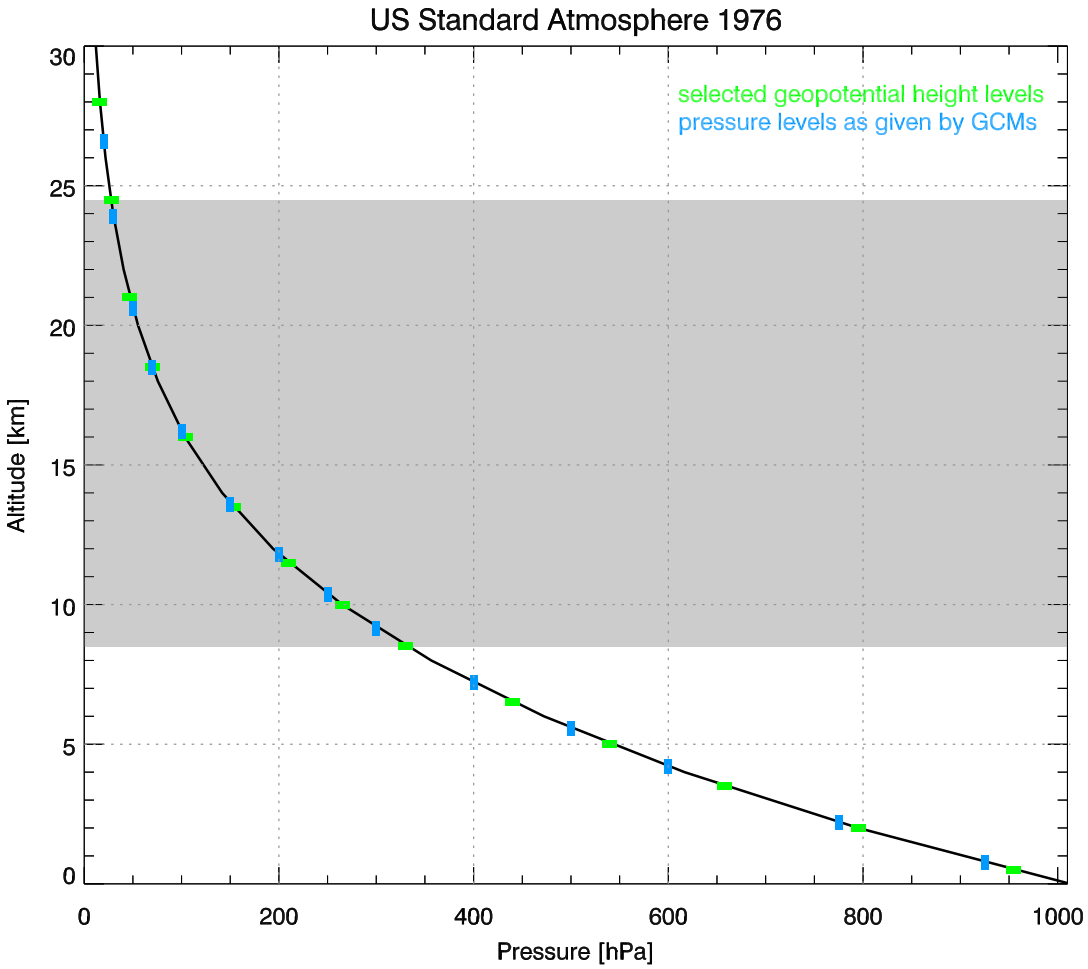

Figure 3.10: Pressure versus altitude based on the U.S. Standard Atmosphere 1976 model. The used geopotential height levels (which are within $< 100\,\mathrm{m}$ of the altitudes) are marked in green, the model based pressure levels in blue. The gray shaded area marks the focus region of this study between 8.5 km and 24.5 km, corresponding to $\approx 300\,\mathrm{hPa}$ to $\approx 30\,\mathrm{hPa}$.

applied by averaging simply all longitudinal values at one latitude arithmetically, averages over the latitudes require adjustments due to the latitudinal dependent surface area, which is caused by the spherical shape of the Earth.

The lateral surface area on a sphere between two latitudes, $A_{\Delta\varphi}$ is given as

$$A_{\Delta\varphi} = 2r^2\pi(\sin\varphi_2 - \sin\varphi_1), \tag{3.10}$$

where r is the constant radius of the sphere, φ_2 the latitude of the considered latitudinal

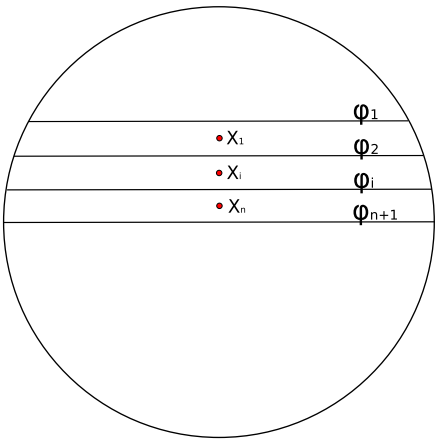

Figure 3.11: Schematic illustration of area weighting to calculate latitudinal means.

band closer to the equator, and φ_1 the latitude closer to the respective pole, see Figure 3.11. The mean latitudinal parameter value $x_{\overline{\varphi}}(\lambda, h)$, where h stands for any vertical coordinate and λ for any longitude, can thus be determined as weighted mean of all n single latitudinal values, using the $(n+1)$ latitudinal boundaries:

$$x_{\overline{\varphi}}(\lambda, h) = \frac{\sum_{i=1}^{n} \left[x(\varphi_i, \lambda, h) \, |\sin \varphi_i - \sin \varphi_{i+1}| \right]}{\sum_{i=1}^{n} |\sin \varphi_i - \sin \varphi_{i+1}|}. \tag{3.11}$$

3.4.5 Determination of Refractivity

Within the regridding routine for GCMs and re-analysis, refractivity values were calculated at each p-level by means of the regridded T and specific humidity (q) values, using the EGOPS routine "N_fromTPQ", which is based on the Smith-Weintraub formula for Microwave (**MW**) refractivity (Smith and Weintraub 1953). The formula employed (referenced in the EGOPS routine with Bean and Dutton 1968) can be written as:

$$N(T, p, q) = c_1 \frac{p}{T} + c_2 \frac{p\,q}{T^2 (a_q + b_q\,q)}, \tag{3.12}$$

where $c_1 = 77.6 \times 10^{-6}\,\mathrm{K\,hPa^{-1}}$ and $c_2 = 0.373\,\mathrm{K^2\,hPa^{-1}}$ are empirically determined constants, differing by a factor 10^6 from the values given in equation (2.2). Thus, the result for N achieved with the EGOPS routine "N_fromTPQ" has to be multiplied by 10^6 to get the correct refractivity values. The specific humidity q enters the equation in $\mathrm{kg\,kg^{-1}}$. a_q is the quotient of the dry air gas constant, $R_{\mathrm{dry}} = 287.06\,\mathrm{J\,kg^{-1}\,K^{-1}}$, and the water vapour gas constant, $R_\nu = 461.52\,\mathrm{J\,kg^{-1}\,K^{-1}}$. The second bracket term b_q is simply related to a_q with $b_q = 1 - a_q$.

4 Climate Change Indicators of Radio Occultation Data

An *indicator* is commonly defined as a pointer or index that suggests or predicts something. In environmental sciences, e.g., indicators tell us what is happening in or with our environment, in medical sciences it can be a substance making processes or conditions visible and measurable. Here, the term is used to pinpoint parameters and regions which react particularly sensitive to climate change. A sensitive reaction implies a high signal-to-noise ratio (**SNR**) in climate data. In the context of climate change, the signal can be addressed as changes in time and the noise as internal natural climate variability. As the emphasis is on Radio Occultation (**RO**) climatologies, this study focuses on RO-accessible parameters in the upper troposphere-lower stratosphere (**UTLS**).

Various studies have already treated the potential of RO data to track climate change, in the following only a selection of them is presented in short. Vedel and Stendel (2003) investigated the climate change assessment capability of geopotential height, pressure, and refractivity. They found that geopotential height as a function of pressure is well suited for climate monitoring near the tropopause (**TP**). Refractivity as a function of height was also named to be appropriate for climate monitoring. In the lower stratosphere (**LS**), they propose to use geopotential height as a function of iso-refractivity fields, which is slightly more sensitive to global warming than using pressure dependent variables. To monitor climate change, Leroy (1997) discussed the use of geopotential height fields on constant pressure levels, which can be interpreted as tropospheric bulk temperature. Basing his analysis on summer climatologies, he also addressed geopotential height error estimates and some regional considerations. The discussion of data dependency was taken on some years later by Leroy et al. (2006*b*). In their paper, they propose to use refractivity preferably as function of geopotential height fields, as this is the more natural independent coordinate. Also integrated refractivity, yielding dry pressure, is mentioned as well suited for climate monitoring. Above the lower troposphere, where the water vapor contribution to refractivity is negligible, these log-dry pressure trends are similar to geopotential height trends. The trend detection capability of different RO parameters for summer seasons was also analyzed by Foelsche et al. (2008*a*), performing on observing system simulation experiments over a 25-year period. They concluded that the RO parameters show complementary climate change sensitivity in different regions of the UTLS for optimized climate monitoring.

4.1 Climate Change Indicators—Study Setup

This study differs from the above mentioned ones insofar, as it assesses the capability of fields from all (but one) commonly used RO parameters. The analysis is done for fields given as a function of geopotential height and as a function of pressure. Furthermore, different spatial and temporal resolutions are employed, so that annual mean characteristics and seasonal differences can be assessed. The goal is to deduce the most promising indicators in space and time to monitor and diagnose changes of the thermo-dynamical state in the UTLS due to climate change.

4.1.1 Data

By reason of the still limited length of available RO measurements, General Circulation Model (**GCM**) simulations of three selected models and two re-analyses are used as *proxy* data to estimate long-term changes in the UTLS. See Table 3.3 for an overview on the data.

Investigated Periods & Temporal Resolutions

Based on the data availability and on requirements of the applied method (cf., section 4.1.2), three different time periods are investigated (see Table 4.1).

The *re-analyses* period (1980 to 2001) allows an assessment of recent, *short*-term climate change. Less reliable data from the pre-satellite era before 1980 were excluded. The end of the period, December 2001, is based on the availability of ECMWF Re-Analysis (**ERA-40**) data (until mid-2002) and the requirement to be able to calculate seasonal and annual means for the whole period.

The *long-term* picture of climate change is based on the GCM simulations. The 50-years analysis period from 2001 to 2050 is long enough to allow the climate change

	1980–2001	2001–2025	2001–2050
ERA-40	✓		
NRA	✓		
CCSM3	✓	✓	✓
ECHAM5	✓	✓	✓
HadCM3	✓	✓	✓
MAECHAM5		✓	

Table 4.1: Overview on time periods used for the climate change indicator study.

signal to emerge clearly from natural variability in the UTLS. At the same time it guarantees a still approximately linear behavior of the trend and little differences between the Special Report on Emission Scenarios (**SRES**) A2 and B1.

The third investigated period 2001 to 2025 rests upon the availability of the Middle Atmosphere Mode of ECMWF Hamburg Model, version 5 (**MAECHAM5**) simulations. The middle atmosphere model output was used to assess the influence of low model tops in GCMs with regard to their representation of trends in the UTLS.

To get an overall picture of the trend behavior, seasonal and annual mean data are analyzed. Seasonal slicing has the advantage that autocorrelation can be neglected (see section 4.2.3). RO data are frequently used as seasonal climatologies, because their sampling errors are smaller than those of monthly climatologies due to three times as many occultation events (Foelsche et al. 2008*b*). Furthermore, parts of short term variability are removed by temporal averaging, which enhances the SNR.

Spatial Resolutions

The GCM and re-analysis data were brought to a common resolution of $2.5° \times 2.5°$ in latitude and longitude, which corresponds to the horizontal extension of a RO event (see section 3.4). All data were made available as function of geopotential height (Z) and as function of pressure (p), as described in section 3.4.3. The focus of this study is on the analysis of fields at constant Z-levels, as this vertical coordinate is insensitive to thermal changes in the atmosphere. Nevertheless, the results will be compared to those gained by analyzing the fields at constant p-levels. In the vertical, priority is given to the UTLS between 8500 m and 24 500 m altitude, which corresponds approximately to the 300 hPa to 30 hPa range (see Figure 3.10). Results for lower levels are also shown in the figures for the sake of completeness.

Based on the provided gridded fields, area weighted means for 37 regions (Figure 4.1) were calculated, using equation (3.11) to gain averages over several latitudes. The regions are given 3-letter acronyms, which are defined in appendix B. The focus regions are 9 global-scale to large-scale zonal means (marked in Figure 4.1 at both sides), as they are typically used in single satellite RO studies, spanning from global, over hemispheric, to some 30° latitudinal zonal means. As ongoing and future multi-satellite missions will enable the calculation of regional climatologies, the analysis was also performed for regions as defined in chapter 11 (Christensen et al. 2007) of the Intergovernmental Panel on Climate Change (**IPCC**) Fourth Assessment Report (**AR4**). This definition is based on Giorgi and Francisco (2000), who introduced land area regions according to several criteria:

- the regions should show a horizontal extent of at least a few thousand kilometers in each direction in order to include at least several model grid points or the smallest resolved wavelength;

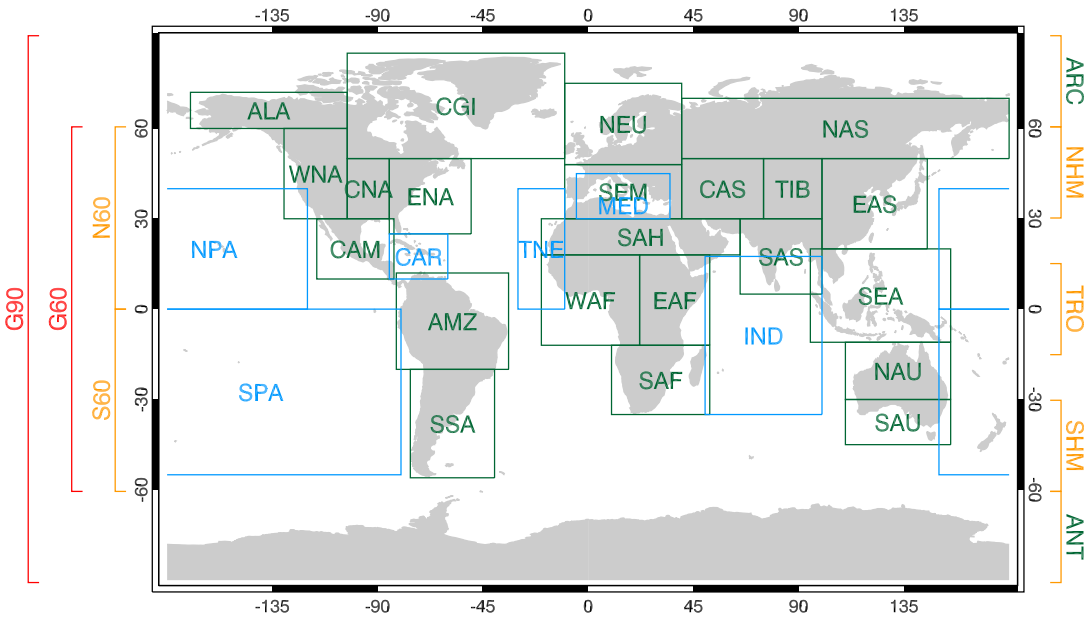

Figure 4.1: IPCC$^+$ regions. Large-scale climate regions over land, including the polar caps ARC and ANT (green), and oceans (blue) based on the IPCC region definition, complemented by global scale zonal bands, marked at boths sides in orange and red. The acronyms are summarized in the appendix B.

- they should be of simple (i.e. rectangular) shape;
- and different climatic regions and physiographic settings should be properly represented.

The enhanced IPCC AR4 region definition, in the following addressed as IPCC (2007) regions and large-scale zonal mean bands (**IPCC$^+$**), includes 22 land regions, 6 oceanic areas, and the 2 polar caps (ARC, ANT), which are carried along with the large-scale zonal mean regions.

Parameter Space

RO measurements allow the retrieval of atmospheric profiles for bending angles (α), refractivity (N), pressure (p), geopotential height (Z), temperature (T), and, if background information is available, specific humidity (q). The GCMs and re-analyses provide $Z(p), T(p), q(p)$, so that on the one hand N can be easily derived, as shown with equation (3.12), and that on the other hand the parameters can be converted into Z-level data.

layer	bottom level		top level	
	Z-level	p-level	Z-level	p-level
UT	8500 m	300 hPa	11500 m	200 hPa
TP	11500 m	200 hPa	16000 m	100 hPa
LS	16000 m	100 hPa	24500 m	30 hPa

Table 4.2: Definition of layers to calculate layer gradients for climate change indicator study.

In the climate change indicator study, the parameters N, Z or p, and T were analyzed for each vertical Z- and p-level. Furthermore, three derived parameters, i.e. layer gradients, were considered. The layers were chosen to represent the upper troposphere (**UT**), the tropopause (TP) region, and the lower stratosphere (LS) in accordance with the classification for low to mid-latitudes. Table 4.2 gives an overview on the used layer classification (bottom and top level) for Z-levels and respective $\approx p$-levels. The refractivity gradient can be regarded as the mean bending angle for a layer and the pressure gradient as a layer mean refractivity (density).

Relative gradients were determined for N and p. The relative layer gradients $\Delta x_{\text{rel}}/\Delta Z$ were calculated for each time step t as relative layer difference related to the geopotential height difference of the upper and lower level. The relative layer difference Δx_{rel} was derived by weighting the differences between upper and lower layer level with the respective value of the lower layer level:

$$\begin{aligned} \frac{\Delta x_{\text{rel}}}{\Delta Z}(t) &= \left(\frac{\Delta x_{\text{rel}}(t)}{Z_{\text{upper level}} - Z_{\text{lower level}}} \right) 100 \\ \Delta x_{\text{rel}}(t) &= \left(\frac{x_{\text{upper level}}(t) - x_{\text{lower level}}(t)}{x_{\text{lower level}}(t)} \right) 100. \end{aligned} \tag{4.1}$$

For temperature, the lapse rate was calculated as respective layer gradient:

$$\frac{\Delta T}{\Delta Z}(t) = \left(\frac{T_{\text{upper level}}(t) - T_{\text{lower level}}(t)}{Z_{\text{upper level}} - Z_{\text{lower level}}} \right) 100. \tag{4.2}$$

In both cases, i.e. in equation (4.1) and in equation (4.2), ΔZ values were given in meters so that a multiplication of the ratio by 100 yields (relative) layer gradients per 100 m.

Figure 4.2 shows mean climatologies for the 6 analyzed parameters. They are based on annual mean ERA-40 data of the 1980 to 2001 period. For the latitudinal resolution, 5 large-scale zonal mean regions, ARC, NHM, TRO, SHM, ANT, were employed.

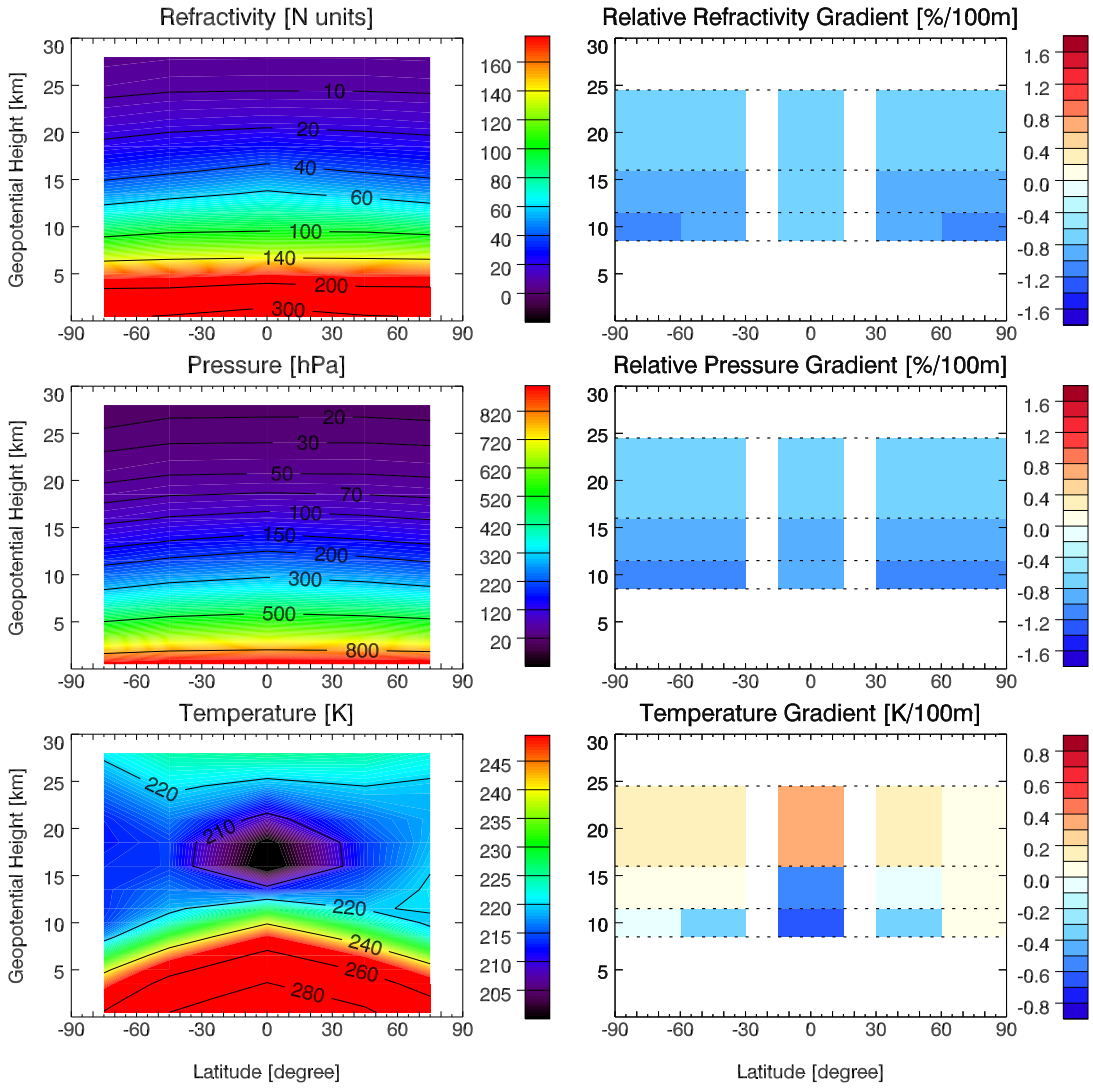

Figure 4.2: Annual mean parameter climatologies (latitude-height slices) based on ERA-40 1980 to 2001 data. For the latitudinal resolution, 5 regions (ARC, NHM, TRO, SHM, ANT) were taken.

While a contour plot was used for N, p, and T climatologies, the layer climatologies depict the gradients in the respective boxes, as defined in Table 4.2. N and p data decrease exponentially with height, T shows in the mean a decrease up to around 15 km altitude, and an increase above. N gradients and p gradients are generally negative, since these parameters decrease with height. The values specify the percentaged change

per 100 m in the vertical relative to the lower level values. At lower levels (UT, TP region), the gradients are stronger pronounced. Temperature lapse rates yield negative values in the troposphere, where temperature decreases with height. The ERA-40 temperatures exhibit for the period 1980 to 2001 lapse rates of at least $-0.6\,\mathrm{K}/100\,\mathrm{m}$ in the UT tropics, and of around $-0.2\,\mathrm{K}/100\,\mathrm{m}$ at UT mid- and high latitudes. In the stratosphere, the lapse rate values are positive, since the temperature increases with height, and range between around $0.4\,\mathrm{K}/100\,\mathrm{m}$ in the tropic and around $0.2\,\mathrm{K}/100\,\mathrm{m}$ at higher latitudes.

4.1.2 Method Used to Determine Climate Change Indicators

Following the goal of the study to describe changes of parameters during a certain period, a trend analysis was carried out. The basis of trend analyses are time series of model data or observations, the aim is to describe changes in time and to find regularities. In the classical model, a time series of a random variable y_t can be described by three main components (Dodge 2008):

$$y_t = T_t + S_t + R_t, \text{ with } t = 1, \ldots, n. \tag{4.3}$$

T_t is the *trend component*, indicating the general direction of the long-term development of the time series, S_t is the *seasonal component*, describing recurring regularities with fixed periods (e.g., daily or yearly changes in temperature data), and R_t is the *residual component*, comprising all unknown, irregular components, e.g., long-term fluctuations such as the El Niño-Southern Oscillation (**ENSO**) or the Quasi-Biennial Oscillation (**QBO**). In climate research, this residual component is generally addressed as natural climate variability and the trend component reflects—in the optimal case—the anthropogenic impact on the climate system. Seasonal components are automatically removed, when sliced data (e.g., time series of summer seasons only) are employed. To derive the trend component from a time series, various methods can be used. The four most often mentioned in textbooks are:

Optical estimation of trends The most trivial method, where a trend line is just estimated from looking at a scatter plot of the data (useless in scientific analyses).

Averages of data halves This method splits the data into two parts of same size. For each part the average is calculated. Either the difference of the means is assessed or a trend line is passed through the first and second mean. Sometimes, averages of starting and ending parts of records are used.

Moving averages This method can remove periodic phenomenons, if the exact period is known. After applying a moving average for this exact period, the trend line should be left over.

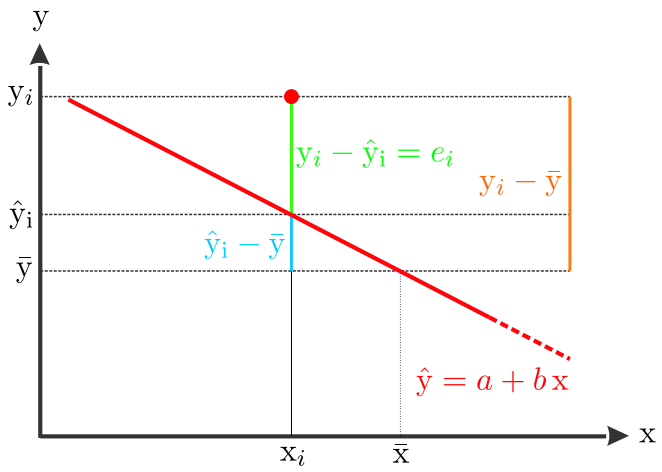

Figure 4.3: Elements of a regression line (red) exemplified by one observation point (red dot).

Method of least-squares The mathematical standard method. A curve is fitted to the data points in such a manner that the sum of the squared deviations between the fitted curve and the data points is a minimum.

To determine the climate trends, simple linear regression (method of least squares) was used. Theoretically one can distinguish between descriptive and probabilistic regression. Descriptive regression specifies the context between an independent (typically time) and a dependent (e.g., temperature) variable, emphasizing only on the numerical aspects. Probabilistic regression is based on descriptive regression, but in addition the regression model is analyzed by means of statistical tests.

Simple Linear Regression

The basis of this study is classical trend testing using simple linear regression. In this section, the basic theory, following e.g., Draper and Smith (1981) or Wilks (2006), is presented.

A linear regression model, as formulated in equation (4.4) and depicted in Figure 4.3, is always linear in the parameters, i.e. α and β, but not necessarily in the independent variables ($\mathbf{x}$). The order of the model is given by the highest order of the independent variable. The order of the model in equation (4.4) is 1, due to $\mathrm{x}^{\mathbf{1}}$.

$$\mathbf{y} = \alpha + \beta\mathbf{x} + \mathbf{e} \tag{4.4}$$

The regression model assigns for each time step x a regression value $\hat{y}(x)$ and an error term $\mathrm{e}(x)$. α and β are unknown, constant parameters. The aim in the regression analysis is to find estimates (a, b) for the two parameters (α, β) by means of the data, so that the regression line ($\hat{y}$) can be defined as

$$\hat{\mathbf{y}} = a + b\ \mathbf{x}. \tag{4.5}$$

The estimation of the parameters is commonly based on the least-squares method. This method, which was independently developed and introduced by Carl Friedrich Gauss and Adrien Marie Legendre around 1800, aims at defining a straight line, for which the sum of squares of errors (**SSE**) is a minimum:

$$\begin{aligned} \mathrm{SSE} &= \sum_{i=1}^{n} \mathrm{e}_i^2 && (4.6) \\ &= \sum_{i=1}^{n} (\mathrm{y}_i - \alpha - \beta \mathrm{x}_i)^2 \stackrel{!}{=} \text{Minimum.} && (4.7) \end{aligned}$$

The distances between the measurement points and the regression line, which determine the SSE, are defined as vertical distances from the regression line, not as perpendicular ones (see the green line in Figure 4.3). The advantages of taking the vertical distance are that the regression line defines the dependent variables as function of the independent ones, that uncertainties in measurement values can easily be integrated in the calculations, that the analytical representation of the regression parameters is simpler this way, and that a general formulation of the method (for higher orders of regression) is possible (Weisstein 2007). Equation (4.7) can be solved by setting the partial derivatives for the parameters equal zero and by replacing α and β by their estimates a and b. This yields the so called *normal equations*, given in equation (4.9) and equation (4.11), where $\sum a = na$ and $\sum(b\,\mathrm{x}_i) = b \sum \mathrm{x}_i$:

$$\begin{aligned} \frac{\partial \mathrm{SSE}}{\partial \alpha} = \quad & -2 \sum_{i=1}^{n} (\mathrm{y}_i - \alpha - \beta \mathrm{x}_i) && = 0 && (4.8) \\ & a\,n + b \sum_{i=1}^{n} \mathrm{x}_i && = \sum_{i=1}^{n} \mathrm{y}_i && (4.9) \\ \frac{\partial \mathrm{SSE}}{\partial \beta} = \quad & -2 \sum_{i=1}^{n} \mathrm{x}_i (\mathrm{y}_i - \alpha - \beta \mathrm{x}_i) && = 0 && (4.10) \\ & a \sum_{i=1}^{n} \mathrm{x}_i + b \sum_{i=1}^{n} \mathrm{x}_i^2 && = \sum_{i=1}^{n} \mathrm{x}_i \mathrm{y}_i && (4.11) \end{aligned}$$

The normal equations are a set of linear equations and can be solved for a and b by multiplying, e.g., equation (4.9) by $-\frac{\sum x_i}{n}$ and adding it to equation (4.11), yielding for the slope b

$$\begin{aligned} b &= \frac{\sum(\mathrm{x}_i \mathrm{y}_i) - \frac{\sum \mathrm{x}_i \sum \mathrm{y}_i}{n}}{\sum \mathrm{x}_i^2 - \frac{\left(\sum \mathrm{x}_i\right)^2}{n}} && (4.12) \\ &= \frac{\sum \left[(\mathrm{x}_i - \overline{\mathrm{x}})\,(\mathrm{y}_i - \overline{\mathrm{y}})\right]}{\sum \left[(\mathrm{x}_i - \overline{\mathrm{x}})\,(\mathrm{x}_i - \overline{\mathrm{x}})\right]} \\ &= \frac{\mathrm{SS}_{\mathrm{xy}}}{\mathrm{SS}_{\mathrm{xx}}}. \end{aligned}$$

In the following, sums of squared deviations of one (or more) variables from the mean will be addressed as sum of squares (**SS**) with the variable as index, e.g., $\mathrm{SS}_{\mathrm{xx}} = \sum[(\mathrm{x}_i - \overline{\mathrm{x}})\,(\mathrm{x}_i - \overline{\mathrm{x}})]$, or $\mathrm{SS}_{\mathrm{xy}} = \sum[(\mathrm{x}_i - \overline{\mathrm{x}})\,(\mathrm{y}_i - \overline{\mathrm{y}})]$. Thus, the numerator and denominator of equation (4.12) can be deduced to SS as follows:

$$\begin{aligned}
\mathrm{SS}_{\mathrm{xy}} &= \sum[(\mathrm{x}_i - \overline{\mathrm{x}})(\mathrm{y}_i - \overline{\mathrm{y}})] \\
&= \sum \mathrm{x}_i\mathrm{y}_i - \overline{\mathrm{x}}\sum \mathrm{y}_i - \overline{\mathrm{y}}\sum \mathrm{x}_i + n\overline{\mathrm{x}}\overline{\mathrm{y}} \\
&= \sum \mathrm{x}_i\mathrm{y}_i - n\overline{\mathrm{x}}\overline{\mathrm{y}} - n\overline{\mathrm{x}}\overline{\mathrm{y}} + n\overline{\mathrm{x}}\overline{\mathrm{y}} \\
&= \sum \mathrm{x}_i\mathrm{y}_i - \frac{(\sum \mathrm{x}_i \sum \mathrm{y}_i)}{n}
\end{aligned} \tag{4.13}$$

$$\begin{aligned}
\mathrm{SS}_{\mathrm{xx}} &= \sum (\mathrm{x}_i - \overline{\mathrm{x}})^2 \\
&= \sum \mathrm{x}_i^2 - 2\,\overline{\mathrm{x}}\sum \mathrm{x}_i + n\overline{\mathrm{x}}^2 \\
&= \sum \mathrm{x}_i^2 - 2\,\frac{\sum \mathrm{x}_i \sum \mathrm{x}_i}{n} + \frac{n\sum \mathrm{x}_i}{n}\frac{\sum \mathrm{x}_i}{n} \\
&= \sum \mathrm{x}_i^2 - \frac{(\sum \mathrm{x}_i)^2}{n}
\end{aligned} \tag{4.14}$$

If the slope b is known, the intercept a can be easily determined by means of equation (4.9):

$$\begin{aligned}
a &= \frac{\sum \mathrm{y}_i}{n} - b\,\frac{\sum \mathrm{x}_i}{n} \\
&= \overline{\mathrm{y}} - b\,\overline{\mathrm{x}}.
\end{aligned} \tag{4.15}$$

By substituting a in equation (4.5) yields the regression line as a function of the slope:

$$\hat{\mathbf{y}} = \overline{\mathrm{y}} + b\,(\mathbf{x} - \overline{\mathrm{x}}). \tag{4.16}$$

Equation (4.16) shows that the regression line passes through the mean of the dependent and independent variable.

Goodness-of-Fit

To discuss the quality of a regression line, some geometrical considerations are helpful. Figure 4.3 shows that a residuum e_i, i.e. the vertical distance between the regression line and a measurement point, can be constructed of two parts:

- $\mathrm{y}_i - \overline{\mathrm{y}}$: the distance between the measurement point and the mean of all measurements;

- $\hat{y}_i - \overline{y}$: the distance between the respective regression point and the mean of all measurements,

which can be formulated as follows:

$$e_i = y_i - \hat{y}_i = (y_i - \overline{y}) - (\hat{y}_i - \overline{y}). \tag{4.17}$$

Since the mean of all regression values $\sum \hat{y}_i/n$ is equal to the mean of the measurements $\sum y_i/n$, the sum and the mean of the residuals must be equal zero:

$$\sum e_i = \sum (y_i - \hat{y}_i) = n\,\overline{y} - n\,\overline{y} = 0. \tag{4.18}$$

Equation (4.17) can be rewritten as:

$$(y_i - \overline{y}) = (\hat{y}_i - \overline{y}) + (y_i - \hat{y}_i) \qquad |^2, \sum_{i=1}^{n} \tag{4.19}$$

$$\sum (y_i - \overline{y})^2 = \sum (\hat{y}_i - \overline{y})^2 + \sum (y_i - \hat{y}_i)^2 \tag{4.20}$$

$$\text{SST} \;=\; \text{SSR} \;+\; \text{SSE} \tag{4.21}$$

The right-hand side cross-product term, which arises from squaring equation (4.19), vanishes (see, e.g., Draper and Smith 1981, p. 18). Equation (4.21) indicates that three sums of squares can be distinguished:

total sum of squares (SST) describes the total variation in the data and is proportional to the variance of the measurements by $(n-1)$, which is also the number of the degrees of freedom (**DOF**); the DOF correspond to the number of observations minus the number of parameters used to describe the model, which is in case of the total variability only the mean;

regression sum of squares (SSR) also named the explained variance, it comprises the variance described by the regression line; if the explained variance is large, then the regression line values deviate strongly from the data mean, i.e. the slope is well defined; the DOF is equal to 1, matching the number of explained variables without the constants;

sum of squares of errors (SSE) the residual variance or not explained variance, includes the deviations of the measurements from the regression line; SSE shows $(n-2)$ DOF according to the number of observations minus the number of estimated parameters (a and b).

The three sums of squares can be used to determine the goodness of fit (**GOF**). In a *perfect* regression, the regression values will be identical to the measurements, i.e. the total sum of squares (**SST**) = the regression sum of squares (**SSR**) and SSE=0. A

meaningless (linear) regression is given, when there is no linear relationship between the variables, i.e. the slope of the regression line and thus SSR is zero and SST=SSE.

A commonly used indicator for the GOF, which is also employed in this study, is the coefficient of determination ($\mathbf{R}^2$), which is defined as

$$\begin{aligned} \mathrm{R}^2 &= \frac{\mathrm{SSR}}{\mathrm{SST}} && (4.22) \\ &= 1 - \frac{\mathrm{SSE}}{\mathrm{SST}} \\ &= \frac{\sum (\hat{\mathrm{y}}_i - \overline{\mathrm{y}})^2}{\sum (\mathrm{y}_i - \overline{\mathrm{y}})^2}. && (4.23) \end{aligned}$$

R^2 defines the share of the variation due to regression on the total variability around the mean. It is the squared correlation between the independent variable y and the regression values $\hat{\mathrm{y}}$, as evidenced in equation (4.23). A *perfect* regression will thus show a R^2 equal to 1, a *meaningless* regression a R^2 equal to zero.

Significance of Trends

The significance of trends was assessed via a Student's t-test. The test value t_b can be regarded as a kind of SNR, given by the ratio between the trend b and its standard deviation s_b:

$$t_b = \frac{b}{\mathrm{s}_b} \tag{4.24}$$

To determine the significance of the calculated trends, the following assumptions have to be made concerning the trend model as defined in equation (4.4):

- the residuals e_i are random variables with a zero mean, $\mathrm{E}(\mathrm{e}_i) = 0$, and a constant, but unknown variance, $\mathrm{Var}(\mathrm{e}_i) = \sigma_{\mathrm{e}}^2$;
- the residuals are not correlated, i.e. for all $i \neq j : \mathrm{Cov}(\mathrm{e}_i, \mathrm{e}_j) = 0$;
- the residuals are normally distributed, $\mathbf{e} \sim N(0, \sigma)$.

The standard error of the trend, s_b, can be derived from equation (4.12) and equation (4.13), using the fact that $\overline{\mathrm{y}} \sum(\mathrm{x}_i - \overline{\mathrm{x}}) = 0$. The trend b can then be written as:

$$b(\mathrm{y}) = \frac{\sum [(\mathrm{x}_i - \overline{\mathrm{x}})\mathrm{y}_i]}{\sum(\mathrm{x}_i - \overline{\mathrm{x}})^2}. \tag{4.25}$$

The variance of a random variable X multiplied by a constant c is generally given as $\mathrm{Var}(\mathrm{c}X) = \mathrm{c}^2 \mathrm{Var}(X)$. Taking the term $\sum(\mathrm{x}_i - \overline{\mathrm{x}}) / \sum(\mathrm{x}_i - \overline{\mathrm{x}})^2$ for the constant c and the variance of the y_i as the SSE divided by the DOF, i.e. $\mathrm{Var}(\mathrm{y}_i) = \sum(\mathrm{y}_i - \hat{\mathrm{y}}_i)^2 /$

$(n-2) = \sum \mathrm{e}_i^2/(n-2) = \mathrm{s}_\mathrm{e}^2$, yields for the variance and the standard deviation of the trend:

$$\begin{aligned} \mathrm{Var}(b) &= \mathrm{c}^2 \ \mathrm{Var}(\mathrm{y}_i) \\ &= \frac{\sum(\mathrm{x}_i - \overline{\mathrm{x}})^2}{\sum(\mathrm{x}_i - \overline{\mathrm{x}})^2} \ \frac{\sum(\mathrm{y}_i - \hat{\mathrm{y}}_i)^2}{n-2} \\ &= \frac{1}{\sum(\mathrm{x}_i - \overline{\mathrm{x}})^2} \ \frac{\sum \mathrm{e}_i^2}{n-2} \end{aligned} \tag{4.26}$$

$$\begin{aligned} \mathrm{s}_b &= \frac{1}{\sqrt{\sum(\mathrm{x}_i - \overline{\mathrm{x}})^2}} \frac{\sqrt{\sum \mathrm{e}_i^2}}{\sqrt{n-2}} \\ &= \frac{\mathrm{s}_\mathrm{e}}{\left[\sum (\mathrm{x}_i - \overline{\mathrm{x}})^2\right]^{1/2}}. \end{aligned} \tag{4.27}$$

The accuracy of the slope of the regression line (s_b) is thus directly proportional to s_e, the estimated standard deviation of the residuals. Using the definition of the standard deviation of the trend, as formulated in equation (4.27) for deriving the test value in equation (4.24) yields:

$$t_b = b \ \mathrm{s}_\mathrm{e}^{-1} \ \left[\sum(\mathrm{x}_i - \overline{\mathrm{x}})^2\right]^{1/2}. \tag{4.28}$$

To determine the significance of the trend, the null hypothesis $H_0 : \beta = 0$ is tested (the alternative hypothesis is $H_1 : \beta \neq 0$; β is the *true* trend slope), i.e. if the slope is significantly different from zero. If the absolute value of the calculated test value $\mid t_b \mid$ is greater than the theoretical one, $t(n-2, 1-\alpha/2)$, the null hypothesis can be rejected, meaning that the data show a linear dependency between $\mathbf{x}$ and $\mathbf{y}$ and that the trend is significantly different from zero at the given significance level α. This case describes a two-tailed test, which was employed in this study.

Autocorrelation Considerations

Due to system inertness and periodic phenomenons, data of atmospheric time series are often correlated with itself when a certain time-delay is considered. This means in the case of larger regional means and time-ranges that similar atmospheric states occur periodically linked with periodic phenomenon, as, e.g., ENSO. This temporal interrelation is addressed as autocorrelation and can be determined for different temporal *lags*, i.e. different intervals in the time steps. A simplified formula to calculate the autocorrelation coefficient r for a time-lag k is given by, e.g., Wilks (2006), who also provides a derivation of the exact formula. As approach, the following equation

can be used:

$$r_k \approx \frac{\sum_{i=1}^{n-k} \left[\left(\mathrm{x}_i - \overline{\mathrm{x}} \right) \left(\mathrm{x}_{i+k} - \overline{\mathrm{x}} \right) \right]}{\sum_{i=1}^{n} \left(\mathrm{x}_i - \overline{\mathrm{x}} \right)^2}. \tag{4.29}$$

Largest autocorrelation, namely $r = 1$ is of course given for a zero-lag ($k = 0$), i.e. correlating the time series with itself. To test a time series for autocorrelation, a correlogram comes in useful. It is a graph of the autocorrelation coefficients plotted for different lags $k = 0, 1, \ldots, n - k$. Autocorrelation is mainly an issue when statistical tests are applied. In a regression analysis, it is assumed that the residuals are not correlated, which is not the case for autocorrelated data. In order to not reject the null hypothesis too often, an existing autocorrelation has to be considered in significance assessments. Various scientist, such as, e.g., Santer et al. (2000) or Wilks (2006), deem an integration of lag-1 autocorrelation appropriate for climate data. An easy way to do this, is to use an *effective* sample size n_e instead of n, which considers the lag-1 autocorrelation coefficient r_1 so that n_e can be specified as

$$n_e = n \, \frac{1 - r_1}{1 + r_1}. \tag{4.30}$$

The use of the effective sample size leads to *corrected* values for the standard deviation of the trend s_b, see equation (4.27), for the variance of the residuals s_e^2, and thus for the calculated t-value, see equation (4.28). A stricter assessment is still possible by using the effective sample size in addition for the determination of the tabulated test values.

Autocorrelation for different lags was assessed in this study and will be addressed in section 4.2. It was not used for the significance assessment, as the use of sliced data appear to prevent autocorrelation per se.

Determination of Climate Change Indicators

A *climate change indicator*, or indicator in short, was defined as a variable which succeeds best to map the process of anthropogenic climate change in a certain space and time domain.

The indicators were computed for ERA-40 re-analysis and GCM trends of the shorter period 1980 to 2001 and for GCM trends of the period 2001 to 2050. Based on the results of the trend analysis (trends, significances, and GOF), the *climate change indicators* were identified as regions and height domains with significant trends and sound GOF values. For the longer analysis period based on GCMs, the agreement of trends from different models and simulations was an additional prerequisite to identify as indicator regions. In order to avoid unequal weighting of the three models, which provide a different number of simulations per scenario (see Table 3.2), a maximum of two simulations per model was used to determine the indicator regions. Tests showed,

	re-analyses (ERA-40 only)	GCMs
trend sign	—	for each scenario (SRES A2 and B1) at least all but one trends have the same algebraic sign
GOF	$R^2 \geq 0.25$	at least 3/4 of all runs (SRES A2 and B1) offer a $R^2 \geq 0.50$
significance	trend significance $\geq 90\,\%$	at least 3/4 of all runs (SRES A2 and B1) offer a trend significance $\geq 90\,\%$

Table 4.3: Criteria used to define climate change indicators for the two employed data sets.

that the indicators are insensitive to the specific ensemble of simulations used (for a discussion see section 4.3). The formulation of the best climate change indicators is detailed in Table 4.3. The criteria were carefully selected to ensure the unveiling of the most robust spatially dependent trend characteristics of all RO-accessible parameters in the UTLS. The less stringent criteria for ERA-40 were based on the stronger data variability due to the shorter analyzed time period. The trend criterion (trends of same algebraic sign) was irrelevant, as only ERA-40 results were considered. This decision was based on known differences in NCEP/NCAR Re-Analysis (**NRA**) and ERA-40 trends, which are due to the different generations of the analysis models.

4.2 Results of the Climate Change Indicator Study

In this section, results of the climate change indicator study, including analyses of data variability, autocorrelation issues, trends and their GOF and significances, are presented.

The study was performed for all data in two ways: (1) the data were analyzed at constant geopotential height levels, and (2) the data were analyzed at constant pressure levels. Figure 4.4 shows 10-year trends for the parameters refractivity (N), pressure (p), geopotential height (Z), and temperature (T) as function of geopotential height (left panel) and as function of pressure (right panel). For the parameters which change exponentially with height, namely N and p, relative trends are depicted. They specify the percentage of change of a parameter per decade. The relative trends b_{rel} were determined for each grid point by putting the grid point trend value in relation to the grid point temporal mean ($\overline{\mathrm{x}}$) of the whole time series considered, i.e. 2001 to

2050 for this figure:

$$b_{\mathrm{rel}} = \left[\left(\frac{\overline{\mathrm{x}} + b}{\overline{\mathrm{x}}}\right) - 1\right] 100 = \frac{b}{\overline{\mathrm{x}}} 100. \tag{4.31}$$

The height ranges (near surface to 30 km altitude for Z-level fields and 1000 hPa to 12 hPa for p-level fields) were chosen to match in the graphical display. Geopotential height and relative pressure trends as well as temperature trends show a very similar pattern, independent from the vertical coordinate. Temperature features a tropospheric trend maximum in the tropics and sub-tropics between around 10 km and 15 km for Z-level data, and slightly lower between 300 hPa and 200 hPa for p-level data. The geopotential height trends mirror the atmospheric expansion due to tropospheric temperature increase, the strongest signal is thus moved to higher altitudes of 15 km to 20 km (corresponding to around 100 hPa to 50 hPa). The 200 hPa level, e.g., is moved 20 m higher per decade, the 100 hPa level is moved around 30 m per decade. In contrast to temperature and geopotential height/pressure, the refractivity trend patterns depend on the vertical coordinate. While refractivity trends are inverse proportional to temperature trends when pressure is used as fixed vertical coordinate, this is no longer the case if geopotential height is employed as vertical coordinate. Z-level data are in contrast to p-level data independent of climatic changes of the atmosphere. Refractivity is proportional to the pressure to temperature ratio, see first right-hand side term in equation (2.2). The relative change of refractivity in time can be derived via the total derivative, which is for any function f defined as

$$\mathrm{d}\, f = \sum_{i=1}^{n} \frac{\partial f}{\partial x_i} \mathrm{d}\, x_i. \tag{4.32}$$

If $N(t) \propto p(t)/T(t)$, the total derivative of N and in the following the relative trend is given as:

$$\mathrm{d}\, N \propto \frac{1}{T} \mathrm{d}\, p - \frac{p}{T}\frac{1}{T} \mathrm{d}\, T \qquad | \cdot \frac{T}{p}\frac{1}{\mathrm{d}\, t} \tag{4.33}$$

$$\frac{T}{p}\frac{\mathrm{d}\, N}{\mathrm{d}\, t} \propto \frac{1}{T}\frac{T}{p}\frac{\mathrm{d}\, p}{\mathrm{d}\, f} - \frac{p}{T}\frac{1}{T}\frac{T}{p}\frac{\mathrm{d}\, T}{\mathrm{d}\, t}$$

$$\frac{1}{N}\frac{\mathrm{d}\, N}{\mathrm{d}\, t} \propto \frac{1}{p}\frac{\mathrm{d}\, p}{\mathrm{d}\, t} - \frac{1}{T}\frac{\mathrm{d}\, T}{\mathrm{d}\, t}. \tag{4.34}$$

Thus, on constant p-levels, the relative refractivity trends are proportional to relative temperature trends, since $\mathrm{d}\, p/\mathrm{d}\, t = 0$, see equation (4.34). If constant Z-levels are used as vertical coordinate, the relative refractivity trends are proportional to the difference between relative pressure and relative temperature trends (relative trends for all parameters are shown in Figure 4.9 and Figure 4.10). Above ≈ 70 hPa, Z-level and p-level refractivity trends develop again similar patterns, but still with different pattern

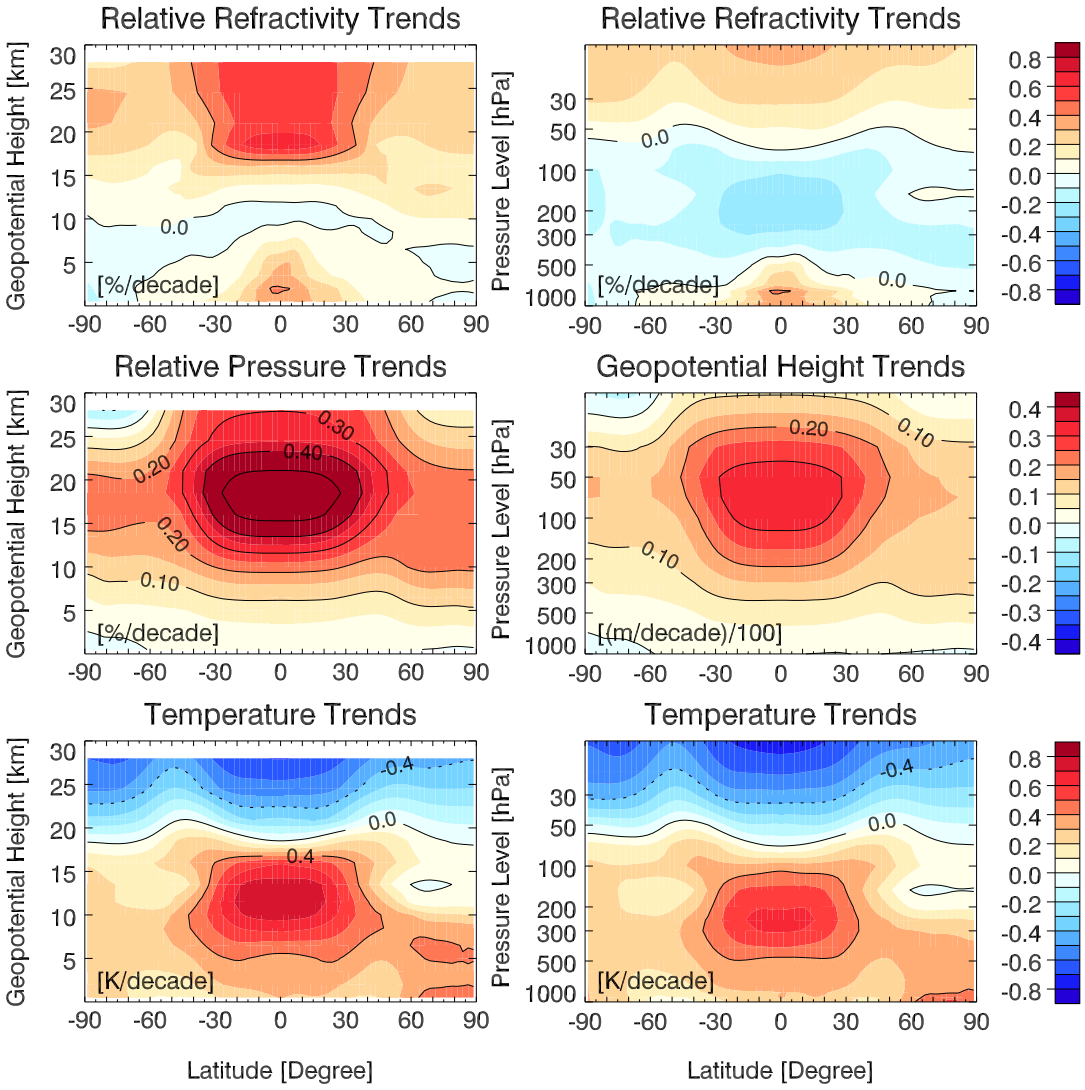

Figure 4.4: *left* 10-year trends of RO parameters as function of geopotential height; *right* the same as function of pressure. Geopotential height dependent fields range from near surface to 30 km altitude, pressure dependent fields are depicted between 1000 hPa and 12 hPa, the latter corresponding to 30 km as defined by the U.S. Standard Atmosphere 1976. The trends are based on zonal annual means of one ECHAM5 simulation (SRES A2, run 1) of the period 2001 to 2050, featuring the pristine 2.5° resolution of latitudinal bands.

amplitudes. Thus trend differences between Z-level and p-level temperature, pressure/ geopotential height data are negligible, while for refractivity differences occur, mainly in the 500 hPa to 70 hPa region. The focus of this study is on Z-level data, p-level results are mentioned if appropriate. A summary of the main findings of a p-level analysis can be found in Lackner et al. (2009).

4.2.1 Data Variability

Before having a look at the characteristics of GCM and re-analyses trends, the question if re-analyses and GCMs are suitable proxies for RO observations is addressed. A suitable proxy should at least succeed in (1) reproducing the mean state of the atmosphere and (2) in a realistic representation of atmospheric variability. A realistic picture of atmospheric variability is also essential for the determination of the significance of trends.

Figure 4.5 shows the variability, namely one standard deviation of the de-trended temperature record, for all seasons and annual means of the Challenging Mini-Satellite Payload (**CHAMP**) RO record and of each data set of the trend analysis. For the GCMs, the first run of each climate of the 20th century experiment (**20C3M**) simulation was chosen. The variability is based on the 09/2001 to 07/2008 period for the RO record and on the 1980 to 2001 period for the other data sets. Seasons influenced by volcanic eruptions were excluded from the re-analyses to ensure better comparability with the RO and GCM records. Results for pressure and refractivity (not shown) exhibit variability patterns consistent with temperature results.

All seasonal data sets reflect the annual cycle with higher variability at mid to high latitudes of the winter hemisphere. For the *observational* data sets (RO and re-analyses) best agreement is given between RO and ERA-40, while NRA features slightly less variability, particularly in the tropical LS. The GCM simulations exhibit generally less variability than the observations. Largest discrepancies occur in the LS at low and mid-latitudes, probably as consequence of the lack of the QBO in GCMs. A roughly realistic tropical and subtropical LS variability is only present in Community Climate System Model 3 (**CCSM3**), even though it is shifted about 5 km downwards compared to the observations. In the UT tropics around 12 km, enhanced observed variability is only present in December–January–February (**DJF**) and partly in March–April–May (**MAM**), while the GCMs, particularly ECHAM5 and Hadley Centre Coupled Model, version 3 (**HadCM3**), show an increased pattern throughout all seasons and thus also in annual mean data.

In summary, re-analyses and GCMs reproduce the annual mean and the annual course of variability reasonably well. The seasonal patterns of spatial variations are very well presented in the re-analyses. GCMs underestimate LS variability, particularly in the tropics and subtropics. This has to be kept in mind for the discussion of trend significances, because a small data variance and thus a smaller variance of the

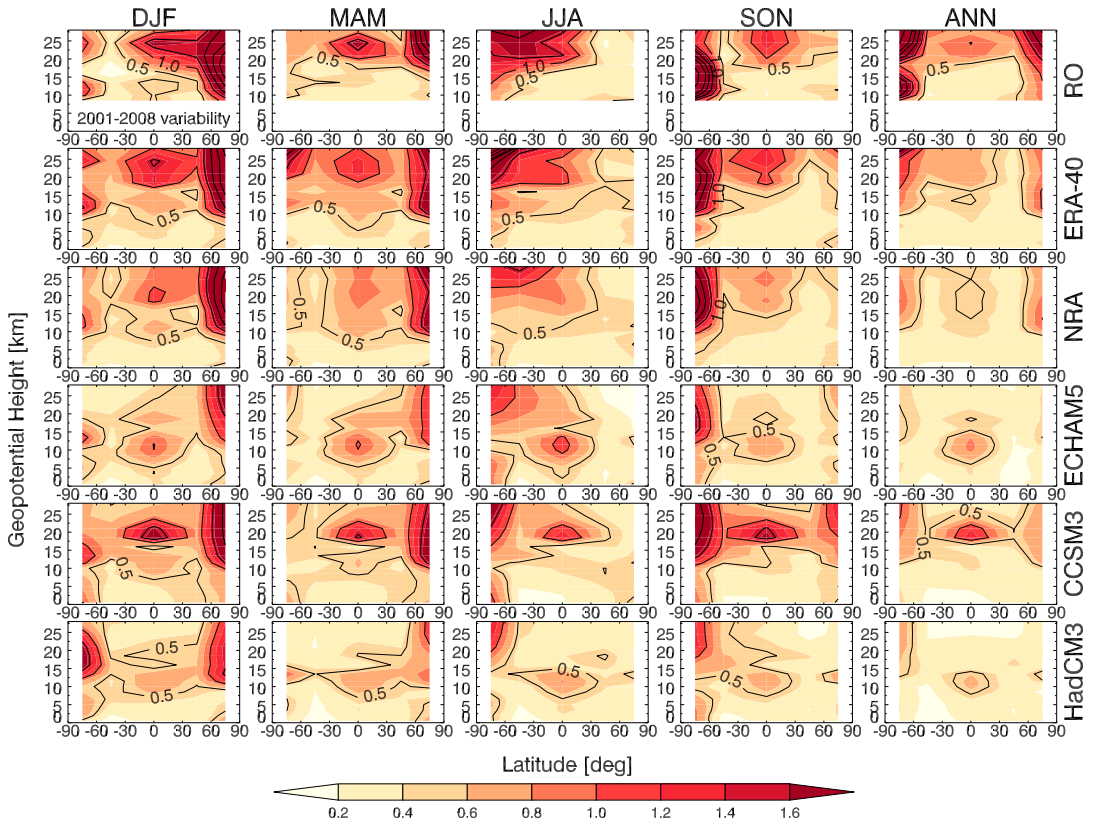

Figure 4.5: Seasonal (DJF, MAM, JJA, SON) and annual (ANN) temperature variability [K], i.e. one standard deviation of centered and de-trended data, based on 7 years for RO data and on 22 years for reanalyses (ERA-40, NRA) and GCMs (first run of 20C3M simulations was used). The latitudinal resolution is given by 5 zonal means (ARC, NHM, TRO, SHM, ANT).

regression residuals will lead to higher significances than can be expected in real data. Even though no perfect long-term upper air data record exists, various studies (e.g., Cordero and de Forster 2006; Reichler and Kim 2008), showed that the data sets used here reproduce the mean state and the variability of our atmosphere sufficiently well.

4.2.2 Characteristics of GCM and Re-analyses Trends

Several questions arise when analyzing trends from different data sets:

- Do the low model tops of GCMs have an influence on LS trends?

- How large are the differences in trends between the two re-analyses, between the GCM simulations, and between re-analyses and GCMs? How well do the data sets agree in respect of large-scale and regional trends?
- Is there a difference in the representation of trends at p-levels or at Z-levels?
- What period length is needed to obtain reasonable stable UTLS trend values?

To answer these questions, on the one hand GCM trends, including those of the middle atmosphere model MAECHAM5 for the 2001 to 2025 period, and on the other hand re-analyses and GCM trends for the period 1980 to 2001 were examined. An estimate for the period length for stable trends was calculated by means of ERA-40 data.

Do Low Model Top Levels Influence LS Trends?

The commonly low top levels (≈ 10 hPa) of the IPCC AR4 GCMs rise concern that the LS is not reliably represented in those models. This assumed deficiency would also influence the reliability of trend estimates. The trend performance of the AR4 models was thus examined by comparing the GCM AR4 trends to those of MAECHAM5, which extents up to 0.01 hPa and thus is expected to reproduce the stratosphere as a whole. Figure 4.6 shows 10-year temperature trends based on the period 2001 to 2025[1] for MAECHAM5 and for the selected 20 A2/B1 GCM simulations. The 6 ECHAM5 simulations (3/3 simulations of A2/B1 scenario) are marked in dark gray.

For large-scale zonal means (with the exception of the polar caps) the temperature trends of the data sets agree quite well in all seasons (MAM shown in Figure 4.6). The ECHAM5 trends (consistent with the findings of Ladstädter et al. (2009) with visualization tools) and GCM ensemble trends are almost equal (the ensemble mean is not shown explicitly). MAECHAM5 generally shows slightly smaller positive tropospheric trends and slightly larger negative stratospheric trends than the GCM or ECHAM5 simulations.

The trend deviations between the middle atmosphere model simulation and the low top level simulations is rather small over large-scale regions. In smaller regions, the trends differ depending on the season. The deviations are not restricted to the LS and tropospheric differences between the models can even exceed stratospheric ones. The model simulations for regions at higher latitudes, such as the polar caps (ARC, ANT), Alaska (ALA), Northern Europe (NEU), East Canada, Greenland and Iceland (CGI), or Northern Asia (NAS), generally exhibit more variety in the trend values, as indicated by the larger spread of the single simulations in Figure 4.6. In these regions, the deviations of the MAECHAM5 trends from the GCM trends are often large and sometimes they even show opposite sign. As these regions are also characterized by large annual and inter-annual variability, leading to less significant trend results,

[1] The linear trend for the whole noted period was determined. As periods of different length are used in this study, the plots always show derived 10-year trends for better comparison.

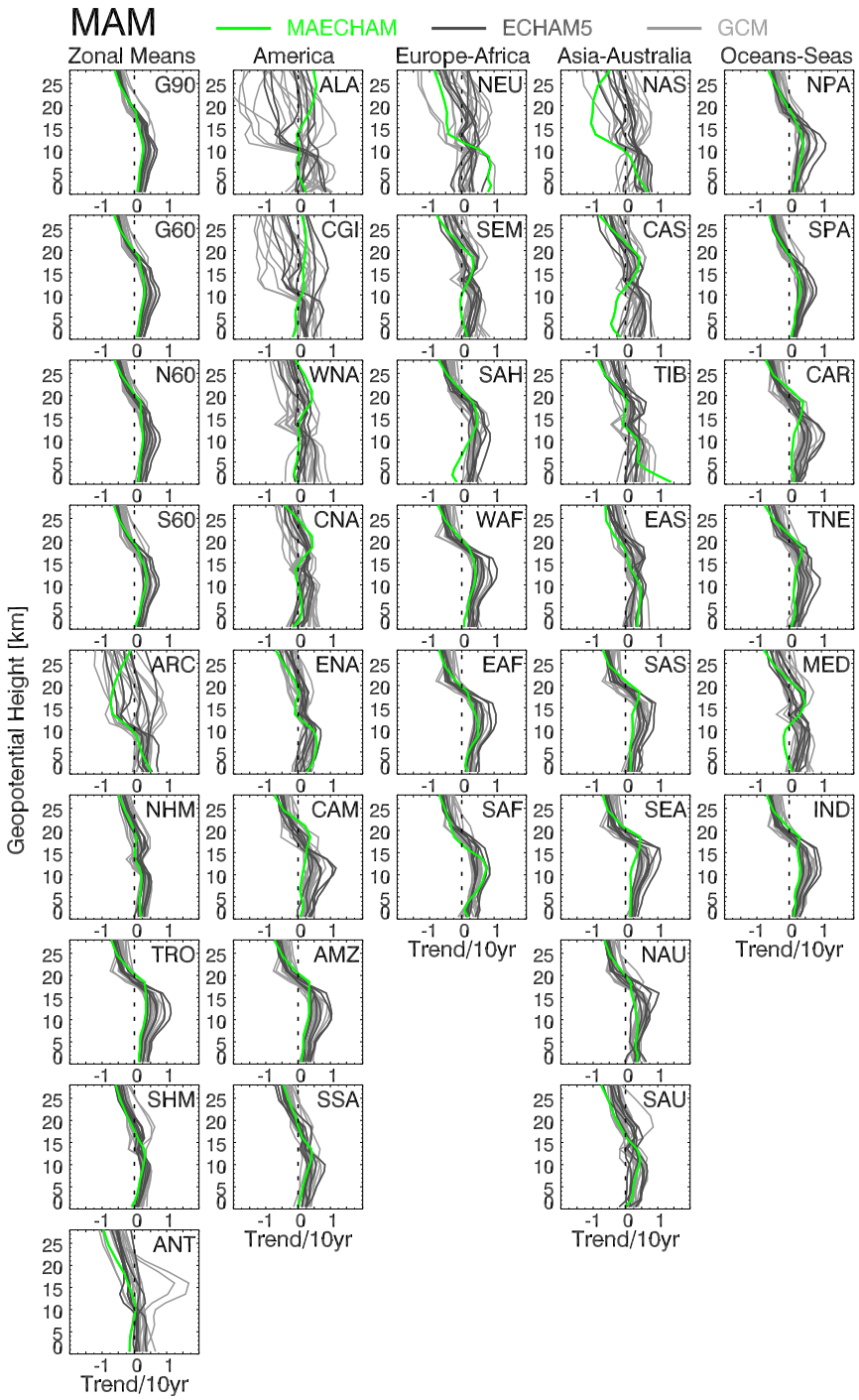

Figure 4.6: MAM temperature trends [K/10-years] as function of geopotential height (based on the 2001 to 2025 period) for MAECHAM5 (green), 6 ECHAM5 only (dark gray) and the 14 remaining GCM (light gray) simulations, shown for 9 zonal means (left column) and 28 regional means as indicated in Figure 4.1.

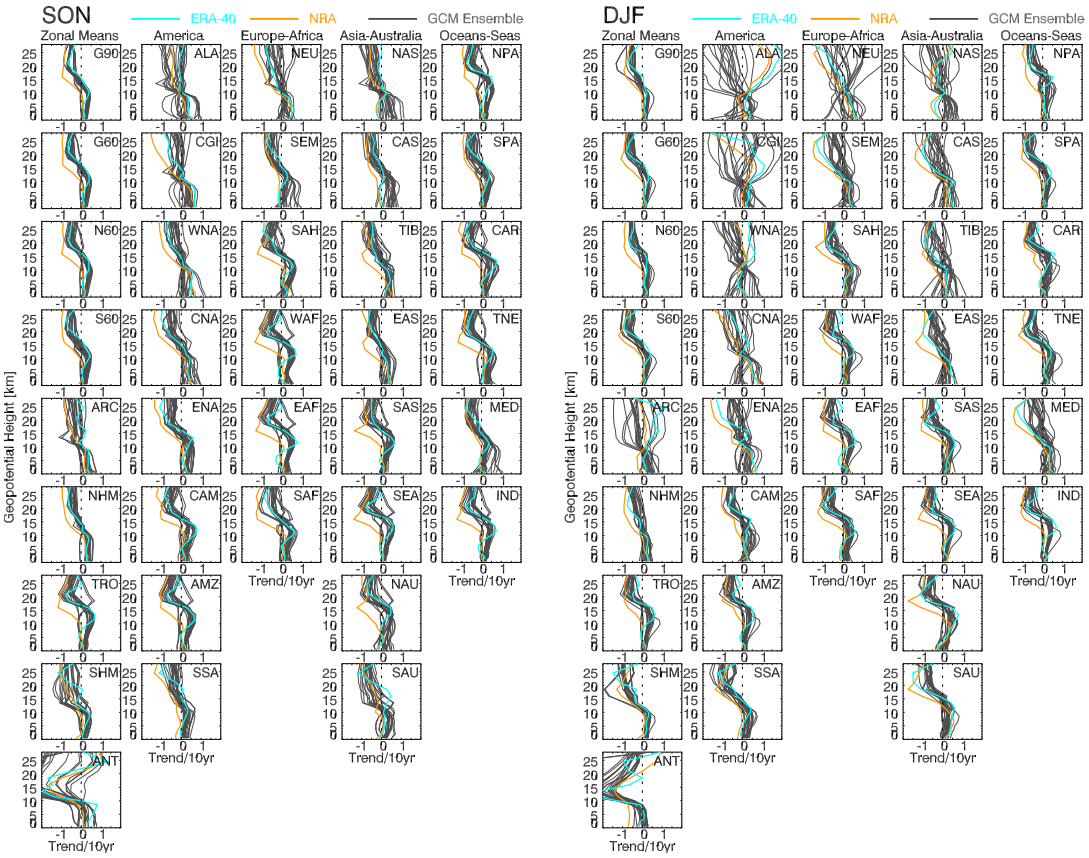

Figure 4.7: *left* SON temperature trends [K/10-years] based on 1980 to 2001 period for the re-analyses ERA-40 (blue) and NRA (orange) and the GCM simulations (gray); *right* Same illustration for DJF trends.

they will not qualify as indicator regions anyway. Nevertheless, it should be mentioned again that the three selected models use stratospheric ozone forcings, which certainly influences their general trend performance positively in the LS.

Comparison of Reanalyses and GCM Trends

The performance of GCM trends in relation to the re-analyses was explored via the 1980 to 2001 period. Figure 4.7 displays September–October–November (**SON**) and DJF temperature trends of the re-analyses (ERA-40, NRA) and the GCMs for all regions. For the re-analyses, seasons (years) influenced by the volcanic eruption of El Chichón in April 1982 and of Pinatubo in June 1991 were removed before calculating the trends. In the style of (Santer et al. 2000), the following years of the respective seasons were

ignored:

DJF: 1982/1983; 1991/1992

MAM: 1982, 1983; 1992

JJA: 1982, 1983; 1991, 1992

SON: 1982; 1991, 1992

ANN: 1982, 1983; 1991, 1992.

For large-scale zonal means in general but also for several smaller scale regional means, ERA-40 and GCM trends are consistent within the ±1 standard deviation uncertainty estimates of GCM trends. Appreciable differences can be mainly found in regions of higher northern latitudes or smaller scales in DJF, i.e. northern hemispheric winter. These disagreements between ERA-40 and GCM trends are not reflected in regions of high southern latitudes in June–July–August (**JJA**), the southern hemispheric winter (not shown). Around 5 km height and throughout all seasons, ERA-40 trends are in many smaller-scale regions (mostly of the southern hemisphere, but also in the tropics) smaller than the GCM trends, a fact that has been discussed in various studies (e.g., Karl et al. 2006; Santer et al. 2008).

Regions of smaller dimensions and higher variability, such as those at higher latitudes in the winter hemisphere, generally show a stronger internal variability. It seems that GCMs have problems to get the trends right in these regions, which is reflected by larger variation within the simulations. However, for most regions and especially for large-scale means, the trends of the GCMs agree quite well in magnitude and sign throughout all seasons. The trends of different simulations of individual models show generally similar vertical characteristics, as depicted in Figure 4.8 for three selected regions (from large to small scale). The temperature trends in this figure are based on the 2001 to 2050 period, to be able to also show the differences due to the two scenarios A2 and B1. Models and scenarios are coded with colors, so that the bundling of the models and scenarios is easily visible. The figure shows 2 regions (G60, tropics), where DJF trends agree quite well, and one region, Northern Europe (NEU), where the trends, even from single models as, e.g., CCSM3, spread considerably. Up to around 15 km height, CCSM3 and HadCM3 B1 simulations are similar and exhibit smaller trends than ECHAM5. In the LS this is still true for both models, but HadCM3 features a higher crossing point from positive tropospheric to negative stratospheric temperature trends and also less pronounced LS trends. Concerning the A2 scenario (darker colors in the plot), the differences between the models are less distinctive, above all in the troposphere, yet the bundling is still visible. The ECHAM5 tendency towards stronger tropospheric trends compared to CCSM3 is also apparent in NEU, even though the spread of trends is large within the models themselves.

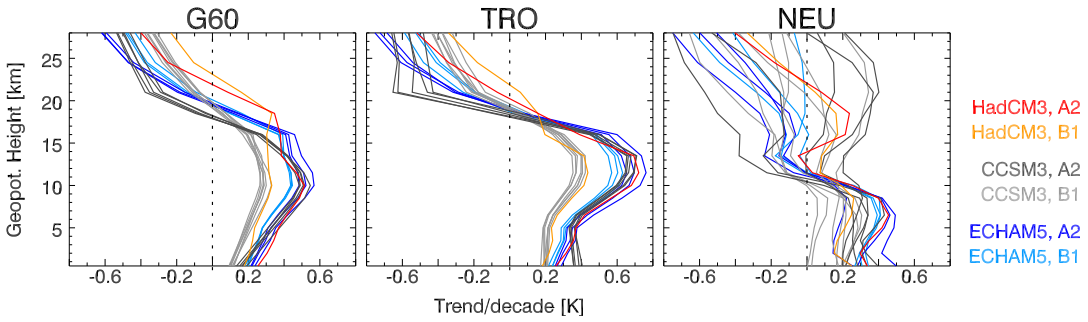

Figure 4.8: *left* DJF temperature trends [K/10-years] in the G60 region based on the 2001 to 2050 period for SRES A2 (dark colors) and B1 (light colors) GCM simulations; *middle* The same for tropical (TRO) trends, and *right* for Northern European (NEU) trends. The trends of single models and scenarios are coded with colors (see legend) to make the bundling visible.

Averaging over large areas decreases the variability in general and also within the simulations, which is visible in the zonal means in Figure 4.7. Good agreement of trends of individual GCM simulations in their sign is important for our definition of climate change indicators, because only regions with individual trends of the same sign can qualify as indicator regions (see section 4.1.2). Thus, regions where the trends of the individual model simulations differ strongly and furthermore do not agree in the sign, such as the polar caps, ALA, CGI, NEU, or NAS, drop out as indicator regions. Since these regions are generally dominated by high inter- and intra-annual variability, they evidence a low SNR and thus will not qualify as indicator regions anyway.

The most striking difference within the three data sets for the 1980 to 2001 period in Figure 4.7 is presented by NRA trends, which seem to be negatively biased compared to ERA-40 and GCMs in all seasons. This shift is clearly visible above 5 km to 10 km height so that for large-scale zonal means only negative trends appear above these levels, while the crossing points from positive tropospheric to negative stratospheric trends are around 5 km higher for ERA-40 and GCMs. Since NRA, a first generation analysis, has known and already discussed shortcomings (see section 3.2), the focus is in the following on ERA-40 as observational data set.

Representation of Trends at p-Levels Versus Z-Levels

In the following, the differences in N, Z, p, and T trends on Z-levels and p-levels for ERA-40 and the GCMs are addressed (see also beginning of section 4.2).

Figure 4.9 and Figure 4.10 depict for the parameters N, p, Z, and T *relative* trends in three regions (G60, TRO, ARC) as function of geopotential height and pressure. The trends are based on the 1980 to 2001 period in Figure 4.9, which gives results for ERA-

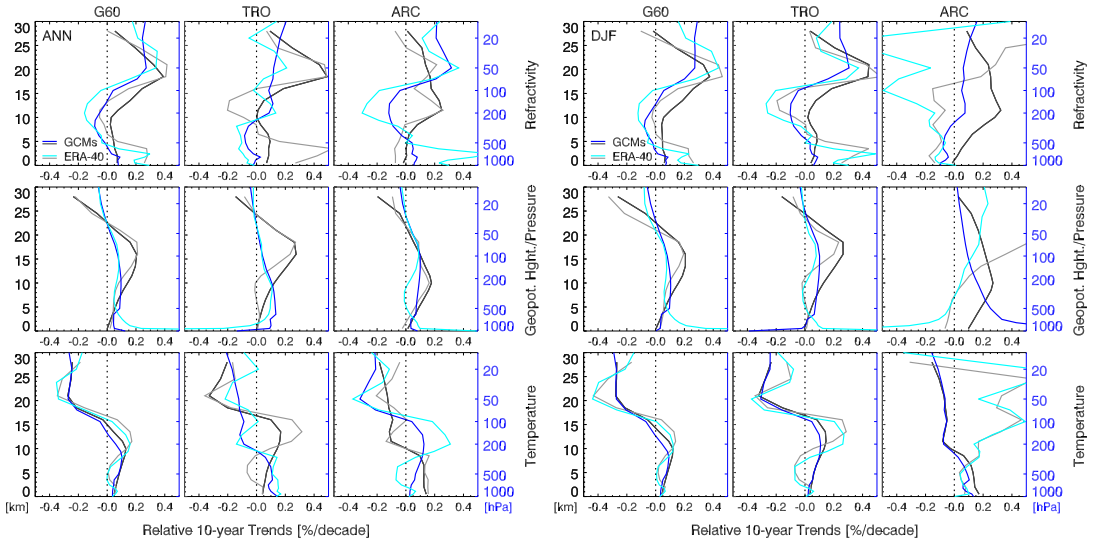

Figure 4.9: *left* Relative annual mean 10-year trends [%] based on the 1980 to 2001 period for ERA-40 and GCM ensemble average. *right* The same plot for DJF. Z-level trends are presented in gray shades, p-level trends in blue shades. ERA-40 results are light colors, GCM results in dark colors.

40 and the whole GCM ensemble average. Trends for 2001 to 2050 period are shown in Figure 4.10 for the GCM average. Z-level data are depicted in gray shades, p-level data in blue shades. Figure 4.9 evidences the good agreement between ERA-40 and mean GCM trends in large-scale regions (as G60) independent of the season considered (shown are annual mean and DJF values). In the tropics, the agreement between the re-analysis and the GCM ensemble is good for pressure and geopotential height trends and acceptable for refractivity and temperature, where largest deviations can be found in the UT between around 10 km to 15 km in Z-level trends. For the highly variable atmosphere of the rather small Arctic region, the differences between ERA-40 and GCM ensemble are very large, the trends are even sometimes diametrical (refractivity and temperature trends in DJF).

Figure 4.10 shows relative trends for the three parameters based on the GCM ensemble (2001 to 2050). The differences and amplitudes in the three parameters at p-levels and at Z-levels are easy detectable. The most salient feature is the agreement of p-level and Z-level trends for temperature with largest but still negligible differences confined to the UT. The maximum temperature trend signal of around ± 0.2 % change per decade can be found in the UT and at the highest analyzed LS level. Relative geopotential height trends are less prominent and show less vertical differentiation than pressure trends. The latter exhibit, at least for G60 and TRO, a pronounced

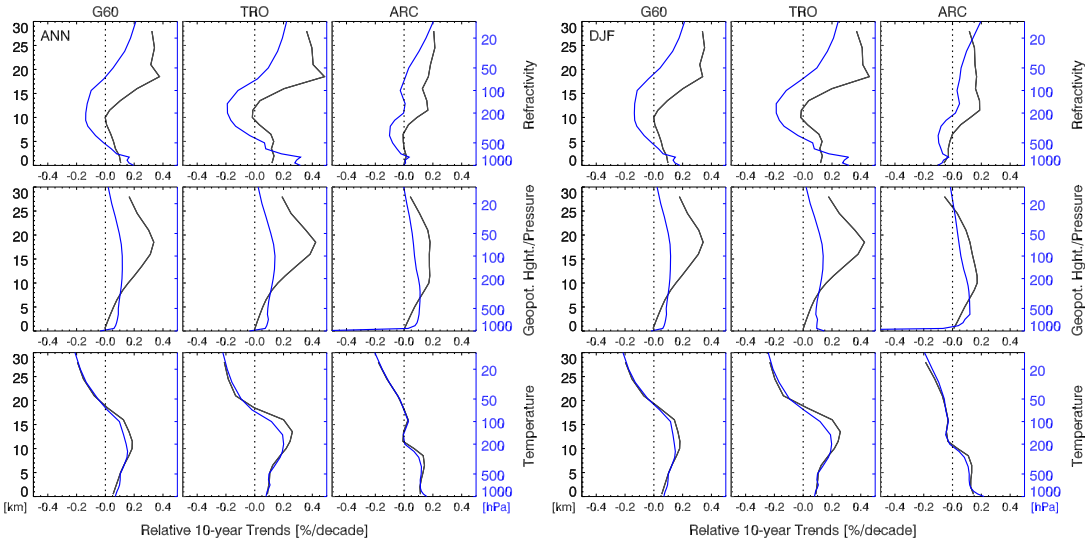

Figure 4.10: *left* Relative annual mean 10-year trends [%] based on the 2001 to 2050 period for the GCM ensemble average. *right* The same plot for DJF, shown for completeness. z-level trends are presented in gray, p-level trends in blue.

relative trend maximum of 0.4 % per decade around 20 km height. This signal is due to an expansion of the atmosphere caused by tropospheric warming, which results in an upward displacement of constant pressure levels (an atmospheric cooling results in contraction of the atmosphere and a downward displacement of constant pressure levels). Refractivity trends show the most pronounced difference between the representation at z-levels and p-levels. While relative refractivity trends are negative in the UT at p-levels, they show nearly persistent positive trends throughout the UTLS at z-levels. G60 and TRO refractivity trends at z-levels show similar to pressure trends a distinctive maximum of ≈ 0.4 % change per decade between 15 km and 20 km height. This can be explained by the fact that relative refractivity trends at constant p-levels are indirectly proportional to relative temperature trends (provided that dry air can be assumed). At constant z-levels, relative refractivity trends result as the difference between relative pressure and relative temperature trends, see equation (4.34).

It is thus of importance at which levels trend are compared, as the signal strengths can differ with height. It also has to be kept in mind that usually model data are given at pressure levels and observational data at geopotential height levels. In this study the focus is on trends on constant geopotential height levels. UTLS refractivity trends are in this case not indirectly proportional to temperature trends but capture the combined trend signal of temperature and pressure due to atmospheric warming/cooling.

Temporal Representation of Trends

The last question addressed concerning trends is their characteristics in time. Therefore, the temporal representation of trends following Rapp (2000) was examined by means of ERA-40 data. Rapp defines *temporal representation* of trends as the alterability of trend values due to changes in the analysis period. A time series is thus analyzed for trends based on moving periods of different lengths. If the sign of trend changes for a certain period length, the trend of this period is not stable. In his study of monthly mean surface temperature data for a German city, Rapp identified a minimum period of around 20 years for stable trends. For the free atmosphere in the UTLS, shorter periods can be expected for stable trends, due to less atmospheric variability.

Since the GCMs provide rather uniform long-term time series, see, e.g., Figure 3.8, ERA-40 p-level data are used to assess the period for rather stable trends in the UTLS. Figure 4.11 illustrates the temporal representation of annual mean ERA-40 refractivity, geopotential height, and temperature trends at three selected height levels (30 hPa, 100 hPa, and 300 hPa) for the G60 region. The illustration is based on ERA-40 data of the more reliable satellite era from 1981 to 2001. Moving 10-year trends are marked by a black line. They are already stable for refractivity and temperature at 30 hPa and 300 hPa, and for geopotential height at 100 hPa and 300 hPa. The 100 hPa refractivity and temperature trends as well as the 10 hPa geopotential height trends need longer periods of at least 15 years to establish stable results. This is most probably caused by the fact that the parameters feature close to these height levels the crossing point from positive to negative trends. At height levels where the trend signal emerges very clearly, stable trend can be expected earlier (compare to light blue line in Figure 4.9, left column).

When 15-years are considered to calculate moving trends, the results (presented by the upper left corner in each plot of Figure 4.11) of all parameters increase their stability at all height levels, so that for the UTLS a trend period of 10 years to 15 years can be considered as sufficiently long to obtain rather stable trend results in RO parameters.

4.2.3 Significance and Goodness-of-Fit

The trend significance and GOF results govern the determination of climate change indicator regions. The significance and GOF values are calculated for each data set (i.e. for each GCM simulation), parameter, region, and level/layer. Figure 4.12 and Figure 4.13 present examples for the annual mean (left) and DJF (right) significances and goodness of fit results for refractivity. Figure 4.12 shows results for GCMs only for European-African regions based on the period 2001 to 2050. Figure 4.13 shows results for ERA-40 and GCMs for large-scale zonal means based on the period 1980 to 2001.

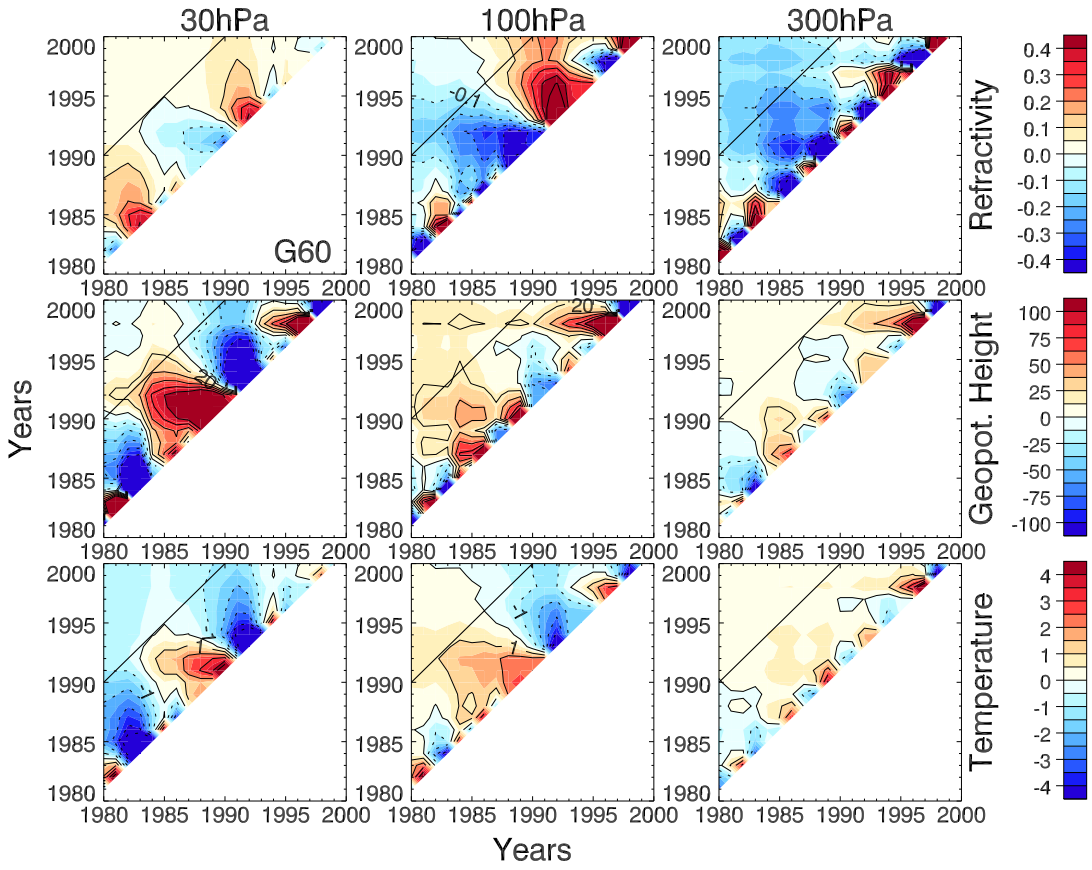

Figure 4.11: Temporal representation of ERA-40 trends based on annual mean data for G60 at three selected hight levels (from left to right) and for three parameters: *top* refractivity, *middle* geopotential height, *bottom* temperature. Plotted are trends for different period lengths. For each starting year on the x-axis, trends are calculated up to each year on the y-axis, so that a maximum of a 21-year trend was gained for the period 1980 to 2000.

Plots for all data sets, parameters, seasons, and regions can be found on the enclosed DVD (for a summary of the DVD content see appendix C).

The Long-Term Picture: 2001 to 2050 Trends

The GCM trends of the 2001 to 2050 period exhibit for most regions and seasons a significance at the 99 % level. As example plot, annual mean (**ANN**) and DJF trend significances of refractivity are shown for European and African regions (Figure 4.12, left column in each of the two panels). Each column in the significance plot presents the results of one GCM simulation, the level results are given in the rows. The color of each box indicates the sign of the trend, the shading the level of the trend significance.

Distinct and highly significant positive *refractivity* trends can be found for all shown regions in the LS at ≈18.5 km to 28 km for ANN. The two tropical regions, WAF and EAF, also exhibit significant positive trends in the lower troposphere (< 8.5 km), and significant negative trends in the UT at the 10 km and 11.5 km height level. This significant negative trends around the 10 km level can be found throughout all seasons in all tropical regions beside WAF and EAF, i.e. AMZ and SEA, and of course the zonal mean tropical band TRO. Some sub-tropical regions, such as CAR, TNE, or SAF, show a similar but attenuated signal. The positive LS and the negative tropical UT signal is the best pronounced refractivity trend signal throughout all seasons and regions. For JJA, all IPCC$^+$ regions except ANT exhibit the highly significant positive LS trends. DJF (shown in Figure 4.12, left, for European and African regions) and partly also MAM trends of high latitude regions (such as ALA, CGI, or NEU) feature a more inhomogeneous trend significance picture in regard to the different model simulations. In addition, differences in SRES A2 and SRES B1 simulations become evident, visible as less significant B1 trends. Positive tropospheric trend significances are given for the two large-scale regions G90 and G60. For the hemispheric means N60 and S60, a seasonal dependence with less significances in winter seasons can be observed. Some regions around 30° N and S, such as SSA, SEM, MED, NAU, and SAU, show no significant tropospheric trends throughout all seasons, while in ANT negative trends occur at lower tropospheric levels. All other further discussed parameter results are not shown here but the respective plots are provided on the enclosed DVD (see also appendix C).

Highly significant *pressure* trends can be found in most regions and seasons at all considered levels. Exceptions are polar caps and regions at high latitudes of the northern winter hemisphere, such as ALA, CGI, WNA, CNA, NEU, and NAS. At the 1000 hPa level, CCSM3 exhibits for G90, G60, and N60 peculiar negative trend significances, which are opposed or at least not present in the other model simulations.

Temperature trend significances are high throughout the whole UTLS, with negative LS and positive tropospheric trends. Exceptions are again restricted to regions at high latitudes, such as ARC, ALA, CGI, NEU, NAS, where at various levels high signifi-

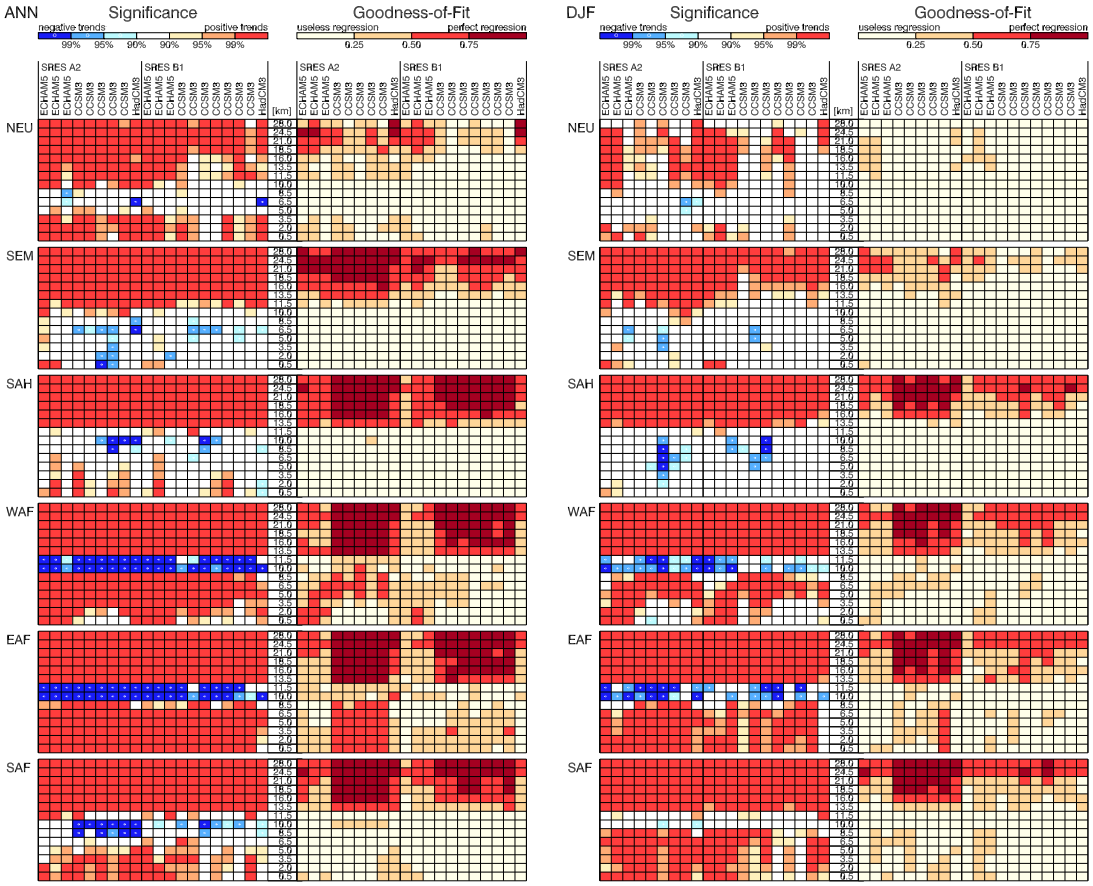

Figure 4.12: *left* Annual mean refractivity trend significance and GOF results for European and African IPCC regions for all GCM simulations and geopotential height levels based on the 2001 to 2050 period; *right* DJF results of the same data. Dark colors mark high significance (red colors for positive trends, blue colors for negative trends) and a high GOF value.

cances are only yielded by few simulations. Most regions show a sharp vertical change, limited to less than 3 vertical levels, from highly significant positive tropospheric to negative stratospheric trends. A vertically less restricted tropospheric-stratospheric change is given for the high latitude regions mentioned above and also for some smaller-scale regions, such as CAS, TIB, MED, or partly SAU in winter seasons.

A similarly clear trend significance picture is provided by layer gradients (see Table 4.2 for the layer definition). *Relative refractivity gradient* trends are mostly positive and highly significant in large-scale zonal mean regions, independent of the season considered. In the UTLS, refractivity is directly proportional to density and thus to the

pressure versus temperature ratio (see equation (2.3)), relative refractivity trends can be derived from the difference of relative pressure and relative temperature trends (see equation (4.34). Since in most regions and UTLS height domains pressure trends are larger than temperature trends (see Figure 4.10), relative refractivity trends are predominantly positive for the 2001 to 2050 period and increase with height. A layer gradient only depends on the magnitude of the trends at the both marginal levels. In tropical regions, such as TRO, WAF, EAF, SEA, or IND, relative refractivity trends are always very small or even negative at the upper UT level (11.5 km) and positive at the lower level (8.5 km), leading to negative refractivity gradient trends. A similar effect occurs for further smaller tropical and sub-tropical regions, but there it is restricted to single seasons. Less significant trends of relative refractivity gradients are again found for smaller-scale and high latitude regions in the winter hemisphere.

Relative pressure layer gradients feature highly significant trends for large-scale mean regions in all seasons, based on negative trends for the LS-layer and positive trends for the lower layers (compare to the relative pressure trend characteristics in Figure 4.10). Significances are again lacking for regions of high latitudes.

UTLS *temperature layer gradient* significances are approximately inverse to relative refractivity layer gradient significances, showing significant negative trends for the upper two layers (LS and TP) and positive trends for the lowest (UT) layer in tropical regions, with a striking homogeneity of the GCM simulations. Large-scale zonal means exhibit best significance results, smaller-scale regions at high latitudes show no explicit significances.

In general, the trend significances are best pronounced in large-scale means and regions or height domains with low internal variability, such as the tropical regions. The strong relative refractivity trend signal in the LS favors significances there. Regions which are dominated by dynamical variability, e.g., regions at high latitudes of the winter hemisphere, show too low trend significances to be considered as climate change indicator regions.

While trend significances already provide an indication where the individual parameters can be expected to show promising results, GOF turned out to be the limiting factor for the assessment. Best fits mostly agree with high significances, but as GOF reproduces the ratio between total variance in the data and the variance explained by the linear regression, regions with higher variability (or low signal) are sorted out. The GOF plots (right column of each panel of Figure 4.12) for refractivity trends also illustrate the similar internal variability and signal amplitude in various simulations of one individual model. Generally, CCSM3 trend simulations feature higher GOF results for all parameters than ECHAM5 or HadCM3. For the 6 parameters, the GOF results can be summarized as follows:

- Best GOF results for refractivity trends are given above around 13.5 km for large-scale zonal means, the tropical and sub-tropical regions, and the European and

African regions.

- Pressure trends give best GOF results between around 5 km to 21 km.
- Temperature trend GOF is best above 24.5 km and below 16 km.
- Relative refractivity layer gradients give best GOF results for large-scale zonal means and tropical regions for the TP and LS layer. Differences between the models are not very pronounced.
- Relative pressure layer gradients feature higher GOF values for the UT and TP of the same regions as refractivity gradients do. Differences between ECHAM5 and CCSM3 simulations are very distinct.
- High GOF temperature layer gradient values are mostly restricted to the LS layer, even though CCSM3 yields for some regions as good fit values as for the TP.

The Short-Term Picture: 1980 to 2001 Trends

Similar results are obtained for the shorter trend period of the ERA-40 and GCM records, but due to the more limited time span the trend signals and thus the significances and GOF values are weaker. Figure 4.13 shows significances and GOFs for annual mean (left) and DJF (right) refractivity trends in large-scale zonal regions. The first column in each figure table presents the ERA-40 results, the following columns the GCM results in the same format as presented in Figure 4.12.

For *refractivity*, highest significance results are mainly found between 10.5 km and 21 km for GCMs, and between 13.5 km and 21 km for ERA-40. ERA-40 also shows highly significant results at the lowest levels in most regions, which is only exceptionally the case for the GCM simulations. Refractivity trend significances depend on the season, most pronounced results can be discovered in ANN, JJA, and SON, the only seasons with reasonable refractivity GOF results in addition. Even though high significances extent over several levels around 16 km, higher GOF values are only given at single levels (mostly between 13.5 km and 21 km). Two regions, namely TRO and ANT, show significance patterns different from all other regions. The tropical region, TRO, exhibits in ERA-40 throughout all seasons negative trends of high significance at the 10 km and 11.5 km level, which are accompanied by acceptable GOF values. These ERA-40 feature is not reflected by all model simulations. The antarctic region, ANT, develops compared to TRO a kind of inverted trend significance pattern. Significant trends are negative in the LS above around 18.5 km and in the UT up to around 6.5 km and positive around 13.5 km.

A clear and significant *pressure* decrease at the top LS levels of ERA-40 is only visible in selected regions (and seasons), such as the global and hemispheric means or the northern and southern mid-latitudes. The significant pressure increase at lower height levels, i.e. below around 16 km, depending on region and season, is stronger

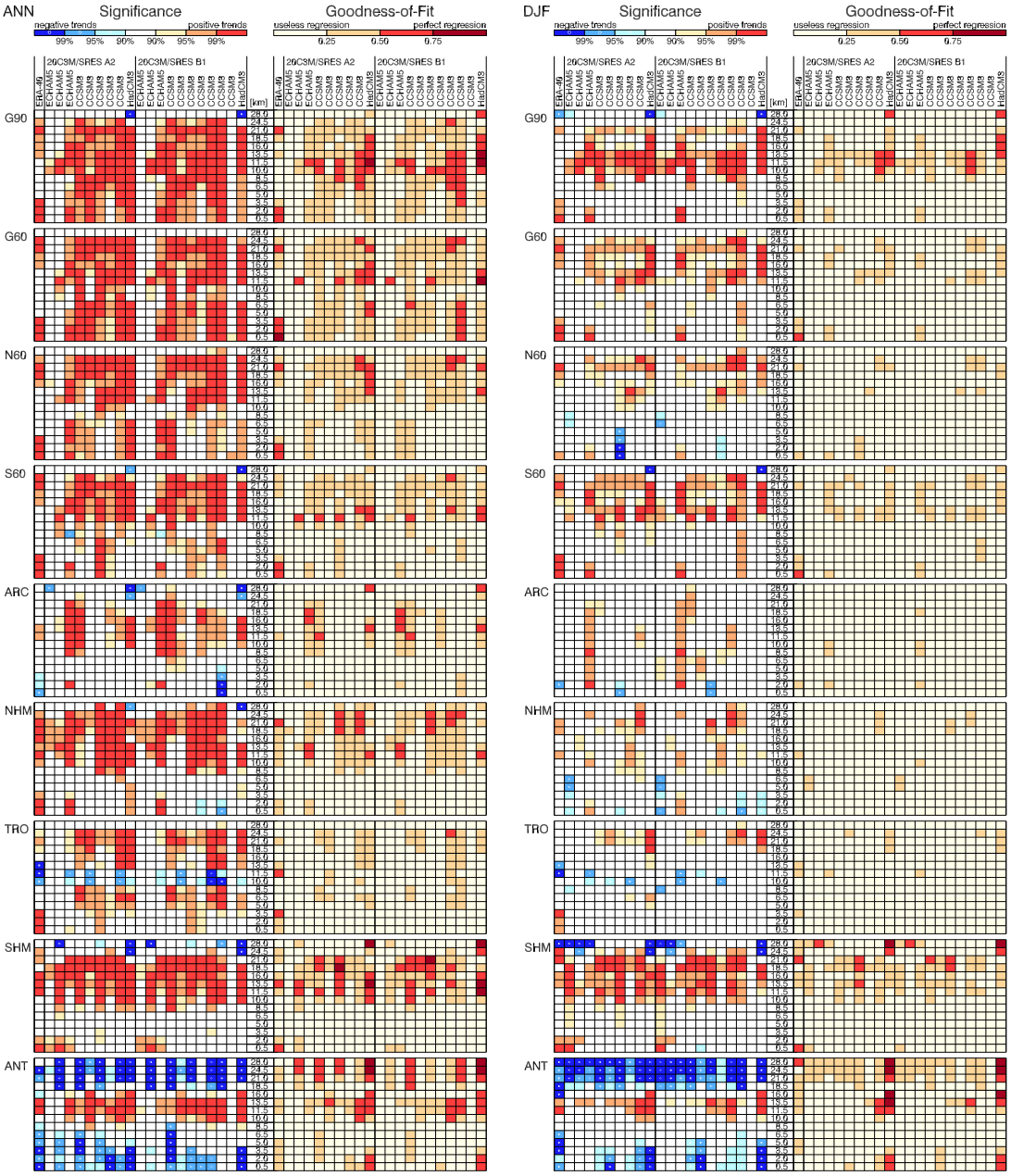

Figure 4.13: *left* Annual mean refractivity trend significances and GOF results for large-scale zonal mean regions for ERA-40 and GCM simulations based on the 1980 to 2001 period; *right* DJF results of the same data. Dark colors mark high significances (red colors for positive trends, blue colors for negative trends) and a high GOF value.

pronounced. The GCMs show highly significant negative trends in the antarctic region above around 16 km for all seasons but JJA. This feature can also be found in ERA-40 data, but only for MAM and DJF. Compared to the other parameters, pressure indicator regions are mostly constricted by GOF values, which are particularly low in the UTLS.

Highest *temperature* trend significances are found above 18.5 km and below 11.5 km, whereas acceptable GOF results are mainly restricted to large-scale zonal means in the LS. ERA-40 results are stronger confined to single levels, e.g., the 21 km and 24.5 km level in the LS, than GCM results. Most pronounced ERA-40 temperature trend significance and GOF results are given for ANN, JJA, and SON.

Relative refractivity layer gradients show best significance and GOF results for zonal-mean and some tropical regions. ERA-40 data feature significant trends mostly for the UT and TP, with the most prominent feature of highly significant negative trends in the tropical UT, while subtropical and mid-latitudes show positive trend results. The GCMs exhibit higher trend significances for zonal mean regions, but GOF values are comparable to ERA-40.

The highly significant negative LS trends of the *pressure layer gradients* are a result of pronounced relative pressure trends between 10 km to around 20 km height and a crossing point from positive to negative relative pressure trends around 25 km (see also Figure 4.9). Even though significant positive trend gradients can be found in the UT for both, ERA-40 and GCMs, GOF values are generally lower than in the LS. The seasonal results show less trend significances and worse GOF values than the annual means. Compared to the 2001 to 2050 trends, the height levels with significant trends are more confined and the thermal expansion of the atmosphere is just beginning to form, so that the crossing point of pressure and also temperature trends is lower (around 11.5 km for temperature and around 18.5 km for pressure).

LS *temperature layer gradients* are significantly pronounced in ERA-40 and GCMs. For ERA-40, they are mostly found in the LS layer, while GCMs also give significant results in the TP. Similar to the refractivity layer gradients, the tropical regions show for the UT significant positive trends with acceptable GOF values, while trends in regions at higher latitudes are negative. Compared to the other parameters, temperature gradient trends exhibit also higher significances in smaller-scale regions.

In general, the GCM results are similar to ERA-40 results, even though the GCMs feature better GOF values and partly higher trend significances, which are probably caused by less model variability. While the long-term picture of analyzed trends for the 2001 to 2050 period gives a rather rough estimate of high trend significance and good GOF results, the shorter period based on ERA-40 data of the satellite 1980 to 2001 era with less pronounced trends and higher data variability allowed to gain more insight in the behavior of the different parameters in the IPCC$^+$ regions and to thus approach the RO indicator regions.

Autocorrelation of Sliced Data

As mentioned in section 4.1.2, temporal correlation within a time series can influence trend significance estimates. For climate data, attention should be generally payed to lag-1 autocorrelation. The autocorrelation issue was here addressed by analyzing correlograms of time series where the linear trend, which would introduce a spurious autocorrelation, was removed. Figure 4.14 shows correlograms for the three main parameters exemplarily for three regions and the 8.5 km level and the 25.8 km level. The autocorrelations were computed for ERA-40 JJA data, results for other seasons (not shown) are very similar.

The three regions illustrate different spatial characteristics, from a large-scale mean (G60), over a typical zonal mean region (TRO), to a small-scale region influenced by higher variability (NEU). The plot shows that the autocorrelations coefficients remain within the ± 0.25 range for most lags. Furthermore, the lag-1 autocorrelation coefficient is not necessarily the largest one, it sometimes can be even very close to zero. In 5 out of the 18 displayed cases the lag-1 coefficient is between $\mid \pm 0.25 \mid$ and $\mid \pm 0.50 \mid$.

Assuming an lag-1 autocorrelation coefficient of $r_1 = 0.25$ (i.e. the margin of the light gray shaded range in Figure 4.14), the effective sample size, n_e, can be determined with equation (4.30) as $n_\mathrm{e}(n = 22; r_\mathrm{e} = 0.25) = 13.2$ for the 1980 to 2001 period or as $n_\mathrm{e}(n = 50; r_\mathrm{e} = 0.25) = 30$ for the 2001 to 2050 period. For the critical t-value t_c in the (2-tailed) significance test with a 10 % error rate α, this would mean an increase of 0.05 (from $t_\mathrm{c}(n = 22, \alpha = 0.10) = 1.72$ for to $t_\mathrm{c}(n_\mathrm{e} = 13.2, \alpha = 0.10) = 1.77$) for the shorter trend period and an increase of 0.02 (from $t_\mathrm{c}(n = 50, \alpha = 0.10) = 1.68$ to $t_\mathrm{c}(n_\mathrm{e} = 30, \alpha = 0.10) = 1.70$) for the longer trend period. If a 1 % error rate is used, the critical t-value increase is slightly larger, i.e. 0.08 (from 2.82 to 3.00) for the shorter period and 0.07 (from 2.68 to 2.75) for the longer period. Thus, the difference between the t-values for $\alpha = 1\,\%$ and $\alpha = 10\,\%$ (corresponding to the highest and lowest significance level used in the trend analysis) is always much larger than the influence of including the effective sample size for the determination of the critical value.

In fact, the significances gained in the trend analysis are clearly above the 99 % probability level, so that the integration of an effective sample size would hardly influence the results. Furthermore, GOF was identified as the limiting factor in the determination of indicators.

4.3 Discussion of Climate Change Indicators

For discussion of the climate change indicators with respect to RO climatologies only results above 8.5 km (dry air assumption, see section 2.3.1) are considered. Only z-level data are discussed. Figure 4.15 and Figure 4.16 summarize results of all parameters and seasons for the two analyzed periods; for the sake of completeness and tropospheric

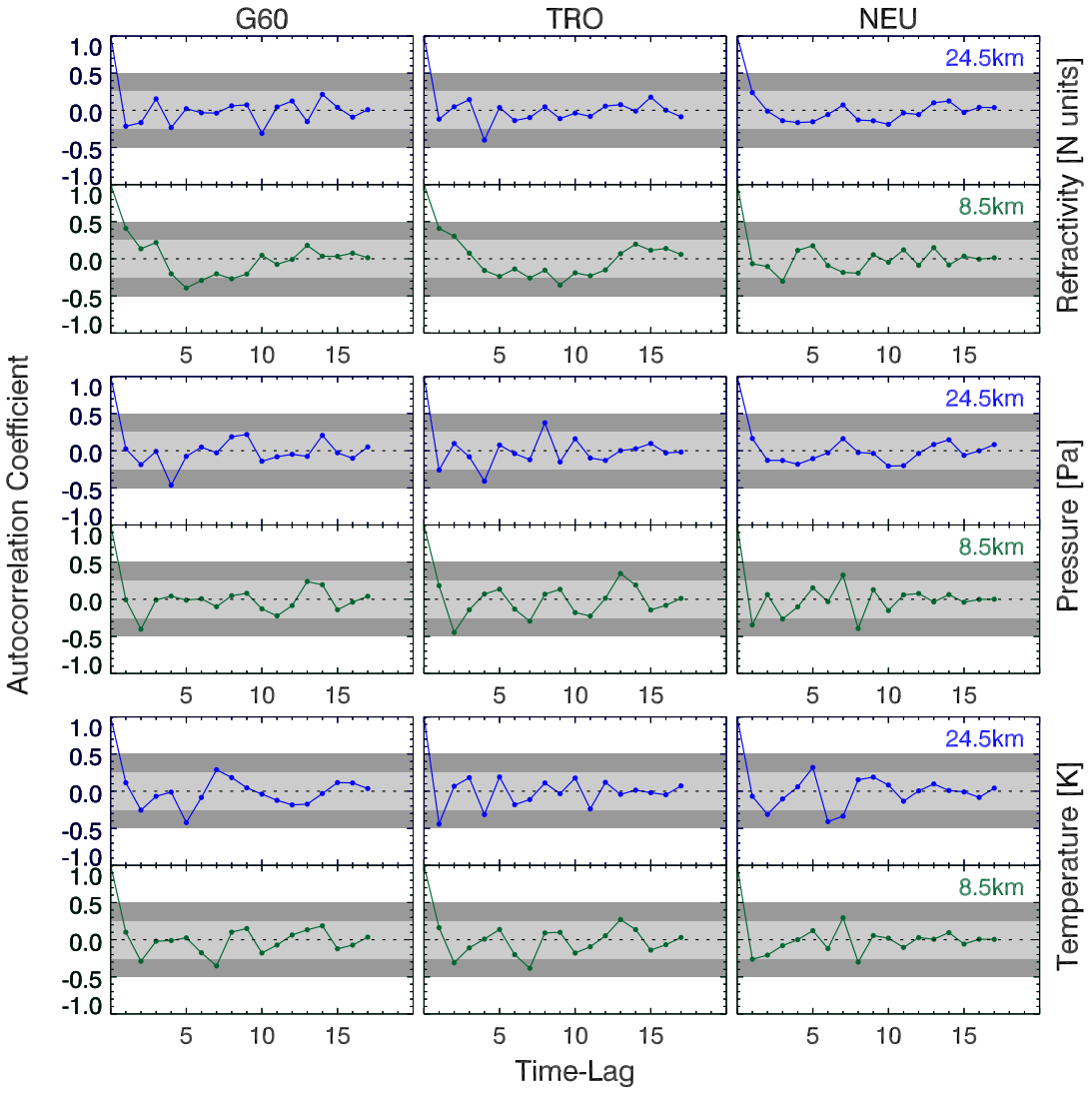

Figure 4.14: *top* JJA refractivity correlograms for G60 (left), TRO (middle), and NEU (right) based on ERA-40; upper plots show results for a LS level (24.5 km) and are marked by blue color, lower plots show results for an UT (8.5 km) level and are marked by green color; the ±0.25 range is shaded with light gray, the ±0.5 range with dark gray; *middle* Same illustration for pressure data; *bottom* Same illustration for temperature data.

context, the lower levels are also shown. Furthermore, the focus is on large-scale zonal means, the RO single-satellite focus regions. More recent multi-satellite missions, such as Formosa Satellite Mission #3/Constellation Observing System for Meteorology, Ionosphere, and Climate (**FORMOSAT-3/COSMIC**), will provide an increasing insight into regional issues due to to a better spatial coverage by occultation events in consequence of a whole constellation of satellites in orbit. If appropriate, regional results are also mentioned.

Based on the results of the trend analysis, the climate change indicators are now defined as regions where the proxy data (re-analyses and GCMs), which are expected to respond similar to external forcings as RO data, feature a high SNR.

Indicators Based on the 2001 to 2050 Period

The 2001 to 2050 indicators are based on 10 randomly selected GCM simulations to afford a more equally weighting of the models, which provide a different number of simulations per scenario (see Table 3.2). For each A2 and B1 scenario 2 ECHAM5, 2 CCSM3 simulations, and the one available HadCM3 simulation were used. Tests, using different randomly chosen simulations, showed that the indicators are insensitive to the specific ensemble of simulations. The results based on different ensembles only differ for single height levels and (mainly smaller-scale) regions, while the overall picture remains the same.

To qualify at a certain height level or layer as indicator region, at least 8 out of the 10 simulations have to (see Table 4.3)

- show trends of the same sign,
- exhibit high trend significances and
- sound GOF results.

The combination of these requirements reveals domains with on the one hand high trend SNR and on the other hand similar characteristics of model simulations. The GCM based indicator regions for the trends of the first part of the 21st century are illustrated for all 6 parameters in Figure 4.15. Overall consistent results for all zonal mean regions except the polar caps are given for level-based parameters. For the layer trends, the mid-latitude regions show differences depending on the season.

Refractivity, the RO parameter closest to bending angle (the first derived parameter in the RO retrieval chain as discussed in section 2.2), turns out as suitable LS indicator in all large-scale zonal regions except the polar caps. Averaging over very large areas or exclusion of the high latitudes, as reflected in G90, G60, N60, and S60, leads to better results not only in the LS but also at lower levels down to $\approx$ 13 km. The zonal mean bands of around 30° latitudinal width give best results above $\approx$ 18 km independent of the season considered.

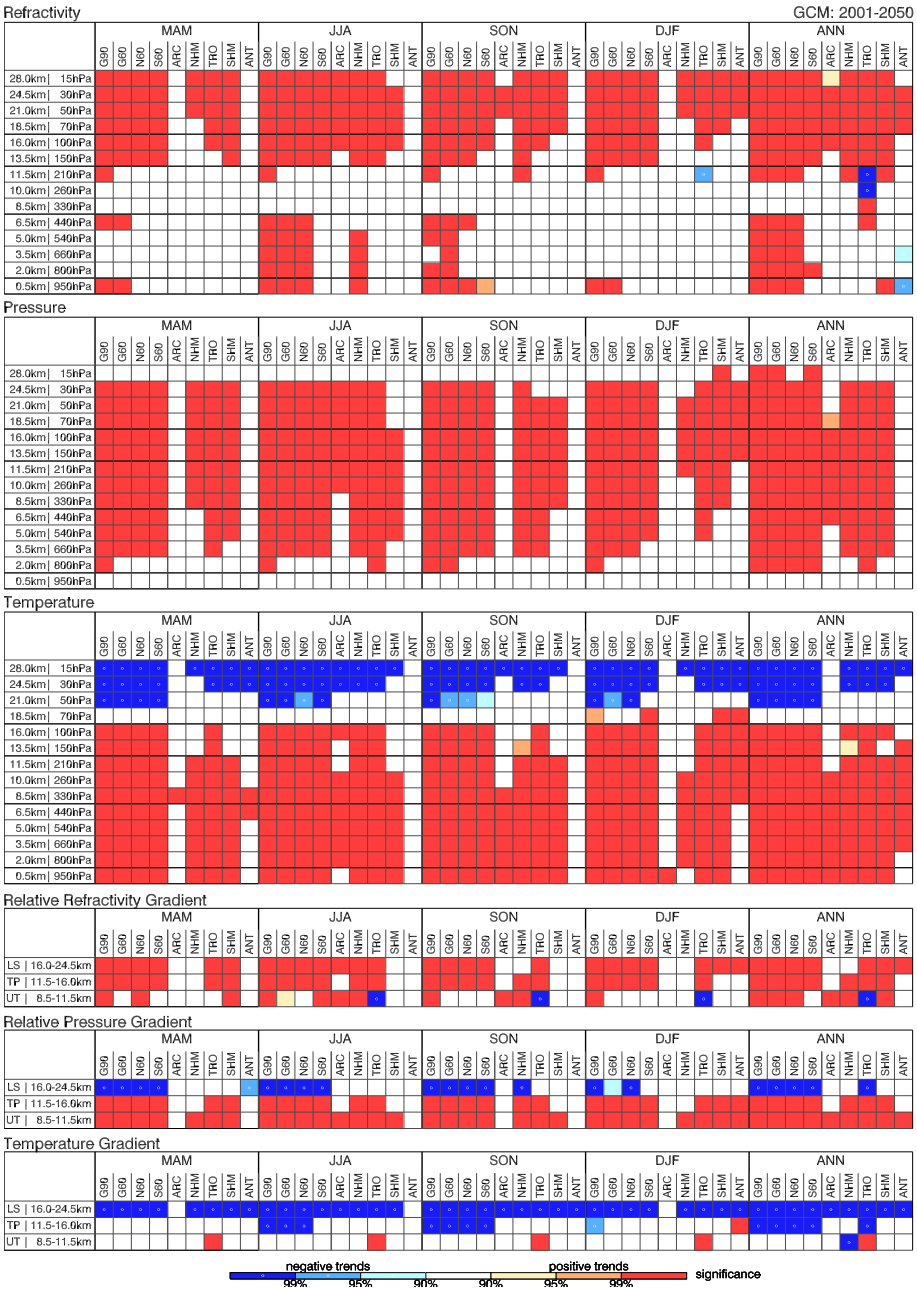

Figure 4.15: *top to bottom* GCM indicators for all seasons and large-scale and zonal means based on the 2001 to 2050 period for all parameters. The significance level of the respective trends is indicated by the shading, the trend sign by the color. Trends where analyzed at Z-levels. Corresponding p-levels are indicated for completeness.

A striking indicator is presented by the UT tropical region in DJF and ANN, where negative trends of high trend significance and GOF values occur (see the significance and GOF discussion in section 4.2.3). Refractivity is the parameter showing the largest trend differences between p-level and Z-level data. Thus, refractivity based indicator regions differ considerably depending on the chosen vertical coordinate. While Z-level based data provide best UTLS indicator results (based on mostly positive trends) above $\approx$ 13 km, p-level data produce best indicator results above $\approx$ 30 hPa ($\equiv$ 24.5 km) based on positive trends and between 400 hPa ($\equiv$ 7.2 km) and 100 hPa ($\equiv$ 16.0 km) based on negative trends. Above $\approx$400hPa, the refractivity p-level indicator results are comparable to temperature Z-level results, only the sign of the trend has to be inverted.

Pressure, which can be considered as integrated refractivity, emerges as UTLS indicator for RO climatologies between $\approx$ 3 km to below 24.5 km for global and hemispheric means. The polar caps are excluded again for spring and fall in general and for the respective winter season. In the ANN data, ANT has to be excluded as indicator region and the ARC indicator region is stronger limited in height (between 6.5 km and 16 km).

Temperature reflects the variation in height of the simulations' crossing points from tropospheric warming to stratospheric cooling at $\approx$ 18.5 km. Global and hemispheric means qualify consistently as indicator regions above $\approx$ 20 km and below $\approx$ 16 km. Concerning the zonal bands, best results are gained for the tropics. The mid-latitudinal bands reflect the higher variability of the respective winter season so that tropospheric indicator regions are constrained below $\approx 11\,km$ and stratospheric ones above $\approx$ 24 km. Results for the polar caps again depend on the season and thus should be disregarded as indicators.

All *layer gradients* meet the requirements for indicators in global and hemispheric means with emphasis on different layers. While *pressure gradients* perform well at all height domains, *refractivity gradients* are more restricted to the LS and *temperature gradients* exclusively to the LS. This is consistent with a model study, where Ringer and Healy (2008) showed that the bending angle climate change signal in the tropical UTLS, which is comparable to the refractivity gradient signal, may become distinguishable from natural variability after approximately ten to sixteen years of measurements. For the mid-latitudes, a clear dependence on stronger winter variability is evidenced. The most striking feature emerges in the tropical UT. There, positive temperature gradient changes emerge in all seasons and negative relative refractivity gradient changes in all but one season. For temperature gradients, this is important, as none of the other zonal regions qualifies as indicator in the UT.

In the tropics, refractivity gradient changes are negative as a result of positive refractivity trends at 8.5 km and negative (or negligible small) trends at 11.5 km height. These trends of opposite sign at around 10 km thus lead to a strong UT layer signal, even though the level trends at these heights are not qualified due to too low GOF

results. Similarly, the temperature gradient changes in the tropical UT are positive (decrease of lapse rate[2]) result from the stronger temperature trends at the upper level compared to the lower one. Besides these tropical UT trends, temperature gradients in the LS qualify as indicators throughout all seasons and all zonal mean regions except the polar caps.

As to the GCMs, the *typical* RO parameters refractivity and pressure (as function of geopotential height) alone are adequate indicators for the UTLS, but temperature and most notably layer gradients provide additionally good sensitivity, mainly in the tropics.

Indicators Based on the 1980 to 2001 Period

The results for ERA-40 indicators based on the 1980 to 2001 period are presented for all parameters in Figure 4.16. Since the analyzed time period is shorter and only one data set is taken into account, the criteria to qualify as indicator were adjusted to achieve interpretable results. Only trend significance (at least 90 %) and goodness of fit (> 0.25) were considered (see section 4.1.2). Compared to the 50-year GCM trend results, the ERA-40 indicators are stronger limited to certain height levels, regions, and seasons.

The UTLS *refractivity* indicators, based on positive trends, are centered at 21 km height for global and hemispheric means (and down to 16 km in SON). In the tropical and mid-latitudinal regions, refractivity is an acceptable indicator only in SON, JJA, and ANN. In contrast to the 50-year trends of GCMs, ERA-40 features indicator regions in the tropical UT at 11.5 km and 13.5 km throughout all seasons, which are based on remarkably strong (absolute and relative) negative refractivity trends and high GOF values. The high GOF values appear first of all at 11.5 km. The GCMs show an indicator signal only in ANN and DJF at 11.5 km, the significance is weaker (see Figure 4.15). This UT tropical indicator is not limited to the zonal tropical band but also clearly pronounced in the small-scale African and Asian tropical regions throughout all seasons, i.e. SAH, WAF, EAF, SAF, SAS, and SEA, as well as in the Indian ocean. Antarctica catches one's eye (also for the other parameters) with negative LS indicators in DJF and partly ANN and MAM (for the latter also in the troposphere). But as the quality of ERA-40 is deficient in high southern latitudes according to Santer et al. (2004) and as visually explored by Kehrer et al. (2008), one should not attach great importance to this pattern.

Pressure reflects the seasonality of ERA-40 indicators. Best results emerge almost exclusively in ANN and SON in the TP region (13.5 km and 16 km) and partly in the UT of global and hemispherical means as well as at northern mid-latitudes. In the UT, pressure proves to be also an acceptable indicator (based on trend significances of more

[2]The lapse rate is defined as the negative vertical temperature gradient.

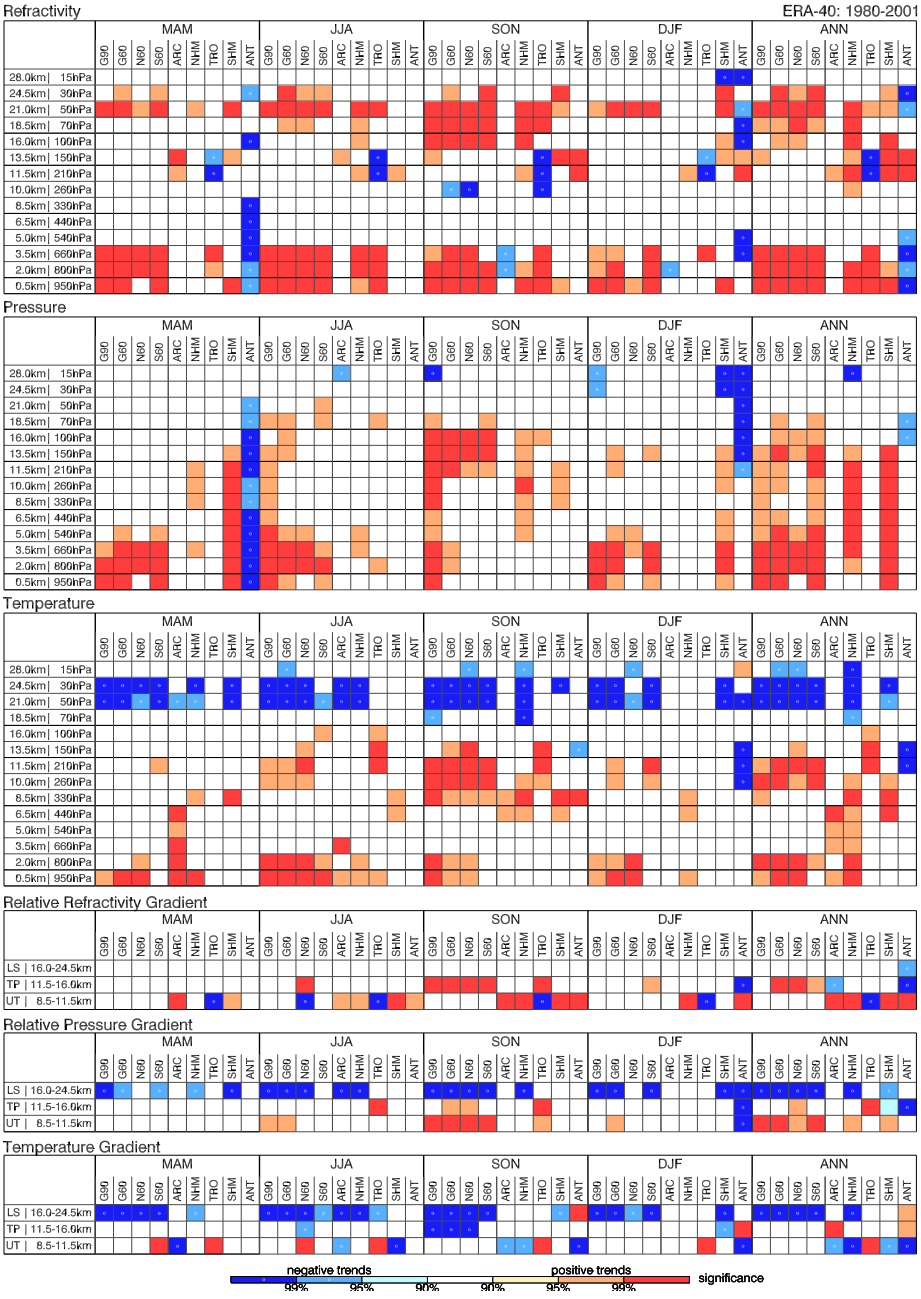

Figure 4.16: *top to bottom* ERA-40 indicators for all seasons and large-scale and zonal means based on the 1980 to 2001 period for all parameters. The significance level of the respective trends is indicated by the shading, the trend sign by the color. Trends where analyzed at Z-levels. Corresponding p-levels are indicated for completeness.

than 95 %) for the mid-latitudes in MAM, SON, and most clearly in ANN. Similar to refractivity, ANT complies with indicator requirements up to ≈ 21 km height in MAM and above ≈ 11 km height in DJF. In contrast to refractivity, no small-scale regions shows distinct indicators for pressure.

The most striking difference between the 2001 to 2050 GCM and the 1980 to 2001 ERA-40 *temperature* trends is the lower crossing point from positive to negative trends in ERA-40, which is reflected in the indicator regions. Compared to the GCMs, where no difference in the occurrence between LS and UT indicators emerges, the LS results are more pronounced than the tropospheric ones in ERA-40 (except for large-scale and hemispheric means in SON and ANN). In addition to the global and hemispherical means, the northern mid-latitudes turn out to be good LS indicators from northern spring to fall, the southern mid-latitudes in southern summer and fall, and at both hemispheres for ANN. The small-scale North American regions WNA, CNA, and ENA, as well as the South European regions SEM and MED, present themselves also as LS indicator regions in all seasons but DJF. In the tropics, temperature trends feature in JJA, SON, and ANN an UT pattern consistent with refractivity at 11.5 km and 13.5 km height.

The minor atmospheric expansion during the ERA-40 trend period compared to the 50-year GCM trend period is found again in ERA-40's *layer indicators*. The global and hemispheric mean *relative refractivity gradient* indicators are restricted to the TP layer in SON and ANN. They are complemented in all season only by the African regions SAH, EAF, and SAF. In JJA, and more significant in SON and ANN, the UT gradients of all zonal mean bands turn out as indicators. The most striking relative refractivity gradient indicator is based on the strong negative refractivity gradient changes in the tropical UT in all seasons, which is consistent with the GCM results (see above).

While the pressure level indicators are rather poorly developed throughout all seasons, the *relative pressure gradients* exhibit distinct indicators, mainly for global and southern hemispherical means in the LS in all seasons. For hemispherical spring and summer, the mid-latitudes are as well good LS indicator regions. In JJA, SON, and ANN some small-scale North American, European, African, and Asian regions as well as oceans, namely CNA, ENA, SEM, SAH, TIB, EAS, TNE, and MED turn out as LS indicator regions as well. The tropics, including TRO, CAM, AMZ, WAF, EAF, SEA, and IND, show good indicator results in the middle layer, again for JJA, SON, and SON, while for the UT only SON results are noteworthy.

For the LS *temperature gradient* indicators, a similar picture as for pressure gradients is seen. The tropics form, in line with the relative refractivity gradients, a continuous pattern of positive UT temperature gradient indicators, which is again consistent with GCM results and based on the stronger warming trend at the top level of the layers. This UT tropical positive indicator pattern is again reflected in the small-scale tropical and sub-tropical regions AMZ, SAH, WAF, EAF, SAF, SEA, and IND, indicating the steadiness of this climate change feature in the tropical atmosphere.

While ERA-40 climate change indicators show promising results for RO parameters in the UTLS, GCMs feature hardly indicators for the 1980 to 2001 period (not shown). Only LS temperature, temperature gradients, and relative refractivity gradients in large-scale, hemispheric, and partly zonal means qualify as indicators. This is caused by too low GOF results for the ensemble of all GCM simulations, which are required by the criteria.

Compared to the 50-year based GCM indicators, ERA-40 indicators show stronger characteristics at certain distinct height ranges and more seasonality. Thus, the different parameter's indicators can be better assigned in height. This reflects more specifically where trend signals may emerge first, while the GCMs 50-year trends reflect the more robust broad picture. In general, besides the large-scale means (G90, G60, N60, S60), the tropics, selected small-scale tropical regions, and the mid-latitudes emerge as most interesting regions, where climate change should be traced. Even though the GCMs show less seasonality in their indicators, their behavior is similar to ERA-40, where the best SNR in the RO parameters develops mainly in SON and ANN but also in JJA.

4.3.1 Summary of Climate Change Indicators Study

The climate utility of RO-accessible climate change indicators was demonstrated by means of climate simulations of the three representative IPCC AR4 models ECHAM5, CCSM3, HadCM3, investigated for the 2001 to 2050 period and the ERA-40 re-analysis for the 1980 to 2001 period. The adequacy of these proxies for RO data was demonstrated in section 4.2.1 and section 4.2.2 by means of variability and trend investigations. The latter included an analysis of GCM's LS trends compared to those of the middle atmosphere version of the ECHAM5 model, MAECHAM5. The study showed that the LS trend performance of the used models with the uppermost level at 10 hPa shows no striking differences to middle atmosphere model trends (top level at 0.01 hPa) in large-scale regions. Trend differences in small-scale regions and at higher latitudes are on the one hand not limited to the LS and on the other hand do not influence the study results, because these regions are also governed by high internal variability, leading to less significant trend results. For the trend analysis, the focus was on large-scale zonal means of refractivity, pressure, and temperature Z-level and vertical gradient data. Indicators were defined as regions with high trend SNR, which was determined by means of trend significances, GOF, and—for GCMs—by the agreement between the individual simulations in their trend sign. Indicator differences between Z-level and p-level data are mostly restricted to refractivity and the respective layer gradients, as discussed in section 4.3. For pressure/geopotential height and temperature, differences of Z-level and p-level results are negligible.

The GCMs show for the years 2001 to 2050 a strong climate change signal in various height domains, depending on the respective physical processes governing the individ-

ual parameters (Figure 4.15). As to zonal means, seasonality only plays a minor role for such long-term trends.

The shorter time period of analyzed ERA-40 trends, 1980 to 2001, draws a more narrowed picture of regions with high trend SNR (Figure 4.16). Single zonal bands, such as the tropical regions, turned out to be good indicator regions for several parameters and height domains. Compared to the GCMs, indicator regions are less repeatable throughout all seasons; ANN, SON and next JJA exhibit best indicator results for the UTLS. This supports individual seasonal differentiation when investigating climate change on shorter time-scales. Nevertheless, ERA-40 and GCM results are generally consistent with regard to indicators, with the latter showing the longer-term broad picture.

Regarding altitude dependence of earlier climate change signal emergence, refractivity turned out as good indicator at about 18 km to 24 km ($\approx$ 70 hPa to 30 hPa levels), pressure at lower levels of 13 km to 16 km ($\approx$ 150 hPa to 100 hPa levels), and temperature at around 9 km to 12 km ($\approx$ 300 hPa to 200 hPa levels). The latter also emerges as LS indicator above 20 km as well as refractivity in the tropics around $\approx$ 12 km. Beside the level based considerations, layer gradients support the applicability of RO data for climate monitoring and show promising results, particularly for the tropics. When the boundary height levels of the layers used to calculate gradients are properly chosen, the layer gradients appear more sensitive to climate change than single level data do, providing additional information. Collectively, the set of RO-accessible parameters qualifies for climate monitoring in the whole UTLS, since the sensitivity of the parameters neatly differs with height.

Specifically per parameter, from more basic to more derived products, refractivity and pressure and the respective layer gradients alone are adequate climate change indicators, but also temperature can be well used as additional indicator. By end of 2010, a continuous RO record of 10 years, and—including the Global Positioning System/Meteorology (**GPS/MET**) data—an intermitted record of 15 years will be available, fulfilling the needs of climate monitoring and diagnosis.

5 Detecting Atmospheric Climate Change by Means of Radio Occultation Data

The detection of climate change signals in rather short satellite data sets is a challenging task in climate research and requires high quality data with good error characterization. Due to characteristics such as long-term stability, self-calibration, and a good height-resolution, Radio Occultation (**RO**) retrieved parameters are highly qualified to investigate atmospheric climate change in the upper troposphere-lower stratosphere (**UTLS**). Hegerl et al. (2010) define *detection* as

> the process of demonstrating that climate or a system affected by climate has changed in some defined statistical sense without providing a reason for that change. An identified change is detected in observations if its likelihood of occurrence by chance due to internal variability alone is determined to be small, for example, $< 10\,\%$.

Detection differs from the often simultaneously mentioned *attribution*, which is defined as

> the process of evaluating the relative contributions of multiple causal factors to a change or event with an assignment of statistical confidence.

Attribution requires detection beforehand.

A review paper on detection and attribution (**D &A**) studies is given by Barnett et al. (2005). A further survey of more recent D&A studies is provided in the Intergovernmental Panel on Climate Change (**IPCC**) Fourth Assessment Report (**AR4**) by Hegerl et al. (2007). Many of the presented studies addressed the human influence on surface temperature changes, making use of different statistical techniques and basing the investigations on observations and different General Circulation Model (**GCM**) simulations. Comparisons with (near) surface observations evidenced the GCMs an adequate representation of internal variability, which is important for D&A studies. As to the free atmosphere, detection studies were mainly based on temperature records of different radiosonde and (Advanced) Microwave Sounding Unit (**MSU/AMSU**) data sets. Even though the anthropogenic influence on climate change of the free atmosphere is beyond question, the observational data sets used for D&A exhibit inconsistencies in the warming rates of the free atmosphere on longer than annual time scales. Radiosondes and MSU/AMSU have not been designed for climate monitoring but for weather

monitoring. The construction of a consistent climate record requires inter-calibration and homogenization of the data, which is a demanding task. The errors in radiosonde and MSU/AMSU records are discussed by, e.g., Karl et al. (2006) or Steiner et al. (2007).

A lot of studies have already addressed the climate monitoring potential of RO data (see section 2.4), but RO based detection studies are still rare, and no attribution study was implemented until now. Leroy et al. (2006*b*) performed a sensitivity analysis for RO data by using an optimal fingerprinting approach and employing a range of IPCC AR4 models. The focus of the study was on synthetic (i.e. on GCM based) RO trends in log-dry pressure, which is comparable to vertically integrated refractivity. They estimated UTLS trend detection times of 7 to 13 years for the RO record and noted that "the detection times are nearly independent of which model is used to prescribe natural variability" (ECMWF Hamburg Model (**ECHAM5**) is referred to as more sensitive than other models because it features more variability). Furthermore, they identified the pole-ward motion of mid-latitude jets as strongest indicator of climate change. A first detection study based on real RO data was performed by Steiner et al. (2009*a*), showing that RO temperature trends within February 1995 to 2008 are significant in the lower stratosphere (**LS**) and are consistent with RO detection time estimates of Leroy et al. (2006*b*) and Ringer and Healy (2008). They used multiple linear regression to estimate the trend signal and tested its significance relative to natural climate variability gained from observations and GCMs. Additional comparisons of UTLS RO, GCM, and radiosonde trends revealed a general agreement between the data sets, although trends for radiosondes are not significant.

This chapter presents a detection study based on real RO data by using an optimal fingerprint detection technique. It investigates, whether the RO record shows already evidence of a forced climate change signal within 1995 to 2008. Trends of refractivity (N), geopotential height (Z), and temperature (T) at pressure (p)-levels are therefore investigated in the UTLS between 50°N and 50°S. Furthermore, Quasi-Biennial Oscillation (**QBO**) and El Niño-Southern Oscillation (**ENSO**) based UTLS variability is discussed. Section 5.1 gives an overview on the data and its fields of application and introduces the fingerprinting method. The study results are presented in section 5.2 and discussed in section 5.3.

5.1 Climate Change Detection—Study setup

The optimal fingerprinting technique relies on data from observations and climate model simulations. Beside those data sets, the ECMWF Re-Analysis (**ERA-40**) and the Hadley Centre gridded free-atmosphere temperatures from radiosondes (**HadAT2**) record are employed for further pattern analyses and comparisons (see Table 3.3 for a summary of the data sets used). Since the UTLS variability is also governed by large-scale atmospheric patterns, such as the ENSO or the QBO, their share on the total UTLS

variability is estimated via linear regression on short time scales.

The first part of this section gives a very short overview of the spatio-temporal study setup and the data employed.

The remaining part of this section introduces in the methods used. Ordinary least squares fingerprinting is presented in detail in section 5.1.2. The analysis of large-scale patterns and their share in the total variability was implemented with multiple linear regression. It is detailed together with the Mann-Whitney U-test, which was used to assess the significance of differences in modes of atmospheric patterns, in section 5.1.3.

5.1.1 Datasets Used for Climate Change Detection

The study is based on single refractivity, geopotential height, and temperature trend patterns of monthly mean UTLS RO climatologies from the Global Positioning System/ Meteorology (**GPS/MET**) experiment and the Challenging Mini-Satellite Payload (**CHAMP**) satellite.

Optimal fingerprinting requires that the space-time scales of the analysis are advisedly chosen. It has to be assured that only scales are kept, where the GCMs represent the internal variability reasonably well. At the same time it has to be guaranteed that enough scales are kept to represent the signal vector reasonably well (Zwiers 2009). Furthermore, characteristics of data have to be kept in mind. Therefore, the focus region of the study is the UTLS between 50° N/S, where best RO data quality is provided (Steiner et al. 2009*a*). A horizontal resolution of 5 zonal mean regions was employed, comprising the following zonal bands:

- 1 tropical band between 10°N and 10°S;
- 2 sub-tropical bands from 10°N to 30°N and 10°S to 30°S, respectively;
- 2 mid-latitude bands from 30°N to 50°N and 30°S to 50°S, respectively.

The focus is on the resolution with the 5 zonal regions, but the analysis was also performed for a 10° zonal mean grid in latitude. The data are used on 8 pressure levels spanning from 300 hPa ($\approx$ 8500 m) to 30 hPa ($\approx$ 24 500 m). Monthly mean time series for the 1995 to 2008 period were analyzed, from which the average seasonal cycle over the CHAMP analysis period was removed.

The setup of the analysis is closely tied to the availability of *RO measurements*. For the detection study, the combined GPS/MET–CHAMP record spanning more than 12 years is employed. GPS/MET data from the two prime times (see section 3.1.1) October 1995 and February 1997 are used (2 months). CHAMP data are employed from September 2001 to February 2008, except July/August 2006 (76 months), see Figure 3.1 for the number of available measurements. Two time periods are considered for the detection study:

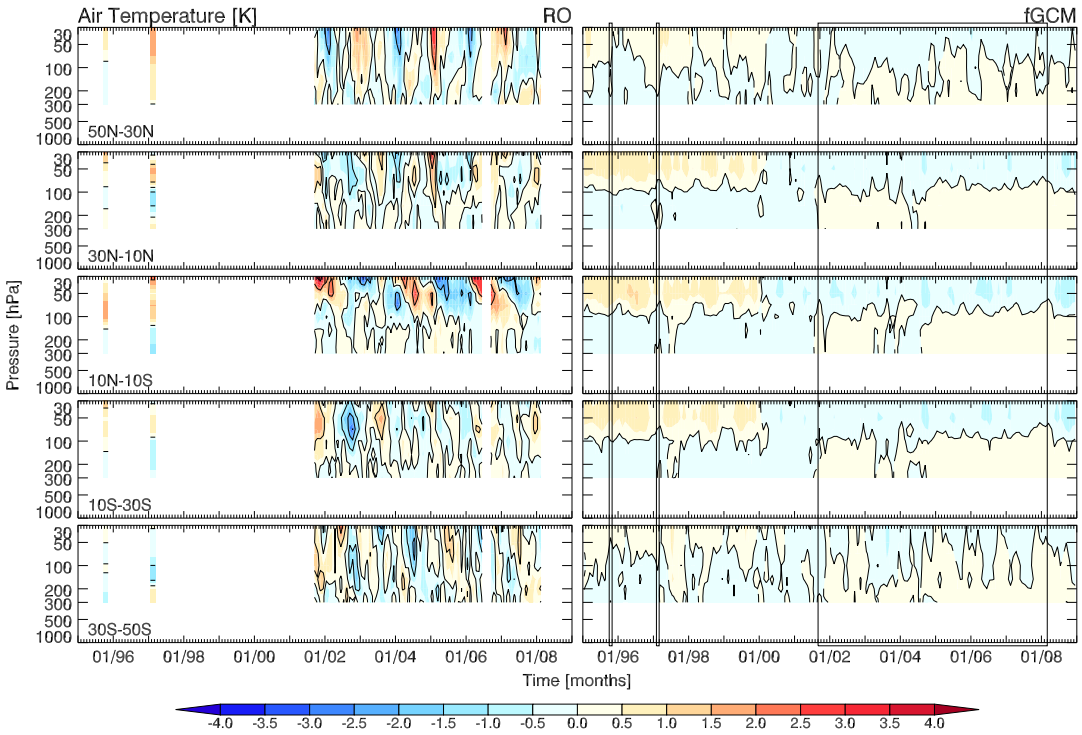

Figure 5.1: *Left* Time series of RO temperature anomalies for the GPS/MET–CHAMP period for 5 zonal bands. Anomalies are relative to the 2002 to 2007 mean. *Right* The same for fGCMs, where anomalies are relative to the 1995 to 2008 mean. The boxes mark the RO period.

1. **GPS/MET–CHAMP period**: intermittently 10/1995 to 02/2008, based on the the combined GPS/MET–CHAMP record;
2. **CHAMP only period**: 09/2001 to 02/2008, excluding 07-08/2006, only considering CHAMP measurements.

The *multi-model, multi-realization GCM data set* is used to estimate the expected climate signal and the natural climate variability for optimal detection. The anticipated climate change signal is estimated with the average of the 20 SRES A2 and B1 GCM simulations (fGCM) record comprising the Community Climate System Model 3 (**CCSM3**), the ECHAM5, and the Hadley Centre Coupled Model, version 3 (**HadCM3**). The period to calculate the trend signals is chosen consistently to the RO record, for the GPS/MET data, climate of the 20th century experiment (**20C3M**) simulations are used. The acronym fGCM stands for *forced* GCM and refers to the Hegerl et al. (2010) definition of external forcing, which they define as "a forcing factor outside the climate

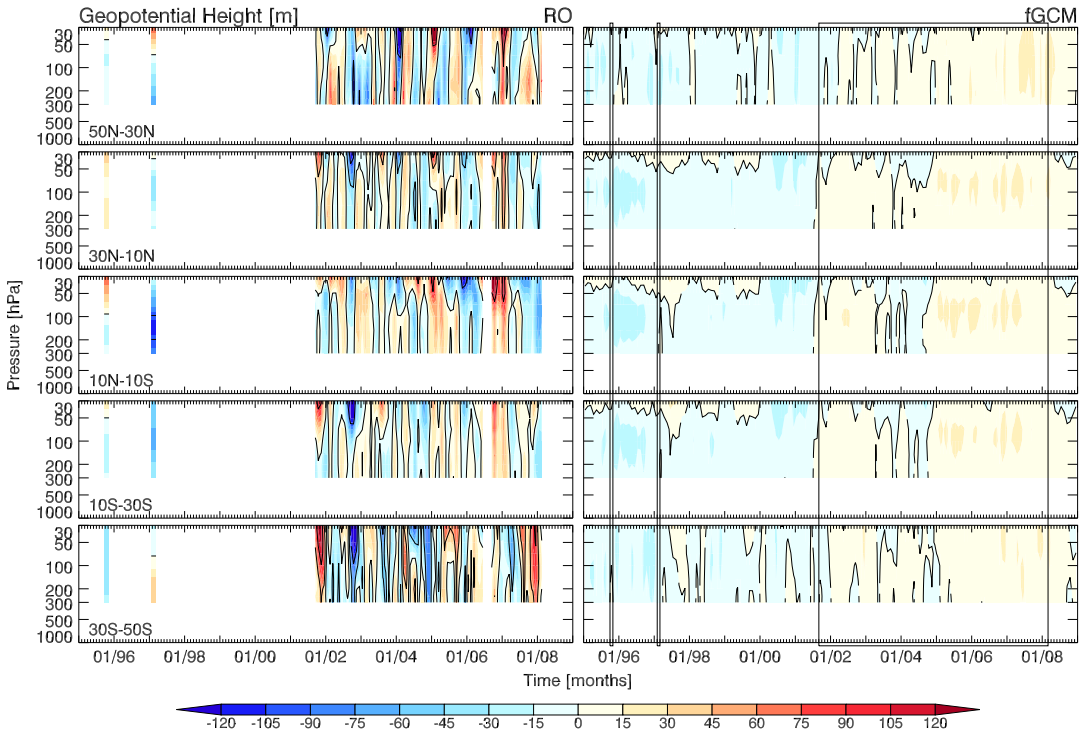

Figure 5.2: *Left* Time series of RO geopotential height anomalies for the GPS/MET–CHAMP period for 5 zonal bands. Anomalies are relative to the 2002 to 2007 mean. *Right* The same for fGCMs, where anomalies are relative to the 1995 to 2008 mean. The boxes mark the RO period.

system that causes a change in the climate system. Volcanic eruptions, solar variations, anthropogenic changes in atmospheric composition and land-use are examples of external forcing that can affect both climate and non-climate systems".

Figure 5.1 shows temperature anomaly time series for the RO and fGCM data for each of the 5 zonal mean bands. RO data feature higher variability with anomalies fluctuating between around $-3\,\mathrm{K}$ and $4\,\mathrm{K}$, while the multi-ensemble mean of the fGCM record only varies within $-1.5\,\mathrm{K}$ to $1.5\,\mathrm{K}$. The plot also evidences that the GCMs do not succeed in reproducing the QBO pattern, which is clearly visible in the tropical band in the RO data, presenting three full periods of LS temperature anomaly changes. In contrast, the climate change signal can be seen at first glance in the smooth fGCM record, despite its short length. Figure 5.2 shows geopotential height anomalies for the same period and zonal regions. The RO geopotential height anomalies fluctuate for the 1995 to 2008 period between around $-100\,\mathrm{m}$ and $100\,\mathrm{m}$, with largest amplitudes in the tropics of the LS and in the mid-latitudes throughout the UTLS. The anomalies

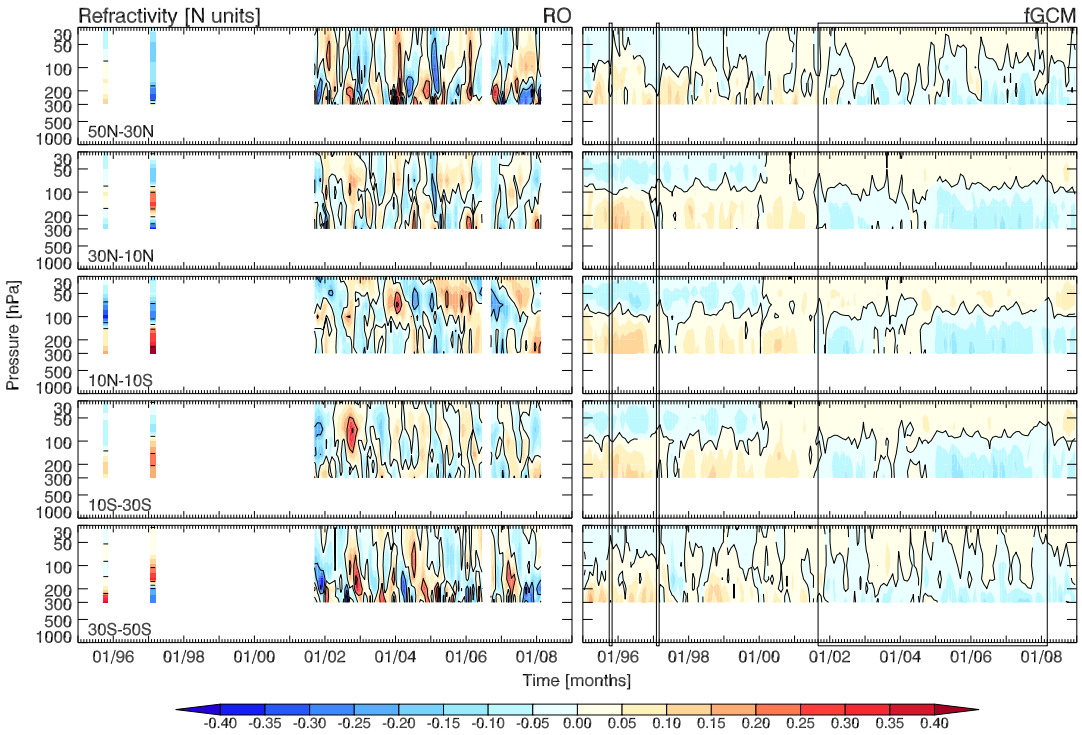

Figure 5.3: *Left* Time series of RO refractivity anomalies for the GPS/MET–CHAMP period for 5 zonal bands. Anomalies are relative to the 2002 to 2007 mean. *Right* The same for fGCMs, where anomalies are relative to the 1995 to 2008 mean. The boxes mark the RO period.

of the fGCM record are about half as large. For the sake of completeness, refractivity, which is inverse proportional to temperature, is shown in Figure 5.3.

Natural variability is based on 4 pre-industrial control experiment (**PICTRL**) simulations of the same models. Details about the available number of forced simulations and PICTRL years are given in Table 3.2. The GCM data were interpolated to the same spatial resolution as the RO data and limited to the same spatial and temporal coverage.

For the analysis of large-scale patterns, such as ENSO or the QBO, ERA-40 output was used. The HadAT2 record was applied to compare with RO results, especially with the goal of assessing the consistency of trends based on the full temporal coverage compared to those based on the incomplete RO record between 1995 and 2001.

5.1.2 Optimal Detection With Ordinary Least-Squares Fingerprinting

The detection study is based on an ordinary least-squares (**OLS**) fingerprinting approach following Hegerl et al. (1996)[1]. In general, optimal fingerprinting (e.g., Hasselmann 1997; Barnett et al. 2005; Hegerl et al. 2007) can be considered as generalized multivariate regression. An observed record $\mathbf{Y}$ is represented by a scaled (β) estimated externally forced climate change pattern (*guess pattern*, $\mathbf{X}$), which contains the natural and anthropogenic response to the forcings, and an estimate for internal climate variability (ϵ):

$$\mathbf{Y}_{\mathrm{RO}} = \mathbf{X}_{\mathrm{fGCM}}\,\beta + \epsilon_{\mathrm{PICTRL}}. \tag{5.1}$$

Thus, signal and noise are assumed to be additive. As *observed climate change signals*, the spatial trend patterns of RO parameters $\mathbf{Y}_{\mathrm{RO}}$ are considered, representing latitude-height slabs. The *guess pattern* $\mathbf{X}$ for the detection is presented by the fGCM mean. The PICTRL data are separated in two halves for the following two issues:

- on the one hand PICTRL data are used to represent the RO and fGCM data in a dimension-reduced Empirical Orthogonal Function (**EOF**) space, where the covariance matrices of the noise are diagonal, and to estimate the scaling factors $\hat{\beta}$, which modulate the amplitudes of the guess patterns;
- on the other hand, a second statistically independent sample of PICTRL data (**CONTROL**) is employed to access the uncertainty in the detection variables.

To obtain the two samples, the PICTRL data of each simulation was divided into halves. In order to avoid very disproportional weighting, 115 years of each model simulation were used to compose a sample, since the shortest PICTRL simulation provides 230 years. Thus, based on the two multi-simulation samples with each 460 years of data, two PICTRL trend pattern matrices equivalent to the used RO periods were generated. The individual trend patterns were calculated without temporal data overlap.

To assess whether the climate variability of the PICTRL simulations adequately represent the variability of the observations in the truncated space, a residual consistency test following Allen and Tett (1999) was performed.

The advantage of optimal fingerprinting (for details see, e.g., Hegerl et al. 1996) is that it uses a univariate low-dimensional detection variable to solve the problem. In general, the signal-to-noise ratio (**SNR**) ratio and thus the significance of the signal increases rapidly with a decreasing dimension of the space. Furthermore, in contrast to other approaches, fingerprinting makes use of the full expected climate change pattern, instead of using, e.g., only mean values.

[1] Besides OLS fingerprinting, a *total least-squares* approach is available, which additionally accounts for the GCM uncertainty caused by the limited number of available simulations.

The following sections give a detailed step-by-step description of OLS optimal fingerprinting. The explanations mainly refer to the data sets used, but can also be applied in general for optimal detection studies. The space-time scale for this study is based on trend patterns for climatologies with a resolution of 5 latitudes and 8 p-levels, i.e. 40 grid points per trend pattern. It is required that all data sets correspond to the observational record, i.e. same spatial resolution, same missing values. Table 5.1 summarizes the used notations in equations of the detection study.

notation	data set	comment
N	–	number of trends ($N = 1$ for observations and fGCM)
p	–	40 grid points (5 latitudinal bands, 8 p-levels)
k	–	number of retained EOFs; $k = 1, \ldots, p$
$\mathbf{Y}^{\text{data}}_{N\times p}$	RO, PICTRL	trend pattern(s) in the detection space
$\mathbf{X}_{N\times p}$	fGCM	fGCM trend pattern in the detection space
$\epsilon_{N\times p}$	PICTRL	climate noise in the detection space
$\mathbf{C}_{p\times p}$	PICTRL	covariance matrix of the noise ϵ in the detection space
$\mathbf{\Sigma}_{p\times p}$	PICTRL	covariance matrix of $\mathbf{Y}^{\text{PICTRL}}$ in the detection space
$\mathbf{A}_{N\times k}$	PICTRL	matrix of EOF expansion coefficients
$\mathbf{a}_1, \ldots, \mathbf{a}_k$	PICTRL	EOF expansion coefficients, also called principal components (each with length N)
$\mathbf{F}_{p\times k}$	PICTRL	matrix containing the eigenvectors of $\mathbf{\Sigma}$ in the columns
$\mathbf{f}_1, \ldots, \mathbf{f}_k$	PICTRL	eigenvectors, i.e. EOFs, of $\mathbf{\Sigma}$ (each with length p)
$\mathbf{\Lambda}_{k\times k}$	PICTRL	diagonal matrix of the eigenvalues of $\mathbf{\Sigma}$
$\lambda_1, \ldots, \lambda_k$	PICTRL	eigenvalues of $\mathbf{\Sigma}$
$\mathbf{b}^{\text{data}}$	RO, fGCM, CONTROL	scalar trend pattern (patterns in case of CONTROL data set) in dimension-reduced EOF space
$\hat{a}^{\text{data}}_k$	RO, CONTROL	estimated scaling factors for $\mathbf{X}$ in the EOF space (estimates for β of the detection space)
r_k	PICTRL	regression residuals in EOF space

Table 5.1: Notations used in equations of the optimal detection study as well as data sets for which the quantity in question has to be calculated.

Step 1—Determine EOFs of PICTRL Data

Optimal fingerprinting holds some constraints on dimensionality, including the invertibility of the covariance matrix $\mathbf{\Sigma}$, which is based on the signals, i.e. patterns of change in space. Therefore, the observations and the other data sets are represented in a dimension-reduced space, which is gained by projecting the data onto low-order EOFs.

The EOF space is commonly spanned by decomposing the trend matrix based on the first half of the PICTRL data. Non-overlapping trends were computed, resulting in N trends for p grid points. Each trend covers the same period length and considers the same missing data as the RO data feature. The trends are pooled in the matrix $\mathbf{Y}^{\mathrm{PICTRL}}_{N\times p}$. Each row of $\mathbf{Y}$ contains one trend map and each column all trends of non-overlapping periods for one grid point:

$$\mathbf{Y}^{\mathrm{PICTRL}}_{N\times p} = \begin{pmatrix} y_{1,1} & y_{1,2} & \cdots & y_{1,p} \\ y_{2,1} & y_{2,2} & \cdots & y_{2,p} \\ \vdots & \vdots & \ddots & \vdots \\ y_{N,1} & y_{N,2} & \cdots & y_{N,p} \end{pmatrix} \begin{array}{l} \rightarrow \text{trend map for one time period} \\ \\ \\ \\ \downarrow \text{time series (trends) for first grid point } p=1 \end{array}$$

The covariance matrix $\mathbf{\Sigma}$, which contains the covariances between any two grid points, is derived from the trend matrix $\mathbf{Y}$ with

$$\mathbf{\Sigma}_{p\times p} = \frac{1}{N-1} \left(\mathbf{Y}^{\mathrm{PICTRL}}\right)^{\mathsf{T}}_{p\times N} \mathbf{Y}^{\mathrm{PICTRL}}_{N\times p}. \tag{5.2}$$

An EOF analysis (for details see, e.g., Jolliffe 2002; von Storch and Zwiers 2002) aims at finding a set of orthogonal functions that characterize $\mathbf{\Sigma}$, i.e. the directions of (graded) maximum variances. These orthogonal functions, named EOFs if derived empirically, are the eigenvectors $\mathbf{f}_i$ of the covariance matrix $\mathbf{\Sigma}$, with the corresponding eigenvalues λ_i. Any symmetrical matrix, such as $\mathbf{\Sigma}$ can be presented by its eigenvectors and eigenvalues, as given in the following equation for the PICTRL trend matrix:

$$\mathbf{\Sigma}_{p\times p} = \mathbf{F}^{\mathrm{PICTRL}}_{p\times k}\, \mathbf{\Lambda}^{\mathrm{PICTRL}}_{k\times k} \left(\mathbf{F}^{\mathrm{PICTRL}}\right)^{\mathsf{T}}_{k\times p}, \text{ with } k = 1,\ldots,p. \tag{5.3}$$

The eigenvectors $\mathbf{f}_i$ of $\mathbf{\Sigma}$, which are pooled in the columns of $\mathbf{F}$, are here scaled in such a way that $\mathbf{f}_i^{\mathsf{T}}\,\mathbf{f}_i = 1$. $\mathbf{\Lambda}$ is a diagonal matrix, with the eigenvalues of $\mathbf{\Sigma}$ in its diagonal. In a dimension-reduced space, usually not all p eigenvectors are used, but only a subset of $k \leq p$. The so-called expansion coefficients $\mathbf{a}_i$, summarized in the columns of $\mathbf{A}$, which are needed to re-transform the data from the reduced EOF space

into the detection space, can be derived by means of the eigenvector matrix and the trend matrix via

$$\mathbf{A}_{N\times k} = \mathbf{Y}_{N\times p}\,\mathbf{F}^{\mathrm{PICTRL}}_{p\times k},\ \text{with } k = 1,\ldots,p. \tag{5.4}$$

Using the matrix of expansion coefficients and a subset of $k \leq p$ eigenvectors, the respective data matrix can be retrieved by the following relation:

$$\hat{\mathbf{Y}}_{N\times p} = \mathbf{A}_{N\times k}\,\left(\mathbf{F}^{\mathrm{PICTRL}}\right)^{\mathsf{T}}_{k\times p},\ \text{with } k = 1,\ldots,p. \tag{5.5}$$

If $k = p$, $\hat{\mathbf{Y}}$ will be equal to $\mathbf{Y}$.

Step 2—Spanning fGCM and RO Data in the PICTRL EOF Space

All further calculations are performed in the PICTRL EOF-space. Thus, RO, fGCM, and CONTROL data are projected on the EOFs gained in step 1. Considering any ith EOF, a pattern $\mathbf{Y}^{\mathrm{data}}_{\mathbf{1\times p}}$ can be presented as scalar in the EOF space as

$$b_i^{\mathrm{data}} = \frac{\left(\mathbf{Y}^{\mathrm{data}}\right)_{1\times p}\left(\mathbf{f}_i^{\mathrm{PICTRL}}\right)_{p\times 1}}{(\mathbf{f}_i^{\mathrm{PICTRL}})^{\mathsf{T}}_{1\times p}\,(\mathbf{f}_i^{\mathrm{PICTRL}})_{p\times 1}},\ \text{with } i = 1,\ldots,k. \tag{5.6}$$

The denominator in equation (5.6) is a scaling factor, which is here equal to 1, based on the scaling of the eigenvectors. Thus, the trend pattern, a vector of p values in the detection space, is represented by the scalar value b_i in the ith EOF space. Considering k EOFs, the data can be represented in the EOF space using matrix notation as

$$\begin{aligned}\mathbf{b}_k^{\mathrm{data}} &= \left[\left(\mathbf{F}^{\mathrm{PICTRL}}\right)^{\mathsf{T}}_{k\times p}\mathbf{F}^{\mathrm{PICTRL}}_{p\times k}\right]^{-1}\left(\mathbf{F}^{\mathrm{PICTRL}}\right)^{\mathsf{T}}_{k\times p}\left(\mathbf{Y}^{\mathrm{data}}\right)^{\mathsf{T}}_{p\times 1} \\ &\quad \text{with } k = 1,\ldots,p.\end{aligned} \tag{5.7}$$

The following four transformation equations are achieved for the single trend patterns of RO, fGCM, and a selected GCM simulation (used for a detection stability test, see section 5.3.3), and for the multiple trend patterns of the CONTROL data set:

$$\mathbf{b}_k^{\mathrm{RO}} = \left[\left(\mathbf{F}^{\mathrm{PICTRL}}\right)^{\mathsf{T}}_{k\times p}\mathbf{F}^{\mathrm{PICTRL}}_{p\times k}\right]^{-1}\left(\mathbf{F}^{\mathrm{PICTRL}}\right)^{\mathsf{T}}_{k\times p}\left(\mathbf{Y}^{\mathrm{RO}}\right)^{\mathsf{T}}_{p\times 1} \tag{5.8}$$

$$\mathbf{b}_k^{\mathrm{fGCM}} = \left[\left(\mathbf{F}^{\mathrm{PICTRL}}\right)^{\mathsf{T}}_{k\times p}\mathbf{F}^{\mathrm{PICTRL}}_{p\times k}\right]^{-1}\left(\mathbf{F}^{\mathrm{PICTRL}}\right)^{\mathsf{T}}_{k\times p}\left(\mathbf{Y}^{\mathrm{fGCM}}\right)^{\mathsf{T}}_{p\times 1} \tag{5.9}$$

$$\mathbf{b}_k^{\mathrm{GCM}} = \left[\left(\mathbf{F}^{\mathrm{PICTRL}}\right)^{\mathsf{T}}_{k\times p}\mathbf{F}^{\mathrm{PICTRL}}_{p\times k}\right]^{-1}\left(\mathbf{F}^{\mathrm{PICTRL}}\right)^{\mathsf{T}}_{k\times p}\left(\mathbf{Y}^{\mathrm{GCM}}\right)^{\mathsf{T}}_{p\times 1} \tag{5.10}$$

$$\mathbf{b}^{\mathrm{CONTROL}}_{k\times N} = \left[\left(\mathbf{F}^{\mathrm{PICTRL}}\right)^{\mathsf{T}}_{k\times p}\mathbf{F}^{\mathrm{PICTRL}}_{p\times k}\right]^{-1}\left(\mathbf{F}^{\mathrm{PICTRL}}\right)^{\mathsf{T}}_{k\times p}\left(\mathbf{Y}^{\mathrm{CONTROL}}\right)^{\mathsf{T}}_{p\times N}, \tag{5.11}$$

where N in equation (5.11) is the number of CONTROL trend patterns.

Step 3—Estimation of Scaling Factors

The major aim in optimal fingerprinting is to estimate the parameter vector β in equation (5.1), which adjusts the amplitude of the fGCM pattern. In the EOF space, β is estimated with the scaling factors $\hat{a}_i$.

If an OLS approach (e.g., Basilevsky 1983) was employed, β would be estimated as

$$\hat{\beta} = (\mathbf{X}^\intercal \mathbf{X})^{-1} \mathbf{X}^\intercal \mathbf{Y}. \tag{5.12}$$

This approach requires that the columns of $\mathbf{X}$ are nonrandom vectors; that the expected value of the residual term ϵ is zero; that the variance of the residuals is constant; and that $\mathbf{X}$ and $\mathbf{X}^\intercal\mathbf{X}$ are of full rank. The very common problem of OLS (and of atmospheric data) is that $\mathbf{X}^\intercal\mathbf{X}$ is (almost) singular, i.e. the determinant $\mid \mathbf{X}^\intercal\mathbf{X} \mid \simeq 0$. Then, although $\hat{\beta}$ exists, it is unstable. This problem can be overcome by switching to the dimension-reduced EOF space (i.e. considering only EOFs with eigenvalues different from zero) and employing an *optimal* weighting, so that in the detection space, $\hat{\beta}$ would be displayed as

$$\hat{\beta} = \left(\mathbf{X}^\intercal \mathbf{C}^{-1} \mathbf{X}\right)^{-1} \mathbf{X}^\intercal \mathbf{C}^{-1} \mathbf{Y}, \tag{5.13}$$

where $\mathbf{C}$ is the covariance matrix of the noise. In the EOF space, the fGCM patterns $\mathbf{X}$ are given through $\mathbf{b}^{\mathrm{fGCM}}$, the observation vector $\mathbf{Y}$ through $\mathbf{b}^{\mathrm{RO}}$, and the covariance matrix by $\mathbf{\Lambda}$. The inverse of the matrix $\mathbf{\Lambda}$ is a diagonal matrix, containing the inverse eigenvalues and can be written as

$$\left(\mathbf{\Lambda}^{\mathrm{PICTRL}}\right)^{-1}_{k\times k} = \begin{pmatrix} \frac{1}{\lambda_1^{\mathrm{PICTRL}}} & 0 & 0 & 0 \\ 0 & \frac{1}{\lambda_2^{\mathrm{PICTRL}}} & \cdots & 0 \\ \vdots & \vdots & \ddots & 0 \\ 0 & 0 & 0 & \frac{1}{\lambda_k^{\mathrm{PICTRL}}} \end{pmatrix}$$

The *scaling factors* in the EOF-space, $\hat{a}_i$, are estimated for the RO trend pattern and—to assess the uncertainty of the scaling factors as described in the next step—for each trend pattern of the CONTROL data set. The latter is the second half and independent sample of the whole PICTRL data set:

$$\hat{\mathbf{a}}_k^{\mathrm{RO}} = \left[\left(\mathbf{b}^{\mathrm{fGCM}}\right)^\intercal_{1\times k} \mathbf{\Lambda}^{-1}_{k\times k} \mathbf{b}^{\mathrm{fGCM}}_{k\times 1}\right]^{-1} \left(\mathbf{b}^{\mathrm{fGCM}}\right)^\intercal_{1\times k} \mathbf{\Lambda}^{-1}_{k\times k} \mathbf{b}^{\mathrm{RO}}_{k\times 1} \tag{5.14}$$

$$\hat{\mathbf{a}}_{i_k}^{\mathrm{CONTROL}} = \left[\left(\mathbf{b}^{\mathrm{fGCM}}\right)^\intercal_{1\times k} \mathbf{\Lambda}^{-1}_{k\times k} \mathbf{b}^{\mathrm{fGCM}}_{k\times 1}\right]^{-1} \left(\mathbf{b}^{\mathrm{fGCM}}\right)^\intercal_{1\times k} \mathbf{\Lambda}^{-1}_{k\times k} \mathbf{b}^{\mathrm{CONTROL}}_{i_{k\times 1}} \tag{5.15}$$

The fingerprint is defined as the whole right-hand side term of equation (5.14) and equation (5.15), without the last vector of RO or CONTROL patterns. The *optimal* weighting with the inverse of the eigenvalues in $\mathbf{\Lambda}^{-1}$ equates to rotating the fingerprint away from directions of high noise (i.e. high eigenvalues). Thus, a statistically optimal fingerprint is achieved, which maximizes the SNR (Hegerl et al. 1996).

To check the correctness of the computer code, a test comparing non-optimized scaling factors from the EOF-space, a_k^{EOF}, to the one from the detection space, a^{DETECT}, was performed. If the code is correctly implemented, the non-optimized scaling factors as defined in equation (5.17) must convert for $k = 1, \ldots, p$ towards the detection space scaling factor as defined in equation (5.16):

$$\hat{a}^{\mathrm{DETECT}} = \frac{\left(\mathbf{Y}^{\mathrm{fGCM}}\right)^{\mathsf{T}}_{1\times p}\ \mathbf{Y}^{\mathrm{RO}}_{p\times 1}}{(\mathbf{Y}^{\mathrm{fGCM}})^{\mathsf{T}}_{1\times p}\ \mathbf{Y}^{\mathrm{fGCM}}_{p\times 1}} \tag{5.16}$$

$$\hat{a}_k^{\mathrm{EOF}} = \frac{\left(\mathbf{b}^{\mathrm{fGCM}}\right)^{\mathsf{T}}_{1\times k}\ \mathbf{b}^{\mathrm{RO}}_{k\times 1}}{(\mathbf{b}^{\mathrm{fGCM}})^{\mathsf{T}}_{1\times k}\ \mathbf{b}^{\mathrm{fGCM}}_{k\times 1}},\ \text{with } k = 1, \ldots, p. \tag{5.17}$$

Step 4—Assessing the Uncertainty of the Scaling Factors via a Statistical Test

The scaling factors of the CONTROL data set ($\hat{\mathbf{a}}^{\mathrm{CONTROL}}$) are used to estimate the uncertainty of the RO scaling factors ($\hat{a}_k^{\mathrm{RO}}$) employing a statistical test. As these uncertainty estimates are gained from an independent sample of PICTRL data, the CONTROL record, biases are avoided. The null hypothesis that the scaling factors of the observations are zero ($H_0 : \hat{a}_k^{\mathrm{RO}} = 0$, i.e. the observed signal is only due to natural variability), is tested by means of the distribution of the control scaling factors.

The N CONTROL scaling factors are derived by vector multiplication, which is nothing else but a summation. Following the Central Limit Theorem, they can therefore be assumed as Gaussian. For each number k of retained EOFs, the standard deviation σ_k of the set of N CONTROL scaling factors can be estimated. Since a positive scaling factor is expected, a one-tailed Student's t-test is performed (climate change is caused by an increase of Green House Gas(es) (**GHG**)). For a certain number of retained EOFs, the null hypothesis can then be rejected with a risk of 10 %, if $\hat{a}_k^{\mathrm{RO}} > 1.28\sigma$ and with a risk of 5 %, if $\hat{a}_k^{\mathrm{RO}} > 1.64\sigma$. Rejecting the null hypothesis implies only that the observed climate change signal deviates significantly from the natural variability as estimated with the CONTROL data set. In contrast, if the null hypothesis cannot be rejected, a statistically significant climate change signal could not be detected in the observational data set at the chosen risk level.

Step 5—Residual Consistency Check

As it becomes clear, optimal fingerprinting relies strongly on the GCMs and their representations of internal variability at the chosen space-time domain. To assess whether the climate variability of the PICTRL simulations adequately represent the variability of the observations in the truncated space, a residual consistency test following Allen and Tett (1999) was performed. Therefore, the residuals from the regression model (see equation (5.18) for the residual definition in the detection space) are used to assess the agreement between model and observation based variability.

$$\epsilon^{\mathrm{PICTRL}} \quad = \quad \mathbf{Y}^{\mathrm{RO}} - \mathbf{X}^{\mathrm{fGCM}}\,\beta \tag{5.18}$$

The aim is to have no explicit reason to distrust the uncertainty estimates in the analysis. This is the case if the H_0 : the regression residuals (r) behave like mutually independent normally distributed random noise (Allen and Tett 1999), cannot be rejected. The regression residuals can be presented in the EOF space as

$$r_k^2 = \sum_{i=1}^{k} \left[\left(b_i^{\mathrm{RO}} - \hat{a}_i^{\mathrm{RO}}\; b_i^{\mathrm{fGCM}} \right)^2 \;\; \lambda_i^{-1} \right] \sim \chi^2_{k-1}, \tag{5.19}$$

where k is the number of retained EOFs. As long as the residuals stay for changing k within the respective χ^2-limits, which are commonly chosen for a 5 % to 95 % probability range, there is no cause for concern. Exceeding of the limits in either direction indicates too high or too low model variance compared to the observations for the respective number of retained EOFs. As the GCMs generally cannot resolve the variability at smaller spatial scales, there will always be a break at a certain number of k, which can be used to determine the maximum number of EOFs that can be used for an interpretation.

5.1.3 Methods to Assess the Influence of Atmospheric Patterns

To analyze atmospheric patterns in the observational data record, the share of the patterns in the total variance was estimated via general multiple linear regression (**MLR**). The significance of differences of atmospheric modes (e.g., differences between average El Niño and average La Niña conditions) was assessed via a Mann-Whitney U-test. The methods are shortly presented in the following.

Multiple Linear Regression

The UTLS variability is mainly influenced by two atmospheric patterns, the QBO and ENSO. Originating in the tropics, they also impact higher latitudes' conditions. To

estimate the share of the patterns in UTLS variability a MLR model was employed, which formulates for each grid point the time series $\mathbf{y}$ as

$$\mathbf{y} = a_0 + a_1\mathbf{t} + a_2\mathbf{QBO} + a_3\mathbf{ENSO} + \mathbf{e}. \tag{5.20}$$

The regression coefficients are the constant term a_0, the trend coefficient a_1, the QBO coefficient a_2, the ENSO coefficient a_3. $\mathbf{e}$ denotes the residual error term. For the QBO, the monthly mean 50 hPa zonal wind index[2] of the Climate Prediction Center (**CPC**)/ National Oceanic and Atmospheric Administration (**NOAA**) was employed. For ENSO, the seasonally smoothed monthly N3.4 index[3] was used, which is available from the Physical Sciences Division of the NOAA. For the latter, a four months atmospheric lag was identified and considered, which is consistent with Seidel et al. (2004). The coefficients of determination were used for an estimate of the model explained variability due to the individual patterns. The IPCC AR4 models do not manage to reproduce the QBO. This can be seen, e.g., in the central plot of Figure 5.1, which shows tropical (10°N to 10°S) temperature time series of RO data (left) and the fGCMs (right). While three QBO periods are clearly visible in the RO record (best above 100 hPa), the signal is lacking in the fGCMs, as it does for individual GCMs, not shown. Thus, the QBO signal was removed from the RO data for the detection study, applying equation (5.20) without the ENSO term.

Furthermore, the significance of the MLR coefficients was tested. The MLR model can be written in matrix notation as

$$\mathbf{y}_{N\times 1} = \mathbf{X}_{N\times l}\,\mathbf{a}_{l\times 1} + \mathbf{e}_{N\times 1}, \tag{5.21}$$

where the columns $\mathbf{X}$ contain the l influencing variables (i.e. time series of trend, QBO, and ENSO indices) and $\mathbf{a}$ the respective coefficients, which are of interest. Using an OLS approach, the coefficients can be estimated as

$$\hat{\mathbf{a}} = (\mathbf{X}^\intercal\mathbf{X})^{-1}\,\mathbf{X}^\intercal\mathbf{y}, \tag{5.22}$$

as already addressed in equation (5.12). In MLR, the estimate for the data is $\hat{\mathbf{y}} = \mathbf{X}\hat{\mathbf{a}}$, the estimate for the residual vector is given by $\hat{\mathbf{e}} = \mathbf{y} - \hat{\mathbf{y}}$. The sum of squares of errors (**SSE**) can then be written as $\mathrm{SSE} = \hat{\mathbf{e}}^\intercal\hat{\mathbf{e}}$. The variance of the residuals,

$$\mathrm{s}_e^2 = \frac{\hat{\mathbf{e}}^\intercal\hat{\mathbf{e}}}{N - l - 1}, \tag{5.23}$$

[2] available via `www.cpc.ncep.noaa.gov/data/indices/qbo.u50.index` (November 2009); The index values are based on the NCEP/NCAR re-analysis data and are the zonally averaged winds at 50 hPa taken from over the equator.

[3] available via `www.esrl.noaa.gov/psd/forecasts/sstlim/global/indices_global` (November 2009)

leads to the standard error for the estimated coefficients,

$$\mathrm{s}_{\hat{a}_i} = \sqrt{\mathrm{s}_e^2 \left\{ (\mathbf{X}^\intercal \mathbf{X})^{-1} \right\}_{ii}}, \text{ with } i = 1, \ldots, l, \tag{5.24}$$

where $\{(\mathbf{X}^\intercal \mathbf{X})^{-1}\}_{ii}$ denotes the matrix element of the ith column and row. As the regression coefficients are assumed to be Gaussian, a Student's t-test can be employed to estimate their significance. The null hypothesis for each of the $i = 1, \ldots, l$ parameters is $H_0 : a_i = 0$. The goal is of course to reject the H_0, which means that the tested parameter contributes significantly to the MLR model. The significance is determined by comparing the estimated $\hat{t}$ and tabulated t-values and H_0 is rejected, if $\mid \hat{t} \mid > t$:

$$\mid \hat{t}_{a_i} \mid = \mid \frac{\hat{a}_i}{\mathrm{s}_e(\hat{a}_i)} \mid \sim t(N - l - 1, 1 - \alpha/2), \text{ with } i = 1, \ldots, l. \tag{5.25}$$

Mann-Whitney U-Test

To further investigate ENSO and QBO patterns in the UTLS, ERA-40 and RO data were used to gain mean conditions for each mode of the patterns. The different modes were determined via the index values. A *Mann-Whitney U-test*, also known as *Wilcoxon rank-sum test*, was performed to assess the differences in the modes for ERA-40 data. The assessment based on the RO record was not feasible, because the short record covers not enough periods of modes.

The Mann-Whitney U-test is a non-parametric alternative to the Student's t-test and tests whether two independent samples belong to the same distribution.

The two independent samples—sample A containing m values and sample B containing n values—are merged into one combined sample. The combined values are rearranged according to their magnitude from the lowest to highest. According to their arrangement, each value is assigned the respective rank $(1, 2, \ldots m + n)$. Then for each of the original samples A and B, a so-called rank sum (R_A, R_B) is calculated. This is done by adding up the ranks of the values belonging to sample A resulting in R_A and summing up the ranks of the values belonging to sample B resulting in R_B.

The rank sums are needed to calculate the test statistics U for each sample (i.e. U_A, U_B).

$$U_A = m \cdot n + \frac{m \cdot (m+1)}{2} - R_A \tag{5.26}$$

$$U_B = m \cdot n + \frac{n \cdot (n+1)}{2} - R_B \tag{5.27}$$

The test can be one- or two-tailed. The one-tailed test checks whether $A > B$ and $A < B$, respectively. In the two-tailed test, the null-hypothesis $H_0 : A = B$, i.e. there are no differences between the distributions, is tested. In this study the two-tailed

$m = n$	$\alpha = 10\,\%$	$\alpha = 5\,\%$
4	1	0
8	15	13

Table 5.2: Tabulated U-statistics for two defined risk levels and the number of $m = n$ ENSO and QBO modes available in ERA-40 within 1980 to 2001.

test was implemented. Therefore, the minimum of the calculated test statistics U, $\min(U_A, U_B)$, is compared to a tabulated U-value.

To calculate the relevant values of the Mann-Whitney U-test, the Interactive Data Language (**IDL**) function *RS_test* was employed. For comparing the empirical and theoretical test statistics, IDL requires a minimum sample size of 10 values per sample (i.e. 10 different average atmospheric modes), which was not available from the used data. But the function does calculate the rank sums also for smaller samples correctly. Knowing the rank sums (R_A, R_B), the test statistics can be easily determined with the equations (5.26) and (5.27). The respective tabulated U-values were taken from Milton (1964).

The ERA-40 1980 to 2001 record, which was de-trended and from which the annual cycle was removed, enabled the calculation of 4 average El Niño and 4 average La Niña conditions, as well as of 8 average QBO conditions of each phase. The respective tabulated U-values are given for a 10 % risk and a 5 % risk in Table 5.2.

Thus, calculated $\min(U_A, U_B)$-values ≤ 1 signify a 90 % significant difference between two modes based on 4 averages each. Values ≤ 0 stand for a 95 % significant difference, when $m = n = 4$. This is based on the null hypothesis H_0 : the samples are from the same distribution.

5.2 Results of Detection Study

In this section the results of the detection study are presented. This includes a detailed analysis of trend patterns for the RO periods as well as an examination of large-scale patterns, such as the ENSO and the QBO, and associated atmospheric conditions, which may have an influence on the trend patterns. Variability patterns and amplitudes from different data sets are compared and discussed, as a realistic representation of GCM variability is an important requirement for optimal detection. The ability of PICTRL EOFs to reconstruct trend patterns of other than PICTRL data sets is addressed at the end of this section.

5.2.1 Atmospheric Patterns Influencing the Analysis Period

Before moving on to the trend patterns of the RO parameters, which are the basis of the detection study, the influence of large-scale atmospheric patterns on atmospheric conditions during the investigation period are addressed. Therefore, it is also necessary to look farther back in time, as the RO period is short and thus may give altered results for atmospheric patterns with longer recurrence periods.

For the UTLS between 50°N and 50°S, two atmospheric modes are particularly important, the ENSO and the QBO. Both patterns have their origins in the tropics, but they do also influence the atmospheric conditions at higher latitudes.

As mentioned in section 5.1.3, the N3.4 index (e.g., Trenberth and Stepaniak 2001) is used to assess ENSO. This atmospheric–oceanic pattern is characterized by changes in sea surface temperature of the tropical pacific, which are accompanied by variations in the tropical atmospheric circulation. Warm phase conditions, called El Niño, feature weakened and sometimes even reversed trade winds and warmer surface water than usual in the eastern tropical Pacific off the South American coast. The tropical rainstorms, which are coupled with high sea surface temperatures, also shift eastwards. Opposite conditions, i.e. the cold phase called La Niña, show a large-scale strengthening of the trade winds and a cooling of the water in the eastern and central tropical Pacific due to upwelling of cool water from beneath. The N3.4 index is based on sea surface temperatures of the so-called Niño 3.4 region, which stretches from 5°N to 5°S, and from 120°W to 170°W. Changes in sea surface temperature in this region show the strongest effect on shifting rainfalls driven by heating in the western Pacific, which influences also the global atmospheric circulation. According to the definition of Trenberth (1997), El Niño and La Niña conditions are given for $\mathrm{N3.4} > |\pm 0.4|$, which is marked by the color in Figure 5.5.

To assess the QBO conditions, the 50 hPa zonal wind index is employed. The QBO (for details see, e.g., Baldwin et al. 2001) is the dominating stratospheric (above ≈ 100 hPa) variability pattern in the tropics. It appears as changes in zonal mean easterly and westerly wind regimes, which show a downward propagation and vary with a period of ≈ 28 months. A positive QBO index (QBO+) refers to a phase governed by westerly winds and positive temperature anomalies around 50 hPa. The easterly phase, coupled with negative temperature anomalies, shows an approximate twice as large amplitude and is hereinafter referred to as QBO−.

Figure 5.4 depicts the evolution of the two indices in the RO analysis period. The QBO index shows a rather steady progress of the oscillation, covering almost exactly three periods between fall 2001 and winter 2008. The two months of the GPS/MET measurement period in 1995 and 1997 were each influenced by a different QBO phase of medium amplitude. For the N3.4 index, which is based on sea surface temperatures, a 4-month atmospheric lag was considered (see section 5.1.3), which corresponds to the average inertia of the atmospheric reaction to oceanic changes. The lag was determined

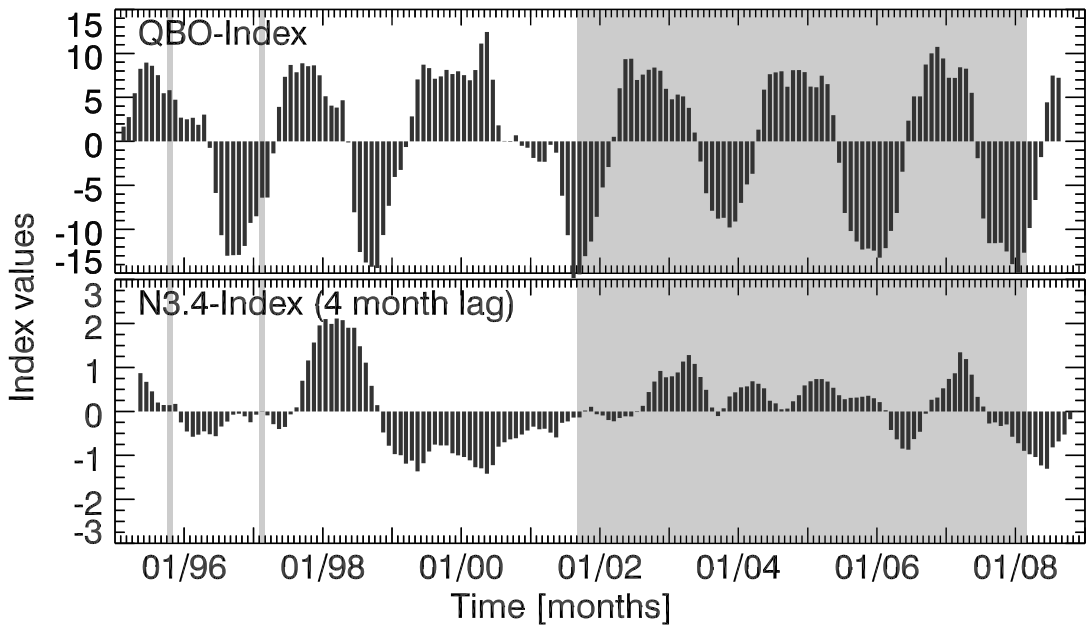

Figure 5.4: *top* Evolution of the QBO index from 1995 to 2008. The gray shaded area marks the periods of RO measurements that are used in the detection study. *bottom* The same for the N3.4 index, for which a 4-month atmospheric lag was considered.

by analyzing N3.4 MLR correlation coefficients for different lags. ENSO exhibited only weak to moderate events during the RO period and, most importantly, the first two measurement months fall in a period with almost no ENSO signal. During the fall 2001 to winter 2007 period, weak to moderate El Niño conditions prevailed, while end of 2007 a La Niña event developed.

The ENSO and QBO Signal in the Free Atmosphere

Because of the lack of pronounced El Niño and La Niña events within the analysis period, ERA-40 data were used in addition to investigate the patterns influence in the UTLS. Again, only the satellite era from 1980 to 2001 was considered. Figure 5.5 depicts, similar to Figure 5.4, the evolution of the QBO and the ENSO index for this period. The evolution of the QBO is very steady, while ENSO events occur rather randomly.

Based on the index time series, 4 El Niño, 4 La Niña, and 4 neutral ENSO periods during 1980 to 2001 were selected to calculate mean atmospheric states for each condition. As El Niño/La Niña events predominantly take shape in northern-hemispheric

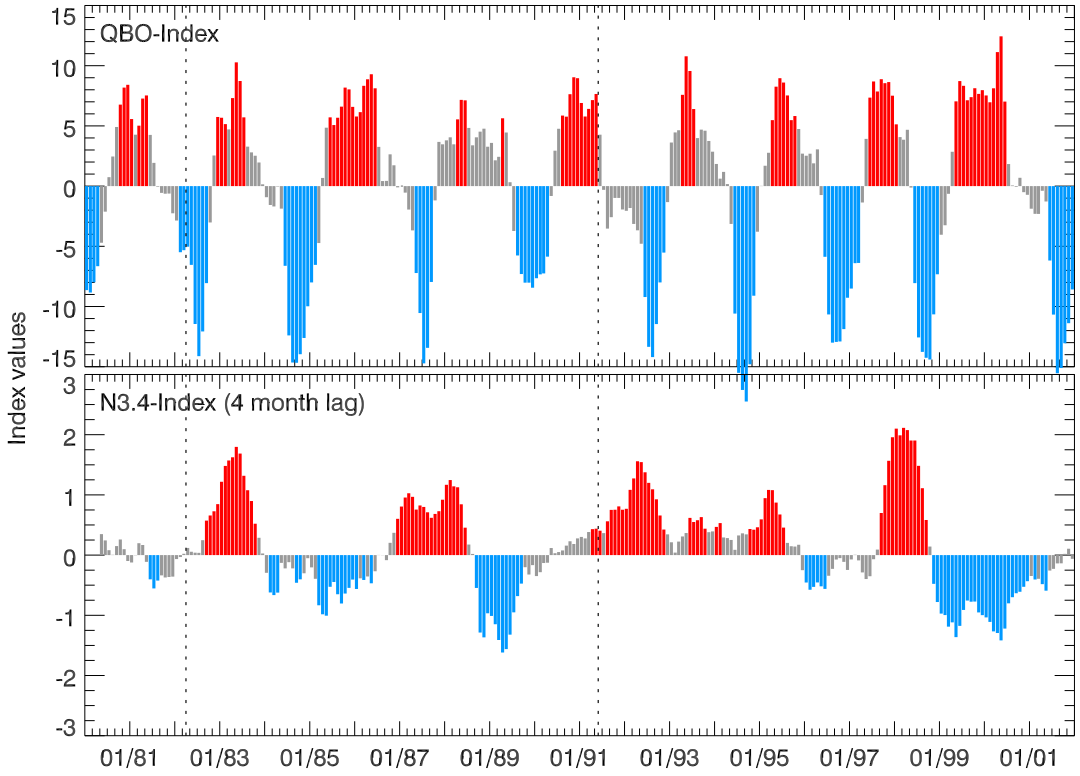

Figure 5.5: *top* Evolution of the QBO index from 1980 to 2001. Index values greater than | ±5 | are colored. *bottom* The same for the N3.4 index, for which a 4-month atmospheric lag was considered. Index values greater than | ±0.4 | are colored. The two dotted vertical lines mark the volcanic eruptions of El Chichón and Pinatubo.

winter, each mean state was calculated by averaging monthly means from August to ensuing July.

The following years were used for the calculations:

- The mean **El Niño** patterns were calculated from the 1986/87, 1987/88, 1994/95, and 1997/98 events, including very pronounced events which were not present in the RO period. The 1982/83 and 1991/92 El Niño events, which coincided with volcanic eruptions (El Chichón in 1982 and Pinatubo in 1991) were disregarded.
- The mean **La Niña** patterns were derived from the 1984/85, 1988/89, 1998/99, and 1999/2000 events.
- The **neutral** patterns are based on the years 1980/81, 1981/82, 1989/90, and 1992/93.

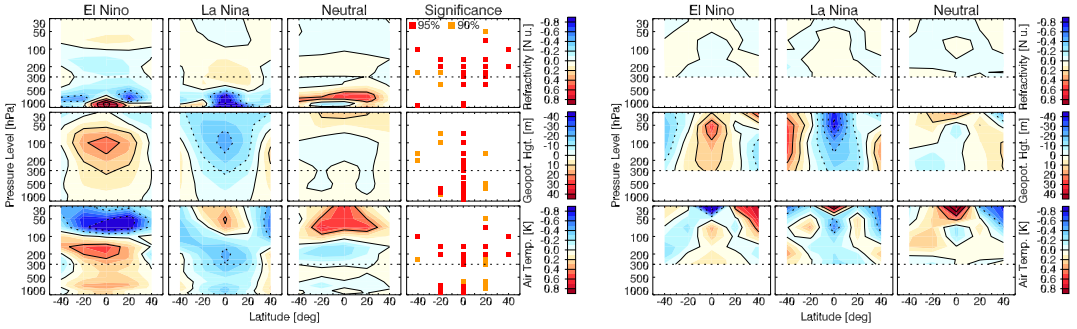

(a) ERA-40 based average ENSO patterns

(b) RO based average ENSO patterns

Figure 5.6: *(a)* Average El Niño/La Niña/neutral patterns for the parameters refractivity (top), geopotential height (middle), and temperature (bottom) based on the ERA-40 record. The last column shows grid points with significant differences between average El Niño and La Niña conditions, based on a Mann-Whitney U-test. *(b)* Same illustration for RO data, but without significant differences plot.

Consistent to ERA-40, the RO patterns are achieved from averaging August to ensuing July values. For El Niño, the years 2002/03, 2004/05, and 2006/07 are used, for La Niña the years 2005/06 and 2007/08, and for the neutral phase the years 2001/02 and 2003/04. Comparing the periods to the N3.4 time-series depicted in Figure 5.4, it is obvious that the atmospheric conditions within this period do not differ as much as in the ERA-40 period depicted in Figure 5.5. Testing for significant differences of the mean RO patterns was impossible due to insufficient events.

Figure 5.6 illustrates zonal mean average El Niño, La Niña, and neutral conditions based on ERA-40 data between 1980 and 2001 (a) and on RO data (b).

For refractivity and temperature, strongest and spatially most confined UTLS ENSO characteristics are found in the tropics and sub-tropics between 300 hPa and 100 hPa. El Niño exhibits positive temperature anomalies up to around 100 hPa (with a maximum at ≈ 150 hPa) and negative anomalies above. Significant differences between the two phases (assessed via the U-test), as shown in the right column plots of Figure 5.6a, are likewise agglomerated in the tropical/sub-tropical upper troposphere (**UT**) below the 100 hPa levels, where 10 out of 12 grid points, i.e. 83 %, respond to the test (only values from 300 hPa and above are considered). The remaining grid points show only in 21 % a significant difference between average El Niño and La Niña conditions. A similar picture is given for refractivity, with 11 out of 12 tropical/sub-tropical grid points below 100 hPa, which refer to significant differences.

For geopotential height, the strongest ENSO pattern signal emerges around 100 hPa and turns out as positive anomalies from surface to 30 hPa within 30°N and 30°S.

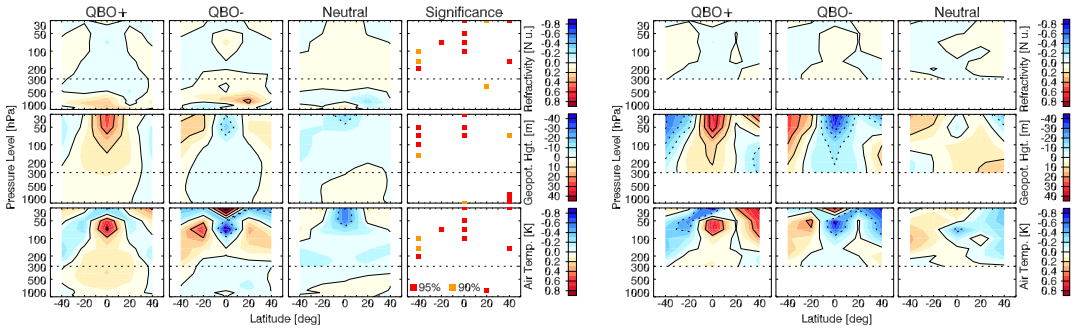

(a) ERA-40 based average QBO patterns

(b) RO based average QBO patterns

Figure 5.7: *(a)* Average QBO+/QBO−/neutral patterns for the parameters refractivity (top), geopotential height (middle), and temperature (bottom) based on the ERA-40 record. The last column shows grid points with significant differences between QBO+ and QBO− conditions, based on a Mann-Whitney U-test. *(b)* Same illustration for RO data, but without the significant differences plot.

Thus, significant differences appear also at higher levels than for refractivity and temperature and also extend downwards in the tropical troposphere. Yet the significant differences are more restricted to the tropical bin (±10°N/S), where all grid points show distinct patterns with at least 95 % significance. Outside the tropical band, nearly no significance is achieved.

Since the GCMs simulate ENSO events with different amplitudes and phases, the signal was not removed from the data. As for the fGCM, the ENSO signal is strongly reduced by averaging over the 20 simulations (see, e.g., Figure 5.1, right). For the PICTRL, possibly higher ENSO amplitudes compared to the observations without any major ENSO event, might lead to a broader distribution of sample trends and thus make a detection more difficult.

The RO patterns (Figure 5.6b) are based on few and not very distinct events and should thus be considered with care. Generally similar to the ERA-40 patterns. They feature smaller amplitudes and are more confined to the tropics, so that the change in sign of the anomalies occurs around 20°N and 20°S.

The zonal mean average ERA-40 and RO based QBO signals are depicted in Figure 5.7. The mean QBO conditions in the ERA-40 period are based on 8 events for each mode. The following periods were used:

- **QBO+:** 09/1980 to 06/1981, 12/1982 to 07/1983, 05/1985 to 06/1986, 07/1990 to 06/1991, 02/1993 to 10/1993, 04/1995 to 11/1995, 06/1997 to 04/1998, 05/1999 to 06/2000; the 1988/1989 QBO+ phase was not considered, as only three months exceeded the threshold value of 5.

- **QBO+:** 02/1982 to 09/1982, 06/1984 to 03/1985, 05/1987 to 09/1987, 08/1989 to 04/1990, 05/1992 to 11/1992, 06/1994 to 11/1994, 06/1996 to 03/1997, 06/1998 to 01/1999;
- **neutral phase:** 07/1981 to 01/1982, 08/1983 to 05/1984, 07/1986 to 04/1987, 10/1987 to 03/1988, 07/1991 to 04/1992, 11/1993 to 05/1994, 12/1996 to 05/1997, 07/2000 to 05/2001.

For the RO period, the mean QBO+ conditions were determined by averaging all months with index values greater than 5, the mean QBO− conditions are based on months with index values less than −5, and for neutral conditions index values between ±5 were employed.

Figure 5.7 shows the well-defined stratospheric signature of the pattern, particularly for geopotential height and temperature. Compared to the ENSO pattern, the most distinct QBO signature is stronger limited to the tropical region. The significance test (right column in Figure 5.7a) was again based on ERA-40 data only. Significant differences between the positive and negative QBO phase are restricted to the tropics above 100 hPa and pole-wards of 30° latitude to around 200 hPa and 100 hPa. The subtropical bands between 10° and 30° on each hemisphere exhibit hardly any significant differences in the mean patterns. In total, around 20 % to 30 % of all UTLS grid points show significant differences. Considering only grid points at and above the 100 hPa level (which if often referred to as lower limit of the QBO pattern), at least 35 % of the grid points respond positively in the U-test (100 % in the tropical band).

The RO patterns (Figure 5.7b) feature stronger amplitudes of the QBO phases and a more pronounced contrast between the low- and mid-latitudes. They agree much better with the ERA-40 results than it is the case for mean ENSO signals. Indeed, the difference between RO average ENSO and QBO modes is rather small, which is caused by the weak ENSO conditions during the RO analysis period and by the fact that La Niña periods coincide with QBO− phases and El Niño periods with QBO+ phases. As the QBO is not included in GCMs, it was removed from the RO record via MLR as described in section 5.1.3, in order to not compare apples and oranges in the detection study.

Explained Variance of QBO and ENSO

Before discussing the share of QBO and ENSO explained variance in the data set, the significance of the MLR coefficients is addressed. Figure 5.8 shows the significances for the MLR trend, ENSO, and QBO coefficients (see section 5.1.3 for the theory) at each grid point for the ERA-40 (left) and RO (right) data. A first glance reveals higher significances for ERA-40 coefficients than for RO coefficients. A significant MLR coefficient means that the respective parameter (i.e. trend, ENSO, QBO) makes a statistical significant contribution to the MLR estimate for the observations at the grid point. For the longer ERA-40 period, trend and ENSO coefficients feature about the same sig-

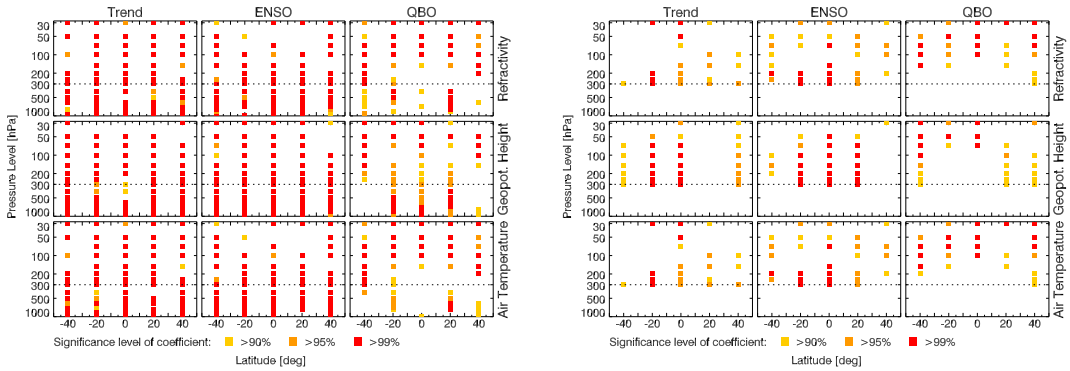

(a) Significance of ERA-40 based MLR coefficients

(b) Significance of RO based MLR coefficients

Figure 5.8: *(a)* Significances of MLR trend (left), ENSO (middle), and QBO (right) coefficients at each grid point for the parameters refractivity, geopotential height, and temperature (from top to bottom) based on the 1980 to 2001 ERA-40 time series. *(b)* Same illustration based on the RO record of the 1995 to 2008 period.

nificances (ENSO mostly below ≈ 50 hPa for refractivity and temperature), while the QBO coefficient is slightly less significant and rather concentrated above 200 hPa.

For the RO record the three parameters explain less of the total variance in the MLR model than it is the case for the ERA-40 record (see also Figure 5.10). In exchange, the RO record gives a more distinct picture with regard to the height ranges. The highest significance of ENSO coefficients (Figure 5.8b, middle) is grouped around 300 hPa to 200 hPa in the tropics and sub-tropics (and also higher for geopotential height). Highly significant QBO coefficients are almost exclusively given at and above 100 hPa. Only the mid-latitude grid points exhibit significances around the 90 % probability level down to 300 hPa. The plot of RO MLR coefficient significances also shows that the two patterns contribute considerably (each at least as much as the trend pattern) to the explanation of the variability in the observational record.

The proportion of QBO or ENSO variability on the total variability of the ERA-40 and the RO data is illustrated in Figure 5.9. It was assessed with the linear correlation coefficients R^2 in the multi-linear regression model. The result is consistent with the mean ENSO and QBO patterns, showing for the RO record the greatest QBO explained variability in the tropical stratosphere ($\approx$ 30 % QBO explained variability). ENSO governs the tropical UT and the LS above 50 hPa for refractivity and temperature, and the tropical UTLS between 300 hPa and 50 hPa for geopotential height ($\approx$ 20 % ENSO explained variability). QBO and ENSO both impact the stratospheric refractivity and temperature variability at northern mid-latitudes ($\approx$ 10 % to 20 % explained variability). For ERA-40, the share on the total variability is much stronger and more extended

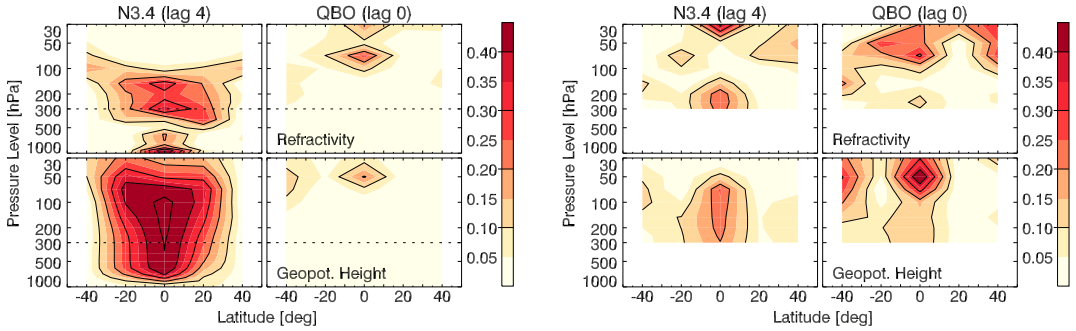

(a) ERA-40 based partial R^2 (b) RO based partial R^2

Figure 5.9: *(a)* Linear coefficients of determination (R^2) for ENSO (left) and QBO (right) explained variances in refractivity (top) and geopotential height (bottom) time series in the MLR model set up for ERA-40 data. *(b)* Same illustration based on RO data.

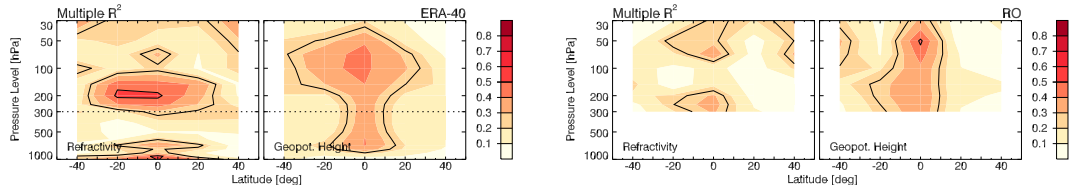

(a) ERA-40 based multiple R^2 (b) RO based multiple R^2

Figure 5.10: *(a)* Explained total variance (multiple R^2) of the MLR model for refractivity (left) and geopotential height (right) based on ERA-40 data. *(b)* Same illustration based on the RO record.

for ENSO and a less for the QBO. The total explained variability in the MLR model, i.e. the variability explained by trend, ENSO, and QBO, is represented by the multiple linear correlation coefficient and shown in Figure 5.10. The figure depicts refractivity and geopotential height results for ERA-40 based and RO based regression. Temperature results are almost identical to refractivity and thus not shown. Overall, the RO record contains more unexplained variability than ERA-40, mainly with regard to refractivity. The MLR model provides best results for lower latitudes, where it explains about 30 % to 40 % of the variability in the RO record, while lower values of about 10 % to 20 % dominate at higher latitudes. For the longer ERA-40 record about the same results are gained for geopotential height. For refractivity and temperature, the MLR model explains with up to 60 % of the variance in the tropical and sub-tropical tropopause regions considerably more than it does for the RO record.

What About the Solar Influence?

The magnitude of atmospheric temperature changes due to solar variations is still under discussion. Outside the scientific community, the sun is often used as a welcome culprit for climate change. A recent study from Benestad and Schmidt (2009) estimated the contribution of solar forcing to global warming as only around 7 % for the 20th century. Lockwood and Fröhlich (2007) assessed that over the about last 20 years solar trends are likely to have been in opposite direction in regard to expected global temperature changes. The solar signal in the RO record comes in via residual ionospheric errors. Gobiet and Kirchengast (2004) or Rocken et al. (2009) estimated a temperature bias of 0.1 K to 0.2 K at 20 km to 25 km height for solar maximum versus solar minimum conditions. This bias should become negligible, if more than 10-years are used in a trend study, so that about a total solar cycle is covered.

A simple MLR model for the RO data, only based on trend and solar flux as explanatory variables, shows that the solar variations during the RO analysis period would rather act contrary to the expected climate change signal. Figure 5.11b shows in the bottom plot the monthly evolution of the 10.7 cm wavelength solar flux with the solar flux unit (**sfu**), i.e. $10^{-22}\mathrm{Wm}^{-2}\mathrm{Hz}^{-1}$. The F10.7 cm variations during the last solar cycle (cycle 23, which started in May 1996 and ended in early 2008) were relatively weak, ranging between ≈ 80 sfu and ≈ 230 sfu. GPS/MET measurements took place around the beginning of the last solar cycle, when solar variability was at a minimum. The beginning of CHAMP measurements coincided with the maximum of the cycle and lasted until the ensuing minimum. Thus, the solar signal during the CHAMP only period will counteract a climate change signal caused by increasing GHG. This is also visible in the upper plots of Figure 5.11b, depicting the MLR share of the solar signal. In contrast, the MLR linear trend share is given in Figure 5.11a. As only trend and solar flux are used for the MLR model, the absolute values of the plotted patterns are not meaningful. The solar effect on the trends is probably slightly adjusted by the low solar activity during the first two months of GPS/MET measurements.

5.2.2 RO Trend Patterns

The RO and fGCM refractivity, geopotential height, and temperature trend patterns for the GPS/MET–CHAMP and CHAMP only period are presented in Figure 5.12. The fGCM ensemble is plotted in the right columns of each panel of the figure. It shows for temperature across the latitudes a rather smooth tropospheric warming (up to around 70 hPa for GPS/MET–CHAMP and 50 hPa for CHAMP only) and a stratospheric cooling above. Refractivity features a reversed trend pattern and the geopotential height field exhibits a general increase, following the thermal expansion of the troposphere. The RO record, in contrast, presents more distinct patterns, which are stronger affected by atmospheric variability. The trend patterns do not depend very much on taking

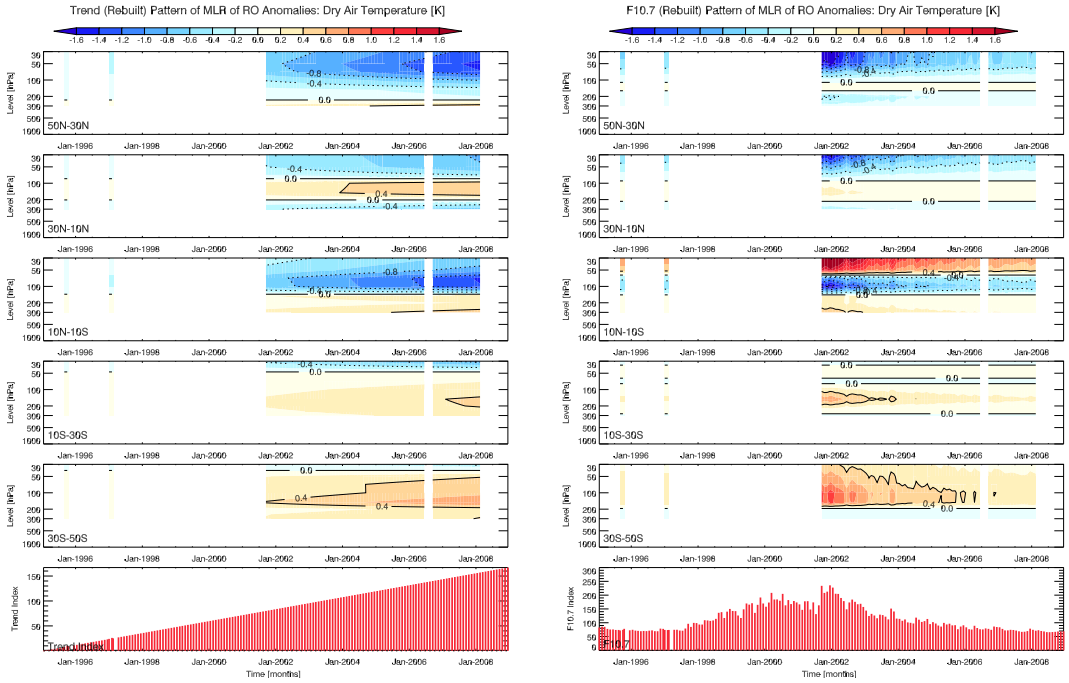

(a) MLR trend pattern (b) MLR solar pattern

Figure 5.11: *(a)* The trend signal time series during RO study period for 5 zonal band determined by a simple MLR model, based only on trend and solar flux as explanatory variables. The bottom plot depicts the trend variable used in the model. *(b)* The same illustration for the solar signal, based on the solar 10.7 cm wavelength flux. The time series of the solar flux, given in solar flux units ($10^{-22}\mathrm{Wm}^{-2}\mathrm{Hz}^{-1}$), is depicted in the bottom plot.

the GPS/MET measurements into account, but the pattern amplitudes increase considerably when the CHAMP only period is used (compare the left side columns of each panel in Figure 5.12, which depict the RO anomalies' trends). Largest disparities occur for the temperature patterns. There, the CHAMP only period features strong positive anomalies above 50 hPa at northern mid-latitudes and around 100 hPa in the tropics and sub-tropics. Similar features of reversed sign affect the refractivity patterns. In both cases (though more pronounced in the tropics and sub-tropics), these trends are caused by rather low temperatures in 2002 and higher ones around the turn of 2006/2007. The GPS/MET months show temperatures similar to 2007 and thus no striking positive trend pattern emerges when considering the longer period. Negative UT temperature trends can be found below 200 hPa in the Northern Hemisphere (**NH**) sub-tropics of the GPS/MET–CHAMP period, the tropics and NH sub-tropics of the CH-

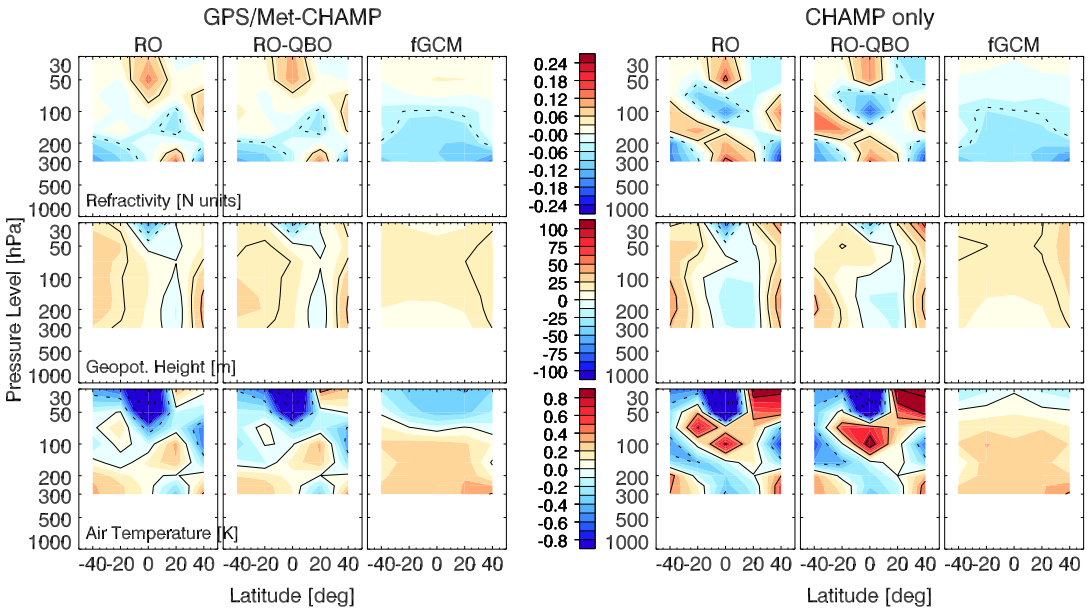

Figure 5.12: *left* 10-year trend patterns of the GPS/MET–CHAMP measurement period for refractivity (top), geopotential height (middle), and temperature (bottom). The trend patterns are depicted for RO anomalies (left), RO anomalies with the QBO removed (middle), and fGCM anomalies. *right* Same illustration for the CHAMP only period.

AMP only period. These patterns are also evident at higher levels in the geopotential height fields. They are caused by a drop in the temperature time series in the second half of 2007, which is most likely due to the emerging La Niña event (see Figure 5.4). In the GPS/MET–CHAMP period, these negative 2001 to 2008 trends are counterbalanced (apart from the NH subtropics) by moderately cool GPS/MET anomalies. As the used GCMs do not reproduce the QBO signal, it was removed from the observations for all further calculations (see section 5.1.3). The RO trend patterns without QBO signal are shown in the middle columns of each panel plot in Figure 5.12. Elimination of the QBO signal primarily influences the trend amplitudes in the LS, but hardly affects the trend patterns and also does not considerably change the pattern correlations with the fGCMs.

To verify the correctness of the RO patterns and to make a rough estimate of the influence of the lacking months between 1995 and 2001 on the trend signal, the HadAT2 radiosonde temperature trend patterns were compared to the RO patterns. Figure 5.13 depicts in the first row the RO temperature trend patterns for the two periods and in the second row the equivalent HadAT2 trend patterns. Except for minor differences

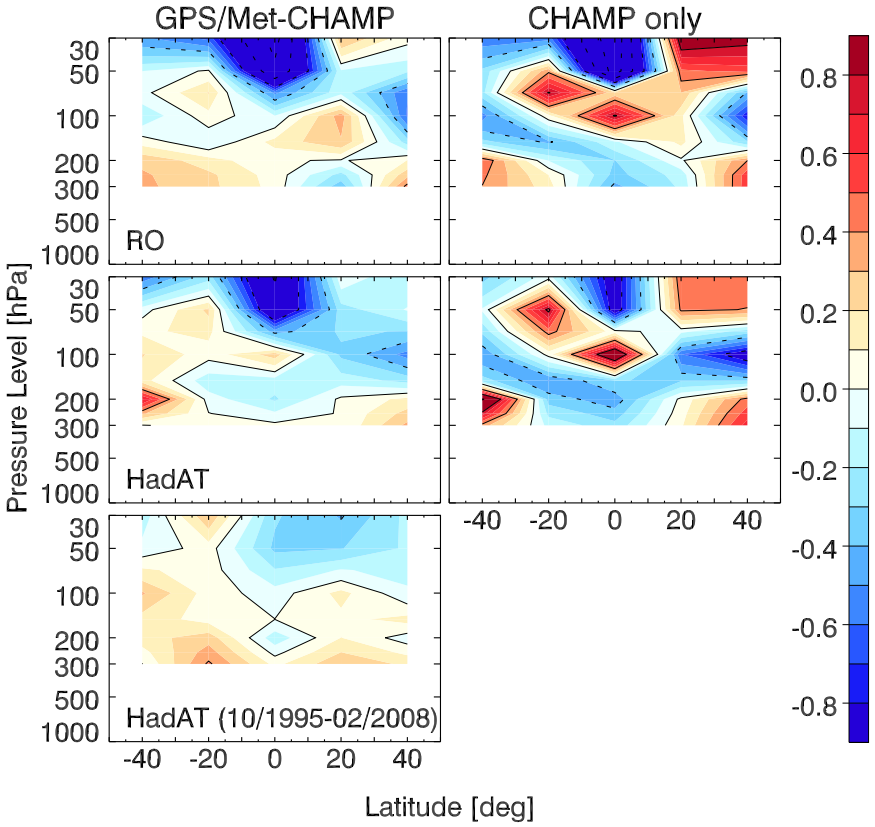

Figure 5.13: *left* 10-year temperature trend patterns for the GPS/MET–CHAMP period based on RO anomalies (top) and HadAT2 anomalies (middle and bottom). The bottom plot shows the HadAT2 pattern based on all months from 10/1995 to 02/2008. *right* 10-year temperature trend patterns for the CHAMP only period based on RO anomalies (top) and HadAT2 anomalies (middle).

below 100 hPa during the GPS/MET–CHAMP period, the RO and radiosondes patterns are very similar and also exhibit comparable amplitudes. In the last row of Figure 5.13 the HadAT2 trend pattern based on more than 13 years of continuous monthly data between 10/1995 and 02/2008 is presented. Apart from the strength of the stratospheric pattern amplitude, it is similar to the RO pattern, which lacks many months within the 1995 to 2001 period. The potential dependence of the RO GPS/MET–CHAMP trend patterns on the GPS/MET points can be considered as essential weak point regarding the pattern. But the close match of the intermittent RO pattern and the continuous HadAT2 pattern confirms the quality and robustness of the RO GPS/MET–CHAMP trend pattern and its adequacy for the detection study.

level	RO	RO-QBO	HadAT2	HadAT2 all months	fGCM
Refractivity [N-units/decade]					
50 hPa	+0.14	+0.11	N.A.	N.A.	+0.04
300 hPa	−0.03	−0.04	N.A.	N.A.	−0.09
Geopotential Height [m/decade]					
50 hPa	− 4.7	+ 8.5	N.A.	N.A.	+17.1
300 hPa	+10.5	+14.2	N.A.	N.A.	+ 9.1
Temperature [K/decade]					
50 hPa	−1.51	−1.25	−1.06	−0.18	−0.44
300 hPa	+0.07	+0.10	+0.04	+0.18	+0.28

Table 5.3: Values for 10-year tropical (10°N–10°S) refractivity, geopotential height, and temperature trends derived from the GPS/MET–CHAMP period from RO, RO record with QBO signal removed, HadAT2, and fGCM record. *HadAT2 all months* stands for trends for the continuous period 10/1995 to 02/2008.

Table 5.3 summarizes 10-year refractivity, geopotential height, and temperature trend values for the GPS/MET–CHAMP period for one stratospheric and one tropospheric level in the tropics (10°N–10°S). It shows clearly the strong LS temperature signal in the RO data compared to all other data. In contrast, for the UT, the RO temperature trend is rather small. Removing the QBO signal from the RO record slightly decreased this RO specific feature. HadAT2 trends for the equivalent period compare best with RO trends, while the ensemble mean of the GCM simulations feature an about 3.5 times smaller LS and a 4 times large UT trend for the tropics. Same relations are achieved for refractivity trends The geopotential height trends show a different behavior for RO and fGCM. While they agree very well at 300 hPa (featuring a trend of $\approx$ 10 m per decade), they show opposite trends in the LS. The higher crossing point from positive to negative trends in temperature and thus also in geopotential height (due to the thermal expansion of the troposphere) leads to very pronounced and still positive fGCM trends at 50 hPa, where the RO record already shows the LS cooling induced signal.

5.2.3 Data Variability

Optimal fingerprinting is based on matching observed and model simulated patterns and thus relies on reasonably realistic simulated variability from the climate models at the analyzed space and time scales. Figure 5.14 depicts ratios between RO and GCM

month-to-month (based on time series of monthly means) and year-to-year (based on time series of annual means) variability (standard deviation) for refractivity and geopotential height. Temperature results are not shown as they are similar to refractivity. The calculation was based on de-trended RO and fGCM data for the 2002 to 2007 period corresponding to full years of CHAMP data availability. The fGCM variability was calculated by stringing the 20 different fGCM simulations of the 6 years each (2002 to 2007) together, so that in total 120 years of fGCM data were used for the calculation. The PICTRL variability is based on all data of the 4 available simulations, which were combined into one continuous data record. For comparison of RO to single models, the respective PICTRL simulations of the 3 models were considered.

The three used climate models feature different variability characteristics. The observed and model *month-to-month variability* vary at most in a factor of 2 (Figure 5.14, left). The CCSM3 temperature and refractivity variability patterns show best agreement to the RO patterns, even though the GCM amplitudes are slightly smaller, particularly in the stratosphere. HadCM3 exhibits a less distinct variability between UT and LS but slightly higher amplitudes than CCSM3. ECHAM5 shows, most notably for refractivity and temperature, very strong UT variability (three times stronger values than the RO record) and, compared to the other models, average LS variability. For geopotential height, the tropical and subtropical ECHAM5 simulated variability is stronger than the RO variability and about two times as strong as in the other two models. All three models show for this parameter less mid-latitudinal variability than the RO record does. Thus, larger fGCM deviations in UT refractivity and temperature are mainly caused by ECHAM5, which attributes with 6 out of 20 simulations (besides CCSM3 with 12 out of 20 simulations) considerably to the mean fGCM variability. For geopotential height, the observed and fGCM or PICTRL variability agree very well over large areas except at mid-latitudes and above 50 hPa.

A different picture is given for the *year-to-year variability*, where the GCMs show nearly everywhere an up to 4 times larger variability (Figure 5.14, right). Only in the tropical LS RO variability prevails. This GCM dominated variability behavior is most probably caused by the fact that only 6 years of RO data were used to determine the year-to-year variability (compared to the 72 months for the month-to-month variability), which seem to be too short to get a reasonable estimate.

At large, the ensembles of the three models do cover a representative range of observed variability. They fulfill the requirements for optimal fingerprinting, since all calculations are based on a monthly basis.

Similar results are gained when the 2002 to 2007 RO variability is compared to the 1980 to 2001 ERA-40 results, as shown in Figure 5.15. While month-to-month comparisons are pretty good for all parameters (temperature is again not shown as it is virtually identical to refractivity), the ratios of variability in annual mean data reach again a difference of a factor up to four.

Removing the QBO from the RO data, has only a minor influence on the variability

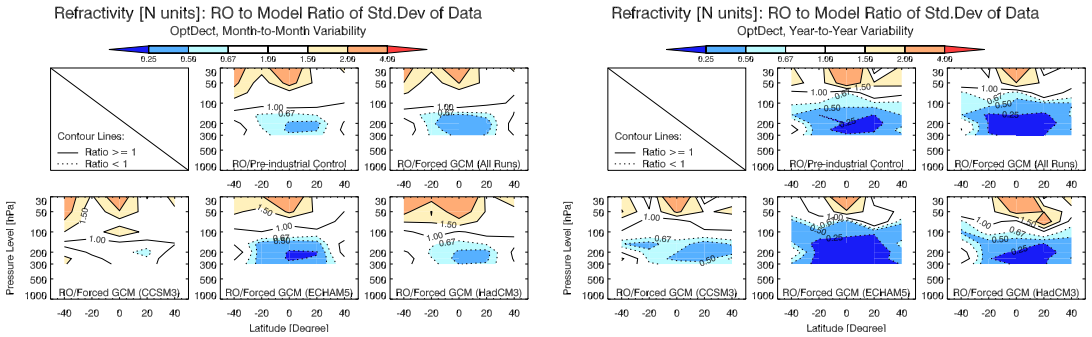

(a) Refractivity

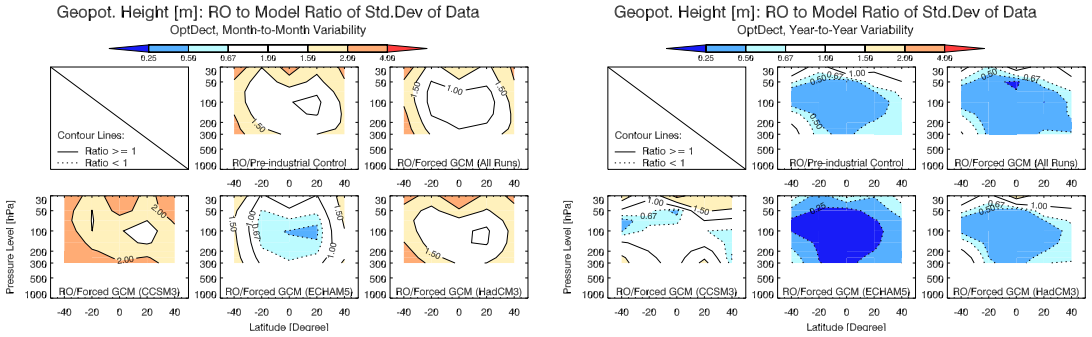

(b) Geopotential Height

Figure 5.14: *(a)* Month-to-month (left) and year-to-year (right) refractivity variability ratio based on one standard deviation of RO and GCM data. The upper row in each panel shows the RO to PICTRL and the RO to fGCM ratio. The bottom row the ratio between RO and CCSM3, ECHAM5, and HadCM3 simulations. RO and fGCM variability is calculated with respect to the 2002 to 2007 period, for the PICTRL record, all available months were used. *(b)* The same illustration for geopotential height.

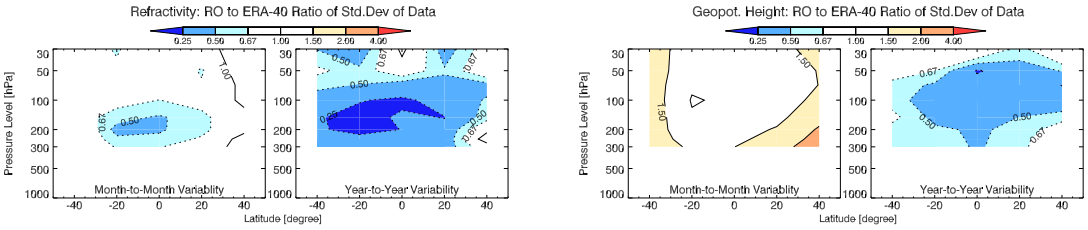

(a) refractivity variability ratio

(b) geopotential height variability ratio

Figure 5.15: *(a)* Month-to-month (left) and year-to-year (right) refractivity RO to ERA-40 variability ratio based on one standard deviation. RO variability is calculated with respect to the 2002 to 2007 period, ERA-40 variability with respect to the 1980 to 2001 period. *(b)* The same illustration for geopotential height.

pattern (not shown). For temperature, the variability (one standard deviation) is then reduced about 0.2 K ($\approx 12\,\%$, which is also valid for refractivity) in the tropics and southern mid-latitudes above 50 hPa, while the variability at lower levels and for geopotential height patterns stays virtually the same.

5.2.4 Reconstruction of Data From EOF Space

For the detection analysis, the RO, fGCM, and CONTROL trend patterns are transfered into a truncated PICTRL EOF space. It is required that these truncated patterns are still able to represent most of the anticipated signal of the data. The fGCM ensembles with their mostly dipole trend patterns (Figure 5.12) only need few EOFs to be reasonably well rebuilt. Figure 5.16a shows for all three parameters the original RO trend patterns (QBO removed), the rebuilt patterns using the first $k = 5$ eigenvectors, and the pattern correlations between original and rebuilt patterns for 1 to 20 EOFs. The pattern correlation is achieved by correlating the map vector of the original and the rebuilt pattern and is therefore a Pearson's correlation coefficient. Generally, the pattern correlations increase quickly with the number of retained EOFs, yielding around 60 % for 5 retained EOFs. Most EOFs are needed to rebuild the more complex RO temperature pattern, though the displayed rebuilt pattern in Figure 5.16a already captures most of the expected UT warming and LS cooling. The boundary between UT warming and LS cooling in the RO data at around 150 hPa is lower than for the fGCM at around 70 hPa, but nevertheless the rebuilt patterns using only few EOFs are very similar to the fGCM patterns. For the CHAMP only period (not shown), the pattern correlations between RO and rebuild patterns using more than 5 EOFs are about 10 % higher than for the GPS/MET–CHAMP period, but the patterns differ stronger from the fGCM patterns.

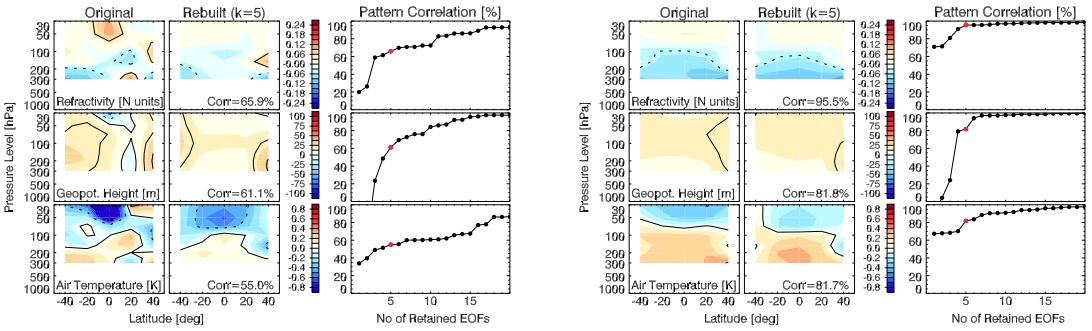

(a) RO trend pattern in EOF space

(b) fGCM trend pattern in EOF space

Figure 5.16: *(a)* Original RO trend pattern (QBO removed, left), rebuilt pattern using 5 EOFs (middle), and pattern correlation between the original and rebuilt pattern for $k = 1, \ldots, 20$ EOFs. Top row shows refractivity, middle row geopotential height, and bottom row temperature results. *(b)* The same illustration for fGCM patterns.

Figure 5.16b depicts the original and rebuilt fGCM trend patterns. The smooth fGCM trend patterns are easier to rebuild and show a pattern correlation of already over 80 % for 5 retained EOFs. For refractivity and temperature, already 60 % correlation of the original and rebuilt pattern is achieved for only considering the first EOF. Geopotential height brakes also rank for the fGCMs, as the rebuilt pattern based on the first EOF shows a negative pattern correlation, which is also the case for the rebuilt RO pattern based on the first two EOFs. The negative correlation of the rebuilt patterns of low EOFs may be caused by the asymmetric geopotential height pattern (largest trend values in the northern mid-latitudes). As low EOFs give generally symmetric patterns (see Figures 5.17 and 5.18), at least some of them are needed to rebuilt the asymmetry of the trend pattern.

5.3 Discussion

This section focuses on three issues:

- the RO fingerprint, which gives hints where GCMs differ from RO data;
- the test results of the residual consistency test and of the uncertainty test for the scaling factors, which are used to evidence climate change detection;
- and an assessment of the stability of the detection study using only model data.

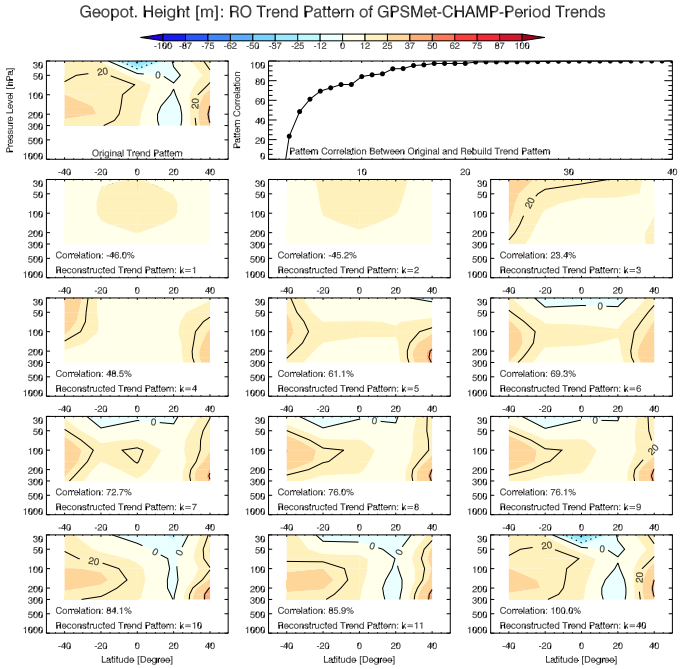

Figure 5.17: Rebuilt geopotential height patterns for RO trends of the GPS/MET–CHAMP period. Top row shows the original trend pattern (left) and the pattern correlation between the original and rebuilt pattern for $k = 1, \ldots, 40$ EOFs. The following plots show the rebuilt patterns for increasing k. The right bottom plot is the rebuilt pattern using all EOFs and thus has to be identical to the original pattern.

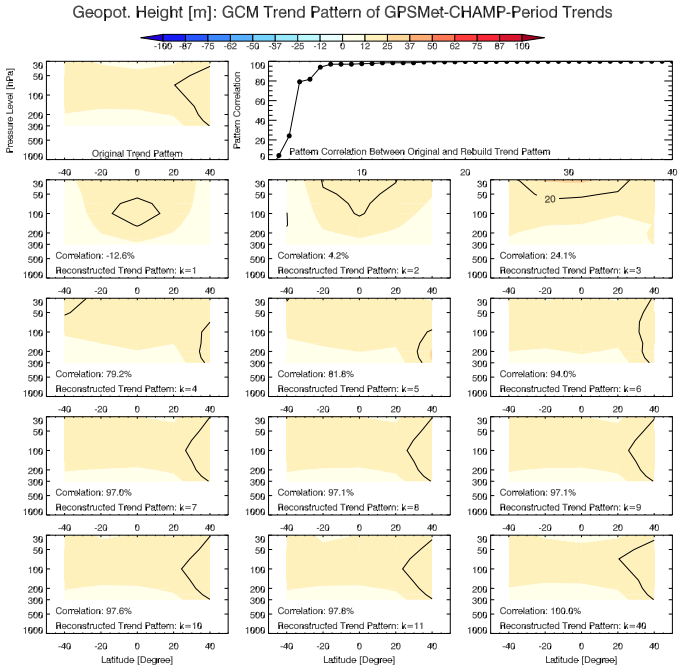

Figure 5.18: Rebuilt geopotential height patterns for fGCM trends of the GPS/MET–CHAMP period. Top row shows the original trend pattern (left) and the pattern correlation between the original and rebuilt pattern for $k = 1, \ldots, 40$ EOFs. The following plots show the rebuilt patterns for increasing k. The right bottom plot is the rebuilt pattern using all EOFs and thus has to be identical to the original pattern.

5.3.1 The RO Fingerprint

The pattern by which the observational data have to be multiplied to obtain an *optimal* estimate for the climate change signal due to GHG increases, is called *optimal fingerprint*. In the reduced EOF space (based on $k = 1, \ldots, p$ EOFs) the kth fingerprint is given as

$$\mathbf{fingerprint}_{1\times k}^{\text{EOF space}} = \left[\left(\mathbf{b}^{\text{fGCM}}\right)^{\mathsf{T}}_{1\times k} \mathbf{\Lambda}^{-1}_{k\times k} \mathbf{b}^{\text{fGCM}}_{k\times 1}\right]^{-1} \left(\mathbf{b}^{\text{fGCM}}\right)^{\mathsf{T}}_{1\times k} \mathbf{\Lambda}^{-1}_{k\times k}, \quad (5.28)$$

which is identical to the right-hand side part of equation (5.14) without the last term, which describes the RO data in the EOF space.

To get the fingerprint pattern in the detection space, the EOF-space fingerprint has to be matrix multiplied by the PICTRL eigenvector matrix $\mathbf{F}^{\text{PICTRL}}$:

$$\mathbf{fingerprint}_{1\times p}^{\text{detection space}} = \mathbf{fingerprint}_{1\times k}^{\text{EOF space}} \left(\mathbf{F}^{\text{PICTRL}}\right)^{\mathsf{T}}_{k\times p}. \quad (5.29)$$

For each truncation k, an optimal fingerprint map is achieved, which points up where the fGCM pattern shows differences to the observational pattern. Figure 5.19 shows the first 12 GPS/MET–CHAMP detection-space fingerprints for geopotential height and temperature (refractivity results, not shown, since inverse to temperature). The geopotential height fingerprints correspond well to the results of the detection study by Leroy et al. (2006*b*), which used single model simulations instead of real RO observations (they investigated log-dry pressure trends, which are proportional by the scale height to geopotential height trends on constant p-levels). They describe as most striking feature the highly weighted fingerprints around 40°N and S, which they assign to the symmetric pole-ward motion of eddy-driven mid-latitude jet streams (for a detailed discussion of the geopotential height fingerprints and the associated EOFs, see Leroy et al. 2006*b*). This jet-migration pattern is clearly visible in Figure 5.19a and stable until 10 retained EOFs. Similar results are also gained for the CHAMP only period.

Also temperature fingerprints (Figure 5.19b) show, mainly in the lower EOFs, the jet-migration pattern, but furthermore, the tropical and sub-tropical area around 100 hPa exhibits a strong fingerprint pattern. This tropical tropopause fingerprint pattern is also independent of the number of retained EOFs, it gains strength with an increasing k. Thus tropical temperature trends around the tropopause region are another candidate to monitor UTLS climate change.

5.3.2 Consistency of Observed to Model Variance and Climate Change Detection

A residual consistency test from Allen and Tett (1999), see section 5.1.2, was used to test the null hypothesis that the climate variability of the control simulations is a

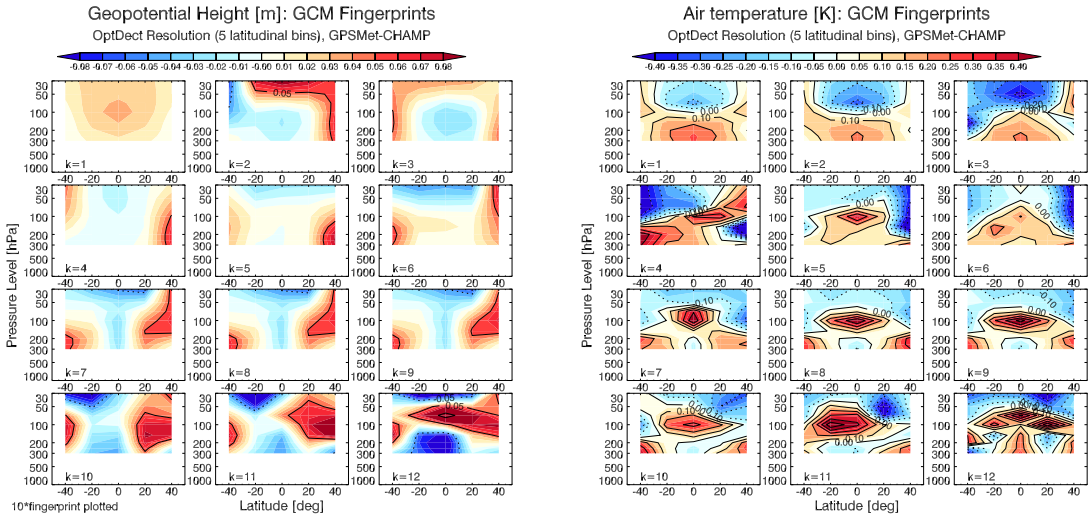

(a) Geopotential height fingerprints

(b) Temperature fingerprints

Figure 5.19: *(a)* Geopotential height fingerprints for the GPS/MET–CHAMP period for $k = 1, \ldots, 12$ retained EOFs. Plotted values are multiplied by a factor 10. *(b)* The same illustration for temperature. Plotted values are not scaled by a factor.

realistic representation of the observed variability in the truncated EOF space. The regression residuals in the EOF space, which are related to a χ^2 distribution, are used to determine the number of retained EOFs, which give a realistic estimate of climate noise. Figure 5.20 depicts the model to observations ratio of cumulative residual variances for 2 to 16 retained EOFs and the respective χ^2 values for 5 % to 95 % confidence limits. The test values are required to fluctuate around one and to remain within the confidence limits for a low number of EOFs. Compliance with these requirements evidences that observations and models exhibit comparable variance for the number of retained EOFs and corresponds to being unable to reject the null hypothesis. For the GPS/MET–CHAMP period, the refractivity values for less than 10 retained EOFs are arranged close to (and for two numbers of EOFs above) the upper confidence limit, indicating a high model variability compared to the observations, which may be well due to the weakly pronounced ENSO during the analysis period. For temperature, good test results are obtained up to 12 retained EOFs. Geopotential height shows a distinct decrease of the test values with an increasing number of retained EOFs, which may indicate that the models only need few spectral wave numbers to describe geopotential height fields.

Concerning the CHAMP only period, better residual consistency test results are obtained for refractivity, slightly worse for temperature, and around the same for

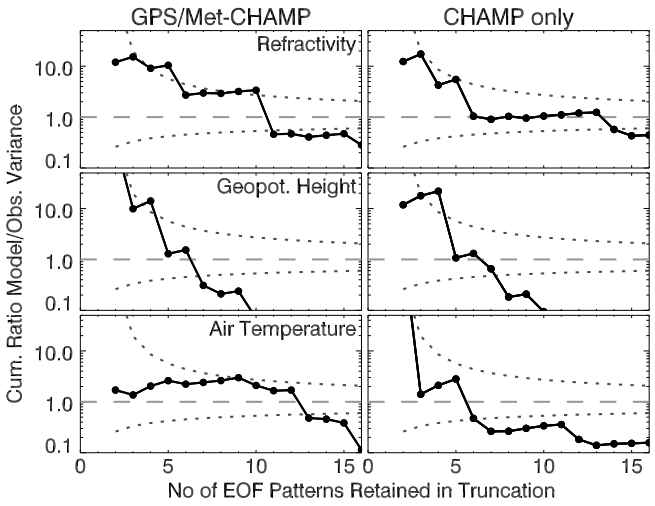

Figure 5.20: *left* Results of the residual consistency test for 2 to 16 retained EOFs for refractivity (top), geopotential height (middle), and temperature (bottom) for the GPS/MET-CHAMP period. Plotted are cumulative model to observation ratios of residual variability ($\frac{k-1}{r^2}$). The dotted lines mark the 5 % (upper line) and 95 % (lower line) χ^2 limits. *right* Same plot for CHAMP only period.

geopotential height. This is very probably caused in case of refractivity by the different amplitudes of the RO patterns and in case of temperature by different features below 100 hPa. Compared to the longer GPS/MET–CHAMP period, the observed refractivity and temperature residual variance is stronger referring to the residual model variance. As for the GPS/MET–CHAMP period, there is no reason to distrust the representation of the model variances for up to 10 retained EOFs for refractivity and for up to 12 retained EOFs for temperature. For geopotential height, at most 6 EOFs can be considered. These EOFs retain a pattern correlation of about 70 % compared to the original pattern for refractivity and geopotential height, and of about 60 % for temperature.

Detection of a climate change signal can be claimed, if the null hypothesis that the observed climate change is part of the natural climate variability can be rejected. This is equivalent to the RO scaling factors including their uncertainty range being different from zero. Based on the distribution of the CONTROL scaling factors, which can be assumed to be Gaussian (Hegerl et al. 1996), the uncertainty in the RO based scaling factors can be determined in a one-tailed *t*-test. The results indicate that the observed trend pattern is significantly different from climate variability and thus likely represents a changing climate, e.g., in response to GHG increases. Consistency between the observed and forced climate signal is given, when the RO scaling factors and uncertainty ranges include unity. Figure 5.21a shows for 1 to 20 retained EOFs the RO scaling factors and their 10 % to 90 % and their 5 % to 95 % uncertainty ranges (error bars), which are estimated as ±1.28 CONTROL standard deviations and ±1.64 CONTROL standard deviations, respectively. Figure 5.21b depicts the exact results (risk levels) of the significance test. For the shorter trend period based on CHAMP, the uncertainty ranges are broader and the values of the scaling factor fluctuate stronger than for the GPS/MET–CHAMP period, impeding the interpretation of the results.

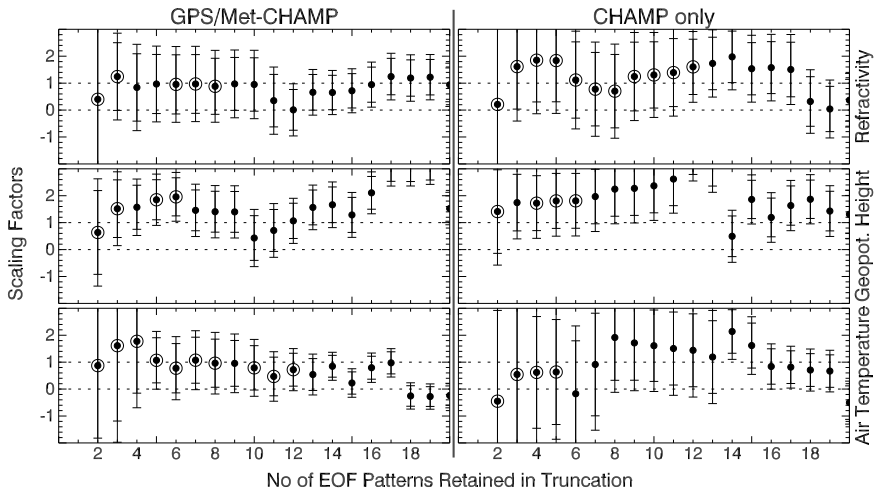

(a) Uncertainty in scaling factors

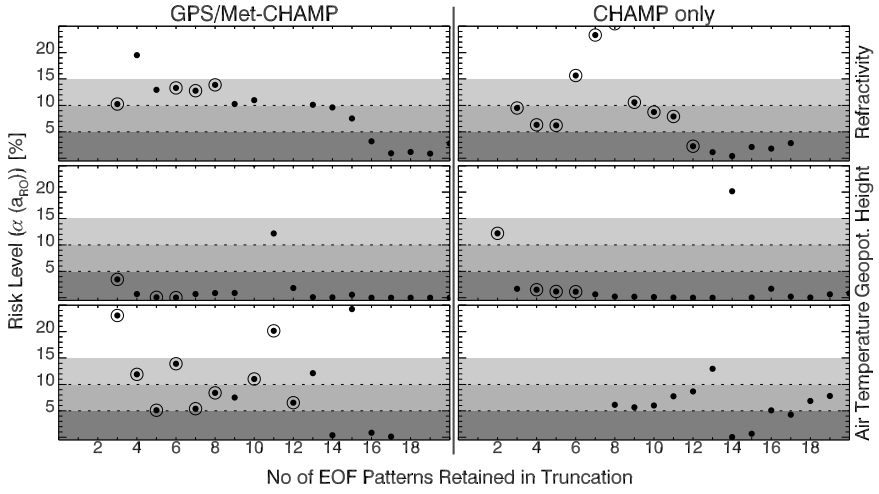

(b) Significances of scaling factors

Figure 5.21: *(a)* Results for the uncertainty in the scaling factors for 2 to 20 retained EOFs of refractivity (top), geopotential height (middle), and temperature (bottom) for the GPS/MET–CHAMP (left) and the CHAMP only (right) period. Error bars indicate the 10 % to 90 % (inner bars) and the 5 % to 95 % (outer bars) uncertainty ranges based on the CONTROL scaling factors. If for a certain k the residual consistency test is passed, it is marked with a circle around the respective scaling factor. *(b)* This plot shows for the same parameters and periods the exact level of achieved significances.

The refractivity and temperature RO scaling factors, corresponding to numbers of retained EOFs which pass the residual consistency test, are very close to unity. At the chosen $\alpha = 10\,\%$ significance level, climate change cannot be detected for refractivity for 5 to 10 retained EOFs, where the α values range between slightly more than 10 % up to around 13 %. Increasing the number of retained EOFs to 13 to 15 supports a detection at a 10 % significance level, but the scaling factors and the residual consistency test results then cannot be considered satisfactory. For temperature, detection can be affirmed at the 10 % significance level for 5 as well as for 7 to 9 retained EOFs.

As to geopotential height, the scaling factors are not very steady and differ more from unity than in refractivity and temperature. Even though a detection could be stated with a 5 % significance level for 3 to 9 retained EOFs, the residual consistency test indicated a strong dependency on the number of retained EOFs concerning a realistic representation of the model simulated variability. For 5 and 6 retained EOFs, which pass the residual consistency test, the 10 % to 90 % uncertainty range of the RO scaling factors does not include unity, and a scaling of nearly 2 is needed to adjust the fGCM trend pattern to the RO pattern. The discussed findings based on the horizontal resolution of 5 zonal bands are similar to the results of the 10°-latitudinal resolution (not shown).

Summing up, the GPS/MET–CHAMP temperature and refractivity records show an emerging climate change signal, which is for the given period of more than 12 years consistent with the GCM projections, while evidence for detection in geopotential height trends is compromised by equivocal residual consistency test results. QBO and ENSO governed atmospheric patterns mask the trends of the shorter CHAMP period and thus delay a climate change detection. The results are consistent with RO detection time estimates from two studies. Leroy et al. (2006*b*) used 12 IPCC AR4 GCMs and an optimal detection approach to estimate the detection time in log-dry pressure trends with a 95 % confidence as 6 to 13 years. Simulations of UTLS RO bending angle profiles (refractivity is deduced by integrating bending angles over height) were used by Ringer and Healy (2008) for detection time estimates of 10 to 16 years based on an autoregressive model approach.

5.3.3 Testing Stability With GCM Simulations as Observational Dataset

In order to assess the stability of the RO results, the calculations were redone based on one fGCM simulation as proxy for the observations. Similar results of this analysis and the one with the real RO data would indicate stable detection results.

Figure 5.22 shows for geopotential height the respective GPS/MET–CHAMP trends for all 20 fGCM simulations. While the average fGCM geopotential height pattern (see Figure 5.12) exhibits a persistent UTLS increase in the field, with a maximum at northern mid-latitudes in the LS, the single fGCM simulations offer a wide range of various patterns. Even though most simulations feature an increase in the geopotential

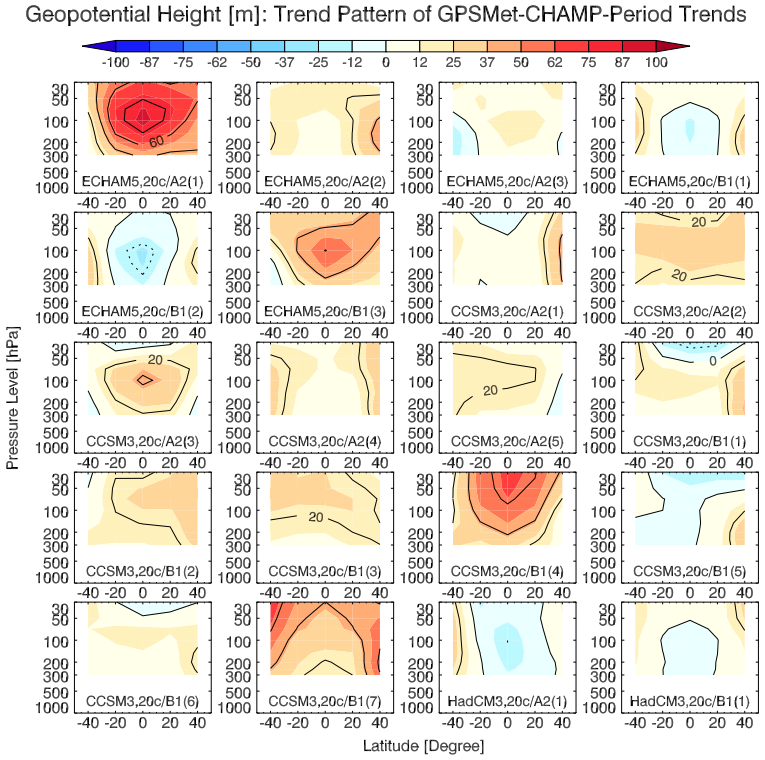

Figure 5.22: Geopotential height trend patterns of the 20 fGCM simulations for the GPS/MET–CHAMP period. The first CCSM3, SRES A2 simulation (depicted in each panel in the second row, third column) was chosen as proxy for the RO record in the stability test.

height field (sometimes with very pronounced amplitudes), around 5 simulation (i.e. 25 %) project a tropical decrease in geopotential height during the GPS/MET–CHAMP period. A similar picture is given for the temperature fields in Figure 5.23 (and thus also for the refractivity fields, which are not shown). Most simulations show a tropospheric warming and stratospheric cooling (13 out of the 20 simulations, with differently high crossing levels from warming to cooling), but some simulations exhibit a reversed pattern or a continuous cooling or warming throughout the UTLS. The first CCSM3, Special Report on Emission Scenarios (**SRES**) A2 simulation was selected as proxy observational record for the stability test, as it features patterns which are quite similar to the RO record for the GPS/MET–CHAMP period.

The results of the residual consistency test and of the uncertainty in the scaling factors for the used data set combination based on GCMs only is shown in Figure 5.24. The residual consistency test identifies the maximal number of EOFs which can be retained, until the observations' variability exceeds the models' variability. It gives of course no meaningful results for higher retained EOFs, as a GCM is compared with other GCMs. As the residual variability of a single model simulation is compared with the residual variability of all models, it can be expected that they agree very well for higher EOFs, as they resolve the same spatial scales. Nevertheless, it is interesting to see how

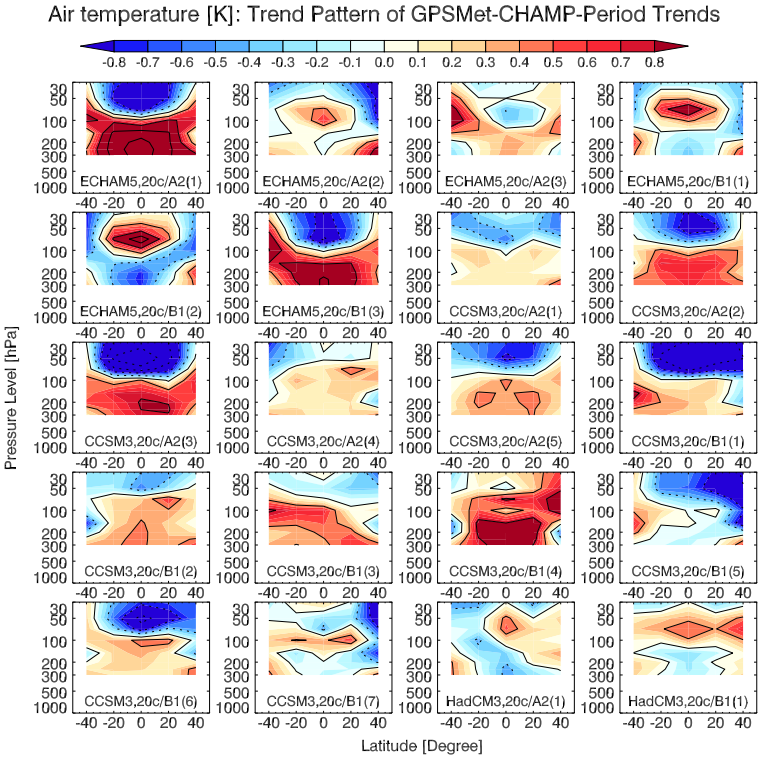

Figure 5.23: Temperature trend patterns of the 20 fGCM simulations for the GPS/MET–CHAMP period. The first CCSM3, SRES A2 simulation (depicted in each panel in the second row, third column) was chosen as proxy for the RO record in the stability test.

the models behave for a low number of retained EOFs, and Figure 5.24a shows that the differences to the RO based results are not very pronounced. Refractivity results are about the same, with rather high *observation* to model residual variance. The same is valid for temperature, even though the real RO record leads to better results for this parameter during the GPS/MET–CHAMP period and already shows acceptable test results for a low number of retained EOFs (see Figure 5.20). Clearest differences appear in the geopotential height fields, where the proxy data set passes the residual consistency test for all numbers of retained EOFs (in contrast to RO data, which show a strong dependency on the number of used EOFs). This again is a hint that the models only need few spectral waves to build the geopotential height fields. The results for the CHAMP only period are also comparable to the RO based results.

Figure 5.24b depicts the uncertainty in the scaling factors, which are based on the one CCSM3 simulation. Focusing on the GPS/MET–CHAMP periods, slightly better detection results are gained for refractivity, where for single numbers of retained EOFs a detection at or very close to the 90 % probability levels is achieved. For geopotential height, a detection at the 95 % level is given when at least 4 EOFs are considered. Similar to the RO results, the scaling factors are rather large, ranging around 2, indicating that the average fGCM trend pattern rather underestimated the climate change signal.

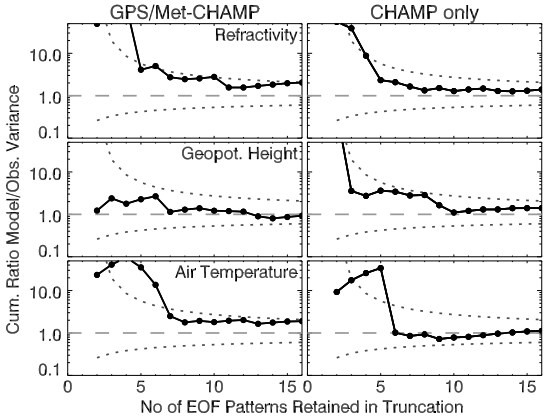

(a) Residual consistency test

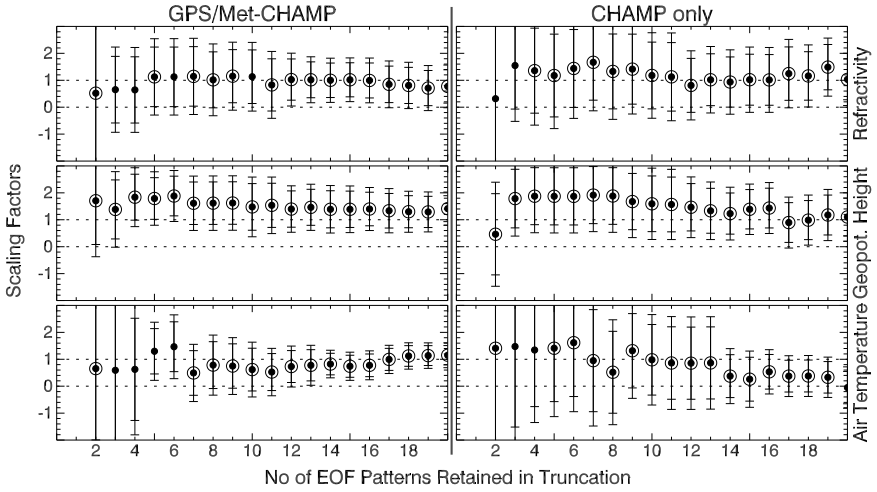

(b) Uncertainty in scaling factors

Figure 5.24: *(a)* Results of the residual consistency test of RO *proxy* data for 2 to 16 retained EOFs for refractivity, geopotential height, and temperature for the GPS/MET–CHAMP (left) and the CHAMP only (right) period. Plotted are cumulative model to observation ratios of residual variability ($\frac{k-1}{r^2}$). The dotted lines mark the 5 % (upper line) and 95 % (lower line) χ^2 limits. *(b)* Uncertainty in the scaling factors for 2 to 20 retained EOFs of refractivity, geopotential height, and temperature for the GPS/MET–CHAMP (left) and the CHAMP only (right) period. Error bars signify the 10 % to 90 % (inner bars) and the 5 % to 95 % (outer bars) uncertainty range based on the CONTROL scaling factors. If for a certain k the residual consistency test is passed, it is marked with a circle around the respective scaling factor. The scaling factors are based on one fGCM simulation (CCSM3, A2, run 1) used as proxy for RO data.

Temperature exhibits slightly worse detection results for the CCSM3 proxy data set, even though for some EOFs < 10, the detection significance level is close to 90 %.

5.3.4 Summary of Climate Change Detection Study

The RO detection study presented in this chapter aimed to investigate the usability of the currently available RO record in climate change science. An optimal fingerprinting approach, which enhances the signal (trend) to noise (natural variability) ratio, was applied to test whether RO observations, available for the rather short period end 1995 to beginning 2008, exhibit an UTLS climate change pattern in refractivity, geopotential height, and temperature fields which is consistent with the expected climate change signal as projected in GCMs. Former studies (Leroy et al. 2006*b;* Ringer and Healy 2008), based on GCMs or simulated RO data, showed that a climate change signal will become detectable in RO parameters within a 6 to 16 years record.

The influence of QBO and ENSO (section 5.2.1), the main patterns of UTLS variability, on trend estimates was assessed via multi-linear regression. Within the analysis period, only weak to medium El Niños and La Niñas occurred. The QBO was removed from the observations for further analysis, since it is not contained in the considered GCMs. Two trend periods were analyzed (section 5.2.2). Though for the longer period only an intermittent RO record is available, the trend pattern is consistent with the intermittent as well as the continuous radiosonde pattern based on the HadAT2 record. The uncertainty in the detection variable was determined via a second statistically independent sample of PICTRL data (CONTROL). The trend signal of the shorter period of CHAMP only measurements for both observations and GCM data is still masked by natural variability, resulting in a broad distribution of CONTROL trends which makes climate change detection difficult.

An emerging climate change signal, consistent with model estimates, can be detected at a 90 % confidence level in the more than 12 year period of GPS/MET–CHAMP measurements in temperature and with slightly lower confidence in refractivity. RO geopotential height trends are stronger than the GCM projected trends and the consistency of observation and model based natural variability strongly depends on the number of EOFs retained in the analysis. A test of the detection results' stability, employing GCM data only, confirmed the consistency of RO and GCM trend results.

6 Summary and Conclusions

Noticeable changes in our climate system are not limited to the Earth's surface, they emerge as well very clearly in the upper troposphere-lower stratosphere (**UTLS**), where the vertical thermal structure reflects a balance between radiative, convective, and dynamical heating and cooling processes. Upper air observations are available since the establishment of radiosondes in the 1960s and the implementation of space borne measurement systems in the late 1970s. Many of these systems were not intended for climate monitoring and thus show shortcomings, e.g., in regard to spatial and temporal sampling, accuracy, or long-term stability. A record suitable for climate monitoring has to supply vertically well-resolved, accurate, long-term stable, and consistent data, which depict the mean state and the variability of the atmosphere with an accuracy better than the expected changes. For the UTLS, these data qualities can be provided by measurements of the Global Navigation Satellite System (**GNSS**) Radio Occultation (**RO**) technique.

This thesis deals with the capability of RO data for climate monitoring in the UTLS. In the beginning, the method, data characteristics and availability were presented and existing studies on the use of RO data for climate monitoring were discussed. The climate monitoring utility of RO data was investigated via two thematic foci. The first question posed was: In which regions and seasons is an early detection of significant trends in RO parameters possible? Therefore, a climate change indicator study was performed based on proxy data and employing classical trend testing. The second question referred to the available RO record and its trend detection capability. A detection study, employing an optimal fingerprinting technique, was performed to learn if the trend signal of the still rather short RO record can be considered as significantly different from natural climate variability.

The climate utility of RO-accessible climate change indicators (chapter 4) was demonstrated by means of climate model simulations and re-analyses. Three representative climate models for the Intergovernmental Panel on Climate Change (**IPCC**) Fourth Assessment Report (**AR4**) were employed: ECMWF Hamburg Model (**ECHAM5**), Community Climate System Model 3 (**CCSM3**), Hadley Centre Coupled Model, version 3 (**HadCM3**). The General Circulation Model (**GCM**)s were investigated for the 2001 to 2050 period; the re-anlyses, ECMWF Re-Analysis (**ERA-40**) and NCEP/NCAR Re-Analysis (**NRA**), for the 1980 to 2001 period. The adequacy of these proxies for RO data was demonstrated in section 4.2.1 and section 4.2.2 by

means of variability and trend investigations. The latter included an analysis of GCM's lower stratosphere (**LS**) trends compared to those of the ECHAM5 model, Middle Atmosphere Mode of ECMWF Hamburg Model, version 5 (**MAECHAM5**). The study showed that the LS trend performance of the used models with the uppermost level at 10 hPa shows no striking differences to the middle atmosphere model trends (top level at 0.01 hPa) in large-scale regions. Layer trend differences in small-scale regions and at higher latitudes are not just limited to the LS. These regions are governed by high internal variability leading to less significant trend results and thus do not meet the criteria for indicator regions. Indicators were defined as regions and seasons with high trend signal-to-noise ratio (**SNR**), which was determined by means of trend significances, goodness of fit (**GOF**), and—for GCMs—by the agreement between the individual simulations in their trend sign. For the trend analysis, the focus was on large-scale zonal means of the RO parameters refractivity (proportional to density), pressure, and temperature and on their vertical gradients.

Since climate model data are provided at pressure (p) levels and RO observations at mean sea level (**MSL**) altitude levels, the data were brought to the same vertical grid. The parameter trends were investigated at both vertical coordinates. Differences in UTLS parameter trends at either p-levels or geopotential height (Z)-levels are most pronounced in refractivity and the respective layer gradients, as discussed in section 4.3. Refractivity shows larger UTLS trends at Z-levels, which are caused by the combined pressure and temperature dependency of this parameter (at constant p-levels, refractivity trends are inversely proportional to temperature). For pressure/geopotential height and temperature, differences in Z-level and p-level trend results are negligible.

The GCMs show for the years 2001 to 2050 a strong climate change signal in different height domains, depending on the respective physical processes governing the individual parameters (Figure 4.15). As to zonal means, seasonality only plays a minor role for such long-term trends.

The shorter time period of analyzed ERA-40 trends, 1980 to 2001, draws a more narrowed picture of regions with high trend SNR (Figure 4.16). Single zonal bands, such as the tropical regions, turned out to be good indicator regions for several parameters and height domains. Compared to the GCMs, indicator regions are less repeatable throughout all seasons; annual mean (**ANN**), September–October–November (**SON**) and next June–July–August (**JJA**) exhibit best indicator results for the UTLS. This supports individual seasonal differentiation when investigating climate change on shorter timescales. Nevertheless, ERA-40 and GCM results are generally consistent in regard of indicators, with the latter showing the longer-term broad picture.

Regarding altitude dependence of earlier climate change signal emergence, refractivity turned out as good indicator at about 18 km to 24 km ($\approx$ 70 hPa to 30 hPa levels), pressure at lower levels of 13 km to 16 km ($\approx$ 150 hPa to 100 hPa levels), and temperature at around 9 km to 12 km ($\approx$ 300 hPa to 200 hPa levels). The latter also emerges as LS indicator above 20 km as well as refractivity also in the tropics around $\approx$ 12 km.

Beside the level based considerations, layer gradients support the applicability of RO data for climate monitoring and show promising results, particularly for the tropics. When the boundary height levels of the layers used to calculate gradients are properly chosen, the layer gradients appear more sensitive to climate change than single level data do, providing additional information. Collectively, the set of RO-accessible parameters qualifies for climate monitoring in the whole UTLS, since the sensitivity of the parameters neatly differs with height.

Specifically per parameter from more raw to more derived products, refractivity and pressure and the respective layer gradients alone are adequate climate change indicators. But in addition, temperature can be well used as supplemental indicator, directly representing warming or cooling of the atmosphere.

The RO trend detection study presented in chapter 5 aimed to investigate the usability of the currently available RO record in climate change science. An optimal fingerprinting approach, which enhances the signal (trend) to noise (natural variability) ratio, was applied to test whether RO observations, available for the rather short period end 1995 to beginning 2008, exhibit an UTLS climate change pattern in refractivity, geopotential height, and temperature fields, which is consistent with the expected climate change signal as projected by GCMs. Former studies (Leroy et al. 2006*b;* Ringer and Healy 2008), based on GCMs or simulated RO data, showed that a climate change signal will become detectable in RO parameters within a 6 to 16 years record.

The influence of Quasi-Biennial Oscillation (**QBO**) and El Niño-Southern Oscillation (**ENSO**) (section 5.2.1), the main patterns of UTLS variability, on trend estimates were assessed via multi-linear regression. Within the analysis period, only weak to medium El Niños and La Niñas occurred. The QBO was removed from the observations for further analysis, since it is not contained in the considered GCMs. Two trend periods were analyzed (section 5.2.2). Though for the longer period only an intermittent RO record is available, the trend pattern is consistent with the intermittent as well as the continuous radiosonde pattern based on the Hadley Centre gridded free-atmosphere temperatures from radiosondes (**HadAT2**) record. The uncertainty in the detection variable was determined via a second statistically independent sample of PICTRL data (**CONTROL**). The trend signal of the shorter period of Challenging Mini-Satellite Payload (**CHAMP**) measurements for both observations and GCM data is still masked by natural variability, resulting in a broad distribution of CONTROL trends which makes climate change detection difficult.

An emerging climate change signal, consistent with model estimates, can be detected at a 90 % confidence level in the more than 12 year period spanned by Global Positioning System/Meteorology (**GPS/MET**)–CHAMP measurements in temperature and with slightly lower confidence in refractivity. RO geopotential height trends are stronger than the GCM projected trends and the consistency of observation and model

based natural variability strongly depends on the number of EOFs retained in the analysis. A test of the detection results' stability, employing GCM data only, confirmed the consistency of RO and GCM trend results.

The thesis showed that the GNSS RO method, featuring characteristics such as global coverage, long-term stability, high accuracy and vertical resolution, offers a high quality climate record for future UTLS climate change studies. The RO parameters refractivity, pressure, temperature and their gradients are sensitive and complementary trend indicators at different UTLS height regions. The still rather short RO record shows a significant climate trend signal in temperature and an emerging signal in refractivity. By end of 2010, a continuous RO record of 10 years, and—including the GPS/MET data—an intermitted record of 15 years will be available, which can be used as climate benchmark record for UTLS climate change detection and attribution studies.

A Interpolation Theory

The interpolation theory of polynomial interpolation, including linear and cubic interpolation, is presented in section A.1, spline interpolation in section A.2, including a short example. Section A.3 details the Gorbunov–Steiner adaption for polynomial interpolation as employed for the horizontal regridding of the fields used in these studies.

A.1 Polynomial Interpolation

If an interpolation function g depends linearly of the parameters c_k, an interpolation polynomial p_n can be defined as:

$$\begin{aligned} g(x,c) &= p_n(x,c) = c_0 + c_1 x + \ldots + c_n x^n = \sum_{i=0}^{n} c_i x^i, \text{ with} \\ p_n(x_k,c) &= f(x_k) = y_k. \end{aligned} \tag{A.1}$$

The polynomial interpolation cases for $\mathrm{n} = 1, \mathrm{n} = 2,$ and $\mathrm{n} = 3$ are called *linear*, *quadratic*, and *cubic* interpolation (having two dimension, they are named bilinear, biquatratic, bicubic).

Polynomial interpolation (e.g., Archer and Weisstein 2010) provides a solution for the problem of finding a polynomial with $(n+1)$ interpolation nodes. The fundamental theorem of algebra guarantees that there exists an interpolation polynomial of nth order for $(n+1)$ distinct data points. The solution of a polynomial interpolation problem is based on solving the linear equation system. In the following, one method to solve such systems, namely the *Lagrange-interpolation*, is presented.

Given $(n+1)$ data points the interpolation polynomial $p_n(x)$, of nth order is given through:

$$p_n(x) = \sum_{i=0}^{n} y_i L_i(x) = y_0 L_0(x) + y_1 L_1(x) + \ldots + y_n L_n(x) \tag{A.2}$$

The L_i in equation (A.2) are the Lagrange supporting polynomials of the order i,

which only depend on the given nodes. They have to fulfill the following condition:

$$L_i(x_k) = \begin{cases} 1 & \text{for i = k,} \\ 0 & \text{for i} \neq \text{k} \end{cases} \qquad i,k = 0,\ldots,n \tag{A.3}$$

$$\begin{aligned} L_i(x) &= \prod_{k=0,k\neq i}^{n} \frac{x - x_k}{x_i - x_k} \\ &= \frac{(x-x_0)(x-x_1)\ldots(x-x_{i-1})(x-x_{i+1})\ldots(x-x_n)}{(x_i-x_0)(x_i-x_1)\ldots(x_i-x_{i-1})(x_i-x_{i+1})\ldots(x_i-x_n)} \end{aligned} \tag{A.4}$$

Linear Interpolation A linear interpolation problem is given when g only depends linearly from the coefficients a_i. The parametric approach can be written as a linear combination of functions $\phi_i(x)$:

$$g(x, a_0, a_1, \ldots, a_n) = a_0 + a_1\phi_1(x) + a_2\phi_2(x) + \ldots + a_n\phi_n(x). \tag{A.5}$$

The most simple and most used mode of linear interpolation is to connect two points by a straight line.

4-Point Polynomial Interpolation (Cubic Interpolation) Using Lagrange interpolation, the interpolation polynomial $p_3(x)$ (with $n = 3$, $k = 0, 1, 2, 3$) through the four nodes $(a, f(a)), (b, f(b)), (c, f(c)), (d, f(d))$ is given through:

$$\begin{aligned} p_3(x) &= \sum_{k=0}^{n=3} f(x_k)L_k(x) \\ &= f(a)L_0(x) + f(b)L_1(x) + f(c)L_2(x) + f(d)L_3(x) \end{aligned} \tag{A.6}$$

The Langrange supporting polynomials $L_k(x)$ are:

$$\begin{aligned} L_0(x) &= \frac{(x-b)(x-c)(x-d)}{(a-b)(a-c)(a-d)} \\ L_1(x) &= \frac{(x-a)(x-c)(x-d)}{(b-a)(b-c)(b-d)} \\ L_2(x) &= \frac{(x-a)(x-b)(x-d)}{(c-a)(c-b)(c-d)} \\ L_3(x) &= \frac{(x-a)(x-b)(x-c)}{(d-a)(d-b)(d-c)} \end{aligned} \tag{A.7}$$

The advantage of polynomials is that they can be very easily integrated or differentiated, thus, they are quite commonly used in mathematics. But with increasing order, polynomials get more and more instable, i.e. they strongly oscillate between

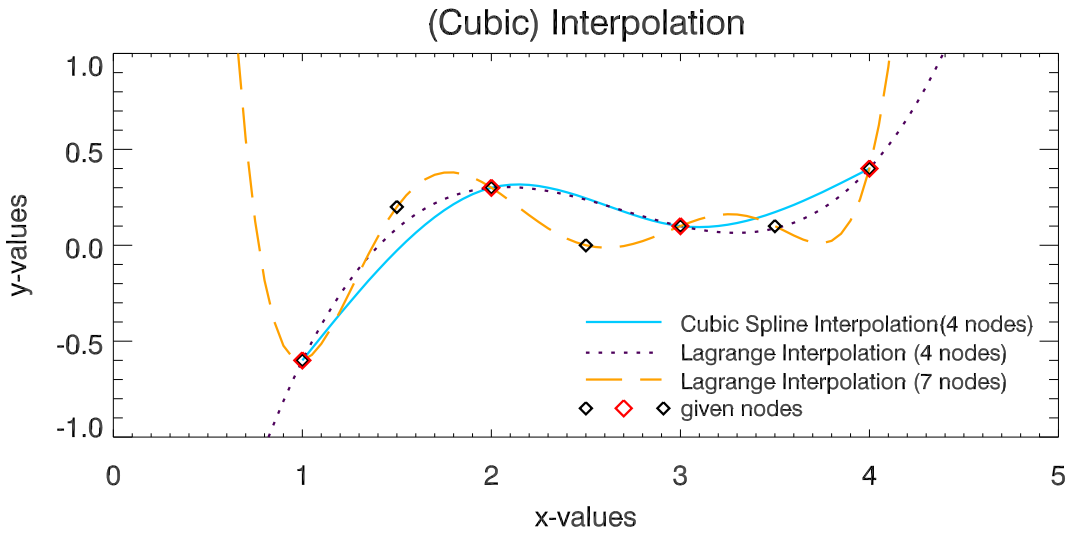

Figure A.1: Differences between polynomial (using 4 and 7 nodes) and spline interpolation.

the nodes. Therefore, integration polynomials are not suitable for more than about 5 nodes. Figure A.1 shows this effect using four and seven nodes. To solve this problem of oscillation called Runge's phenomenon, either linear interpolation between every two following points or spline interpolation can be used among other methods.

A.2 Spline Interpolation

Spline interpolation (e.g., Faires 1998) is based on dividing a given interval into a collection of subintervals $S_i(x)$, see Figure A.2, and on constructing an approximating polynomial on each subinterval. This is called piecewise polynomial approximation. The greatest advantage of splines is their smoothness (the approximation functions are continuously differentiable), which is often also required by physical parameters.

Given $(n+1)$ nodes of pairs $(x_i, f(x_i))$, such that $x_0 < x_1 < ... < x_{n-1} < x_n$, a spline function of degree n can be defined as follows:

$$S(x) \quad = \quad \begin{cases} S_0(x) & x \in [x_0, x_1] \\ S_1(x) & x \in [x_1, x_2] \\ \vdots & \vdots \\ S_{n-1}(x) & x \in [x_{n-1}, x_n] \end{cases} \tag{A.8}$$

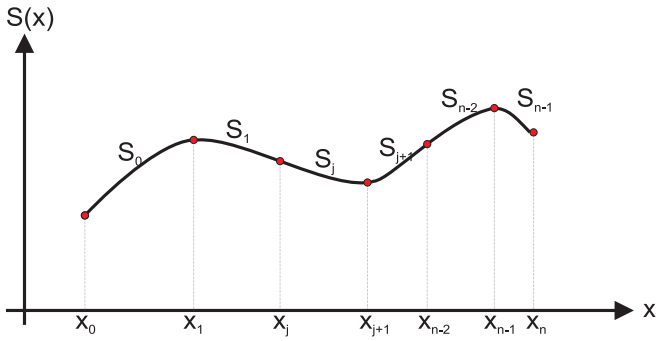

Figure A.2: Definition of subintervals for spline interpolation.

Each $S_i(x)$ in equation (A.8) is a polynomial of degree k, e.g., for $k = 3$:

$$S_i(x) = a_i(x - x_i)^3 + b_i(x - x_i)^2 + c_i(x - x_i) + d_i$$

.

The most common spline interpolation uses cubic splines between every two given nodes and is therefore called *cubic spline interpolation*. A cubic spline interpolant S for a given function f and a set of $(n + 1)$ nodes x_i, with $i = 0, \ldots, n$, has to fulfill the following requirements:

interpolating property	$S_j(x_j) = f(x_j),$	$j = 0, \ldots, n$
continuity	$S_j(x_j) = S_{j-1}(x_j),$	$j = 1, \ldots, n-1$
no break	$S'_j(x_j) = S'_{j-1}(x_j),$	$j = 1, \ldots, n-1$
same curvature	$S''_j(x_j) = S''_{j-1}(x_j),$	$j = 1, \ldots, n-1$

Concerning the boundary conditions, two possibilities are given:

natural boundary condition	$S''(x_0) = S''(x_n) = 0$
clamped boundary condition	$S'(x_0) = f'(x_0)$ and $S'(x_n) = f'(x_n)$

Calculation of a Natural Cubic Spline—An Example Starting from four given points (x_0, y_0),(x_1, y_1),(x_2, y_2),(x_3, y_3), we define:

- $n = 3$
- $k = 0, 1, 2, 3$
- $h_i = x_{i+1} - x_i$, for $i = 0, 1, 2$ (leading to h_0, h_1, h_3)
  $h_i \ldots$ size of the i^{th} interval $[x_i, x_{i+1}]$
- $z_0 = z_3 = 0$, $z_i \ldots$ second derivatives for the (x_i, y_i)

To compute the second derivatives z_1, z_2 for the remaining two points in the middle, equation (A.9), leading to the two linear equations (A.10) and (A.11), has to be solved:

$$h_{i-1}z_{i-1} + 2(h_{i-1} + h_i)z_i + h_i z_{i+1} = 6\left(\frac{y_{i+1} - y_i}{h_i} - \frac{y_i - y_{i-1}}{h_{i-1}}\right) \tag{A.9}$$

leading for $i = 1$ and $i = 2$ to:

$$2(h_0 + h_1)z_1 + h_1 z_2 = 6\left(\frac{y_2 - y_1}{h_1} - \frac{y_1 - y_0}{h_0}\right) \tag{A.10}$$

$$h_1 z_1 + 2(h_1 + h_2)z_2 = 6\left(\frac{y_3 - y_2}{h_2} - \frac{y_2 - y_1}{h_1}\right). \tag{A.11}$$

Adding equation (A.10) multiplied with (h_1) and equation (A.11) multiplied with $[-2\,(h_0 + h_1)]$ leads to the values for the second derivatives in the points (x_1, y_1) and (x_2, y_2), which only depend on the given nodes:

$$z_2 = \frac{6}{h_1^2 - 4(h_1 + h_2)(h_0 + h_1)} \cdot \left[h_1\left(\frac{y_2 - y_1}{h_1} - \frac{y_1 - y_0}{h_0}\right) - 2(h_0 + h_1)\left(\frac{y_3 - y_2}{h_2} - \frac{y_2 - y_1}{h_1}\right)\right] \tag{A.12}$$

$$z_1 = \frac{2}{h_1}\left[3\left(\frac{y_3 - y_2}{h_2} - \frac{y_2 - y_1}{h_1}\right) - (h_1 + h_2)z_2\right] \tag{A.13}$$

Using equation (A.14) for $i = 0, 1, 2$ yields the required cubic splines $S_0(x)$, $S_1(x)$, $S_2(x)$:

$$\begin{aligned} S_i(x) = {} & \frac{z_{i+1}}{6h_i}(x - x_i)^3 + \frac{z_i}{6h_i}(x_{i+1} - x)^3 + \\ & + \left(\frac{y_{i+1}}{h_i} - \frac{h_i}{6}z_{i+1}\right)(x - x_i) + \left(\frac{y_i}{h_i} - \frac{h_i}{6}z_i\right)(x_{i+1} - x) \end{aligned} \tag{A.14}$$

$$S_0(x) = \frac{z_1}{6h_0}(x - x_0)^3 + \left(\frac{y_1}{h_0} - \frac{h_0}{6}z_1\right)(x - x_0) + \frac{y_0}{h_0}(x_1 - x) \tag{A.15}$$

$$\begin{aligned} S_1(x) = {} & \frac{z_2}{6h_1}(x - x_1)^3 + \frac{z_1}{6h_1}(x_2 - x)^3 + \\ & + \left(\frac{y_2}{h_1} - \frac{h_1}{6}z_2\right)(x - x_1) + \left(\frac{y_1}{h_1} - \frac{h_1}{6}z_1\right)(x_2 - x) \end{aligned} \tag{A.16}$$

$$S_2(x) = \frac{z_2}{6h_2}(x_3 - x)^3 + \frac{y_3}{h_2}(x - x_2) + \left(\frac{y_2}{h_2} - \frac{h_2}{6}z_2\right)(x_3 - x) \tag{A.17}$$

Figure A.1 shows the characteristics of cubic polynomial using the Lagrange method and cubic spline interpolation. Spline and polynomial interpolation are approximately the same, employing 4 nodes. The spline interpolation yields a directer connection of the points, less exceeding of the points. Increasing the nodes from 4 to 7 results in an oscillation in the polynomial interpolation (Runge's phenomenon).

A.3 Gorbunov–Steiner Adaption of Polynomial Interpolation

The Gorbunov–Steiner adaption for polynomial interpolation of atmospheric fields[1] is based on cubic interpolation, but only makes use of four (three in the case of the field boundary) adjacent grid points. Depending on the position of the point required relative to the points employed for the adapted polynomial interpolation, three cases may occur:

1. **default**: see Figure A.3, middle;
2. **left-side margin**: see Figure A.3, left;
3. **right-side margin**: see Figure A.3, right.

Two combined polynomials P_{weights}, passing through the two middle points, are used. One polynomial, the cubic P_{f_i}, is fitted to the function values f_2 and f_3 of x_2 and x_3, the other, the quadratic P'_{d_i}, to the mean slope between three points.

For the given four points $(x_1, f_1), (x_2, f_2), (x_3, f_3), (x_4, f_4)$, the interpolation polynomial is chosen in a way that between x_2 and x_3 the following four boundary conditions, defining the four coefficients of the cubic polynomial, are fulfilled:

1. $f(x_2) = f_2$
2. $f(x_3) = f_3$
3. $\frac{\mathrm{d}f}{\mathrm{d}x}\,|_{x=x_2} = \frac{1}{2}\left(\frac{f_3-f_2}{x_3-x_2} + \frac{f_2-f_1}{x_2-x_1}\right) = d_2$
4. $\frac{\mathrm{d}f}{\mathrm{d}x}\,|_{x=x_3} = \frac{1}{2}\left(\frac{f_4-f_3}{x_4-x_3} + \frac{f_3-f_2}{x_3-x_2}\right) = d_3$

$f(x)$ it can be written as $f(x) = P_1 f_1 + P_2 f_2 + P_3 f_3 + P_4 f_4$, where P_1, P_2, P_3, P_4 are universal polynomials. The weights (w_i) for the f_i are the coefficients of the combined cubic and quadratic polynomials:

$$\begin{aligned} P^{\text{default}}_{\text{weights}} &= w_1 f_1 + w_2 f_2 + w_3 f_3 + w_4 f_4 \\ P^{\text{left/right-side margin}}_{\text{weights}} &= w_1 f_1 + w_2 f_2 + w_3 f_3 \end{aligned} \tag{A.18}$$

[1] "Weight4" written by M. E. Gorbunov and A. K. Steiner, 1999.

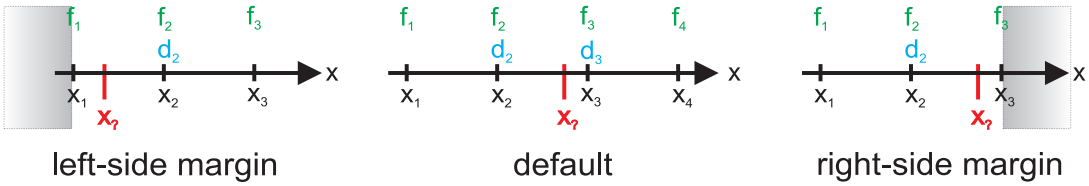

Figure A.3: Cases for the Gorbunov–Steiner adaption for polynomial interpolation.

In the following, the weighting factors for the three different cases (default, left and right side margin) are derived.

A.3.1 Default Case

In the *default case*, the required point is situated such that two given points can be found on its left and right side. In a first step, the polynomials for $P_{d_2} = \text{func}(x_2, x_3)$ and $P_{d_3} = \text{func}(x_2, x_3)$, with P'_{d_3} as the mean slopes between three points are constructed. Afterward, they are combined with the mean slopes $d_2 = \text{func}(x_1, x_2, x_3, f_1, f_2, f_3)$ and $d_3 = \text{func}(x_2, x_3, x_4, f_2, f_3, f_4)$.

Derivation of the Polynomials P_{d_2} and P_{d_3}

Only the values of x_2 and x_3 are taken into account. The formulation is based on the cubic polynomial of equation (A.19) and the condition of equation (A.20):

$$P_{d_i}(x) = \alpha(x - x_i)(x - x_{\text{adjacent}})^2, \tag{A.19}$$

$$d_2 - P_{d_2}(x_2) = P_{d_3}(x_3) \;=\; 0. \tag{A.20}$$

To derive the polynomial P_{d_2}, the first derivative of $P_{d_i}(x)$ (with $i = 2$) in equation (A.19) has to be calculated resulting in a quadratic polynomial. The boundary conditions are given as $P'_{d_2}(x_2) = 1$ and $P'_{d_2}(x_3) = 0$:

$$\begin{aligned}
P_{d_2}(x) &= \alpha(x - x_2)(x - x_3)^2 \\
P'_{d_2}(x) &= \alpha\left[(x - x_3)^2 + 2(x - x_2)(x - x_3)\right] \\
P'_{d_2}(x)\,|_{x=x_2} &\stackrel{!}{=} 1 \;=\; \alpha(x_2 - x_3)^2 \;\rightarrow\; \alpha_{d_2} = \frac{1}{(x_2 - x_3)^2} \\
P_{d_2}(x) &= \frac{1}{(x_2 - x_3)^2}(x - x_2)(x - x_3)^2
\end{aligned} \tag{A.21}$$

In the same way, the polynomial P_{d_3} can be found. The boundary conditions are now $P'_{d_3}(x_3) = 1$ and $P'_{d_3}(x_2) = 0$:

$$\begin{aligned}
P_{d_3}(x) &= \alpha(x - x_3)(x - x_2)^2 \\
P'_{d_3}(x) &= \alpha\left[(x - x_2)^2 + 2(x - x_3)(x - x_2)\right] \\
P'_{d_3}(x)\,|_{x=x_3} &\stackrel{!}{=} 1 \;=\; \alpha(x_3 - x_2)^2 \;\rightarrow\; \alpha_{d_3} = \frac{1}{(x_3 - x_2)^2} \\
P_{d_3}(x) &= \frac{1}{(x_3 - x_2)^2}(x - x_3)(x - x_2)^2
\end{aligned} \tag{A.22}$$

Derivation of the Mean Slopes d_2 and d_3

The mean slope is established by using finite differences between three points. The first three points $(x_1, f_1), (x_2, f_2), (x_3, f_3)$ are used to derive d_2, the second three points $(x_2, f_2), (x_3, f_3), (x_4, f_4)$ to derive d_3:

$$\begin{aligned} d_2 &= \frac{1}{2}\left(\frac{f_2 - f_1}{x_2 - x_1} + \frac{f_3 - f_2}{x_3 - x_2}\right) \\ &= -f_1\left[\frac{1}{2(x_2 - x_1)}\right] + f_2\left[\frac{1}{2(x_2 - x_1)} - \frac{1}{2(x_3 - x_2)}\right] + f_3\left[\frac{1}{2(x_3 - x_2)}\right] \\ d_2 &= -f_1\left[\frac{1}{2}\frac{1}{(x_2 - x_1)}\right] + f_2\left[\frac{1}{2}\frac{x_3 - 2x_2 + x_1}{(x_2 - x_1)(x_3 - x_2)}\right] + f_3\left[\frac{1}{2}\frac{1}{(x_3 - x_2)}\right] \end{aligned} \quad \text{(A.23)}$$

$$\begin{aligned} d_3 &= \frac{1}{2}\left(\frac{f_3 - f_2}{x_3 - x_2} + \frac{f_4 - f_3}{x_4 - x_3}\right) \\ &= -f_2\left[\frac{1}{2(x_3 - x_2)}\right] + f_3\left[\frac{1}{2(x_3 - x_2)} - \frac{1}{2(x_4 - x_3)}\right] + f_4\left[\frac{1}{2(x_4 - x_3)}\right] \\ d_3 &= -f_2\left[\frac{1}{2}\frac{1}{(x_3 - x_2)}\right] + f_3\left[\frac{1}{2}\frac{x_4 - 2x_3 + x_2}{(x_3 - x_2)(x_4 - x_3)}\right] + f_4\left[\frac{1}{2}\frac{1}{(x_4 - x_3)}\right] \end{aligned} \quad \text{(A.24)}$$

Derivation of the Polynomials P_{f_2} and P_{f_3}

To derive the overall polynomial, the two cubic polynomials $P_{f_2} = \text{func}(x_2, x_3)$ and $P_{f_3} = \text{func}(x_2, x_3)$ are required in addition. The formulation to derive theses polynomials differs from the one for the P_{d_i} and is given as follows:

$$P_{f_i}(x) = (x - x_{\text{adjacent}})^2(\alpha + \beta x) \quad \text{(A.25)}$$

$$\begin{aligned} P_{f_i}(x_i) &= 1 \implies P'_{f_i}(x_i) \stackrel{!}{=} 0 \quad \text{(A.26)} \\ P_{f_i}(x_{\text{adjacent}}) &= 0 \implies P'_{f_i}(x_{\text{adjacent}}) \stackrel{!}{=} 0 \end{aligned}$$

Using equation (A.25) and the values for $P_{f_i}(x)$ and $P'_{f_i}(x)$, α and β can be determined in a first step and the polynomial $P_{f_i}(x)$ in a second step:

$$\begin{aligned} P_{f_2}(x_2) &= (x_2 - x_3)^2(\alpha_{f_2} + \beta_{f_2} x_2) \stackrel{!}{=} 1 \implies \\ &\quad (\alpha_{f_2} + \beta_{f_2} x_2) = \frac{1}{(x_2 - x_3)^2} \end{aligned}$$

$$
\begin{aligned}
P'_{f_2}(x_2) &= 2(x_2 - x_3)(\alpha_{f_2} + \beta_{f_2} x_2) + \beta_{f_2}(x_2 - x_3)^2 \implies \\
\beta_{f_2} &= -\frac{2}{(x_2 - x_3)^3} \\
\alpha_{f_2} &= \frac{1}{(x_2 - x_3)^2} - \beta_{f_2} x_2 = \frac{1}{(x_2 - x_3)^2} + \frac{2x_2}{(x_2 - x_3)^3} \\
\alpha_{f_2} &= \frac{3x_2 - x_3}{(x_2 - x_3)^3}
\end{aligned}
$$

$$
\begin{aligned}
P_{f_2}(x) &= (x - x_3)^2 \left[\frac{3x_2 - x_3}{(x_2 - x_3)^3} - \frac{2x}{(x_2 - x_3)^3} \right] \\
P_{f_2}(x) &= (x - x_3)^2 \left[\frac{(3x_2 - x_3 - 2x)}{(x_2 - x_3)^3} \right] \qquad \text{(A.27)}
\end{aligned}
$$

In a similar way, the polynomial $P_{f_3}(x)$ can be found:

$$
\begin{aligned}
P_{f_3}(x_3) &= (x_3 - x_2)^2(\alpha_{f_3} + \beta_{f_3} x_3) \stackrel{!}{=} 1 \implies \\
(\alpha_{f_3} + \beta_{f_3} x_3) &= \frac{1}{(x_3 - x_2)^2}
\end{aligned}
$$

$$
\begin{aligned}
P'_{f_3}(x_3) &= 2(x_3 - x_2)(\alpha_{f_3} + \beta_{f_3} x_3) + \beta_{f_3}(x_3 - x_2)^2 \implies \\
\beta_{f_3} &= -\frac{2}{(x_3 - x_2)^3} \\
\alpha_{f_3} &= \frac{1}{(x_3 - x_2)^2} - \beta_{f_3} x_3 = \frac{1}{(x_3 - x_2)^2} + \frac{2x_3}{(x_3 - x_2)^3} \\
\alpha_{f_3} &= \frac{3x_3 - x_2}{(x_3 - x_2)^3}
\end{aligned}
$$

$$
\begin{aligned}
P_{f_3}(x) &= (x - x_2)^2 \left[\frac{3x_3 - x_2}{(x_3 - x_2)^3} - \frac{2x}{(x_3 - x_2)^3} \right] \\
P_{f_3}(x) &= (x - x_2)^2 \left[\frac{(3x_3 - x_2 - 2x)}{(x_3 - x_2)^3} \right] \qquad \text{(A.28)}
\end{aligned}
$$

Determination of the Combined Polynomial P_{weights}

The overall combined polynomial P_{combined} is formulated as:

$$P_{\text{combined}} = f_2 P_{f_2} + f_3 P_{f_3} + d_2 P_{d_2} + d_3 P_{d_3}. \qquad \text{(A.29)}$$

As d_2 and d_3 are functions of x_i and f_i, P_{weights} (cp., equation (A.18)) can be derived from P_{combined} by inserting the calculated polynomials:

$$\begin{aligned} P_{\text{combined}}(x) &= f_2\left[\frac{(x-x_3)^2(3x_2-x_3-2x)}{(x_2-x_3)^3}\right] + f_3\left[\frac{(x-x_2)^2(3x_3-x_2-2x)}{(x_3-x_2)^3}\right] - \\ & f_1\left[P_{d_2}\ \frac{1}{2(x_2-x_1)}\right] + f_2\left[P_{d_2}\ \frac{x_3-2x_2+x_1}{(x_2-x_1)(x_3-x_2)}\right] + \\ & f_3\left[P_{d_2}\ \frac{1}{2(x_3-x_2)}\right] - f_2\left[P_{d_3}\ \frac{1}{2(x_3-x_2)}\right] + \\ & f_3\left[P_{d_3}\ \frac{x_4-2x_3+x_2}{2(x_3-x_2)(x_4-x_3)}\right] + f_4\left[P_{d_3}\ \frac{1}{2(x_4-x_3)}\right] \end{aligned} \tag{A.30}$$

The weighting factors w_i can now be determined by comparing the coefficients of the f_i in the combined polynomial:

$$f_1: \quad w_1 = \frac{1}{2}\ \frac{(x-x_2)(x-x_3)^2}{(x_1-x_2)(x_2-x_3)^2} \tag{A.31}$$

$$\begin{aligned} f_2: \quad w_2 &= \frac{(x-x_3)^2(3x_2-x_3-2x)}{(x_2-x_3)^3} + \frac{1}{2}\ \frac{(x-x_2)(x-x_3)^2(x_3-2x_2+x_1)}{(x_2-x_3)^2(x_2-x_1)(x_3-x_2)} - \\ & \frac{1}{2}\ \frac{(x-x_3)(x-x_2)^2}{(x_2-x_3)^2(x_3-x_2)} \\ w_2 &= \frac{(x-x_3)}{(x_2-x_3)^3}\left[(x-x_3)(3x_2-x_3-2x) + \right. \\ & \left. \frac{1}{2}(x-x_2)\left(\frac{(x-x_3)(x_3-2x_2+x_1)}{(x_1-x_2)} + x - x_2\right)\right] \end{aligned} \tag{A.32}$$

$$\begin{aligned} f_3: \quad w_3 &= \frac{(x-x_2)^2(3x_3-x_2-2x)}{(x_3-x_2)^3} + \frac{1}{2}\ \frac{(x-x_2)(x-x_3)^2}{(x_3-x_2)(x_2-x_3)^2} + \\ & \frac{1}{2}\ \frac{(x-x_3)(x-x_2)^2(x_4-2x_3+x_2)}{(x_3-x_2)^2(x_4-x_3)(x_3-x_2)} \\ w_3 &= \frac{(x-x_2)}{(x_3-x_2)^3}\left[(x-x_2)(3x_3-x_2-2x) + \right. \\ & \left. \frac{1}{2}(x-x_3)\left(\frac{(x-x_2)(x_4-2x_3+x_2)}{(x_4-x_3)} + x - x_3\right)\right] \end{aligned} \tag{A.33}$$

$$f_4: \quad w_4 = \frac{1}{2}\ \frac{(x-x_3)(x-x_2)^2}{(x_4-x_3)(x_3-x_2)^2} \tag{A.34}$$

A.3.2 Left Side Margin

To interpolate any value situated between the first and second point of the given vector, the *left side margin case* takes place (cp., Figure A.3). The determination of the combined polynomial follows the one of the default case, but the formulation polynomials are now quadratic instead of cubic. This is due to only three points and three boundary conditions used, which uniquely define the three coefficients of square polynomial.

Derivation of the Polynomial P_{d_2} and the Mean Slope d_2

To determine the polynomial P_{d_2}, only the values of x_1 and x_2 and the first derivative (set equal to one) are used:

$$\begin{aligned} P_{d_2}(x) &= \alpha(x - x_2)(x - x_1) \\ P'_{d_2}(x) &= \alpha\left[(x - x_1) + (x - x_2)\right] \\ P'_{d_2}(x)\,|_{x=x_2} &\stackrel{!}{=} 1 \;=\; \alpha(x_2 - x_1) \;\rightarrow\; \alpha_{d_2} = \frac{1}{(x_2 - x_1)} \\ P_{d_2}(x) &= \frac{(x - x_2)(x - x_1)}{(x_2 - x_1)} \end{aligned} \tag{A.35}$$

The mean slope between first and third point, $d_2 = \mathrm{func}(x_1, x_2, x_3, f_1, f_2, f_3)$, is the same as in the default case, shown in equation (A.23).

Derivation of the Polynomial P_{f_1} and P_{f_2}

The polynomials for the f_i are now quadratic:

$$\begin{aligned} P_{f_1}(x) &= \alpha_{f_1}(x - x_2)^2 \\ P_{f_1}(x_1) &= \alpha_{f_1}(x_1 - x_2)^2 \stackrel{!}{=} 1 \Longrightarrow\; \alpha_{f_1} = \frac{1}{(x_1 - x_2)^2} \\ P_{f_1}(x) &= \frac{(x - x_2)^2}{(x_1 - x_2)^2} \end{aligned} \tag{A.36}$$

$$\begin{aligned} P_{f_2}(x) &= (x - x_1)(\alpha_{f_2} + \beta_{f_2} x) \\ P_{f_2}(x_2) &= (x_2 - x_1)(\alpha_{f_2} + \beta_{f_2} x_2) \stackrel{!}{=} 1 \\ & (\alpha_{f_2} + \beta_{f_2} x_2) \;=\; \frac{1}{(x_2 - x_1)} \end{aligned}$$

$$
\begin{aligned}
P'_{f_2}(x_2) &= (x_2 - x_1)\beta_{f_2} + (\alpha_{f_2} + \beta_{f_2} x_2) \stackrel{!}{=} 0 \implies \\
\beta_{f_2} &= -\frac{1}{(x_2 - x_1)^2} \\
\alpha_{f_2} &= \frac{1}{(x_2 - x_1)} - \beta_{f_2} x_2 = \frac{2x_2 - x_1}{(x_2 - x_1)^2}
\end{aligned}
$$

$$
P_{f_2}(x) = \frac{(x - x_1)(2x_2 - x_1 - x)}{(x_2 - x_1)^2} \tag{A.37}
$$

Determination of the Combined Polynomial P_{weights}

The overall combined polynomial P_{combined} is formulated as:

$$
P_{\text{combined}} = f_1 P_{f_1} + f_2 P_{f_2} + d_2 P_{d_2}. \tag{A.38}
$$

Again, P_{weights} can be derived from P_{combined} by inserting the calculated polynomials. The three weighting factors are made up as follows:

$$
f_1: \quad w_1 = \frac{(x - x_2)}{2(x_2 - x_1)^2} \, (x_1 - 2x_2 + x) \tag{A.39}
$$

$$
f_2: \quad w_2 = \frac{(x - x_1)}{(x_2 - x_1)^2} \left[2x_2 - x_1 - x + \frac{1}{2} \frac{(x - x_2)(x_1 - 2x_2 + x_3)}{(x_3 - x_2)} \right] \tag{A.40}
$$

$$
f_3: \quad w_3 = \frac{(x - x_2)(x - x_1)}{2(x_2 - x_1)(x_3 - x_2)} \tag{A.41}
$$

A.3.3 Right Side Margin

The derivation of the coefficients for the *right side margin* (cp., Figure A.3), follows the one for the left side margin. As Figure A.4 shows a summary of the formulations for all three cases, only the results (the weighting coefficients) should be given here:

$$
f_1: \quad w_1 = \frac{(x - x_2)(x - x_3)}{2(x_1 - x_2)(x_2 - x_3)} \tag{A.42}
$$

$$
f_2: \quad w_2 = \frac{(x - x_3)}{(x_2 - x_3)^2} \left[2x_2 - x_3 - x + \frac{1}{2} \frac{(x - x_2)(2x_2 - x_3 - x_1)}{(x_2 - x_1)} \right] \tag{A.43}
$$

$$
f_3: \quad w_3 = \frac{(x - x_2)}{2(x_3 - x_2)^2} \, (x_3 - 2x_2 + x) \tag{A.44}
$$

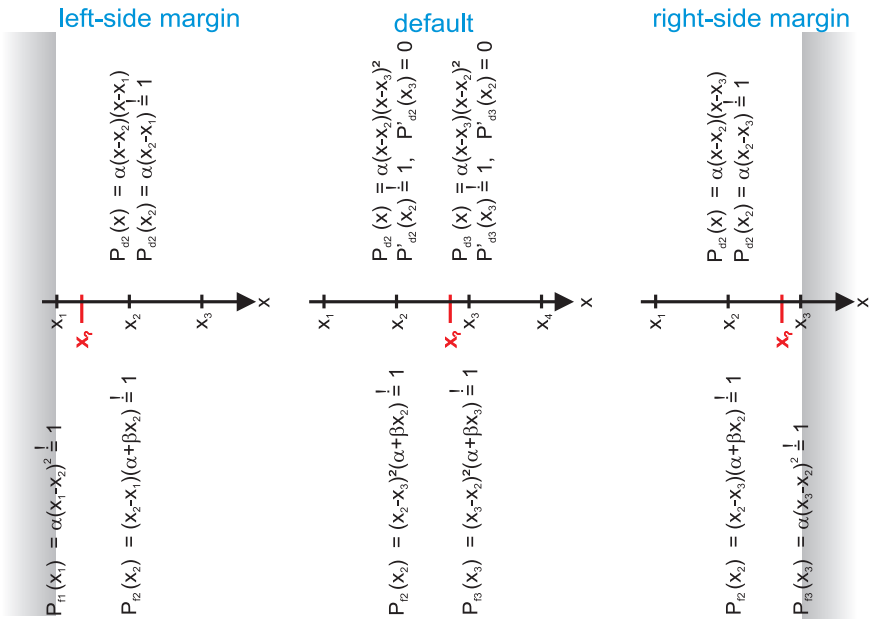

Figure A.4: Summary of the formulations for the adapted EGOPS interpolation routine for the three cases depending on the position of the point to be interpolated (left-side margin, default, right-side margin).

B IPCC$^+$ Region Definitions

Nr.	Abbrev.	Region	Latitude	Longitude
		Zonal Bands		
1	G90	Global90	90S–90N	180W–180E
2	G60	Global60	60S–60N	180W–180E
3	N60	Northern60	00N–60N	180W–180E
4	S60	Southern60	60S–00S	180W–180E
5	ARC	Arctic	60N–90N	180W–180E
6	NHM	Northern Hemisphere Mid–Latitudes	30N–60N	180W–180E
7	TRO	Tropics	15S–15N	180W–180E
8	SHM	Southern Hemisphere Mid–Latitudes	60S–30S	180W–180E
9	ANT	Antartic	90S–60S	180W–180E
		America		
10	ALA	Alaska, NW Canada	60N–72N	170W–103W
11	CGI	East Canada, Greenland and Iceland	50N–85N	103W–010W
12	WNA	Western North America	30N–60N	130W–103W
13	CNA	Central North America	30N–50N	103W–085W
14	ENA	Eastern North America	25N–50N	085W–050W
15	CAM	Central America	10N–30N	116W–083W
16	AMZ	Amazonia	20S–12N	082W–034W
17	SSA	Southern South America	56S–20S	076W–040W
		Europe–Africa		
18	NEU	Northern Europe	48N–75N	010W–040E
19	SEM	Southern Europe Mediterranean	30N–48N	010W–040E
20	SAH	Sahara	18N–30N	020W–065E
21	WAF	Western Africa	12S–18N	020W–022E
22	EAF	Eastern Africa	12S–18N	022E–052E
23	SAF	Southern Africa	35S–12S	010E–052E

continued on next page

Nr.	Abbrev.	Region	Latitude	Longitude
		Asia–Australia		
24	NAS	Northern Asia	50N–70N	040E–180E
25	CAS	Central Asia	30N–50N	040E–075E
26	TIB	Tibetan Plateau	30N–50N	075E–100E
27	EAS	Eastern Asia	20N–50N	100E–145E
28	SAS	Southern Asia	05N–30N	065E–100E
29	SEA	Southeast Asia	11S–20N	095E–155E
30	NAU	Northern Australia	30S–11S	110E–155E
31	SAU	Southern Australia	45S–30S	110E–155E
		Oceans–Seas		
32	NPA	Northern Pacific	00N–40N	150E–120W
33	SPA	Southern Pacific	55S–00S	150E–080W
34	CAR	Caribbean	10N–25N	085W–060W
35	TNE	Tropical Northeast Atlantic	00N–40N	030W–010W
36	MED	Mediterranean Basin	30N–45N	005W–035E
37	IND	Indean Ocean	35S–17.5N	050E–100E

Table B.1: IPCC$^+$ region definitions for large-scale zonal means and as used for the IPCC AR4.

C Content of the Enclosed DVD

The enclosed DVD contains all thesis plots and in addition plots, which were generated for the climate change detection study (chapter 4). All files are provided in the Portable Document Format (**PDF**). The README.pdf contains the DVD content as specified here. The files are arranged in 3 directories:

1. `dissertation_plots`: contains all plots of this thesis; they are assigned to the subdirectories of the respective chapters (`appendix, ch02, ch03, ch04, ch05`);
2. `pLevel`: comprises the subdirectory `indicators` with the indicator plots of the climate change indicator study based on constant pressure (p) levels as vertical coordinate;
3. `zLevel`: contains the results of the climate change indicator study based on constant geopotential height (Z) levels, which are split in the following subdirectories:
   - `indicators`: indicator plots;
   - `trend_GoF`: plots for trend goodness of fit (**GOF**) results;
   - `trends`: plots for vertical trends (relative trends for Z and refractivity (N));
   - `trend_significance`: plots for trend significances;
   - `variability`: data variability of Radio Occultation (**RO**), ECMWF Re-Analysis (**ERA-40**), NCEP/NCAR Re-Analysis (**NRA**), Community Climate System Model 3 (**CCSM3**), ECMWF Hamburg Model (**ECHAM5**), and Hadley Centre Coupled Model, version 3 (**HadCM3**).

C.1 Definition of pLevel and zLevel File Names

The file names are composed of six parts (tags) at most:

1. annotation tag (what is plotted),
2. period tag,
3. data set tag,
4. parameter tag,

5. region tag (where applicable), and
6. time tag.

The tags are combined in the following way to specify each plot:

annotation___period___data set___parameter___region___time.pdf.

Table C.1 summarizes all tags used to assemble the file names of the plots.

C.2 Available pLevel and zLevel Files

The plots of the different data sets are available for all parameters, regions, and seasons (exceptions are mentioned in Table C.1). Depending on data availability, the plots are not provided for all periods. Therefore, Table C.2 summarizes the plots and periods which are available for the three data sets.

	Trends	RelativeTrends	TrendSignificance	TrendGoF	Indicators
Re-Analyses	1[a]	1	1	1	1
GCMs	1, 2[b], 3[c]	1, 3	1, 2, 3	1, 2, 3	1, 3
MAECHAM5	2		2	2	

[a] 1980 to 2001 period
[b] 2001 to 2025 period
[c] 2001 to 2050 period

Table C.2: Summary of plots that are available for the three analysis periods, which are coded by numbers (1 for the 1980 to 2001 period, 2 for the 2001 to 2025 period, and 3 for the 2001 to 2050 period).

The re-analyses trend plots show trends for ERA-40, NRA, and the GCM ensemble average. The re-analyses trend significance and trend GOF plots give the results for ERA-40 only together with the GCM results for comparison. NRA, a first generation analysis, was considered as not suitable. The re-analyses indicator plots are therefore also based on ERA-40 results only.

tag	used tags	comment
annotation	Trends	trends at Z-levels
	RelativeTrends	relative trends (for General Circulation Model (**GCM**)s and re-analyses) at Z-levels given in addition to absolute trends for N, p, and temperature (T)
	TrendSignificance	trend significances
	TrendGoF	GOF results
	IndicatorsAllRuns	indicator results using all GCM simulations
	IndicatorsSelectedRuns	indicator results using 10 selected GCM simulations
	IndicatorsERA	indicator results for ERA-40
period	01_1980_to_12_2001	ERA-40 period, also assessed with GCMs
	01_2001_to_12_2025	Middle Atmosphere Mode of ECMWF Hamburg Model, version 5 (**MAECHAM5**) period, also assessed with GCMs
	01_2001_to_12_2050	GCM period
data set	gcmodels	results based on GCM simulations
	reanalys	results based on re-analyses (ERA-40 and/or NRA)
	maecham	results based on MAECHAM5
parameter	refr	refractivity [N-units or %]
	pres	pressure [Pa or %] at Z-levels
	gpht	geopotential height [m or %] at p-levels
	temp	air temperature [K]
	shum	specific humidity [kg kg^{-1} or %]
	dndz	relative refractivity gradient [%]
	dpdz	relative pressure gradient [%]
	dtdz	temperature gradient [K 100 m^{-1}]
	layt	layer thickness [m], for p-level indicator plots only
region	ZonalMeans, America, Europe-Africa, Asia-Australia, Oceans-Seas	
time	ANN	annual mean (January to December average)
	DJF	December–January–February average
	MAM	March–April–May average
	JJA	June–July–August average
	SON	September–October–November average

Table C.1: Tags used to define file names for files on the enclosed DVD.

In the same way, MAECHAM5 trend plots show in addition the ECHAM5 ensemble average and the GCM ensemble average for comparison. The MAECHAM5 trend significance and trend GOF plots contain for comparison also the GCM results.

List of Figures

List of Tables

Bibliography

Allen, M. R. and S. F. B. Tett (1999).
"Checking for model consistency in optimal fingerprinting."
In: *Climate Dynamics* 15, pp. 419–434. See pp. 97, 103, 125.

Allison, I., N. L. Bindoff, R. A. Bindschadler, P. M. Cox, N. de Noblet,
M. H. England, J. E. Francis, N. Gruber, A. M. Haywood, D. J. Karoly, G. Kaser,
C. Le Quéré, T. M. Lenton, M. E. Mann, B. I. McNeil, A. J. Pitman,
S. Rahmstorf, E. Rignot, H. J. Schellnhuber, S. H. S. andS. C. Sherwood,
R. C. J.Somerville, K. Steffen, E. J. Steig, M. Visbeck, and A. J. Weaver (2009).
The Copenhagen Diagnosis. Updating the World on the Latest Climate Science.
The University of New South Wales, Climate Change Research Centre (CCRC),
Sydney, Australia. See p. 7.

Andrews, D. G., J. R. Holton, and C. B. Leovy (1987).
Middle Atmosphere Dynamics. Academic Press, FL, p. 489. See p. 6.

Anthes, R. A., P. A. Bernhardt, Y. Chen, L. Cucurull, K. F. Dymond, D. Ector,
S. B. Healy, S.-P. Ho, D. C. Hunt, Y.-H. Kuo, H. Liu, K. Manning, C. McCormick,
T. K. Meehan, W. J. Randel, C. Rocken, W. S. Schreiner, S. V. Sokolovskiy,
S. Syndergaard, D. C. Thompson, K. E. Trenberth, T.-K. Wee, N. L. Yen, and
Z. Zeng (2008). "The COSMIC/FORMOSAT-3 Mission: Early Results."
In: *Bulletin of the American Meteorological Society* 89, pp. 313–333.
DOI: 10.1175/BAMS-89-3-313. See p. 16.

Archer, B. and E. W. Weisstein (2010). *Lagrange Interpolating Polynomial.* URL:
http://mathworld.wolfram.com/LagrangeInterpolatingPolynomial.html.
See p. 139.

Baldwin, M. P., L. J. Gray, T. J. Dunkerton, K. Hamilton, P. H. Haynes,
W. J. Randel, J. R. Holton, M. J. Alexander, I. Hirota, T. Horinouchi,
D. B. A. Jones, J. S. Kinnersley, C. Marquardt, K. Sato, and M. Takahashi (2001).
"The quasi-biennial oscillation." In: *Reviews of Geophysics* 39, pp. 179–230.
DOI: 10.1029/1999RG000073. See p. 107.

Barnett, T., F. Zwiers, G. Hegerl, M. Allen, T. Crowley, N. Gillett, K. Hasselmann, P. Jones, B. Santer, R. Schnur, P. Stott, K. Taylor, and S. Tett (2005). "Detecting and Attributing External Influences on the Climate System: A Review of Recent Advances." In: *Journal of Climate* 18, pp. 1291–1314. DOI: 10.1175/JCLI3329.1. See pp. 91, 97.

Basilevsky, A. (1983). *Applied Matrix Algebra in the Statistical Sciences.* Elsevier Science Ltd, p. 389. ISBN: 0-444-00756-3. See p. 101.

Bean, B. R. and E. J. Dutton (1968). *Radio Meteorology.* Dover books on electronics and related areas. New York: Dover, p. 435. See p. 46.

Benestad, R. E. and G. A. Schmidt (2009). "Solar trends and global warming." In: *Journal of Geophysical Research* 114.D14, D14101. ISSN: 0148-0227. DOI: 10.1029/2008JD011639. URL: http://dx.doi.org/10.1029/2008JD011639. See p. 115.

Beyerle, G., T. Schmidt, G. Michalak, S. Heise, J. Wickert, and C. Reigber (2005). "GPS radio occultation with GRACE: Atmospheric profiling utilizing the zero difference technique." In: *Geophysical Research Letters* 32.13, L13806. ISSN: 0094-8276. DOI: 10.1029/2005GL023109. URL: http://dx.doi.org/10.1029/2005GL023109. See p. 15.

Borsche, M., G. Kirchengast, and U. Foelsche (2007). "Tropical tropopause climatology as observed with radio occultation measurements from CHAMP compared to ECMWF and NCEP analyses." In: *J. Geophys. Res.* 34.L03702 (Feb. 2007). DOI: 10.1029/2006GL027918. See p. 18.

Buontempo, C., A. Jupp, and M. Rennie (2008). "Operational NWP assimilation of GPS radio occultation data." In: *Atmospheric Science Letters* 9.3, pp. 129–133. ISSN: 1530-261X. DOI: 10.1002/asl.173. URL: http://dx.doi.org/10.1002/asl.173. See p. 16.

Cardinali, C. (2009). *Forecast sensitivity to observation (FSO) as a diagnostic tool.* ECMWF Tech. Memo. 599. See p. 16.

Christensen, J. H., B. Hewitson, A. Busuioc, A. Chen, X. Gao, I. Held, R. Jones, R. K. Kolli, W.-T. Kwon, R. Laprise, V. Magaña Rueda, L. Mearns, C. G. Menéndez, J. Räisänen, A. Rinke, A. Sarr, and P. Whetton (2007). "Regional Climate Projections." In: *Climate Change 2007: The Physical Science Basis. Contribution of Working Group I to the Fourth Assessment Report of the Intergovernmental Panel on Climate Change.* Ed. by S. Solomon, D. Qin, M. Manning, Z. Chen, M. Marquis, K. B. Averyt, M. Tignor, and H. L. Miller. Cambridge, United Kingdom and New York, NY, USA: Cambridge University Press, pp. 847–940. See p. 49.

Cianflone, R. and M. Weingroff (1997).
"Numerical Weather Prediction (NWP). Impact of Model Structure & Dynamics."
E-learning course of the University Corporation for Atmospheric Research.
URL: www.meted.ucar.edu/topics_nwp.php. See p. 30.

Collins, W. D., C. M. Bitz, M. L. Blackmon, G. B. Bonan, C. S. Bretherton, J. A. Carton, P. Chang, S. C. Doney, J. J. Hack, T. B. Henderson, J. T. Kiehl, W. G. Large, D. S. McKenna, B. D. Santer, and R. D. Smith (2006).
"The Community Climate System Model Version 3 (CCSM3)."
In: *J. Climate* 19.11, pp. 2122–2143. DOI: 10.1175/JCLI3761.1. See pp. 31, 39.

Cordero, E. C. and P. M. de Forster (2006).
"Stratospheric variability and trends in models used for the IPCC AR4."
In: *Atmospheric Chemistry and Physics* 6.12, pp. 5369–5380. ISSN: 1680-7316.
URL: http://www.atmos-chem-phys.net/6/5369/2006/. See pp. 35, 65.

Dodge, Y. (2008). *The Concise Encyclopedia of Statistics (Springer Reference).*
Springer. ISBN: 0387317422. See p. 53.

Draper, N. R. and H. Smith (1981). *Applied Regression Analysis.* 2nd ed.
New York: John Wiley & Sons. See pp. 54, 57.

Faires, J. D. R. L. B. (1998). *Numerical Methods.* 2nd ed. Thomson Brooks/Cole, p. 594. See p. 141.

Foelsche, U., G. Kirchengast, A. Steiner, L. Kornblueh, E. Manzini, and L. Bengtsson (2008*a*). "An observing system simulation experiment for climate monitoring with GNSS radio occultation data: Setup and test bed study."
In: *Journal of Geophysical Research* 113.D11108, pp. 1–14.
DOI: 10.1029/2007JD009231. See pp. 7, 16, 38, 47.

Foelsche, U., B. Pirscher, M. Borsche, G. Kirchengast, and J. Wickert. (2009*a*).
"Assessing the climate monitoring utility of radio occultation data: From CHAMP to FORMOSAT-3/COSMIC." In: *Terr. Atmos. and Oceanic Sci.* 20.1, pp. 155–170. DOI: 10.3319/TAO.2008.01.14.01(F3C). See pp. 10, 17.

Foelsche, U., B. Pirscher, M. Borsche, A. K. Steiner, G. Kirchengast, and C. Rocken (2009*b*). "Climatologies Based on Radio Occultation Data from CHAMP and Formosat-3/COSMIC."
In: *New Horizons in Occultation Research: Studies in Atmosphere and Climate.*
Ed. by A. K. Steiner, B. Pirscher, U. Foelsche, and G. Kirchengast, pp. 181–194.
DOI: 10.1007/978-3-642-00321-9_15.
URL: http://www.springerlink.com/content/g2127786622g1764. See p. 15.

Foelsche, U., M. Borsche, A. K. Steiner, A. Gobiet, B. Pirscher, G. Kirchengast, J. Wickert, and T. Schmidt (2008*b*). "Observing upper troposphere-lower stratosphere climate with radio occultation data from the CHAMP satellite." In: *Climate Dynamics* 31, pp. 49–65. DOI: 10.1007/s00382-007-0337-7. See pp. 13, 18, 49.

Forster, P. M., G. Bodeker, R. Schofield, S. Solomon, and D. Thompson (2007). "Effects of ozone cooling in the tropical lower stratosphere and upper troposphere." In: *Geophys. Res. Lett.* 34, L23813. DOI: 10.1029/2007GL031994. See p. 35.

Giorgi, F. and R. Francisco (2000). "Uncertainties in regional climate change prediction: a regional analysis of ensembles simulations with the HADCM2 coupled AOGCM." In: *Clim. Dyn* 16, pp. 169–182. See p. 49.

Gobiet, A. and G. Kirchengast (2004). "Advancements of Global Navigation Satellite System radio occultation retrieval in the upper stratosphere for optimal climate monitoring utility." In: *J. Geophys. Res.* 109, D24110. DOI: doi:10.1029/2004JD005117. See pp. 8, 11, 39, 115.

Gobiet, A., G. Kirchengast, G. L. Manney, M. Borsche, C. Retscher, and G. Stiller (2007). "Retrieval of temperature profiles from CHAMP for climate monitoring: intercomparison with Envisat MIPAS and GOMOS and different atmospheric analyses." In: *Atmospheric Chemistry and Physics* 7.13, pp. 3519–3536. ISSN: 1680-7316. See pp. 8, 17.

Goody, R., J. Anderson, T. Karl, R. Balstad Miller, G. North, J. Simpson, G. Stephens, and W. Washington (2002). "Why We Should Monitor the Climate." In: *Bulletin of the American Meteorological Society* 83, pp. 873–878. DOI: 10.1175/1520-0477(2002)083<0873:WWSMTC>2.3.CO;2. See pp. 5, 6.

Gorbunov, M. E. and A. K. Steiner (1999). *Weight4*. Fortran 90 Subroutine within the EGOPS module GCM_fields.f90. See p. 42.

Gordon, C., C. Cooper, C. A. Senior, H. Banks, J. M. Gregory, T. C. Johns, J. F. B. Mitchell, and R. A. Wood (2000). "The simulation of SST, sea ice extents and ocean heat transports in a version of the Hadley Centre coupled model without flux adjustments." In: *Climate Dynamics* 16, pp. 147–168. See pp. 32, 39.

Hajj, G. A., C. O. Ao, P. A. Iijima, D. Kuang, E. R. Kursinski, A. J. Mannucci, T. K. Meehan, L. J. Romans, M. de la Torre Juarez, and T. P. Yunck (2004). "CHAMP and SAC-C atmospheric occultation results and intercomparisons." In: *Journal of Geophysical Research* 109, D06109. DOI: 10.1029/2003JD003909. See pp. 10, 15, 17.

Hasselmann, K. (1997). "Multi-pattern fingerprint method for detection and attribution of climate change." In: *Climate Dynamics* 13, pp. 601–611. See p. 97.

Healy, S. B. (2001). "Smoothing radio occultation bending angles above 40 km." In: *Annales Geophysicae* 19, pp. 459–468. See p. 11.

Healy, S. B. and J. R. Eyre (2000). "Retrieving temperature, water vapour and surface pressure information from refractive-index profiles derived by radio occultation: A simulation study." In: *Quarterly Journal of the Royal Meteorological Society* 126, pp. 1661–1683. DOI: 10.1256/smsqj.56606. See p. 14.

Healy, S. B. and J. N. Thépaut (2006). "Assimilation experiments with CHAMP GPS radio occultation measurements." In: *Quarterly Journal of the Royal Meteorological Society* 132 (Jan. 2006), pp. 605–623. See p. 16.

Hedin, A. E. (1991). "Extension of the MSIS thermosphere model into the middle and lower atmosphere." In: *J. Geophys. Res.* 96, pp. 1159–1172. DOI: 10.1029/90JA02125. URL: http://www.agu.org/pubs/crossref/1991/90JA02125.shtml. See p. 11.

Hegerl, G. C., H. von Storch, K. Hasselmann, B. D. Santer, U. Cubasch, and P. D. Jones (1996). "Detecting greenhouse-gas-induced climate change with an optimal fingerprint method." In: *Journal of Climate* 9, pp. 2281–2306. See pp. 97, 102, 127.

Hegerl, G. C., F. W. Zwiers, P. Braconnot, N. P. Gillett, Y. Luo, J. A. M. Orsini, N. Nicholls, J. E. Penner, and P. A. Stott (2007). "Understanding and Attributing Climate Change." In: *Climate Change 2007: The Physical Science Basis. Contribution of Working Group I to the Fourth Assessment Report of the Intergovernmental Panel on Climate Change.* Ed. by S. Solomon, D. Qin, M. Manning, M. M. Z. Chen, K. B. Averyt, M. Tignor, and H. L. Miller. Cambridge University Press, Cambridge, United Kingdom and New York, NY, USA. Chap. Understanding and Attributing Climate Change. See pp. 33, 91, 97.

Hegerl, G. C., O. Hoegh-Guldberg, G. Casassa, M. P. Hoerling, R. S. Kovats, C. Parmesan, D. W. Pierce, and P. A. Stott (2010). "Good Practice Guidance Paper on Detection and Attribution Related to Anthropogenic Climate Change." In: *Meeting Report of the Intergovernmental Panel on Climate Change Expert Meeting on Detection and Attribution of Anthropogenic Climate Change.* Ed. by T. F. Stocker, C. B. Field, D. Qin, V. Barros, G.-K. Plattner, M. Tignor, P. M. Midgley, and K. L. Ebi. University of Bern, Bern, Switzerland: IPCC Working Group I Technical Support Unit. URL: http://www.ipcc.ch/pdf/supporting-

material/ipcc_good_practice_guidance_paper_anthropogenic.pdf.
See pp. 91, 94.

Held, I. M. and B. J. Soden (2006).
"Robust Responses of the Hydrological Cycle to Global Warming."
In: *Journal of Climate* 19, pp. 5686–5699. DOI: 10.1175/JCLI3990.1. See p. 13.

Ho, S.-P., G. Kirchengast, S. Leory, C. Rocken, Y.-H. Kuo, J. Wickert, T. Mannucci, S. Sokolvskiy, W. Schreiner, D. Hunt, A. Steiner, U. Foelsche, and C. Ao (2009).
"Estimates of the Uncertainty for using Global Positioning System Radio Occultation Data for Climate Monitoring: Inter-comparisons of Refractivity Derived from Different Data Centers." In: *J. Geophys. Res.* D23107.
DOI: 10.1029/2009JD011969. See p. 19.

Hocke, K., K. Igarashi, and T. Tsuda (2003). "High-resolution profiling of layered structures in the lower stratosphere by GPS occultation."
In: *Geophysical Research Letters* 30.8, 1426. ISSN: 0094-8276.
DOI: 10.1029/2002GL016566.
URL: http://dx.doi.org/10.1029/2002GL016566. See p. 11.

Holton, J. R. (2004). *An introduction to dynamic meteorology.* 4th ed. Vol. 88. International Geophysics. Academic Press, Boston, MA. See p. 6.

Houghton, J. T., G. J. Jenkins, and J. J. Ephraums, eds. (1990).
IPCC First Assessment Report. Scientific Assessment of Climate change–-Report of Working Group I. Cambridge University Press, p. 365. See p. 4.

Houghton, J. T., L. G. Meira Filho, B. A. Callender, N. Harris, A. Kattenberg, and K. Maskell, eds. (1995). *Climate Change 1995: The Science of Climate Change. Contribution of Working Group I to the Second Assessment of the Intergovernmental Panel on Climate Change.* Cambridge University Press, p. 572. See p. 4.

Houghton, J. T., Y. Ding, D. Griggs, M. Noguer, P. J. van der Linden, and D. Xiaosu, eds. (2001). *Climate Change 2001: The Scientific Basis. Contribution of Working Group I to the Third Assessment Report of the Intergovernmental Panel on Climate Change (IPCC).* Cambridge University Press, p. 944.
See pp. 4, 37.

IPCC (2007). *Climate Change 2007: The Physical Science Basis. Contribution of Working Group I to the Fourth Assessment Report of the Intergovernmental Panel on Climate Change.* Ed. by S. Solomon, D. Qin, M. Manning, Z. Chen, M. Marquis, K. B. Averyt, M. Tignor, and H. L. Miller. Cambridge University Press, Cambridge, United Kingdom and New York, NY, USA, p. 996. See p. 7.

Johns, T. C., J. M. Gregory, W. J. Ingram, C. E. Johnson, A. Jones, J. A. Lowe, J. F. B. Mitchell, D. L. Roberts, D. M. H. Sexton, D. S. Stevenson, S. F. B. Tett, and M. J. Woodage (2003). "Anthropogenic climate change for 1860 to 2100 simulated with the HadCM3 model under updated emissions scenarios." In: *Climate Dynamics* 20, pp. 583–612. DOI: 10.1007/s00382-002-0296-y. See pp. 32, 35.

Jolliffe, I. T. (2002). *Principal Component Analysis.* Springer. ISBN: 0387954422. See p. 99.

Kalnay, E., M. Kanamitsu, R. Kistler, W. Collins, D. Deaven, L. Gandin, M. Iredell, S. Saha, G. White, J. Woollen, Y. Zhu, A. Leetmaa, R. Reynolds, M. Chelliah, W. Ebisuzaki, W. Higgins, J. Janowiak, K. Mo, C. Ropelewski, J. Wang, R. Jenne, and D. Joseph (1996). "The NCEP/NCAR 40-year reanalysis project." In: *Bulletin of the American Meteorological Society* 77.3, pp. 437–471. See p. 28.

Karl, T. R. and K. E. Trenberth (2003). "Modern Global Climate Change." In: *Science* 302.5651, pp. 1719–1723. DOI: 10.1126/science.1090228. URL: http://dx.doi.org/10.1126/science.1090228. See p. 5.

Karl, T. R., S. J. Hassol, C. D. Miller, and W. L. Murray (2006). *Temperature Trends in the Lower Atmosphere: Steps for Understanding and Reconciling Differences.* A Report by the Climate Change Science Program and the Subcommittee on Global Change Research,Washington, D. C. See pp. 3, 26, 69, 92.

Keeling, C. D., S. C. Piper, R. B. Bacastow, M. Wahlen, T. P. Whorf, M. Heimann, and H. A. Meijer (2005). "Atmospheric CO_2 and $^{13}CO_2$ exchange with the terrestrial biosphere and oceans from 1978 to 2000: observations and carbon cycle implications." In: *A History of Atmospheric CO_2 and Its Effects on Plants, Animals, and Ecosystems.* Ed. by J. R. Ehleringer, T. E. Cerling, and M. D. Dearing. Vol. 177. Ecological Studies. Berlin: Springer, pp. 83–113. ISBN: 9780387220697. See p. 3.

Kehrer, J., F. Ladstädter, P. Muigg, H. Doleisch, A. Steiner, and H. Hauser (2008). "Hypothesis Generation in Climate Research with Interactive Visual Data Exploration." In: *IEEE Trans. Visual. Comp. Graphics* 14.6, pp. 1579–1586. DOI: 10.1109/TVCG.2008.139. See p. 86.

Kistler, R., E. Kalnay, W. Collins, S. Saha, G. White, J. Woollen, M. Chelliah, W. Ebisuzaki, M. Kanamitsu, V. Kousky, H. van den Dool, R. Jenne, and M. Fiorino (2001). "The NCEP-NCAR 50-year reanalysis: Monthly means CD-ROM and documentation." In: *Bulletin of the American Meteorological Society* 82.2, pp. 247–267. See pp. 28, 39.

Kursinski, E. R. and G. A. Hajj (2001). "A comparison of water vapor derived from GPS occultations and global weather analyses."
In: *Journal of Geophysical Research* 106.D1, pp. 1113–1138. See p. 14.

Kursinski, E. R., G. A. Hajj, K. R. Hardy, J. T. Schofield, and R. Linfield (1997). "Observing the Earth's atmosphere with radio occultation measurements using the Global Positioning System." In: *Journal of Geophysical Research* 102.D19, pp. 23429–23465. See pp. 7, 9, 11.

Lackner, B. C., A. K. Steiner, F. Ladstädter, and G. Kirchengast (2009). "Trend indicators of atmospheric climate change based on global climate model scenarios."
In: *New Horizons in Occultation Research: Studies in Atmosphere and Climate.*
Ed. by A. K. Steiner, B. Pirscher, U. Foelsche, and G. Kirchengast.
Springer Berlin Heidelberg, pp. 245–258. ISBN: 978-3-642-00320-2. See p. 64.

Ladstädter, F., A. K. Steiner, B. C. Lackner, G. Kirchengast, P. Muigg, J. Kehrer, and H. Doleisch (2009).
"SimVis: An interactive visual field exploration tool applied to climate research."
In: *New Horizons in Occultation Research: Studies in Atmosphere and Climate.*
Ed. by A. K. Steiner, B. Pirscher, U. Foelsche, and G. Kirchengast.
Springer Berlin Heidelberg, pp. 233–244. ISBN: 978-3-642-00320-2. See p. 66.

Laštovička, J., R. A. Akmaev, G. Beig, J. Bremer, and J. T. Emmert (2006).
"ATMOSPHERE: Global Change in the Upper Atmosphere."
In: *Science* 314.5803, pp. 1253–1254. DOI: 10.1126/science.1135134.
eprint: http://www.sciencemag.org/cgi/reprint/314/5803/1253.pdf.
URL: http://www.sciencemag.org. See p. 6.

Leroy, S. S. (1997).
"The measurement of geopotential heights by GPS radio occultation."
In: *Journal of Geophysical Research* 102.D6, pp. 6971–6986. See p. 47.

Leroy, S. S., J. A. Dykema, and J. G. Anderson (2006*a*).
"Climate Benchmarking Using GNSS Occultation."
In: *Atmosphere and Climate Studies by Occultation Methods.*
Ed. by U. Foelsche, G. Kirchengast, and A. K. Steiner. Springer Berlin Heidelberg, pp. 287–301. DOI: 10.1007/3-540-34121-8_24. See pp. 7, 10.

Leroy, S. S., J. G. Anderson, and J. A. Dykema (2006*b*).
"Testing climate models using GPS radio occultation: A sensitivity analysis."
In: *J. Geophys. Res.* 111, D17105. DOI: 10.1029/2005JD006145.
See pp. 47, 92, 125, 129, 133, 137.

Lockwood, M. and C. Fröhlich (2007). "Recent oppositely directed trends in solar climate forcings and the global mean surface air temperature." In: *Proceedings of the Royal Society A: Mathematical, Physical and Engineering Science* 463.2086, pp. 2447–2460. DOI: 10.1098/rspa.2007.1880.
URL: http://dx.doi.org/10.1098/rspa.2007.1880. See p. 115.

Loiselet, M., N. Stricker, Y. Menard, and J.-P. Luntamas (2000).
Metop's GPS based Atmospheric sounders. ESA Bulletin N 102.
URL: http://esamultimedia.esa.int/docs/metop/Loiselet_102.pdf.
See p. 16.

Luntama, J. P., G. Kirchengast, M. Borsche, U. Foelsche, A. K. Steiner, S. Healy, A. von Engeln, E. O'Clerigh, and C. Marquardt (2008).
"Prospects of the EPS GRAS Mission for Operational Atmospheric Applications."
In: *Bulletin of the American Meteorological Society,* pp. 1863–1875.
DOI: 10.1175/2008BAMS2399.1. See p. 16.

Manzini, E. and N. A. McFarlane (1998).
"The effect of varying the source spectrum of a gravity wave parameterization in a middle atmosphere general circulation model." In: *J. Geophys. Res.* 103, pp. 31523–31540. DOI: 10.1029/98JD02274. See p. 37.

Manzini, E., N. A. McFarlane, and C. McLandress (1997).
"Impact of the Doppler spread parameterization on the simulation of the middle atmosphere circulation using the MA/ECHAM4 general circulation model."
In: *J. Geophys. Res.* 102, pp. 25751–25762. DOI: 10.1029/97JD01096. See p. 37.

Manzini, E., E. Roeckner, M. Esch, and L. Bengtsson (2006*a*). "Climatology and Forcing of the Quasi-Biennial Oscillation in the MAECHAM5 Model."
In: *Journal of Climate* 19.16, pp. 3882–3901. DOI: 10.1175/JCLI3830.1.
URL: http://dx.doi.org/10.1175\%2FJCLI3830.1. See p. 39.

Manzini, E., M. A. Giorgetta, M. Esch, L. Kornblueh, and E. Roeckner (2006*b*).
"The influence of sea surface temperatures on the Northern winter stratosphere: Ensemble simulations with the MAECHAM5 model." In: *J. Climate* 19, pp. 3863–3881. DOI: 10.1175/JCLI3826.1. See pp. 37, 39.

McGuffie, K. and A. Henderson-Sellers (2005). *A Climate Modelling Primer.*
New York: Wiley. ISBN: 9780470857519. See p. 29.

Meehl, G. A., T. F. Stocker, W. D. Collins, P. Friedlingstein, A. T. Gaye, J. M. Gregory, A. Kitoh, R. Knutti, J. M. Murphy, A. Noda, S. C. B. Raper, I. G. Watterson, A. J. Weaver, and Z.-C. Zhao (2007). "Global Climate Projections." In: *Climate Change 2007: The Physical Science Basis. Contribution of Working Group I to the Fourth Assessment Report of the Intergovernmental Panel on Climate Change.* Ed. by S. Solomon, D. Qin, M. Manning, Z. Chen, M. Marquis, K. B. Averyt, M. Tignor, and H. L. Miller. Cambridge, UK and New York, NY, USA: Cambridge University Press, pp. 747–845. See pp. 34, 35.

Milton, R. C. (1964). "An Extended Table of Critical Values for the Mann-Whitney (Wilcoxon) Two-Sample Statistic." In: *Journal of the American Statistical Association* 59.307, pp. 925–934. See p. 106.

Mohanakumar, K. (2008). *Stratosphere Troposphere Interactions.* Berlin: Springer. ISBN: 9781402082160. See p. 6.

Nakićenović, N., J. Alcamo, G. Davis, B. de Vries, J. Fenhann, S. Gaffin, K. Gregory, A. Grúbler, T. Y. Jung, T. Kram, E. L. La Rovere, L. Michaelis, S. Mori, T. Morita, W. Pepper, H. Pitcher, L. Price, K. Riahi, A. Roehrl, H.-H. Rogner, A. Sankovski, M. Schlesinger, P. Shukla, S. Smith, R. Swart, S. van Rooijen, N. Victor, and Z. Dadi (2000). *IPCC Special Report on Emissions Scenarios.* Ed. by N. Nakićenović and R. Swart. Cambridge University Press, UK., p. 570. See pp. 33–35, 163.

National Oceanic and Atmospheric Administration, National Aeronautics and Space Administration, and United States Air Force (1976). *U.S. Standard Atmosphere 1976.* NAOO-S/T 76-1562. Washington, D. C.: U.S. Government Printing Office, p. 241. See p. 44.

Neftel, A., E. Moor, H. Oeschger, and B. Stauffer (1985). "Evidence from polar ice cores for the increase in atmospheric CO_2 in the past two centuries." In: *Nature* 315, pp. 45–47. DOI: 10.1038/315045a0. See p. 3.

Peixoto, P. J. (2007). *Physics of Climate.* Springer, p. 520. ISBN: 0883187124. See p. 43.

Pirscher, B. (2010). "Multi-Satellite Climatologies of Fundamental Atmospheric Variables From Radio Occultation and Their Validation." PhD Thesis. University of Graz. See pp. 7, 9, 15, 39.

Pope, V. D., M. L. Gallani, P. R. Rowntree, and R. A. Stratton (2000). "The impact of new physical parametrizations in the Hadley Centre climate model: HadAM3." In: *Climate Dynamics* 16, pp. 123–146. See pp. 32, 39.

Randall, D. A., R. A. Wood, S. Bony, R. Colman, T. Fichefet, J. Fyfe, V. Kattsov, A. Pitman, J. Shukla, J. Srinivasan, R. J. Stouffer, A. Sumi, and K. Taylor (2007). "Climate Models and Their Evaluation." In: *Climate Change 2007: The Physical Science Basis. Contribution of Working Group I to the Fourth Assessment Report of the Intergovernmental Panel on Climate Change.* Ed. by S. Solomon, D. Qin, M. Manning, Z. Chen, M. Marquis, K. B. Averyt, M. Tignor, and H. L. Miller. Cambridge University Press, Cambridge, United Kingdom and New York, NY, USA, pp. 589–662. See pp. 30–32.

Randel, W. J., K. P. Shine, J. Austin, J. Barnett, C. Claud, N. P. Gillett, P. Keckhut, U. Langematz, R. Lin, C. Long, C. Mears, A. Miller, J. Nash, D. J. Seidel, D. W. J. Thompson, F. Wu, and S. Yoden (2009). "An update of observed stratospheric temperature trends." In: *Journal of Geophysical Research - Atmospheres* 114.D2, D02107. ISSN: 0148-0227. DOI: 10.1029/2008JD010421. URL: http://dx.doi.org/10.1029/2008JD010421. See p. 7.

Rapp, J. (2000). "Konzeption, Problematik und Ergebnisse klimatologischer Trendanalysen für Europa und Deutschland." PhD thesis. Institut für Meteorologie und Geophysik, Universität Frankfurt/Main. See p. 73.

Reichler, T. and J. Kim (2008). "Uncertainties in the climate mean state of global observations, reanalyses, and the GFDL climate model." In: *Journal of Geophysical Research* 113, D05106. ISSN: 0148-0227. DOI: 10.1029/2007JD009278. See pp. 27, 35, 65.

Rieder, M. J. and G. Kirchengast (2001). "Error analysis and characterization of atmospheric profiles retrieved from GNSS occultation data." In: *J. Geophys. Res.* 106 (Dec. 2001), pp. 31755–31770. DOI: 10.1029/2000JD000052. See p. 11.

Ringer, M. A. and S. B. Healy (2008). "Monitoring twenty-first century climate using GPS radio occultation bending angles." In: *Geophys. Res. Lett.* 35, L05708. DOI: 10.1029/2007GL032462. See pp. 17, 85, 92, 129, 133, 137.

Rocken, C., W. Schreiner, S. Sokolovskiy, and D. Hunt (2009). *Ionospheric Errors in COSMIC Radio Occultation Profiles.* Paper presented at the 89th American Meteorological Society Annual Meeting, Phoenix, AZ, USA. See p. 115.

Roeckner, E., R. Brokopf, M. Esch, M. Giorgetta, S. Hagemann, L. Kornblueh, E. Manzini, U. Schlese, and U. Schulzweida (2003*b*). *The atmospheric general circulaton model ECHAM5, Part II: Sensitivity of Simulated Climate to Horizontal and Vertical Resolution.* Report No. 354. 56 pp. Max-Planck-Insitute for Meteorology, Hamburg, Germany. See pp. 32, 39.

Roeckner, E., G. Bäuml, L. Bonaventura, R. Brokopf, M. Esch, M. Giorgetta, S. Hagemann, I. Kirchner, L. Kornblueh, E. Manzini, A. Rhodin, U. Schlese, U. Schulzweida, and A. Tompkins (2003*a*).
The atmospheric general circulaton model ECHAM5. Report No. 349. 127 pp. Max-Planck-Insitute for Meteorology, Hamburg, Germany. See pp. 31, 39.

Roeckner, E., J. Jungclaus, U. Mikolajewicz, and S. Hagemann (2005).
Model Information of Potential Use to the IPCC Lead Authors and the AR4: ECHAM5_MPI-OM. Available from `www-pcmdi.llnl.gov/ipcc/model_documentation/ipcc_model_documentation.php`, 12/2007. See p. 35.

Santer, B. D., T. M. L. Wigley, J. S. Boyle, D. J. Gaffen, J. J. Hnilo, D. Nychka, D. E. Parker, and K. E. Taylor (2000). "Statistical significance of trends and trend differences in layer-average atmospheric temperature time series."
In: *J. Geophys. Res.* 105.D6, pp. 7337–7356. See pp. 60, 68.

Santer, B. D., T. M. L. Wigley, A. J. Simmons, P. W. Kållberg, G. A. Kelly, S. M. Uppala, C. Ammann, J. S. Boyle, W. Brüggemann, C. Doutriaux, M. Fiorino, C. Mears, G. A. Meehl, R. Sausen, K. E. Taylor, W. M. Washington, M. F. Wehner, and F. J. Wentz (2004). "Identification of anthropogenic climate change using a second-generation reanalysis."
In: *Journal of Geophysical Research* 109.D21104. DOI: `10.1029/2004JD005075`. See p. 86.

Santer, B. D., P. W. Thorne, L. Haimberger, K. E. Taylor, T. M. L. Wigley, J. R. Lanzante, S. Solomon, M. Free, P. J. Gleckler, P. D. Jones, T. R. Karl, S. A. Klein, C. Mears, D. Nychka, G. A. Schmidt, S. C. Sherwood, and F. J. Wentz (2008). "Consistency of modelled and observed temperature trends in the tropical troposphere." In: *International Journal of Climatology* 28, pp. 1703–1722. DOI: `10.1029/2005GL025370`.
URL: `http://dx.doi.org/10.1002/joc.1756`. See p. 69.

Schmidt, G. A., D. T. Shindell, R. L. Miller, M. E. Mann, and D. Rind (2004).
"General circulation modelling of Holocene climate variability."
In: *Quaternary Science Reviews* 23, pp. 2167–2181.
DOI: `10.1016/j.quascirev.2004.08.005`. See p. 32.

Schmidt, T., S. Heise, J. Wickert, G. Beyerle, and C. Reigber (2004).
"GPS radio occultation with CHAMP: monitoring of climate change parameters."
In: *Atmos. Chem. Phys. Discuss.* 4, pp. 7837–7857. See p. 17.

Schmidt, T., J. Wickert, and A. Haser (2010).
"Variability of the upper troposphere and lower stratosphere observed with GPS radio occultation bending angles and temperatures."
In: *Advances in Space Research* In Press, Corrected Proof. ISSN: 0273-1177.
DOI: 10.1016/j.asr.2010.01.021.
URL: http://www.sciencedirect.com/science/article/B6V3S-4Y646NY-3/2/7a7bae7a44e0a535149046a429c0360a. See p. 17.

Schreiner, W. S., D. C. Hunt, C. Rocken, and S. Sokolovskiy (1998). "Precise GPS Data Processing for the GPS/MET Radio Occultation Mission at UCAR." In: *Proceedings of the 1998 National Technical Meeting of the Institute of Navigation.* Westin Long Beach Hotel, Long Beach, CA, pp. 103–112. See p. 21.

Seidel, D. J., J. K. Angell, J. Christy, M. Free, S. A. Klein, J. R. Lanzante, C. Mears, D. Parker, M. Schabel, R. Spencer, A. Sterin, P. Thorne, and F. Wentz (2004). "Uncertainty in Signals of Large-Scale Climate Variations in Radiosonde and Satellite Upper-Air Temperature Datasets." In: *Journal of Climate* 17, pp. 2225–2240. See p. 104.

Sherwood, S. C., J. R. Lanzante, and C. L. Meyer (2005).
"Radiosonde Daytime Biases and Late-20th Century Warming." In: *Science* 309, pp. 1556–1559. DOI: 10.1126/science.1115640. See p. 26.

Simmons, A. J. and J. K. Gibson (2000). *The ERA-40 project plan.*
ERA-40 Project Report Series 1.
Reading, U.K.: European Centre for Medium Range Weather Forecasts.
See pp. 27, 39.

Smith, E. K. and S. Weintraub (1953). "The constants in the equation for atmospheric refractive index at radio frequencies." In: *Proceedings of the I.R.E.* 41, pp. 1035–1037. See p. 46.

Soden, B. J. and I. M. Held (2006).
"An Assessment of Climate Feedbacks in Coupled Ocean Atmosphere Models."
In: *Journal of Climate* 19, pp. 3354–3360. DOI: 10.1175/JCLI3799.1. See p. 7.

Solomon, S., K. Rosenlof, R. Portmann, J. Daniel, S. Davis, T. Sanford, and G.-K. Plattner (2010). "Contributions of Stratospheric Water Vapor to Decadal Changes in the Rate of Global Warming." In: *Science,* pp. 1–6.
DOI: 10.1126/science.1182488.
URL: http://dx.doi.org/10.1126/science.1182488. See p. 7.

Steiner, A. K. and G. Kirchengast (2005). "Error analysis for GNSS radio occultation data based on ensembles of profiles from end-to-end simulations."
In: *J. Geophys. Res.* 110.D15307. DOI: 10.1029/2004JD005251. See p. 18.

Steiner, A. K., G. Kirchengast, M. Borsche, U. Foelsche, and T. Schoengassner (2007). "A multi-year comparison of lower stratospheric temperatures from CHAMP radio occultation data with MSU/AMSU records." In: *J. Geophys. Res.* 112, p. D22110. DOI: 10.1029/2006JD008283. See pp. 7, 17, 92.

Steiner, A. K., G. Kirchengast, B. C. Lackner, B. Pirscher, M. Borsche, and U. Foelsche (2009*a*). "Atmospheric Temperature change detection with GPS radio occultation 1995 to 2008." In: *Geophysical Research Letters* 36.18, L18702. DOI: 10.1029/2009GL039777. See pp. 7, 12, 17, 18, 92, 93, 163.

Steiner, A. K., G. Kirchengast, M. Borsche, and U. Foelsche (2009*b*). "Lower stratospheric temperatures from CHAMP RO compared to MSU/AMSU records: An analysis of error sources." In: *New Horizons in Occultation Research: Studies in Atmosphere and Climate.* Ed. by A. K. Steiner, B. Pirscher, U. Foelsche, and G. Kirchengast. Springer Berlin Heidelberg. Chap. Lower stratospheric temperatures from CHAMP RO compared to MSU/AMSU records: An analysis of error sources, pp. 219–234. ISBN: 978-3-642-00320-2. See p. 18.

Steiner, A., G. Kirchengast, U. Foelsche, L. Kornblueh, E. Manzini, and L. Bengtsson (2001). "GNSS occultation sounding for climate monitoring." In: *Phys. Chem. Earth (A)* 26, pp. 113–124. See p. 16.

Syndergaard, S. (1998). "Modeling the impact of the Earth's oblateness on the retrieval of temperature and pressure profiles from limb sounding." In: *Journal of Atmospheric and Solar-Terrestrial Physics* 60, pp. 171–180. DOI: 10.1016/S1364-6826(97)00056-4. See p. 11.

Syndergaard, S. (1999). *Retrieval analysis and methodologies in atmospheric limb sounding using the GNSS radio occultation technique.* DMI Sci. Rep. 99-6. Danish Meteorol. Inst., Copenhagen, Denmark, p. 131. See p. 11.

Thorne, P. W., D. E. Parker, S. F. B. Tett, P. D. Jones, M. McCarthy, H. Coleman, and P. Brohan (2005*a*). "Revisiting radiosonde upper air temperatures from 1958 to 2002." In: *Journal of Geophysical Research (Atmospheres)* 110, D18105. DOI: 10.1029/2004JD005753. See pp. 24, 26, 159.

Thorne, P. W., D. E. Parker, J. R. Christy, and C. A. Mears (2005*b*). "Uncertainties in Climate Trends: Lessons from Upper-Air Temperature Records." In: *Bulletin of the American Meteorological Society* 86, pp. 1437–1442. DOI: 10.1175/BAMS-86-10-1437. See pp. 19, 39.

Trenberth, K. E. (1997). "The Definition of El Niño." In: *Bull. Amer. Met. Soc.* 78, pp. 2771–2777. See p. 107.

Trenberth, K. E. and D. P. Stepaniak (2001). "Indices of El Niño Evolution." In: *Journal of Climate* 14.8, pp. 1697–1701. DOI: 10.1175/1520-0442(2001)014<1697:LIOENO>2.0.CO;2. See p. 107.

Trenberth, K. E., T. R. Karl, and T. W. Spence (2002). "The Need for a Systems Approach to Climate Observations." In: *Bull. Amer. Meteor. Soc.* 83, pp. 1593–1602. DOI: 10.1175/BAMS-83-11-1593. See pp. 5, 6.

Trenberth, K. E., P. D. Jones, P. Ambenje, R. Bojariu, D. Easterling, A. Klein Tank, D. Parker, F. Rahimzadeh, J. A. Renwick, M. Rusticucci, B. Soden, and P. Zhai (2007). "Observations: Surface and Atmospheric Climate Change." In: *Climate Change 2007: The Physical Science Basis. Contribution of Working Group I to the Fourth Assessment Report of the Intergovernmental Panel on Climate Change.* Ed. by S. Solomon, D. Qin, M. Manning, Z. Chen, M. Marquis, K. Averyt, M. Tignor, and H. Miller. Cambridge University Press, Cambridge, United Kingdom and New York, NY, USA, p. 11. See p. 28.

United Nations Environment Programme, Ozone Secretariat, ed. (2009). *Handbook for the Montreal Protocol on Substances that Deplete the Ozone Layer.* 8th ed. ISBN 9966-7319-0-3. PO Box 30552, Nairobi, Kenya. URL: http://ozone.unep.org. See p. 6.

Untch, A. and A. J. Simmons (1999). "Increased stratospheric resolution in the ECMWF forecasting system." In: *ECMWF Newsletter.* 82. ECMWF, Reading, United Kingdom, pp. 2–8. See p. 15.

Uppala, S. M., P. W. Kållberg, A. J.Simmons, U. Andrae, B. Da Costa, M. Fiorino, J. K. Gibson, J. H. A. Hernandez, G. A. Kelly, X. Li, K. Onogi, S. Saarinen, N. Sokka, R. P. Allan, E. Andersson, K. Arpe, M. A. Balmaseda, A. C. M. Beljaars, L. Van De Berg, J. Bidlot, N. Bormann, S. Caires, F. Chevallier, A. Dethof, M. Dragosavac, M. Fisher, M. Fuentes, S. Hagemann, E. Hólm, B. J. Hoskins, L. Isaksen, P. A. E. M. Janssen, R. Jenne, A. P. Mcnally, J. F. Mahfouf, J. J. Morcrette, N. A. Rayner, R. W. Saunders, P. Simon, A. Sterl, K. E. Trenberth, A. Untch, D. Vasiljevic, P. Viterbo, and J. Woollen (2005). "The ERA-40 re-analysis." In: *Quarterly Journal of the Royal Meteorological Society* 131.612, pp. 2961–3012. ISSN: 0035-9009. DOI: 10.1256/qj.04.176. URL: http://dx.doi.org/10.1256/qj.04.176. See pp. 15, 26–28, 39.

Vedel, H. and M. Stendel (2003).
"On the direct use of GNSS refractivity measurements for climate monitoring."
In: *Proceedings from the 4th Oersted International Science Team Conference (OIST-4).* Ed. by P. Stauning. Copenhagen, DK: Danish Meteorological Institute, pp. 275–278. See p. 47.

Vorob'ev, V. V. and T. G. Krasil'nikova (1994).
"Estimation of the Accuracy of the Atmospheric Refractive Index Recovery from Doppler Shift Measurements at Frequencies used in the NAVSTAR System."
In: *Phys. of Atmos. and Oceans* 29, pp. 602–609. See pp. 8, 11.

Ware, R., M. Exner, D. Feng, M. Gorbunov, K. Hardy, B. Herman, Y. Kuo, T. Meehan, W. Melbourne, C. Rocken, W. Schreiner, S. Sokolovskiy, F. Solheim, X. Zou, R. Anthes, S. Businger, and K. Trenberth (1996).
"GPS Sounding of the atmosphere from Low Earth Orbit: Preliminary results."
In: *Bulletin of the American Meteorological Society* 77.1, pp. 19–40. See p. 15.

Weart, S. (2003). *The Discovery of Global Warming.*
Cambridge: Harvard University Press, p. 228. ISBN: 0674016378. See p. 3.

Weisstein, E. W. (2007). *Least Squares Fitting–Perpendicular Offsets.*
From MathWorld–A Wolfram Web Resource. URL: `http://mathworld.wolfram.com/LeastSquaresFittingPerpendicularOffsets.html`.
See p. 55.

Wickert, J., C. Reigber, G. Beyerle, R. König, C. Marquardt, T. Schmidt, L. Grunwaldt, R. Galas, T. K. Meehan, W. G. Melbourne, and K. Hocke (2001).
"Atmospheric sounding by GPS radio occultation: First results from CHAMP."
In: *Geophysical Research Letters* 28.17, pp. 3263–3266. See p. 15.

Wickert, J., T. Schmidt, G. Beyerle, R. König, C. Reigber, and N. Jakowski (2004).
"The radio occultation experiment aboard CHAMP: Operational data analysis and validation of vertical atmospheric profiles."
In: *Journal of the Meteorological Society of Japan* 82, pp. 381–395. See p. 15.

Wickert, J., G. Beyerle, R. König, S. Heise, L. Grunwaldt, G. Michalak, C. Reigber, and T. Schmidt (2005).
"GPS radio occultation with CHAMP and GRACE: A first look at a new and promising satellite configuration for global atmospheric sounding."
In: *Annales Geophysicae* 23, pp. 653–658. See p. 15.

Wilks, D. S. (2006). *Statistical methods in the atmospheric sciences.* 2nd ed.
Burlington; San Diego; London: Academic Press Inc., p. 648. See pp. 54, 59, 60.

Zwiers, F. W. (2009). "Climate change detection and attribution methods."
Presentation given at the 6th GKSS School on Environmental Research, Lecce, Italy. See p. 93.

von Storch, H. and F. W. Zwiers (2002). *Statistical Analysis in Climate Research.* Cambridge University Press, p. 484. ISBN: 0521012309. See p. 99.

Abstract:
The upper troposphere-lower stratosphere (UTLS) region is reacting particularly sensitive to climate change and variations of its key parameters are promising candidates for the monitoring and diagnosis of climate change. The satellite-based radio occultation (RO) method provides high quality measurements of atmospheric parameters in the UTLS featuring characteristics such as long-term stability, self-calibration, and very good height resolution. This study assesses the potential of RO parameters as climate change indicators and the climate change detection capability of the RO record. For the trend indicator study, 2 re-analyses and 3 representative global climate models (GCM) were used as proxy data for the still short RO record. Seasonal means were systematically explored to find the most robust and sensitive trend indicators based on agreement amongst single model simulations, statistical trend significance, and goodness-of-fit. Different investigated spatial domains allowed a mapping of regions particularly suitable as trend indicators. Refractivity, pressure and respective layer gradients alone turned out as adequate trend indicators. In addition, temperature is a sensitive indicator directly showing UT warming and LS cooling. For climate signal detection an optimal fingerprinting method was applied to the monthly mean RO record. UTLS trends of RO refractivity, geopotential height, and temperature were investigated for two periods. Characteristics of the data and atmospheric variability patterns were discussed. Results showed that a climate change signal consistent with the projections of the GCMs can be detected for temperature with 90% confidence. Lower confidence levels are achieved for the refractivity record. For geopotential height the results are uncertain as the variances between models and observations were found to be only marginally consistent. Overall the results underline the benefit of RO data for climate science.

Zum Inhalt:
Die Region der oberen Troposphäre und unteren Stratosphäre (UTLS) reagiert besonders empfindlich auf den Klimawandel. Veränderungen von Schlüsselparametern in dieser Region sind vielversprechende Kandidaten zur Beobachtung des Klimawandels. Die satellitenbasierte Radiookkultationsmethode (RO) stellt hochqualitative Messungen atmosphärischer UTLS Parameter zur Verfügung, die Charakteristika wie Langzeitstabilität, Selbstkalibrierung und sehr gute Höhenauflösung aufweisen. Diese Arbeit beinhaltet eine Potenzialanalyse verschiedener Radiookkultationsparameter als Klimawandelindikatoren und eine Klimawandeldetektionstudie basierend auf RO Daten. In der Trendindikatorenstudie wurden Proxydaten von 2 Reanalysen und 3 globalen Klimamodellen für den noch kurzen RO Datensatz verwendet. Saisonale Mittelwerte wurden systematisch analysiert, um die robustesten und sensitivsten Trendindikatoren zu finden, welche auf der Übereinstimmung von Trends verschiedener Simulationen, statistischer Trendsignifikanz, und Anpassungsgüte basieren. Die Untersuchung mehrerer Regionen erlaubte eine Identifikation von Gebieten, welche gut als Trendindikatoren geeignet sind. Refraktivität, Druck und die entsprechenden Schicht-Gradienten erwiesen sich als adäquate Trendindikatoren der UTLS. Die Detektion eines anthropogen bedingten Klimasignals in monatlichen RO Daten wurde mit einer Fingerprinting Methode untersucht. UTLS Trends in Refraktivität, geopotentieller Höhe und Temperatur wurden für 2 Perioden analysiert. Datencharakteristika und Muster atmosphärischer Variabilität wurden diskutiert. Die Resultate zeigen für Temperatur ein Klimaänderungssignal konsistent zu den Modellprojektionen auf einem 90% Signifikanzniveau. Geringere Signifikanzniveaus werden für Refraktivität erzielt, während für geopotentielle Höhe noch Unsicherheiten bezüglich der Varianzen zwischen Modellen und Beobachtungen bestehen. Die Ergebnisse unterstreichen den Nutzen der RO Daten für die Klimaforschung.

Wegener Center for Climate and Global Change
University of Graz
Leechgasse 25
A-8010 Graz, Austria
www.wegcenter.at
ISBN 978-3-9502940-5-7